

LEVEL II

AD A070117



Edward L. Ginzton Laboratory

OF THE

W. W. HANSEN LABORATORIES OF PHYSICS

STANFORD UNIVERSITY · STANFORD, CALIFORNIA 94305



DISTRIBUTION STATEMENT A

Approved for public release;
Distribution Unlimited



DDC FILE COPY

11

Research Support and Publications
Activity for the Edward L. Ginzton
Laboratory

JSEP Contract N00014-75-C-0632

G.L. Report No. 2924

11 1 October 1978

13 1 31

AT ...

M. /Chodorow, B. A. /Auld, M. R. Beasley,
S. E. /Harris G. S. /Kino

11 GL 3774

Accession For	
NTIS GRA&I	<input checked="checked" type="checkbox"/>
DDC TAB	<input type="checkbox"/>
Unannounced	<input type="checkbox"/>
Justification	
By	
Distribution/	
Availability Codes	
Avail and/or special	
A	

DDC
RECEIVED
JUN 20 1979
D

DISTRIBUTION STATEMENT A

Approved for public release;
Distribution Unlimited

409 640

JOB

Research Support and Publications Activity for
the Edward L. Ginzton Laboratory
JSEP Contract N00014-75-C-0632

TABLE OF CONTENTS

		<u>PAGE</u>
I.	INTRODUCTION.	1
II.	GINZTON LABORATORY RESEARCH CONTRACTS AND GRANTS (as of 30 September 1978).	3
III.	REPRINTS OF JOURNAL ARTICLES REPORTING JSEP SPONSORSHIP (1 July 1973 through 30 September 1978)	9
	<u>H.L. Report No.</u>	
2179	C. M. Fortunko and H. J. Shaw, "Signal Transformation with Recirculating SAW Delay Lines," (January 1974).	11
2218	J. F. Havlice, G. S. Kino, and C. F. Quate, "Electronically Focused Acoustic Imaging Device," (1 December 1973).	17
2294	H. Hayakawa and G. S. Kino, "Storage of Acoustic Signals in Surface States in Silicon," (15 August 1974)	21
2297	R. A. Lemons and C. F. Quate, "Integrated Circuits as Viewed with an Acoustic Microscope," (1 September 1974)	25
2335	J. H. Goll and B. A. Auld, "Multilayer Impedance Matching Schemes for Broadbanding of Water Loaded Piezoelectric Transducers and High Q Electric Resonators," (January 1975).	29
2445	J. Fraser, J. Havlice, G. Kino, W. Leung, H. Shaw, K. Toda, T. Waugh, D. Winslow, and L. Zitelli, "An Electronically Focused Two-Dimensional Acoustic Imaging System," (February 1975)	31
2518	G. S. Kino, "Acoustoelectric Interactions in Acoustic Interactions in Acoustic Surface Wave Devices," (May 1976)	59
2570.	L. Bui, H. J. Shaw, and L. T. Zitelli, "Study of Acoustic Wave Resonance in Piezoelectric PVF ₂ Film," (September 1977)	85

PAGE

III. REPRINTS OF JOURNAL ARTICLES (continued)

H.L.
Report No.

2573	L. Bui, H. J. Shaw, and L. T. Zitelli, "Experimental Broadband Ultrasonic Trans- ducers using PVF ₂ Piezoelectric Film," (5 August 1976).	91
2586	P. G. Borden and G. S. Kino, "Correlation with the Storage Convolver," (1 November 1976)	93
2605	D. F. Moore, J. M. Rowell, and M. R. Beasley, "Superconductive Tunneling into Niobium-Tin Thin Films," (1976).	97
2622	B. A. Auld, J. J. Gagnepain, and M. Tan, "Horizontal Shear Surface Waves on Corrugated Surfaces," (25 November 1976).	101
2695	C. S. DeSilets, J. D. Fraser, and G. S. Kino, "The Design of Efficient Broadband Piezo- electric Transducers," (May 1978).	105
2708	B. A. Auld and B.-H. Yeh, "Piezoelectric Shear Surface Wave Grating Resonators," (May 1977)	117
2735	A. Atalar, C. F. Quate, and H. K. Wickramasinghe, "Phase Imaging in Reflection with the Acoustic Microscope," (15 December 1977).	125
2819	S. E. Harris, J. Lukasik, J. F. Young, and L. J. Zych, "Anti-Stokes Emission as a VUV and Soft X-ray Source," (June 1978).	129

IV. JSEP Reports (Progress Reports, Technical Reports, Preprints, Publications, and Internal Memoranda Prepared under the Sponsorship of JSEP (1 July 1973 through 30 September 1978)	139
---	-----

SUPPLEMENT: Index of all Ginzton Laboratory Reports on All Contracts
and Grants (1 January 1977 through 30 September 1978).

I

INTRODUCTION

This report has been assembled and prepared at the request of the Scientific Officer for JSEP Contract N00014-75-C-0632 to accommodate the following objectives:

1. To provide information concerning the general thrust of research programs underway within the Edward L. Ginzton Laboratory - not only those of the JSEP project faculty - but for other research faculty as well. Section II lists, for the entire laboratory, all ongoing research contracts and grants, including for each: program title, Principal Investigator, sponsoring agency, annual rate and expiration date. The "Index of Reports" Supplement lists, again for the entire laboratory, all recent reports and publications and includes an abstract of each.
2. To record specific reports and publications activity generated by the JSEP program itself. Section III provides in an organized form, copies of selected representative journal articles of recent years reporting JSEP sponsorship, and Section IV lists all JSEP reports and publications for the same period.

II
GINZTON LABORATORY
Research Contracts and Grants
[30 September 1978]

SOURCE -- CONTRACT/GRANT NO.	P.I.	TITLE	ANNUAL RATE as of 9/30/78	EXPIRATION DATE as of 9/30/78
I. Air Force Office of Scientific Research				
F49620-78-C-0009	Geballe	Film Synthesis and New Superconductors	\$212,025	9/30/78
F49620-77-C-0092	Siegman/Byer	Laser Physics and Laser Techniques	165,637	12/31/78
F49620-78-C-0098	Quate	Acoustic Microscopy for Non-destructive Evaluation of Materials	121,561	6/30/81
AFOSR-76-3059	Auld	Processing of Optical Images with Optically Controlled Acoustic Transducers	54,115	9/30/78
AFOSR-76-3070	Chodorow/Shaw	New Approaches to Optical Systems for Inertial Rotation Sensing	96,837	9/30/78
AFOSR-77-3351	Chodorow	Microwave Tubes	29,571	9/30/78
AFOSR-77-3386	Shaw	PVF ₂ Transducers for Non-destructive Evaluation of Ceramics and Brittle Materials	65,311	6/30/79
AFOSR-77-3455	Quate	Acoustic Microscopic Study of Materials	94,076	9/30/78
AFOSR-78-3726	Kino	Research on Nondestructive Testing	140,000	8/31/79
Air Force Systems Command - Hanscom AFB				
F19628-77-0072	Harris/Young	Research Studies on Radiative Collision Lasers	75,000	1/9/80

II. Department of Commerce

National Bureau of
Standards

5-35899

Quate

The Acoustic Microscope -- A New
Instrument for Viewing Integrated Circuits

104,000

9/30/78

SOURCE -- CONTRACT/GRANT NO.	P.I.	TITLE	ANNUAL RATE as of 9/30/78	EXPIRATION DATE as of 9/30/78
III. Department of Energy				
EY76-S-03-0326, PA #43	Geballe/Beasley	Superconducting and Semi-conducting Properties of Electron Beam Evaporated Materials	\$ 86,400	1/31/79
EY76-S-03-0326, PA #56	Siegman	Ultrashort Pulses at CO ₂ Wavelengths	51,017	3/31/78
EY76-S-03-0326, PA #60	Harris/Young	Techniques for High Power Lasers Using Metastable Energy Storage	60,000	7/31/78
IV. Department of the Army				
Army Research Office				
DAAG-29-77-C-0022	Harrison	Electronic Structure of Transition Model Compounds	20,000	9/30/78
DAAG-29-77-G-0021	Harris/Byer	Tunable Optical Sources	100,000	8/31/79
V. National Science Foundation				
ENG74-00334	Auld	Perturbation and Variational Studies of Acoustic Waveguide Problems	35,800	4/30/78
ENG77-01119	Chodorow	Nonlinear Generation of Sound in the Scanning Acoustic Microscope	40,000	7/14/79
DMR73-02351	Harrison	Pseudopotential Methods in Physics	46,351	11/30/77
DMR75-04368	Beasley	Electromagnetic Properties of Layered Superconducting Structures	32,000	5/31/79

SOURCE -- CONTRACT/GRANT NO.	P.I.	TITLE	ANNUAL RATE as of 9/30/78	EXPIRATION DATE as of 9/30/78
------------------------------	------	-------	---------------------------------	-------------------------------------

V. National Science Foundation (continued)

APR75-07317	Quate	Scanning Acoustic Microscope	\$125,600	3/31/78
PHY77-09687	Schawlow/Hänsch	Spectroscopy and Quantum Electronics	275,000	5/31/79
ENG78-10446	Chodorow/Young	Electron Beam Thin Film Deposition and Evaluation Facility	21,433	7/31/79
ENG75-18681	Kino	Acoustic Wave Phenomena for Signal Processors	46,160	10/14/77
DMR77-21384	Harrison	Pseudopotential Methods in Physics	48,200	12/14/78
DMR76-21575	Geballe	Microscopic Parameters of Transition Metal Superconductors	44,700	8/31/79
CHE76-21987	Byer	Coherent Anti-Stokes Raman Spectroscopy	80,000	4/14/79
ENG77-28528	Kino	Acoustic Wave Transducers	40,000	6/30/79
ENG77-28541	Auld	Variational Methods for Acoustic Wave Scattering and Propagation in Solids	36,000	6/30/79

VI. Electric Power Research Institute

RP609-1	Kino/Shaw	Acoustic Techniques for Measuring Stress Regions in Materials	142,250	9/30/78
---------	-----------	---	---------	---------

VII. Environmental Protection Agency

EPA 8-05750-1	Byer	Remote Atmospheric Measurement of SO ₂ and CH ₄ Using LiNbO ₃	25,000	6/30/79
---------------	------	--	--------	---------

SOURCE -- CONTRACT/GRANT NO.	P.I.	TITLE	ANNUAL RATE as of 9/30/78	EXPIRATION DATE as of 9/30/78
------------------------------	------	-------	---------------------------------	-------------------------------------

VIII. Navy

NO014-76-C-0129	Kino	Acoustical Scanning of Optical Images	\$ 98,732	9/30/80
N00014-78-C-0283	Kino	Measurements of Surface Defects in Ceramics	60,000	2/28/81
N00014-78-C-0317	Weissbluth	Proton Transfer in Hydrogen-Bonded Nucleic Acids	16,667	9/30/79
N00014-78-C-0403	Schawlow	Advanced Laser Source Research	1,022,510	3/31/81
N00014-77-C-0412	Quate	Acoustic Microscopy of Cryogenic Temperatures	94,174	6/30/79
N00014-77-C-0439	Beasley	Superconducting Tunneling and Tunnel Applications in High TC Al ₅ Superconductors	58,000	4/30/79
N00014-75-C-0576	Harris	Laser Induced Inelastic Collisions	60,000	4/30/78
N00014-77-C-0582	Shaw	Piezoelectric PVF ₂ Polymer Films and Devices	50,000	7/31/80
N00014-75-C-0632	Chodorow	Optical and Acoustic Wave Research - JSEP	274,000	3/31/81
N00014-75-C-0841	Hänsch	Narrowband Dye Lasers	60,000	3/31/78
N00014-75-C-1175	Harris/Young	Coherent Vacuum Ultraviolet and Soft X-Ray Radiation	85,714	6/30/78

IX. National Aeronautics and Space Administration

NGL 05-020-103	Harris/Siegman	Lasers and Laser Devices	70,000	3/31/80
NSG 2289	Byer	Application of CARS Spectroscopy to Turbulence Measurements	36,833	12/31/78

SOURCE -- CONTRACT/GRANT NO.	P.I.	TITLE	ANNUAL RATE as of 9/30/78	EXPIRATION DATE as of 9/30/78
X. Subcontracts				
Rockwell International Science Center				
74-20773 (Prime: F33615-74-C-5180)	Kino	New Techniques for Acoustic Nondestructive Testing	\$180,000	9/30/78
77-70946 (Prime: F33615-74-C-5180)	Auld	Methods for the Detection and Characterization of Surface Flaws in materials	40,000	9/30/78
76-63282 (Prime: N00014-76-C-0624)	Kino	Ultrasonic Flaw Detection Studies on Ceramics	14,250	6/30/78
Stanford Research Institute				
14307 (Prime: ENY77-10198)	Byer	Remote Measurement of Air Pollutants	37,625	1/31/79
14374 (Prime: PHY77-01849)	Harris	Excitation of Atomic Inner Shell States	6,808	9/30/78

III

Selected and Representative Reprints of Journal Articles citing JSEP Sponsorship [1 July 1973 through 30 September 1978]

<u>H.L. Report No.</u>		<u>Page</u>
2179	C. M. Fortunko and H. J. Shaw, "Signal Transformation with Recirculating SAW Delay Lines." Preprint. IEEE Trans. on Sonics and Ultrasonics <u>SU-21</u> , 1 (January 1974).	11
2218	J. F. Havlice, G. S. Kino, and C. F. Quate, "Electronically Focused Acoustic Imaging Device." Tech. Report (December 1973). Also, reprint from Appl. Phys. Letters <u>23</u> , 11:581-3 (1 December 1973).	17
2294	H. Hayakawa and G. S. Kino, "Storage of Acoustic Signals in Surface States in Silicon." Preprint (May 1974). Appl. Phys. Letters <u>25</u> , 5:178-80 (15 August 1974).	21
2297	R. A. Lemons and C. F. Quate, "Integrated Circuits as Viewed with an Acoustic Microscope." Preprint (May 1974). Appl. Phys. Letters <u>25</u> , 5:251-3 (1 September 1974).	25
2335	J. H. Goll and B. A. Auld, "Multilayer Impedance Matching Schemes for Broadbanding of Water Loaded Piezoelectric Transducers and High Q Electric Resonators." Preprint (July 1974). IEEE Trans. on Sonics and Ultrasonics <u>SU-22</u> , 1:52-3 (January 1975).	29
2445	J. Fraser, J. Havlice, G. Kino, W. Leung, H. Shaw, K. Toda, T. Waugh, D. Winslow, and L. Zitelli, "An Electronically Focused Two-Dimensional Acoustic Imaging System." Preprint. Acoustical Holography <u>6</u> :275-304 (February 1975).	31
2518	G. S. Kino, "Acoustoelectric Interactions in Acoustic Interactions in Acoustic Surface Wave Devices." Preprint (May 1976). Proc. IEEE <u>724-48</u> (May 1976).	59
2570	L. Bui, H. J. Shaw, and L. T. Zitelli, "Study of Acoustic Wave Resonance in Piezoelectric PVF ₂ Film." Preprint (May 1976). IEEE Trans. on Sonics and Ultrasonics <u>SU-24</u> , 5:331-6 (September 1977).	85
2573	L. Bui, H. J. Shaw, and L. T. Zitelli, "Experimental Broadband Ultrasonic Transducers Using PVF ₂ Piezoelectric Film." Preprint (May 1976). Electronic Letters <u>12</u> , 16:293-4 (5 August 1976).	91
2586	P. G. Borden and G. S. Kino, "Correlation with the Storage Convolver." Preprint (June 1976). Appl. Phys. Letters <u>29</u> , 9:527-9 (1 Nov. 1976).	93
2605	D. F. Moore, J. M. Rowell, and M. R. Beasley, "Superconductive Tunneling into Niobium-Tin Thin Films." Reprint. Solid State Communications <u>20</u> :305-8 (1976).	97
2622	B. A. Auld, J. J. Gagnepain, and M. Tan, "Horizontal Shear Surface Waves on Corrugated Surfaces." Preprint (October 1976). Electronics Letters <u>12</u> :650-1 (25 November 1976).	101
2695	C. S. DeSilets, J. D. Fraser, and G. S. Kino, "The Design of Efficient Broadband Piezoelectric Transducers." Preprint (May 1977). IEEE Trans. on Sonics and Ultrasonics <u>SU-25</u> , 3:115-25 (May 1978).	105

H.L.
Report No.

Page

2708	B. A. Auld and B.-H. Yeh, "Piezoelectric Shear Surface Wave Grating Resonators." Preprint (May 1977). Proc. 31st Annual Symposium on Frequency Control.	117
2735	A. Atalar, C. F. Quate, and H. K. Wickramasinghe, "Phase Imaging in Reflection with the Acoustic Microscope." Preprint (August 1977). Appl. Phys. Letters <u>31</u> , 12:791-3 (15 December 1977).	125
2819	S. E. Harris, J. Lukasik, J. F. Young, and L. J. Zych, "Anti-Stokes Emission as a VUV and Soft X-ray Source." Preprint (June 1978).	129

Signal Transformation with Recirculating SAW Delay Lines

CHRIS M. FORTUNKO AND H. J. SHAW

Abstract A system is described for transforming data by switching it into a bank of recirculating delay lines in one time sequence and switching it out in another sequence. This is applied to row to column conversion when the input data is in the form of an $N \times N$ matrix. An experimental demonstration is shown which uses SAW wrap-around delay line channels, transforming a 3×3 matrix of RF pulses of $16\text{-}\mu\text{s}$ length and 52 MHz carrier frequency.

I. INTRODUCTION

Data processing in real time can be accomplished by storing incoming data in banks of recirculating surface wave delay lines and then reading out these data in such a way as to transform them in a desired fashion. We consider here some of the properties of such systems and describe the operation of a simple prototype system, operating at 52 MHz carrier frequency, which performs an operation equivalent to interchanging the rows and columns of a matrix.

The basic approach to the use of delay lines for such purposes is illustrated in Fig. 1. The essential item is a bank of identical recirculating surface wave delay line loops. Input data fed in at the input terminal of the system are distributed among the delay lines in some desired fashion by means of the WRITE circuitry. The data enter the delay lines through in-

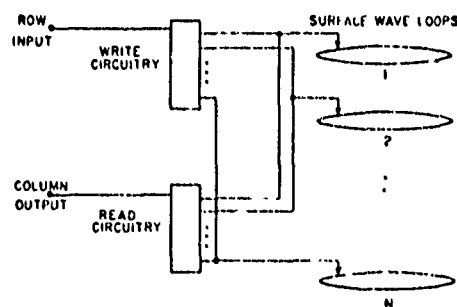


Fig. 1. Block diagram of data transformation system using closed-loop surface acoustic wave delay lines.

terdigital transducers indicated as arrows in the figure. The READ circuitry extracts the data from the delay lines by switching from one delay line to another in a time sequence which is different from that used for writing, to accomplish the required transformation of the data train.

The row-to-column converter can be used to perform the intermediate serial-to-parallel conversion which is required to implement decomposable two-dimensional transforms (e.g., Fourier, Hadamard). It can also be used to interface two systems with different speeds.

II. ROW-TO-COLUMN CONVERSION USING CLOSED-LOOP SURFACE ACOUSTIC WAVE DELAY LINES

We consider now an example of data transformation. Let the input data stream be $A_{11} \cdots A_{1N} \cdots A_{N1} \cdots A_{NN}$, which is ordered according to rows of the $N \times N$ matrix in

Manuscript received June 8, 1973; revised August 24, 1973.
This work was supported by the U. S. Office of Naval Research under the Joint Service Electronics Program by Contract N00014-67-A-0112-0039.

The authors are with the W. W. Hansen Laboratories, Stanford University, Stanford, Calif. 94305.

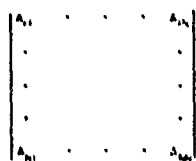


Fig. 2 Matrix notation.

Fig. 2. We now show that it is possible to devise WRITE and READ algorithms which will convert this into a sequence ordered by columns of the matrix, in real time, using only a single transducer on each delay line.

The transducers of Fig. 1 can be addressed at either of two rates, once per row or once per bit. To obtain the row-to-column conversion one of these rates is applied to the WRITE function and the other to the READ function. Either rate may be applied to either function giving two algorithms for the row-to-column operation. Figs. 3(a) and (b) illustrate these two algorithms. In these diagrams successive horizontal lines show the signals seen by the transducer in successive delay lines as a function of time reading to the right. The squares represent the signals introduced into the transducers during the WRITE operation, and the quantities between curved brackets are the signals extracted from the transducers in the READ operation. The dashes indicate time slots containing no signal.

Fig. 3(a) is for the case in which the WRITE function is performed at the row rate and the READ function at the bit rate. Each row of Fig. 2 is fed intact into a separate delay line. As indicated by the diagonal arrays of curved brackets, the sequence of gating on the transducers for readout is a uniform, periodic scan, $1, 2, \dots, N, 1, 2, \dots, N, \dots$, sequentially from line 1 to line N , in repetitive cycles. The final output signal is shown at the bottom of Fig. 3(a). This output sequence is a real-time sequence free of gaps, ordered according to columns (time reversed) of the matrix of Fig. 2.

Fig. 3(b) represents the alternate algorithm in which the WRITE and READ switching rates have been interchanged. For any row of input data of Fig. 2, the first bit enters the first storage loop, the second bit enters the second loop, and so forth until the entire row has been stored, one bit in each delay line. During the READ cycle the entire contents of each delay line are sampled, one row at a time. The sequence (column output) shown at the bottom of Fig. 3(b) is seen to be the same as for Fig. 3(a), ordered according to the columns (time reversed) of the matrix of Fig. 2. We see that the algorithms of Figs. 3(a) and (b) result in output sequences whose rows are columns of the input matrix as desired. However, both the rows and the elements within these rows appear in the opposite time sequence to the corresponding columns of Fig. 2. That is, the output sequences in Figs. 3(a) and (b) are time reversed. For cases of direct concern here, this is not of consequence. If it is not desired, however, it can be corrected by time-reversing the input signal *by rows* before feeding it to the delay line loops. Fig. 3(c) shows this behavior. The signals within each row have been time-reversed before insertion into the delay line loops. This time reversal could be done in a device having a time delay of N -clock intervals,

rather than $N \times N$ as would be required if row-to-row time reversal were also involved. A parametric acoustic time reversal could be employed for this operation.

When one transducer is used on each recirculating delay line, a total of N delay lines are required to store one $N \times N$ matrix and interchange its rows and columns in real time without gaps. The matrix elements which are stored longest make at least $2N - 2$ round trip circulations. The time delay per circulation is $N + 1$ sampling intervals. To accomplish the same for a sequence of $N \times N$ matrices, two identical sets of N delay lines each can be used by feeding successive matrices alternately to the two sets of delay lines. The maximum number of circulations of data around the delay loops can be decreased by using more than one transducer per delay line.

Fig. 4 is a functional diagram of a system which can be used to implement the switching sequences of Figs. 3(a) and (b). The WRITE and READ circuits, which would ordinarily consist of semiconductor circuitry, are represented symbolically by rotary switches which scan a set of terminals at constant rates. The WRITE and READ switches can be conceived of as identical, except that they rotate in opposite directions and, while their rotation rates are constant, they are different for the two switches, in order to implement the different WRITE and READ rates discussed in connection with Fig. 3. For the algorithm of Fig. 3(a) the WRITE switch dwells on each contact for the row time of Fig. 2, i.e., N clock intervals, thus making one complete revolution in the frame time, or N^2 clock intervals. The READ switch makes one revolution in the row time and thus rotates at N times the velocity of the WRITE switch. The READ switch is deactivated while the WRITE switch is activated, and vice-versa. To implement the algorithm of Fig. 3(b) the rotation rates of these two switches are interchanged.

The surface wave delay loops have round trip time delay sufficient for $N + 1$ addresses, to provide real time output sequences, as described in connection with Fig. 3.

III. DELAY LINE DESIGN

The simplest system would use closed-loop wrap-around delay lines [2, 3] directly as recirculating delay lines, keeping the input signals on the delay lines for the entire number of recirculations. Banks of such delay lines are readily constructed to have identical round trip time delay. Surface wave amplifiers could be located within the closed loops to maintain signals at constant level regardless of the total number of circulations [4, 5]. The same surface wave amplifiers could also be used to erase all data remaining in the storage rings following the completion of the READ-WRITE cycle, by reversing the polarity of the applied bias voltage.

If a single transducer is used on each delay line loop as described earlier, the location of the transducer along the delay line axis would not be critical, as it does not effect the round trip time delay. Alternatively, separate WRITE and READ transducers could be used in each loop, with the spacing between transducers made identical from loop to loop. This would present no problem because the WRITE and READ transducers can readily be spaced sufficiently

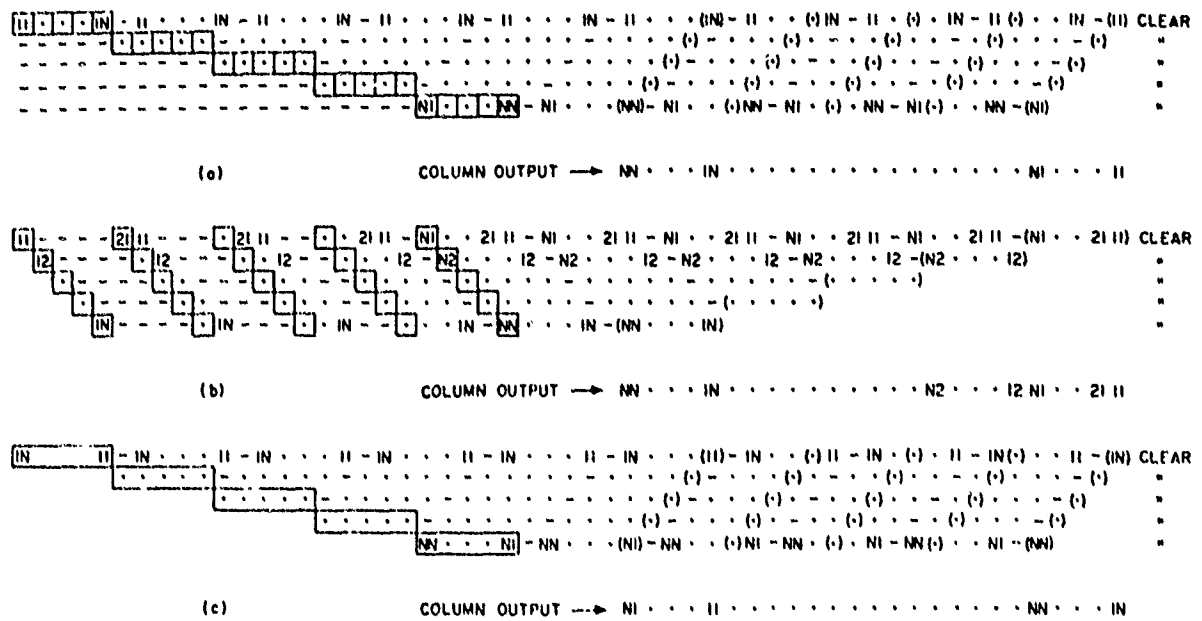
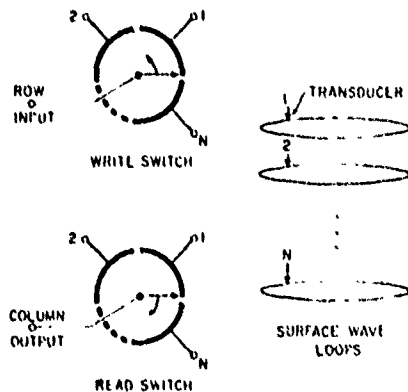


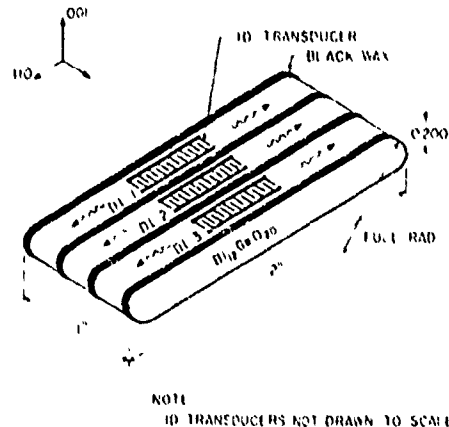
Fig. 3. Gating sequences for row-to-column conversion.

Fig. 4. Functional diagram of row-to-column converter using one transducer per storage loop. WRITE switch switches from one storage loop to next after duration of N bits while READ switch switches from one storage loop to next at every bit, or vice versa.

close together to allow both to be deposited from the same mask. The choice between single transducers and WRITE-READ pairs would be made on the basis of details of the switching algorithm used.

It is important for all surface wave delay loops to have the same round-trip time delay. In the fabrication of wrap-around closed loop lines, this is the easiest specification to satisfy, and it can be accomplished with high accuracy.

If there is only one transducer per loop, the round trip time delay of the loops could be corrected experimentally by localized adjustments made anywhere within the loops. This could be implemented by means of an electronic feedback system which would compensate for effects of temperature change, clock drift, and any other instabilities. Electronically variable phase shifting elements for surface wave delay lines have been demonstrated [6] which would be of interest for this purpose. This approach could also be used to keep the round trip delay around the loops identical to $N + 1$ clock intervals, in cases where the clock frequency is set externally.

Fig. 5. Wrap around delay line configuration used in row-to-column conversion of 3×3 matrix.

IV. EXPERIMENTAL DEMONSTRATION MODEL USING 3×3 MATRIX

We have constructed a prototype model of the system illustrated in Fig. 4. The model uses a single 2×1 in wrap around bismuth germanium oxide plate oriented for propagation of surface acoustic waves along the 110 crystal direction on Z-cut surfaces. The delay line construction and the complete device circuit diagram are shown in Figs. 5 and 6, respectively. The system sampling rate is $16 \mu\text{s}$ bit with each storage loop capable of storing four complete bits of data. The polished surface of the delay line plate has been subdivided into three equivalent storage loops with thin strips of black wax for cross-talk suppression. One interdigital transducer is used in each storage loop. These transducers are of standard design with 8 interdigital periods and 0.050 in acoustic beamwidth, and are fabricated using gold-titanium deposition. Each transducer is individually tuned with a high- Q miniaturized series inductor to cancel the capacitive reactance

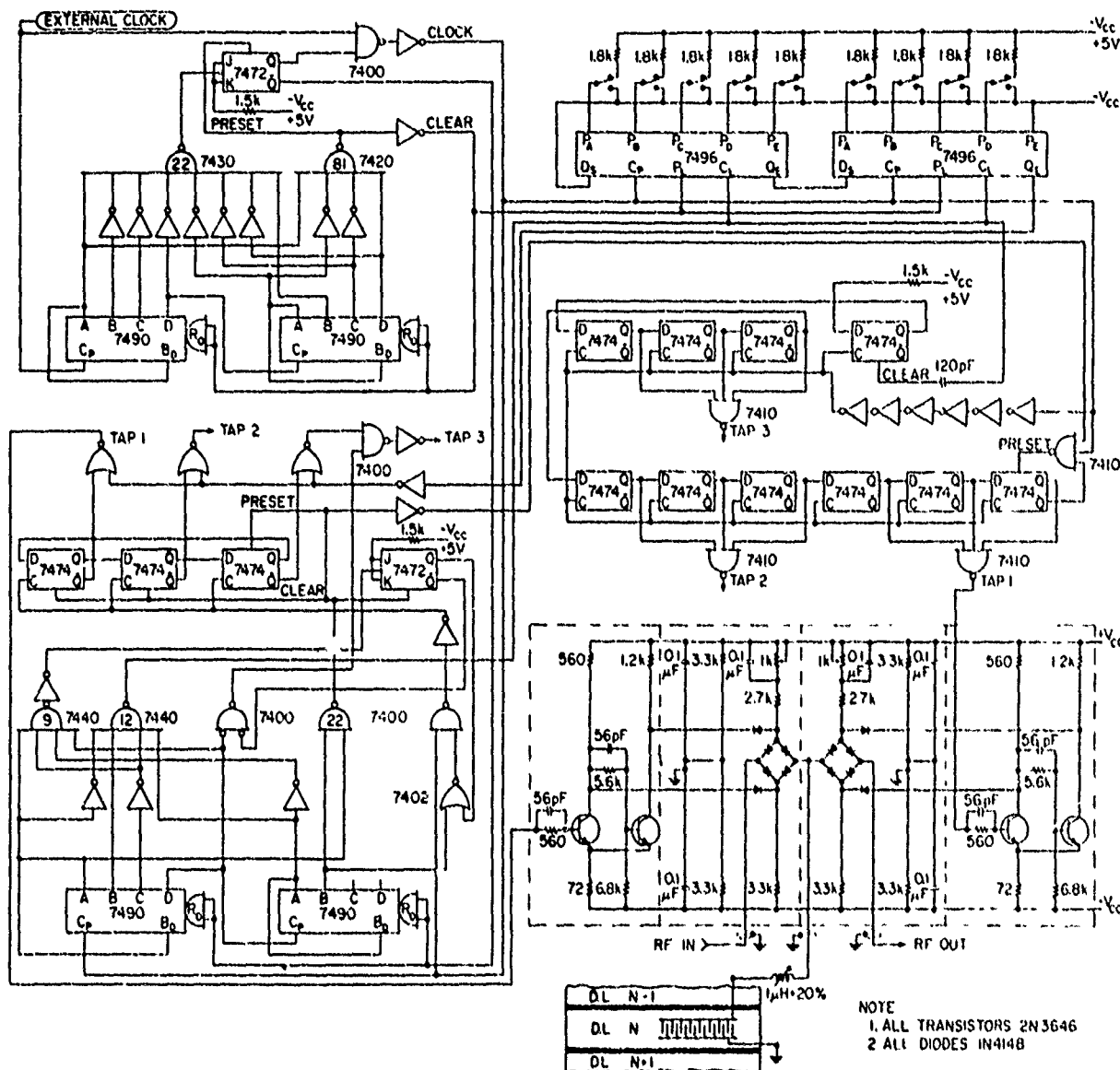


Fig. 6. Electrical circuit diagram of experimental row-to-column converter.

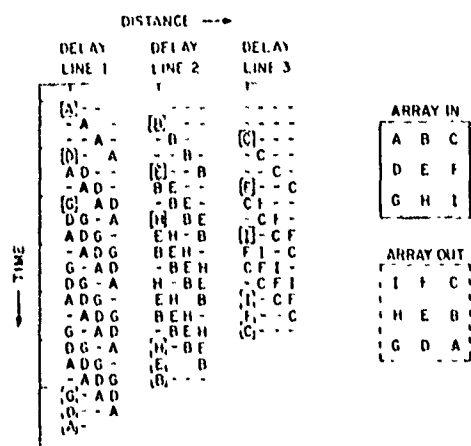
of the interdigital array. This tuning is important for maximizing the off-on ratio of the semiconductor RF switch.

The RF READ and WRITE switches consist of a pair of tandem 6-diode bridges connected to the transducer with a short length of rigid coaxial cable. Each diode bridge is separately controlled by a Schmitt driver circuit which is, in turn, activated by a TTL logical "1" level. The duration of the logical "1" level determines precisely the length of time a particular tap remains connected to a common coaxial bus line. With inductive tuning the physical tap turn on time is less than 30 ns, which is insignificant compared with the length of one bit of data (16 μ s).

The algorithm of Fig. 3(b) was arbitrarily chosen for the READ and the WRITE operations. The input data are written in bit by bit, placing successive bits sequentially in successive storage loops. Each delay line storage loop then has circulating in it the data from one column of the matrix. During

the readout cycle, the entire contents of individual delay loops are sampled in blocks.

In Fig. 7 we make use of a space-time flow diagram to show the location of each bit of data at any time. We restrict the diagram of the special case of the 3×3 matrix used in our experimental model. Thus the individual bits of data are labeled A through I corresponding to the order in time in which they are stored. The solid lines drawn around a particular character denote a WRITE interval while a broken line is used to denote a READ interval. Also shown in Fig. 7 are the relative positions of the 3×3 matrix elements before and after the row-to-column conversion operation. Note that the columns are time reversed, as discussed earlier. In Fig. 8 we show experimental oscilloscope displays of the RF envelopes of two of the many possible data sequences of a binary 3×3 matrix. The lower trace in each display represents the data sequence before storing in the delay line storage bank while



the upper trace shows the rectified RF output signals read from the storage bank. The output signals are not uniform in amplitude because of the differences in propagation loss associated with the different time delays of individual bits. In general, the first bits to be written on the surface of the loop delay line are the last to be read and thus are subject to the most attenuation. (In this demonstration model we did not employ a SAW amplifier to internally compensate for the propagation losses of the signal.) It must also be noted that the lower and upper oscilloscope traces of Fig. 8(a) and (b) do not occur simultaneously. The traces were photographed separately by a double exposure of the film.

V. CONCLUSIONS

A system has been described in which row-to-column conversion is accomplished in a set of simple, identical delay lines, involving tolerances which should be readily achievable, and which could be electronically controlled to compensate for clock errors and temperature changes. Writing in the input data and reading out the output data can be accomplished directly in real time by means of switching circuits. No auxiliary time delays are involved other than those produced in the main bank of identical delay lines. This avoids any problems of matching of dissimilar delay lines.

In these systems, the data move along the delay lines, and are thus scanned by the transducers, by reason of the inherent propagation characteristic of the acoustic wave, without requiring external drivers. The inherent capability of the lines to handle either analog or digital data is also preserved.

Prospects for handling large matrices are good because of the large time delay and bandwidth capabilities of recirculating

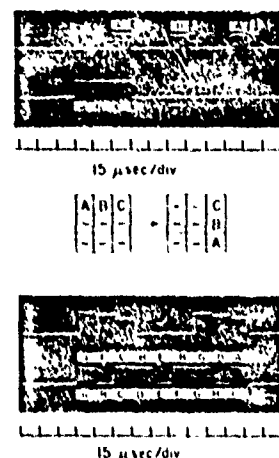


Fig. 8. Experimental oscilloscope traces of two sample matrix transformations accomplished with 3 x 3 matrix row-to-column converter.

surface wave delay lines. Large data rates are in prospect because standard approaches, to broadband surface acoustic wave transducers [7] can be utilized. Also, the systems are compatible with frequency multiplexing in the individual delay lines of the bank, to take further advantage of the very broad band propagation characteristics on the delay line surfaces, allowing a higher physical density of data storage. They are also compatible with time multiplying in the individual lines to allow matching of data rates.

ACKNOWLEDGMENT

The authors would like to thank H. Whitehouse of the Naval Undersea Center, San Diego, Calif., for suggesting the problem of row-to-column conversion, and for very helpful discussions on matrix transformations.

REFERENCES

- [1] G. S. Kino, S. Ludvick, H. J. Shaw, W. R. Shreve, J. M. White, and D. K. Winslow, "Signal Processing by Parametric Interactions in Delay Line Devices," *IEEE Trans. SU* 20, 2, 162 (April 1973).
- [2] W. L. Bond, T. M. Reeder, and H. J. Shaw, *Electronics Letters* 7, 3, 79 (19 January 1971).
- [3] Frederick Y. Cho, Bill J. Hunstetter, and Ronald L. Lawson, *Appl. Phys. Letters* 18, 7, 298 (1 April 1971).
- [4] T. M. Reeder, H. J. Shaw, and M. Westbrook, *Electronics Letters* 8, 14, 365 (13 July 1972).
- [5] L. A. Coldren, "Optimizing Loss Compensated Long Delay Devices," to be published in *Trans. IEEE, Sonics and Ultrasonics*.
- [6] J. A. Alexow, B. F. Burke, and I. Stern, *IEEE Trans. SU* 19, 3, 414 (July 1972).
- [7] G. Judd, *Electronics Letters* 8, 14, 367 (14 July 1972).

Electronically focused acoustic imaging device

J. F. Havlice, G. S. Kino, and C. F. Quate

Microwave Laboratory, W. W. Hansen Laboratories of Physics, Stanford University, Stanford, California 94305
(Received 4 September 1973)

A new type of acoustic imaging device, which scans a large array of piezoelectric detectors is described. Scanning is carried out by a signal traveling along an acoustic surface wave delay line. The device can be electronically focused, and has given images of objects 20 cm from the detector array, illuminated with a 5-MHz acoustic wave, with a definition of 1 mm.

We describe in this paper experiments on a new type of acoustic imaging device, which uses signal-processing techniques to focus on an acoustic image object plane at some distance from the detector, without the use of an acoustic lens.

The basic device is illustrated in one- and two-dimensional forms in Figs. 1(a) and 1(b). In the one-dimensional form, it consists of a large number of piezoelectric detectors, which are used to detect an acoustic image signal from an object illuminated separately either by an acoustic wave passing through it or reflected from it. A multiply tapped delay line (in our case an acoustic surface wave delay line) is used as the basic scanning device. There is one tap for each detector and the output signal from each tap is mixed in a diode mixer with the output from the corresponding piezoelectric detector. If a signal is inserted on the delay line at frequency ω_1 , and the signal corresponding to the acoustic image is at a frequency ω_s , there will be output signals from the individual mixers at the sum frequency $\omega_s + \omega_1$ and the difference frequency $\omega_s - \omega_1$; these signals are the products of the acoustic surface wave signal at each tap and the signal from the corresponding detector. In the system, the mixer outputs are summed and either the sum or difference frequency is passed through a filter into the output circuit.

In order to understand the operation of this device, we first consider the situation when a short pulse of frequency ω_1 is sent along the acoustic delay line. In this case an output signal is obtained at the sum frequency only when the pulsed signal passes by a tap and there is a signal present on the corresponding detector. As the pulse passes along the delay line, it scans each detector in turn so that the output may be used to intensity modulate a cathode ray tube, and hence display a visual image corresponding to one line of the acoustic image. The acoustic pulse thus acts like the scanning electron beam in a vidicon.

In the two-dimensional version of this device, illustrated in Fig. 1(b), a square array of piezoelectric detectors is used with diode mixers placed in series with each element of the array. When a pulse of frequency ω_1 is sent along the acoustic delay line in the x direction and inserted into the piezoelectric detector system along strips in the y direction, it produces a mixed output at a frequency $\omega_1 + \omega_s$. If the output signals are taken out of strips in the x direction and mixed with similar signals passing along another delay line in the y direction, but of frequency ω_2 , an output at a frequency $\omega_1 + \omega_2 + \omega_s$ is obtained only at the time when the two pulses are passing a particular detector element. This corresponds to scanning a line at 45° to the x axis. By

delaying one pulse with respect to the other, a complete raster scan may be obtained in this way.

It would normally be necessary to use a lens to form an image of an acoustically illuminated object at a distance z from the detector system. However, this device, unlike camera film, retains phase information as well as amplitude information. We have shown that with the correct choice of signal sent along the delay line, it is possible to use this phase information in a simple manner to "electronically focus" on an object at some distance from the detector. So no acoustic lens is required.

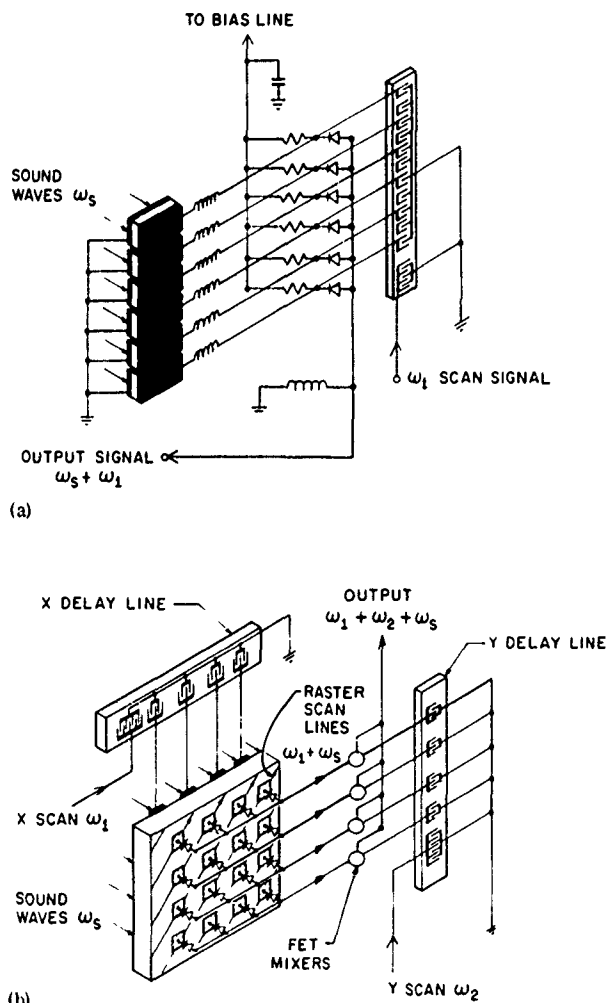


FIG. 1. Schematics of the imaging device: (a) the one-dimensional device (with the complete circuit); (b) the two-dimensional device (without the complete circuit).

We may analyze the focusing properties of the one-dimensional form of this device by considering how it forms an image of a line source a distance z from the detector plane. We take the projection of this line source on the detector plane to be a distance x_0 along it.

The shortest ray path to the detector plane is of length z , and the length of a ray path from the line source to the n th detector element with its center at the element x_n is

$$l_n = [(x_n - x_0)^2 + z^2]^{1/2}, \quad (1)$$

so that in the paraxial approximation, where we take $(x_n - x_0)^2 \ll z^2$, we find that

$$l_n \approx z + (x_n - x_0)^2 / 2z. \quad (2)$$

If the signal emitted from the point source varies as $\exp(j\omega_s t)$, the phase of a signal arriving at a point x_n on the detector array is

$$\phi_{sn} = \omega_s \left(t - \frac{z}{v_w} - \frac{(x_n - x_0)^2}{2zv_w} \right), \quad (3)$$

where v_w is the velocity of sound in the medium between the detector and the source. Thus there will be a square-law variation of phase of the acoustic signal along the plane of the detector. In an acoustic imaging system this square law variation of phase could be compensated by the presence of a lens, so that rays leaving a point source had the same phase delay between the source point and the image point. In our case, we arrange to eliminate this square-law variation of phase by sending an electrical signal along the surface wave delay line which has the same square-law variation in phase, but one with an opposite sense. Therefore, the output signal at the sum frequency has no variation in phase. To obtain this signal, we insert in the delay line a linear FM chirp of frequency $\omega = \omega_1 + \mu t$ which has a phase

$$\phi_D = \omega_1 t + \frac{1}{2} \mu t^2. \quad (4)$$

At a point x_n on the delay line the phase of this signal is

$$\phi_{Dn} = \omega_1 (t - x_n/v) + \frac{1}{2} \mu (t - x_n/v)^2. \quad (5)$$

It follows that the product of the FM chirp and the acoustic image signal has a phase

$$\begin{aligned} \phi_n = & (\omega_1 + \omega_s) t - \frac{\omega_s z}{v_w} - \frac{\omega_s x_n}{v} \\ & + \frac{\mu}{2} \left(t - \frac{x_n}{v} \right)^2 - \frac{\omega_s (x_n - x_0)^2}{2zv_w} \end{aligned} \quad (6)$$

at the n th tap.

It will be seen that if the spacing between taps is chosen so that $\omega_1 x_n/v = 2n\pi$, the sum frequency signals from each mixer all have the same phase if

$$t = t_0 = x_0/v, \quad (7)$$

$$\mu = \omega_s v^2 / zv_w. \quad (8)$$

Equation (7) implies that the system only focuses on the point x_0 at a given time t_0 , i.e., it scans the image at a velocity v . Perfect focusing occurs on a point at a distance z from the detector if the sweep rate is chosen to correspond to that of Eq. (8). Thus changing the sweep rate is equivalent to changing the focal plane of the lens.

The theory of this device has been worked out in some detail. It has been shown that if the total length of the detector system array is L , the output signal from a line source at (x_0, x) varies approximately as

$$\frac{\sin[\omega_s L(x_0 - vt)/2zv_w]}{\omega_s L(x_0 - vt)/2zv_w}.$$

So the effective size of the diffraction-limited spot (the distance between points 4 dB below the maximum amplitude value) is

$$\Delta x = z\lambda/L, \quad (9)$$

where λ is the acoustic wavelength. With the same definition of spot size, this result is identical to that for an optical lens of the same aperture.¹

Because there is a finite number of detector elements, there will be additional sidelobes at points a distance $d_s = z\lambda N/L$ from the main lobe, where N is the number of detector elements. The sidelobes correspond to an extra 2π phase shift between rays reaching neighboring detectors. Thus the number of resolvable spots, $d_s/\Delta x$, is approximately equal to the number of detector elements.

We have carried out a series of experiments with 30 element arrays made from a piezoelectric strip approximately 1 cm wide. One system used detector elements spaced by 2 mm (and operated at 4 MHz), with a 50-MHz signal on the delay line. With this system, we carried out measurements of the chirp rate as a function of the distance to the focal plane. This was determined by using a small source, and changing the sweep rate until the output amplitude reached a maximum, and the width of the output pulse a minimum. As will be seen from Fig. 2, the correspondence between theory and

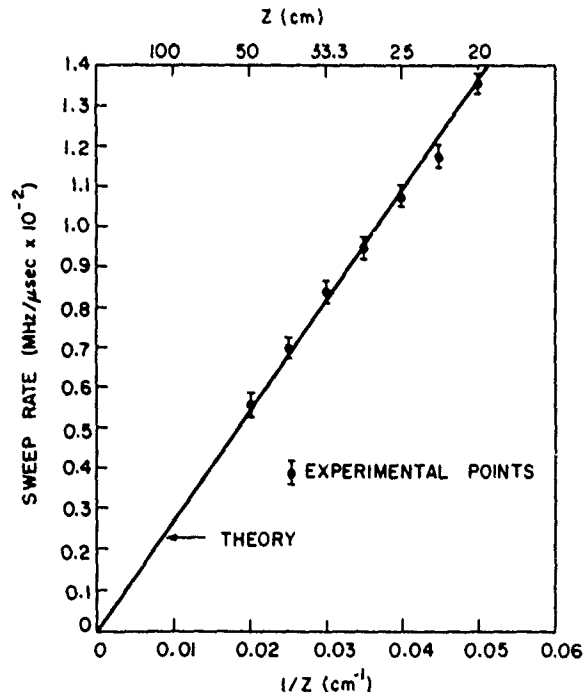


FIG. 2. Theoretical and experimental sweep rates of the linear FM chirp, taken at 4 MHz.



FIG. 3. Acoustic image of a small crescent wrench located 20 cm from the detector array.

experiment is excellent. In this case, the definition at a distance of 25 cm was of the order of 4 mm and the increase in amplitude obtained with only 18 detectors illuminated (due to the small acceptance angle of the initially unslotted piezoelectric strip) was 23 dB over that from a single detector, which corresponded well with theory.

A later 30 element array with slots between the detector elements had a much larger acceptance angle; it operated at 5 MHz with 1.2-mm-wide elements 2 mm apart. With it, it was possible to observe slots, approximately 1 mm wide and 2 mm apart, in a standard metal Air Force chart, 20 cm from the detector plane.

The calculated resolution for this system at the same distance was 0.96 mm.

From behind, through a narrow slit, we also illuminated an object, a simple wrench, 25 cm from the detector. We moved the wrench up and down mechanically so as to obtain a two-dimensional scan. A photograph of this image is shown in Fig. 3. It will be seen that the reproduction is excellent and that the definition is of the order of 1 mm in the horizontal direction, the direction of the electronic scan.

In summary, we have demonstrated a new type of electronically focused scanning system. The system has been tested with an electronic scan in one direction and a mechanical scan in the other. All parameters of the system correspond well to theory. The basic principles of the two-dimensional system are understood and we hope to construct a two-dimensional electronically focused system of the type shown in Fig. 1(b) within the next few months.

The authors would like to thank J. S. Kofol, D. J. Walsh, and L. C. Goddard, who constructed and helped in the design and testing of the experimental devices. They would also like to thank Harper Whitehouse of the Naval Undersea Laboratory for many stimulating conversations on the concepts described in this paper. They wish, also, to acknowledge the U.S. Army Research Office, Durham, for support of the basic work on acoustic scanning that formed a foundation for this work.

*Work supported by the Naval Undersea Center, Contract N000123-C-0886 and the Office of Naval Research, Contract N00014-A-0112-0039

[†]Joseph W. Goodman, *Introduction to Fourier Optics* (McGraw Hill, New York, 1968).

Storage of acoustic signals in surface states in silicon*

H. Hayakawa† and G. S. Kino

Stanford University, Stanford, California 94305

(Received 2 May 1974)

An acoustic wave storage device capable of storing an acoustic surface wave signal for times of up to several milliseconds is described. The principle of the device is based on that of the acoustic surface wave convolver, with the information stored in surface states in silicon. It is expected that the storage time will ultimately be as much as 10–30 msec for signals with modulation frequencies of tens of megahertz. At the present time, we have seen storage of pulses approximately 0.4 μ sec long for times of approximately 2 msec, but some of these early devices seem to be capable of yielding storage times as long as 7 msec.

Storage of acoustic signals for times of several milliseconds may be obtained by using storage of information in surface states in silicon. For this purpose we employ an acoustic surface wave convolver in which the nonlinear coupling between two surface waves is due to electric field interaction with a semiconductor such as silicon separated from the piezoelectric substrate (typically LiNbO_3) by a small airgap.^{1–3} When signals of frequency ω are inserted at each end of this device, the output at a frequency 2ω is obtained between the silicon and a metal plate on the opposite side of the piezoelectric substrate, as illustrated in Fig. 1. If one of the input signals is a short pulse, output will be obtained at a frequency 2ω from the point on the silicon which the pulse is passing at time t . If the surface of the silicon is depleted by a positive dc potential applied between the silicon and the metal plate, the thickness of the depletion layer will depend on the field due to the applied dc potential, and the extra field due to the presence of surface charges at the surface of the silicon. In this case the output signal obtained when the device is used as a convolver, with one of the inputs a short pulse and the other a long pulse, will vary in time in accordance with the spatial variation of surface charge carrier density along the surface. Thus it is possible, by using a convolver, to read out the variation of surface state charge density along the length of the device. This output can be obtained as the modulation of a carrier frequency 2ω .

It is possible to construct a storage device by reading acoustic information into the surface states from an externally applied signal. When a dc potential which is sufficient to bring the surface potential near to the center of the bandgap is applied to the semiconductor, the surface states at the silicon surface will be depleted. Now suppose a large signal short pulse is sent along the device from one of the input transducers. If the signal is large enough at the peak of the rf cycle, the potential at the surface becomes positive enough for electrons to reach the surface from the neutral region of the semiconductor and be trapped in surface states. These electrons will be emitted from the surface states in a time which depends on the surface state recombination time. If an additional signal which we wish to store is inserted between the Si and the ground plate while the pulse is sent down the delay line, the amount of charge stored in the surface states will be modulated by the amplitude of the pulse, and so the signal $F(t)$ applied into the plate will be read spatially into the surface states in the form $F(x/v)$ where v is the velocity of the

acoustic pulse. It is necessary, of course, that in order to obtain storage of a signal the storage pulse length must be shorter than the rise time of the input signal.

Following the treatment of Nicollian and Goetzberger,⁴ it can be shown that, for an n -type semiconductor, the time constant for emission of electrons from a continuum of traps at the surface is approximately

$$\tau_{ne} = \frac{1}{\sigma_n v_{thn} n_{s0}} = \frac{\exp[-q(\psi_s - \psi_b)/kT]}{\sigma_n v_{thn} n_i} \quad (1)$$

where σ_n is the capture cross section for electrons, regarded as essentially uniform over the bandgap, v_{thn} is the thermal velocity of electrons, n_{s0} is the electron charge at the surface after equilibrium has been reached in the presence of an applied dc potential, ψ_s and ψ_b are, respectively, the surface potential and the potential in the neutral region relative to the intrinsic level, and n_i

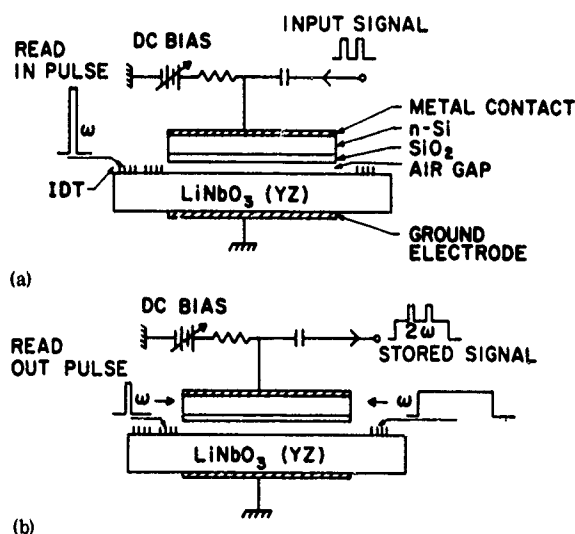


FIG. 1. Schematic representation of the device. (a) Read-in process: An intense 110-MHz acoustic pulse of approximately 1 W whose length is 0.2 μ sec is sent into the delay line from one transducer. The signal which is to be stored (in this case a double pulse) is inserted from a contact on the top surface of the silicon. (b) Read-out process: Two acoustic pulses of frequency 110 MHz, one of which is a short pulse and the other is a long pulse, are sent from either end of the delay line. A signal at a frequency of 220 MHz is detected between contacts on the top surface of the silicon and the grounded bottom side of an LiNbO_3 delay line. In both cases, a dc bias voltage is applied in order to deplete the surface of the silicon.

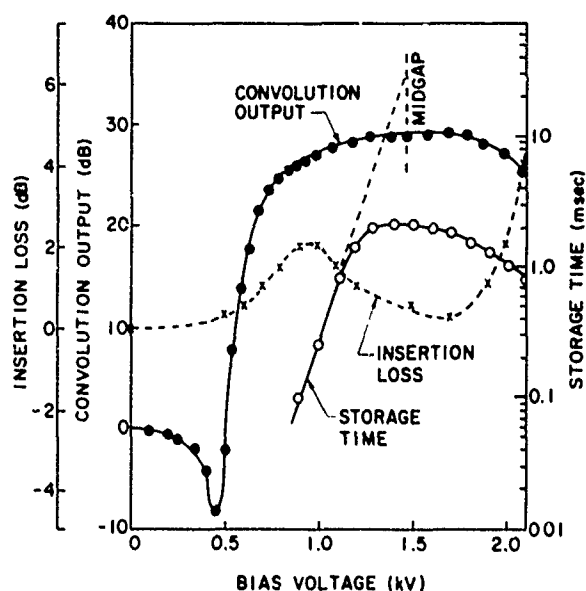


FIG. 2. Storage time, convolution output, and insertion loss as a function of bias voltage. The convolution output and the insertion loss are normalized by taking values without bias as references.

is the intrinsic carrier density. The rate at which the number of surface states $N_{ss}d\psi$ in the range $d\psi$ are filled from the neutral region is

$$1/R_n(l) = N_{ss}\sigma_n v_{thn} n_s d\psi, \quad (2)$$

where it is assumed for simplicity that all states are unfilled initially. Thus if we express n_s in terms of thermal equilibrium statistics, we come to the conclusion that we can deduce a filling time τ_{nF} for the traps by writing $R_n/N_{ss}d\psi = 1/\tau_{nF}$ or

$$\tau_{nF} = \frac{1}{\sigma_n v_{thn} n_s} = \frac{1}{\sigma_n v_{thn} n_i} \exp\left(\frac{-q(\psi_s - \psi_i)}{kT}\right). \quad (3)$$

We might expect, therefore, that when the surface potential is held near the center of the bandgap, the storage time τ_{nF} could be several tens of milliseconds. But as the surface potential is raised to form an accumulation layer near the surface so that $n_s \sim 10^{16} \text{ cm}^{-3}$, the time for filling the traps could be of the order of nanoseconds, although a sufficiently large number of traps would be required so as to make the presence of filled or unfilled traps detectable.

In our experiments, we used a LiNbO_3 substrate with a bulk silicon semiconductor separated from it by an airgap of approximately 3000 Å. The experiments to be described here were carried out using 100-Ω cm *n*-type material, with an oxide layer of approximately 1000 Å thickness and a surface state density of approximately 10^{11} cm^{-2} .

We first operated the device as a convolver in the circuit shown in Fig. 1(b) and measured the convolution output. With a dc bias applied to the system, the semiconductor surface would normally be depleted. Next an intrinsic 1 W 110 MHz rf pulse is inserted and sent along the system. The silicon surface states are charged with electrons so that the depletion layer becomes still thicker and the convolution output decreases. As the surface states discharge, the successive convolution outputs increase to the initial value. The time constant of the surface states, which we define as the storage time, depends on the dc bias voltage. The storage time, the initial convolution output, and the insertion loss as a function of bias are plotted in Fig. 2. It will be seen from this set of results that the storage time and the convolution output reach a maximum around a bias of 1.5 kV, while the insertion loss reaches a minimum. This means that at this bias voltage the sili-

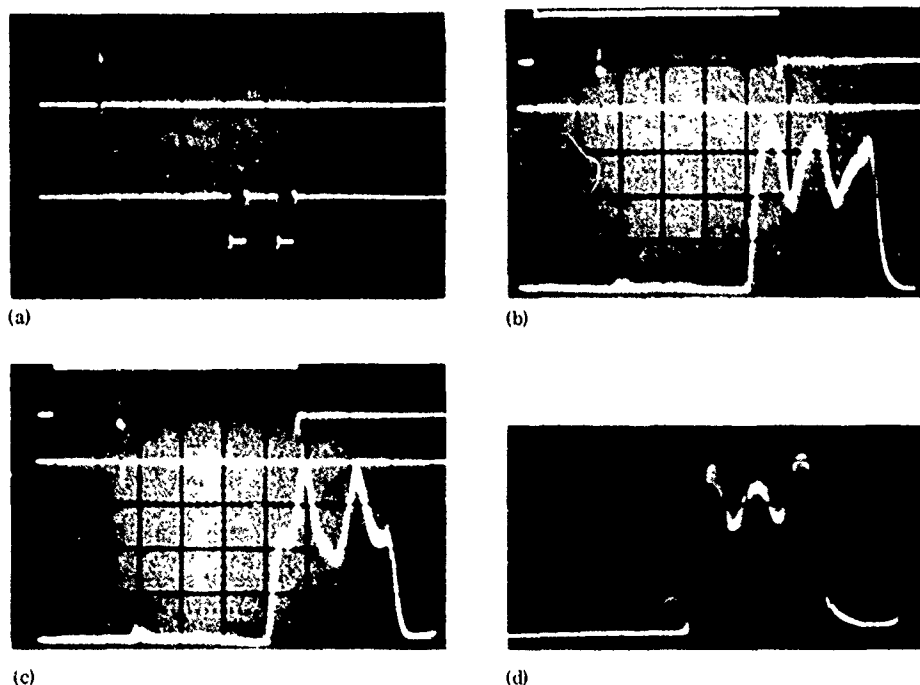


FIG. 3. (a) Read-in signals: The top trace is the acoustic pulse. The bottom trace is a double negative pulse signal. (The pulse amplitude is 50 V.) (b) Read-out signal: The top two traces are the two acoustic pulses which are sent from either end of the delay line. The bottom trace is the stored double negative pulse signal read out at a frequency of 220 MHz after 100 μsec. (c) Read-out signal after 100-μsec double positive pulse input. (d) Read-out signal after 1 msec. In all cases the repetition rate of the signals is much longer than the measured storage time. Time scale: 1.0 μsec/div. dc bias voltage: 1.5 kV.

con surface is completely depleted, i.e., the surface potential reaches the midgap condition. A further increase in the bias causes the surface to be inverted, resulting in a decrease of the storage time because of recombination of trapped electrons with holes. In a lower bias range, the storage time increases exponentially with the bias at the rate predicted by Eq. (1). By extrapolating the curve of the storage time to the midgap point, we can determine the capture cross section σ in Eq. (1) to be $2 \times 10^{16} \text{ cm}^{-2}$, which is in good agreement with the results of Nicollian and Goetzberger.⁴

A second set of experiments involved using a short acoustic pulse as a read-in signal. We used the storage in the surface state as a memory for a double pulse inserted on the semiconductor to which a dc bias was applied, as shown schematically in Fig. 1(a). After these writing processes, we were able to read out the signal in a convolution process by sending a second acoustic pulse through the device as shown in Fig. 1(b). Under optimum conditions, we obtained a double pulse output, the results after 100 μsec being shown in Figs. 3(b) and 3(c), and after 1 msec in Fig. 3(d). In Fig. 3(b), we used a negative double pulse as a signal to be stored so that we detected a negative read-out signal, although the output signal contained a dc level. When a positive double pulse was used, we could obtain a positive read-out signal as shown in Fig. 3(c). The results were critically dependent on the dc bias level, but not very critical with respect to the rf reading and writing pulse levels or the level or sign of the stored input signal.

We conclude that it is possible to store acoustic signals in surface states and read them out again after

relatively long times. At the moment because of the thickness of the LiNbO_3 , the applied voltages are very large. Our future intention is to work with surface wave convolvers using zinc oxide on silicon so as to lower the required potentials by several orders of magnitude.

We have described here one possible mode of operation of this device. There are other possible modes of operation involving use of an input signal to be stored whose carrier frequency is the same as that of the acoustic surface waves. As another example, it is also the reading pulse. In this case the output obtained will be the correlation of the input signal with the reading signal.

We would like to thank Hervé Gautier, whose unpublished experiments on the variation of convolution efficiency with time led us to consider this type of storage process. We would also like to thank E. Stern of Lincoln Labs, who kindly furnished us with a preprint of closely related but independent work by A. Bers and J.H. Cafarella on essentially the same technique for storage of acoustic signals.

*The work reported in this paper was supported by the U.S. Office of Naval Research under Contract No. N00014-67-A-0112-0039.

¹On leave from the Electrotechnical Laboratory, Tanashi, Tokyo, Japan.

²G.S. Kino, W.R. Shreve, and H.R. Gautier, in 1972 *Ultrasonic Symposium Proceedings* (IEEE, New York, 1972) p. 285.

³M. Yamanishi and T. Kawamura, in Ref. 1, p. 288.

⁴W.C. Wang and P. Das, in Ref. 1, p. 316.

⁵E.H. Nicollian and A. Goetzberger, *Bell Syst. Tech. J.* **46**, 1055 (1967).

Integrated circuits as viewed with an acoustic microscope

R. A. Lemons and C. F. Quate

Microwave Laboratory, Stanford University, Stanford, California 94305
(Received 9 May 1974)

The images of a high-frequency bipolar transistor obtained with an acoustic microscope are compared with those of a differential interference optical microscope and a scanning electron microscope in order to illustrate that the acoustic microscope can be used in a reflection-type mode to obtain quality pictures of a surface containing integrated circuits. The frequency of the acoustic beam is 600 MHz and the resolution is near $2\ \mu$.

The acoustic microscope is a new instrument for observing microscopic detail which should enhance our ability to delineate and record detail that is difficult to see with an optical instrument.^{1,2} The features of the instrument that we use have been described previously.^{3,4} We use a piezoelectric film to launch the acoustic beam at one end of a sapphire crystal, and this crystal contains a spherical lens ground into the opposite face. The lens is immersed in water and the beam converges to a sharp focus within the liquid. The large change in sound velocity at the lens interface which divides sapphire and water reduces the spherical aberration to the point where the beam waist is limited only by diffraction effects. With our operating frequency of 600 MHz the effective diameter of the beam at the waist is $2\ \mu$ —a number which determines the resolution limit.

The image in our system is obtained by mechanically scanning the object through the waist of the beam. In previous reports, where we were primarily interested in biological specimens, we monitored the transmission of sound by using a symmetrical crystal with lens and piezoelectric film to collect the scattered beam and convert it to an electrical signal. This information was displayed on a television monitor with the raster synchronized to the mechanical scanning motion of the object.

In this paper we describe a modified mode of operation wherein we monitor the sound wave that is reflected by the object. In this way we are able to view the structure of a planar surface. We report here on our initial results with this type of microscopic imaging so as to give some appreciation of what can be done at this stage in the development of acoustic microscopy. We believe that this mode will be of utility in viewing integrated circuits. The diagrammatic representation of the reflection mode is shown in Fig. 1. The acoustic wave is launched into the sapphire crystal with a conventional sputtered ZnO film transducer. The spherical concave lens, ground into the opposite end of this crystal, focuses the beam into a diffraction limited spot at the surface of the silicon wafer which forms the substrate for the integrated circuitry. This lens of diameter 0.2 mm has an f number of 0.75.

Since the silicon wafer is being scanned the variations due to the integrated circuits appear as a time-dependent modulation of the reflected signal. We are able therefore to distinguish this component from other reflections internal to the instrument by proper filtering, yielding both amplitude and phase information about the object. In much of our work the strongest signal comes from

the change in phase and our images take on the appearance of "interference" microscope images. The phase change comes from variations in the thickness of the circuitry. For example, a metallized stripe $0.51\ \mu$ ($\lambda/4$) in thickness will give a 180° phase difference between the signal reflected from the top of the metallized stripe as compared to the signal reflected from the substrate. Since we are using a coherent cw signal this phase difference is easily recorded by combining the reflected signal with a suitable reference signal. In some of our work we have been able to observe metallized stripes that were $1000\ \text{\AA}$ thick.

The photos that we have recorded with this system are shown in Figs. 2–4. In Fig. 2 we display a comparison between the optical and acoustical image of a bipolar transistor. The device is the hp22, a high-frequency transistor with a maximum operating frequency of 16 GHz. The optical photo was taken with an interference microscope of the Nomarski type. The scale can be judged from the width of the three fingers connected to the squarish pad on the right. These fingers form the emitter and they are $2\ \mu$ wide. Much of the detail found in the optical picture is contained in the acoustic image. The surface features of the silicon substrate are clearly seen as well as the characteristic outline of the transistor. There are, however, distinct differences between the two photos.

In interpreting the acoustic images it should be kept in mind that the present instrument is phase sensitive. Accordingly, variations in surface topography will be recorded in the image as changes in contrast. This feature is evident in Fig. 2(A) both in the detail of the bonding pads and in the region where the fingers cross to the base.

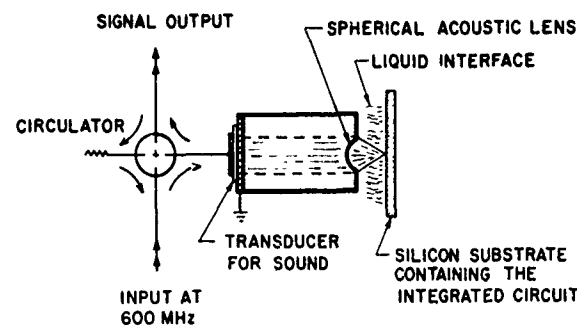


FIG. 1. Diagrammatic scheme for the reflection mode. The silicon substrate is scanned mechanically to obtain the image.

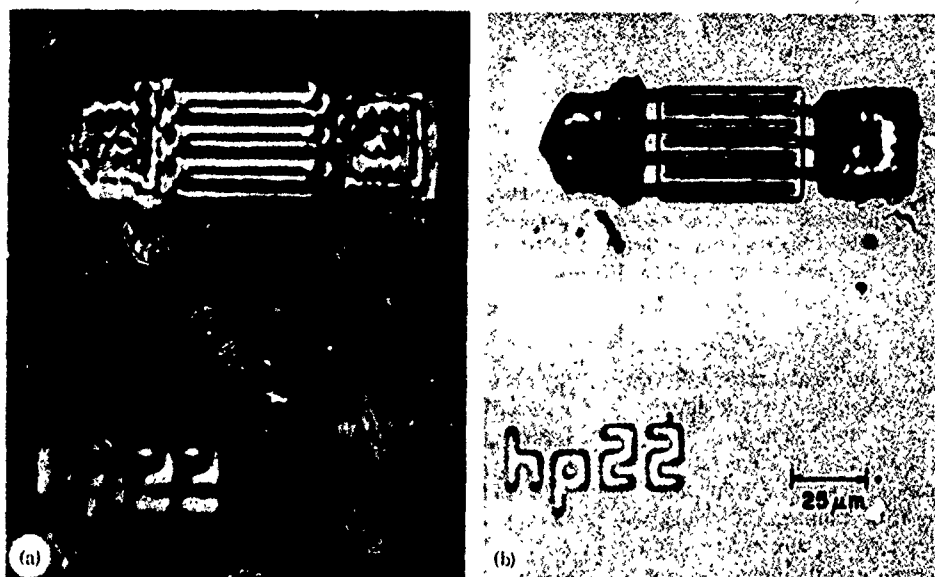


FIG. 2. Acoustic (A) and optical (B) comparison of a bipolar transistor. The width of the three narrow fingers is 2μ .

In Fig. 3 we present a comparison between the acoustic image of the hp22 and the image as obtained with a scanning electron microscope (SEM). The resolution is far greater in the SEM photo but nonetheless the comparison is interesting and it shows that the $2\text{-}\mu$ lines can be easily seen.

Finally, in Fig. 4 we show the acoustic image of an hp122 together with the optical comparison. This again is a bipolar transistor, scaled down from the hp22, and it is the smallest transistor known to us. This object is interesting for this study since the periodicity of the interleaving fingers is 2.5μ and the width of the smaller fingers is near 1μ . These fingers are clearly resolved in the acoustic image and it gives us confidence in our assertion that the waist of our beam is no larger than 2μ .

In future work we must learn how to separate the variation in amplitude in the reflected signal from the variation in phase. This instrument was not initially designed for reflection type operation and it should be possible to improve the quality of these images by incorporating an acoustic beam splitter so as to improve the separation of the reflected beam and the incident beam.

The materials used for IC's are transparent to acoustic waves at this frequency and we should be able to obtain information on the region that lies beneath the metallized surface—a region inaccessible to the optical microscope. We must learn to interpret the images that are formed when we change the plane of focus and probe the region beneath the surface. This capability should allow us to delineate defects such as improper bonds between a metallization layer and the substrate.

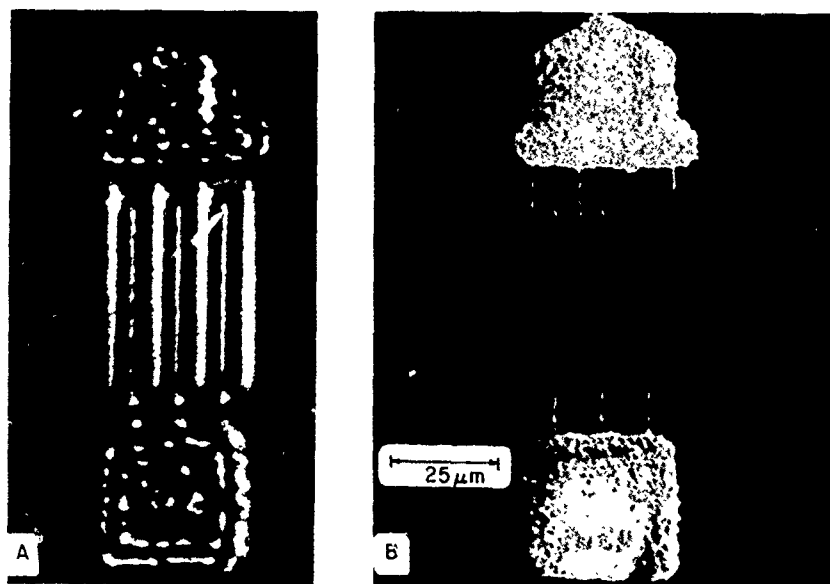


FIG. 3. Comparison between the image from the acoustic microscope (A) and a scanning electron microscope (B). The object is the bipolar transistor as shown in Fig. 2.



FIG. 4. Comparison between the acoustic (a) and optical (b) images of the hp 122—a high-frequency bipolar transistor with a periodicity of 2.5μ and a finger width near 1μ .

It is difficult to uncover problems of this type with either an optical or a scanning electron microscope.

Further, we believe that the various image enhancement techniques which have recently been developed³ could be applied directly to the electrical signals that emerge from the microscope. The use of discrete multiple frequencies in the acoustic system together with color display in the monitoring scope and simple differentiation of the signal for edge enhancement are the more obvious techniques that could be employed to improve the image.

The resolution can be improved by moving to higher frequencies. We have obtained images at 1000 MHz and we are confident that improvements can be made which will allow us to generate images with a resolution sufficient to resolve detail that is less than 1μ in diameter.

We are grateful to Hewlett-Packard Company for furnishing us with the transistors. We appreciate the professional guidance that we received from W. Bond

during this work. The present instrument is a result of the talented and careful work of G. Kotler, G. Bicker, and P. Galle. The optical photos were taken in the integrated Circuits Laboratory at Stanford and the SEM photos were taken with the facilities of the Center for Materials Research. We acknowledge the financial support of the Office of Naval Research.

¹W. Kessler, in *Proceedings of the Symposium on Optical and Acoustical Micro-Electronics*, Vol. XXIII, edited by A. Olmer (Polytechnic Press, New York, 1974).

²J. A. Cunningham and C. F. Quate, *J. Phys. (Paris) Suppl.* 33, 42 (1972); J. A. Cunningham and C. F. Quate, in *Acoustical Holography*, Vol. 5, edited by P. Green, (Plenum, New York, to be published).

³R. A. Lemons and C. F. Quate, *Appl. Phys. Lett.* 24, 163 (1974).

⁴R. A. Lemons and C. F. Quate, in *Proceedings of the Ultrasonics Symposium*, IEEE Catalog No. 73CHO 807-8 SU, edited by J. de Klerk (IEEE, New York, 1973), p. 18.

⁵D. A. O'Hanley and W. B. Green, *Proc. IEEE* 60, 821 (1972).


 RECEIVED PAGE BLANK

Multilayer Impedance Matching Schemes for Broadbanding of Water Loaded Piezoelectric Transducers and High Q Electric Resonators

JEFFREY H. GOLL AND BERTRAM A. AULD, FELLOW, IEEE

Abstract—High efficiency, low ripple piezoelectric transduction into a water load has been achieved experimentally over a bandwidth of about 70% by using a two-layer acoustic impedance matching transformer. Similar performance is predicted for properly designed transducers in a frequency range of 1 to 40 MHz.

THE NARROW bandwidth of piezoelectric transducers radiating into water (or other fluid) loads is partly a consequence of the mismatch of acoustic impedances between the transducer and the load. Broad bandwidth coupling to water has been accomplished previously by using single layer acoustic impedance matching [1]. It is reported here that still broader bandwidths may be obtained by using properly chosen multiple layer impedance matching schemes. Furthermore, while the single layer method requires for the matching layer a material with characteristic acoustic impedance of about 6×10^6 kg/s·m², which must be prepared synthetically, two layer

schemes work very well with readily available materials—glass (or fused quartz) and lucite—as the matching layers.

The theoretical insertion loss and phase transfer in a 50 ohm circuit may be calculated from the Mason model [2]. In the interest of high efficiency, only air-backed transducers have been considered. The role of the acoustic impedance matching layers is to transform the load acoustic impedance into a frequency dependent complex number which depends strongly on the characteristic impedances and thicknesses of the matching layers. This impedance transformation has a pronounced effect on the frequency response of the transducer and, by properly choosing the characteristic acoustic impedances of the layers, a very broadband response can be achieved. For piezoelectric ceramic or LiNbO₃ transducers, fused quartz and lucite matching layers, in the configuration illustrated in Fig. 1, give excellent performance. Over the frequency range in which the coupling is high, the electrical input impedance of the acoustically matched transducer is a reasonable approximation of a simple R - C circuit of low electrical Q . Therefore, series inductive tuning may be used to further improve the insertion loss without affecting the bandwidth significantly. Figure 2 illustrates the insertion loss and phase transfer predicted in a 50 ohm circuit for a 0.688" diameter PZT-5A disk, half wave resonant at 1.55 MHz, with fused quartz and lucite transformers quarter wave

Manuscript received July 30, 1974. This work was supported by the Office of Naval Research under Contract N00014-67-A-0112-0039.

J. H. Goll was with the Microwave Laboratory, Stanford University, Stanford, Calif. 94305. He is now at The Thomas C. Jenkins Department of Biophysics, The Johns Hopkins University, Baltimore, Md.

B. A. Auld is with the Microwave Laboratory, Stanford University, Stanford, Calif. 94305.

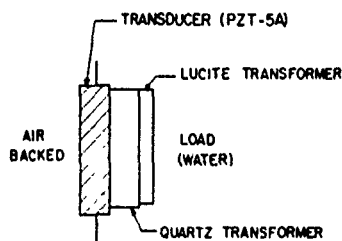


Fig. 1. Physical configuration of the quartz-lucite matching scheme. The transducer itself is one-half wavelength thick at f_0 and the matching layers are each approximately one-quarter wavelength thick at f_0 .

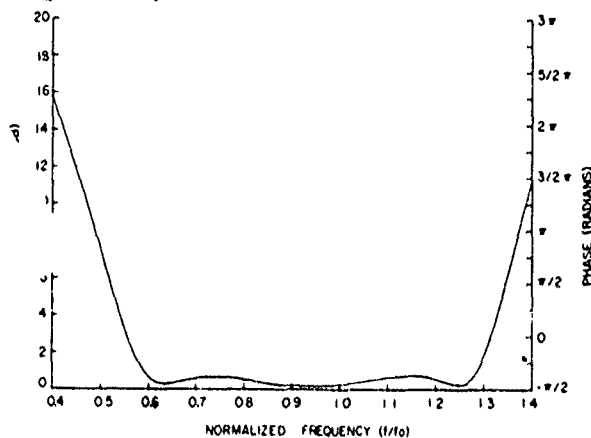


Fig. 2. Frequency dependence of the insertion loss and phase transfer for a PZT-5A transducer, with half-wave resonant frequency $f_0 = 1.55$ MHz and with fused quartz and lucite acoustic transformers, quarter-wave thick at $0.92 f_0$ and $8 \mu\text{H}$ series inductive electrical tuning.

TABLE I

f_0 (MHz)	2-Way Insertion Loss (dB)
0.91	10
0.96	6
1.01	4
1.15	5
1.3	6
1.55	5.5
1.66	5
1.81	6
1.90	8
1.94	10

thick at about 1.43 MHz, and with an 8 microhenry series tuning inductor. The 3 dB bandwidth (about 70%) is considerably wider and the ripple is smaller than for the optimal single transformer designs (which have about 45% 3 dB bandwidth for the corresponding air-backed case). Without the tuning inductor, the performance is similar. The only major differences are that the ripple is slightly greater and the insertion loss is about 2 dB higher without the tuning inductor. The phase transfer is very nearly

linear with frequency over the high coupling region. This property is important in pulse applications.

A transducer was fabricated with fused quartz and lucite transformers corresponding approximately to Fig. 2, and the insertion loss was measured by a pulse propagation method. The results, indicated as two-way insertion loss in Table I, are in good agreement with the theory except that the loss is systematically 2 dB per transducer higher than predicted. This discrepancy may have been partly due to electrodes which were not sufficiently thick.

For a large class of transducers, the bandwidth is mainly determined by acoustic impedance considerations. The value of the loss, however, will be low only when the transducer material and the lateral size (active area) of the transducers are properly chosen. In general, because of their extremely high dielectric constants, piezoelectric ceramics are the proper choice for low (between 1 and 6 MHz) resonant frequency transducers in a 50 ohm circuit. Lithium niobate (LiNbO_3) is the best choice for higher frequency transducers. For any resonant frequency between 1 and 40 MHz in a 50 ohm circuit, proper design yields theoretical 3 dB bandwidths of about 70% with loss across the band of less than 5 dB.

Properly chosen three layer acoustic impedance matching schemes offer still wider band (about 90%), low-loss, low-ripple transducer designs. The materials called for in these designs, however, with acoustic impedances of 22×10^6 , 7.8×10^6 , and $2.8 \times 10^6 \text{ kg/s}\cdot\text{m}^2$, are not all readily available.

An analogous electrical impedance matching problem—the broadband coupling to high Q electric resonators by use of multiple, approximately quarter wave transmission line segments—was also pursued theoretically. It has been reported previously [3] that bandwidths several times $1/Q$ may be obtained by the use of a single properly chosen transmission line segment. It is reported here that significantly broader bandwidths with low insertion loss, low ripple, and good phase linearity may be obtained by using two properly chosen transmission line segments. The characteristic impedances and lengths of the transmission line segments are the important parameters. The utility of such matching schemes is greatly increased by the availability of lumped-element approximations of transmission line segments which require relatively few elements and greatly expand the range of available matching sections [3].

ACKNOWLEDGMENT

Acknowledgment is due to D. K. Winslow for helpful discussions on transducer construction and to F. Futterer for assistance in the fabrication.

REFERENCES

- [1] G. Kossoff, "The Effects of Backing and Matching on the Performance of Piezoelectric Ceramic Transducers," *IEEE Trans. Sonics Ultrasonics*, SU-13, 20-30 (March 1966).
- [2] W. P. Mason, *Electromechanical Transducers and Wave Filters* (Van Nostrand, Princeton, N. J., 1948).
- [3] T. M. Reeder and W. R. Sperry, "Broad-band Coupling to High- Q Resonant Loads," *IEEE Trans. Microwave Theory Tech.*, MTT-20, 453-458 (July 1972).

Reprinted from: ACOUSTICAL HOLOGRAPHY, VOL. 6

Edited by N. Booth

Book available from: Plenum Publishing Corporation
227 West 17th Street, New York, New York 10011

AN ELECTRONICALLY FOCUSED TWO-DIMENSIONAL ACOUSTIC IMAGING SYSTEM

J. Fraser, J. Havlice, G. Kino, W. Leung, H. Shaw,
K. Toda, T. Waugh, D. Winslow, and L. Zitelli

Stanford University, Stanford, California 94305

I. INTRODUCTION

We described a new type of electronically focused and scanned acoustic imaging device in last year's conference. This device made use of a surface acoustic wave delay line to provide the necessary phase references and time delay for the imaging system and for scanning; it employed mechanical scanning in one direction and electronic scanning in the other, and was only focused electronically in one direction. Since that time, we have developed a two-dimensional electronically focused C-scan device operating in a transmission mode using a separate electronically focused receiver and transmitter. The receiver is focused and scanned in the x direction and the transmitter focused and scanned in the y direction. By using this combination of transmitter and receiver, it is possible to scan out a raster and obtain $M \times N$ resolvable spots with only $M + N$ elements in the transmitter and receiver arrays.

At the same time we have been constructing a 100 element receiver array, which is intended to be used either with the electronically focused transmitter or with a mechanically scanned transmitter focused with a lens. In both devices we have demonstrated that the principles of the system are valid; we have improved the sensitivity of the receiver system by several orders of magnitude over the earlier devices, by employing double balanced mixers and amplifiers on every element. However, we have encountered the major difficulty common to all phased array systems - the problem of sidelobes. So far, in both the transmitter

and the receiver array, the sidelobe level is typically 13 dB lower than the main lobe when the system is unapodized, as it should be according to the simple theory of a uniformly excited array.

We have investigated apodizing the system. In theory, by using Hamming weighting, we should obtain a sidelobe level of -43 dB. In practice, we have not succeeded in obtaining better than -20 dB sidelobe levels. The basic reason for this problem is associated with missing elements and errors in the system. So in this paper we carry out a fairly detailed analysis of the problem of missing elements, a problem which will be common to all electronically focused systems. We show that it is possible to predict very closely the amplitudes of the sidelobes when there are elements missing, both by simple techniques and more sophisticated numerical procedures. We also show how it is possible to evaluate a particular system with missing elements and discuss possible procedures for eliminating errors.

II. PRINCIPLES OF THE ELECTRONICALLY FOCUSED SYSTEM

The electronically focused and scanned system on which we have worked can be used either in a transmission mode or a receiver mode, or for both transmission and reception. In order to explain the principles of operation, we will consider a receiver in which the object is illuminated with an acoustic wave of frequency ω_s , as illustrated in Fig. 1. The signal is received by a set of piezoelectric transducers. The electronic system employed scans the signals arriving at these transducers and provides phase compensation for the different rays arriving from a point x, z . We use, as a phase reference, a tapped acoustic surface wave delay line, one tap for each PZT transducer. The reason for the use of an acoustic surface wave delay line is its convenience, flexibility, and ready availability. It is also possible to employ a CCD in the same manner, or to employ a shift register in a very similar system. The output at a frequency ω_s from each transducer is mixed with the output from a corresponding SAW tap in a mixer. Originally these mixers were simple diodes; now we employ balanced integrated circuit mixers, and the outputs from each mixer are summed in an output circuit.

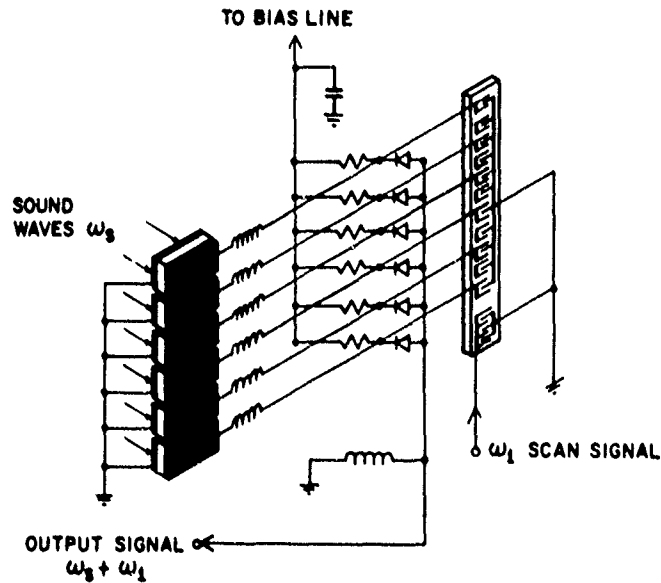


FIG. 1--Schematic-pictorial diagram of acoustic imaging system.

Suppose we wish to detect a signal from the point x, z , at the plane of the transducer array $z = 0$. The phase of the signal at an element with coordinates $x_n, 0$ is

$$\phi_{sn} = \frac{\omega_s}{v_w} \left[\sqrt{(x - x_n)^2 + z^2} \right], \quad (1)$$

where v_w is the wave velocity in the medium of interest. If we insert a signal on the acoustic delay line with a phase ϕ_{An} such that $\phi_{An} + \phi_{sn} = \text{constant}$, then in this case, all the signals from the outputs of the mixer are in phase and can be added. We have therefore constructed a matched filter, matched to a source at the point x, z , i.e., we have constructed an electronic lens.

It is a relatively simple matter to design the correct signal waveform for this purpose. Consider a signal whose phase is

$$\phi = \omega_1 t + A \sqrt{t^2 + B^2} \quad (2)$$

This signal has a frequency

$$\omega = \frac{\partial \phi}{\partial t} = \omega_1 + \frac{At}{\sqrt{t^2 + B^2}} \quad (3)$$

At the n^{th} tap on the surface wave delay line, the phase of this signal is

$$\phi_{An} = \omega_1 \left(t - \frac{x_n}{v} \right) + A \sqrt{\left(t - \frac{x_n}{v} \right)^2 + B^2} \quad (4)$$

It will be seen that the required phase matching condition is satisfied if $\omega_1 x_n/v = \omega n r$, which requires choosing ω_1 correctly, and

$$t = x/v \quad (5)$$

with

$$A = \frac{\omega_1 v}{v_w} \quad (6)$$

$$B = \frac{z \omega_1}{A v_w} = \frac{z}{v} \quad (7)$$

It will be seen from these results that by using this electronic signal processing technique, the system focuses on the point x, z at a time $t = x/v$ and, therefore, scans along the plane z at a velocity v . At the same time, with the correct choice of the parameter A , adjustment of the parameter B of the signal waveform inserted into the acoustic surface wave delay line is equivalent to adjusting the focal length of the lens. In this case, by using the correct waveform, no paraxial approximation is required, and the lens should not suffer from spherical aberration.

In our devices so far, we have not used this waveform. Instead, we have simplified the approach and used a linear FM chirp with a frequency

$$\omega = \omega_1 + \mu t \quad (8)$$

and phase

$$\phi = \omega_1 t + \frac{\mu t^2}{2} \quad (9)$$

In this case, which is equivalent to the paraxial approximation, i.e., assuming that $z^2 \gg (x - x_n)^2$, the chirp rate is varied to vary the focal length of the lens and we find to focus on the plane z ,

$$\mu = \frac{v^2 \omega_s}{2v_w} \quad (10)$$

It should be noted that a still better approximation to the ideal signal waveform, which is easier to realize and which is accurate to terms in $(x - x_n)^4$, is to use an input signal with frequency

$$\omega = \omega_1 + \frac{\omega_s v}{v_w \sqrt{3}} \sin\left(\frac{vt}{z} \sqrt{3}\right) \quad (11)$$

This is normally accurate enough for most practical purposes.

In our first experiments, we employed a receiver system of this kind in a transmission mode with an object placed in front of a narrow strip transducer, the length of the strip being parallel to the length of the array. The object was moved up and down mechanically in the y direction and the receiver was electronically focused and scanned in the x direction. An alternative to this procedure is, of course, to use a focused transmitter, focused on a line within the object. Then either the transmitter can be moved up and down in the y direction, or the objects can be moved up and down in the y direction to obtain a two-dimensional scan. Of course, such a system can also be used in reflection mode with the transmitter placed in the same plane or near to the receiver's array.

A second alternative on which we have been working is to use an electronically focused and scanned transmitter in the arrangement shown on the left of Fig. 2. By inserting a signal in what normally would be the output port of the receiver and a chirp signal on the delay line, it is possible to obtain a focused and scanned transmitting beam. A full two-dimensional image is obtained with the rest of the system of Fig. 2. However, the disadvantage of such a system is that the scan rate is comparable to that of the acoustic velocity along the delay line. Ideally we would prefer to work with a system in which the scan rate in the vertical direction is relatively slow, and comparable to the frame rate required, while the scan rate in the horizontal direction is fast and corresponds to the line time.

An additional desirable feature would be to excite all the transmitting transducers at the same frequency; this would minimize aberrations and also place less severe requirements on the transducer bandwidth. Thus it would be possible to scan out a normal type of TV raster.

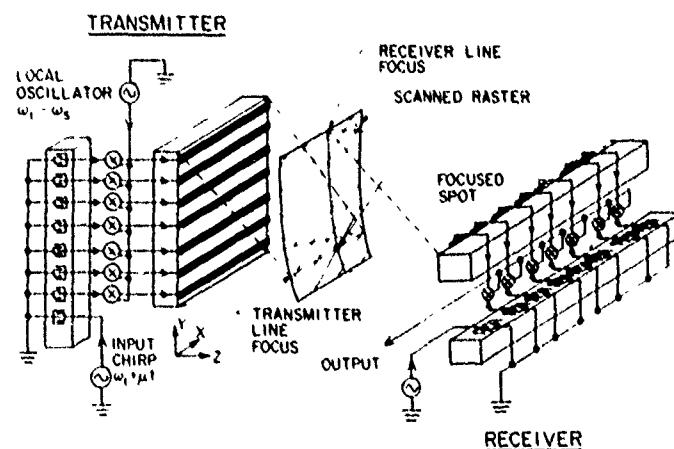


FIG. 2--Schematic-pictorial diagram of an electronically scanned, electronically focused imaging device. On the left side is the transmitter which provides a scan rate comparable to the acoustic velocity on the delay line.

epoxy bonded to a mycalex backing. The array is covered with a thin mylar film. The elements have a center-to-center spacing of 47 mils, but only every other element was excited in the initial system.

In the first system we used FET amplifiers driven from taps on the SAW line, followed by diode mixers for the three frequencies involved, and transistor amplifiers. The system was subject to some phase and amplitude errors and leakage of signals at unwanted frequencies, as well as a low output. But it served to prove the feasibility of the ideas involved. Initially, we used an early developmental model of the receiver array already described with only 22 elements.

By placing an object between the transmitter and receiver, we were able to obtain a focused image, with a definition of approximately 2 mm in the x and y directions, a 60 cycle frame rate and a line time of approximately 100 μ sec. As predicted we could obtain a stationary focus in the y direction or move the line up and down at will by changing the frequency ω_2 manually, thus making it possible to examine an object slowly or fast. By using a slow chirp repeated at a 60 cycle rate we obtained a frame time of 60 cycles.

A picture of a letter S cut in a piece of rubber located 7 cm from the transmitter and 10 cm from the receiver is shown in Fig. 8. By changing the chirp rate by 25% in the horizontal direction, the letter S is seen to be defocused in the horizontal direction. Similarly by changing the chirp rate of the transmitter by 25%, the letter S is seen to be defocused in the vertical direction, as would be expected.

The transmitter system was rebuilt with different mixers and amplifiers, and a 24 element 1.8 MHz array with elements 47 mils apart. In this case, we used double balanced mixers (TI76514), which eliminated the problems with unwanted side-band frequencies. The mixers were followed by transistor amplifiers, (2N3906), and a signal with 20 V peak-to-peak output could be obtained at the transducers. We also made provision for trimming the output amplitude.

With this system we obtained, with Hamming weighting, a 20 dB sidelobe level. We took pictures of simple objects cut in rubber with the system, using a strip receiver mechanically scanned in the horizontal direction. Such a

III. EXPERIMENTAL SYSTEMS

We have been working with two types of experimental arrays, an 80-100 element receiver system, and a 22-29 element transmitter system. It is intended that systems of these types will be used together in a C-scan transmission or reflection mode, as well as employing the receiver array with a mechanically scanned transmitter for two-dimensional C-scan imaging.

A schematic of the basic components of the receiver system is shown in Fig. 5. Each transducer element consists of a cube of PZT 5A 20 mils square and 16 mils high, glued with epoxy to a mycalex backing, and covered on its front side with a mylar film. The elements have a center-to-center spacing of 47 mils; they are square in cross section so that the acceptance angle (measured to be $\pm 30^\circ$) is approximately the same in the horizontal and vertical directions, thus giving approximately the same field of view in both planes. The array itself is mounted on the side of a water tank.

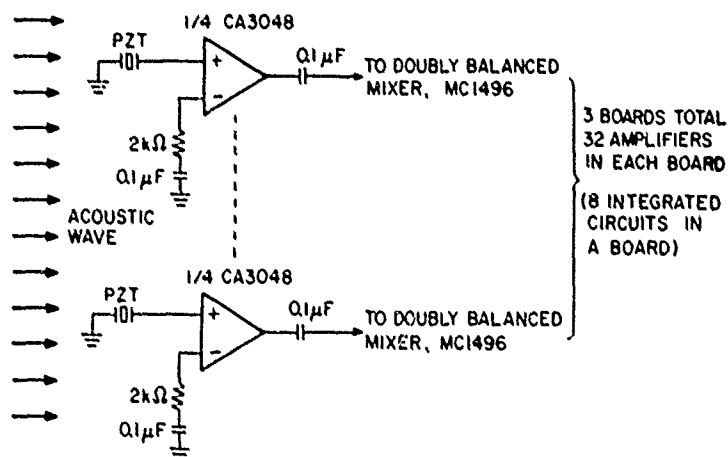


FIG. 5--Schematic diagram of PZT preamplifier system.

a frequency ω_s , filtering it so as to only keep the upper sideband, and then inserting it into the second mixer, we obtain outputs into all the transducers of frequency ω_s .

An analysis of the phase variation of the signals passing along the delay line shows that the phase of the signals at the n^{th} tap are

$$\phi_2(x_n) = (\omega_1 - \omega_2) \left(t - \frac{y_n}{v} \right) + \frac{\mu}{2} \left(t - \frac{y_n}{v} \right)^2 \quad (12)$$

$$\phi_3(x_n) = (\omega_3 - \omega_1) \left(t + \frac{y_n}{v} - \frac{L}{v} \right) - \frac{\mu}{2} \left(t - \frac{L}{v} + \frac{y_n}{v} \right)^2 \quad (13)$$

After these signals are mixed together, we obtain a signal with phase $\phi_2(y_n) - \phi_3(y_n)$. This in turn is mixed with the similar signal from the tap at $y_n = 0$, after it has been modulated with a frequency ω_s . The phase of the resultant signal at the n^{th} tap is

$$\phi(x_n) = (\omega_2 + \omega_3 - 2\omega_1) \frac{y_n}{v} + \frac{\mu}{v^2} \left(y_n - \frac{L}{2} \right)^2 \quad (14)$$

Thus, the output signal has a square law variation of phase along the system, which is equivalent to a lens producing a beam focused at the plane $z = \omega_s v^2 / 2\mu v_w$. In addition there is a linear phase term, which controls the y position of the focal point. If $(\omega_2 + \omega_3 - 2\omega_1)y_n/v = 2m\pi$, the lens focuses on the point $y_n = L/2, z$. Alternatively, if ω_3 or ω_2 is varied slowly the focal point moves along the y axis. Thus by changing one of these frequencies slowly the beam may be scanned along the y axis; this is equivalent to using a slow chirp for the frequency ω_2 and a fast chirp for ω_1 which can be changed at will to vary the focal length of the lens. In practice the chirp lengths are chosen to be of the order of 100 μsec long, sufficient to produce a beam focused on one line of the image, which itself is scanned by the receiver array within this time. Then with a delay of the same order, the chirps are re-inserted in the transmitter delay line and the whole process is repeated, now with the line moved one line along the y axis.

III. EXPERIMENTAL SYSTEMS

We have been working with two types of experimental arrays, an 80 - 100 element receiver system, and a 22 - 29 element transmitter system. It is intended that systems of these types will be used together in a C-scan transmission or reflection mode, as well as employing the receiver array with a mechanically scanned transmitter for two-dimensional C-scan imaging.

A schematic of the basic components of the receiver system is shown in Fig. 5. Each transducer element consists of a cube of PZT 5A 20 mils square and 16 mils high, glued with epoxy to a mycalex backing, and covered on its front side with a mylar film. The elements have a center-to-center spacing of 47 mils; they are square in cross section so that the acceptance angle (measured to be $\pm 30^\circ$) is approximately the same in the horizontal and vertical directions, thus giving approximately the same field of view in both planes. The array itself is mounted on the side of a water tank.

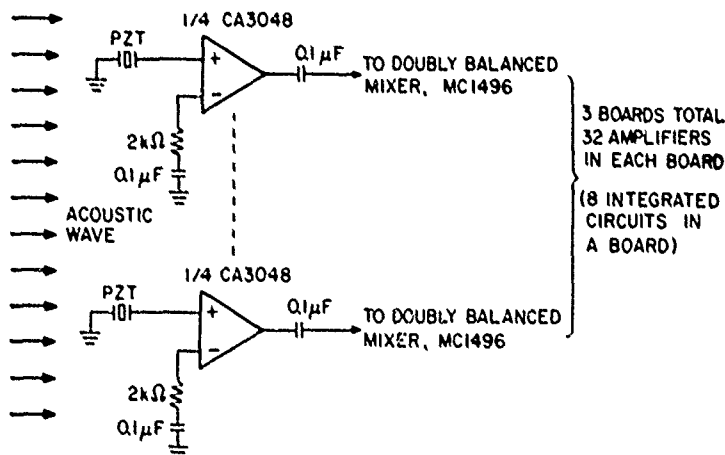


FIG. 5--Schematic diagram of PZT preamplifier system.

The impedances of the individual elements of the array are of the order of 5000 Ω , with a center frequency of 2.25 MHz. The system is, in fact, operated anywhere in the range from 1.6 MHz to 2.5 MHz, with most tests being carried out at 1.8 MHz. Amplifiers for the individual elements (CA3048), 4 to a package, are mounted on the back of the transducer array. Their outputs are taken through coaxial lines into doubly balanced mixers (MC1496), each mixer being driven via an MC1350 amplifier from a tap on a 50 MHz, 100 tap surface wave delay line approximately 5 inches long, made of BGO. The taps are arranged in two rows of 50, side by side, and the total delay through the line is 60 μ sec. The outputs of 4 mixers at a time are summed with a 1350 summing amplifier, whose outputs are in turn connected in parallel. The output of this system is mixed down to 30 MHz, passed through a 1.5 MHz bandwidth filter with 60 dB out of band rejection, to eliminate any feed through from unwanted signals, and the output then passed into an IF amplifier. After detection, this output signal is used to modulate the intensity of a cathode ray display, whose horizontal sweep is synchronized from the FM chirp trigger, and whose vertical motion is controlled either from a mechanical sweep or from the transmitter synchronizing circuits.

The receiver array performed basically as designed. The measured sensitivity of the individual elements was 10^{-11} watt/cm², and the 3 dB width of the main lobe of the focused beam, when illuminated from a 1.8 MHz narrow strip source pulsed for 100 μ sec was about 1.5 mm at a distance of 25 cm. As will be discussed, the sidelobe level was higher than we had hoped thus severely limiting the dynamic range of the receiver system, and the effective uniformity of the illumination of an object placed in front of a uniformly illuminated large area transmitter. For this reason we have, so far, been employing the device to observe objects with relatively good contrast. This is done by placing the object in front of a thin strip transducer approximately 4 inches long, and moving the object up and down mechanically.

One picture of a piece of rubber in which are cut a triangular, circular, and square hole is shown on the top of Fig. 6. On the bottom is the acoustic photograph of a thin metal plate with a number of small holes. It will be observed that the definition of the system is of the order of 1.5 mm.

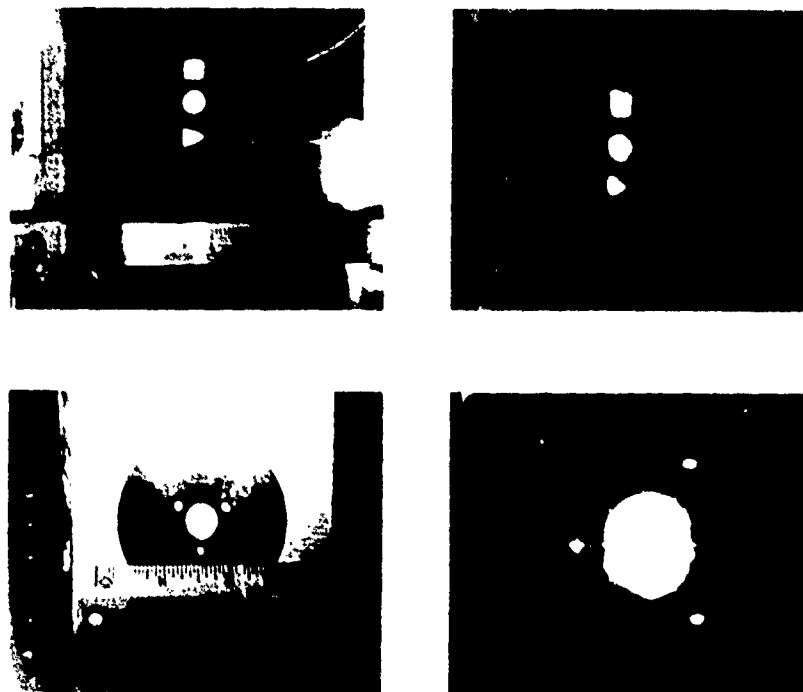


FIG. 1. ---Acoustic photographs using an 8 element receiver array. On the left are optical photos and on the right are acoustic photos.

The sidelobe level in this system was initially very high and of the order of 1 dB, both near in to the main lobe as well as further out. We attempted to apodize the array with either Hamming weighting of the chirp amplitude itself, or better still, by Hamming weighting of the array taps by means of trimmer pots on each element. Our best attempts to date have yielded a sidelobe level 20 dB down from the main lobe. This is mainly due to the fact that initially 15 elements out of 100 were inoperative, and later approximately 4 elements out of 80 were inoperative. This leads to a sidelobe level somewhat worse than we would expect from the theory given in the next section. In part this is due to the difficulty of apodizing accurately, to phase errors as well as amplitude errors, and to some cross coupling in the delay line. But the principle problem is

epoxy bonded to a mycalex backing. The array is covered with a thin mylar film. The elements have a center-to-center spacing of 47 mils, but only every other element was excited in the initial system.

In the first system we used PFT amplifiers driven from taps on the SAW line, followed by diode mixers for the three frequencies involved, and transistor amplifiers. The system was subject to some phase and amplitude errors and leakage of signals at unwanted frequencies, as well as a low output. But it served to prove the feasibility of the ideas involved. Initially, we used an early developmental model of the receiver array already described with only 22 elements.

By placing an object between the transmitter and receiver, we were able to obtain a focused image, with a definition of approximately 2 mm in the x and y directions, a 60 cycle frame rate and a line time of approximately 100 μ sec. As predicted we could obtain a stationary focus in the y direction or move the line up and down at will by changing the frequency ω_2 manually, thus making it possible to examine an object slowly or fast. By using a slow chirp repeated at a 60 cycle rate we obtained a frame time of 60 cycles.

A picture of a letter S cut in a piece of rubber located 7 cm from the transmitter and 10 cm from the receiver is shown in Fig. 8. By changing the chirp rate by 25% in the horizontal direction, the letter S is seen to be defocused in the horizontal direction. Similarly by changing the chirp rate of the transmitter by 25%, the letter S is seen to be defocused in the vertical direction, as would be expected.

The transmitter system was rebuilt with different mixers and amplifiers, and a 24 element 1.8 MHz array with elements 47 mils apart. In this case, we used double balanced mixers (TI76514), which eliminated the problems with unwanted sideband frequencies. The mixers were followed by transistor amplifiers, (2N3906), and a signal with 20 V peak-to-peak output could be obtained at the transducers. We also made provision for trimming the output amplitude.

With this system we obtained, with Hamming weighting, a 20-dB sidelobe level. We took pictures of simple objects cut in rubber with the system, using a strip receiver mechanically scanned in the horizontal direction. Such a

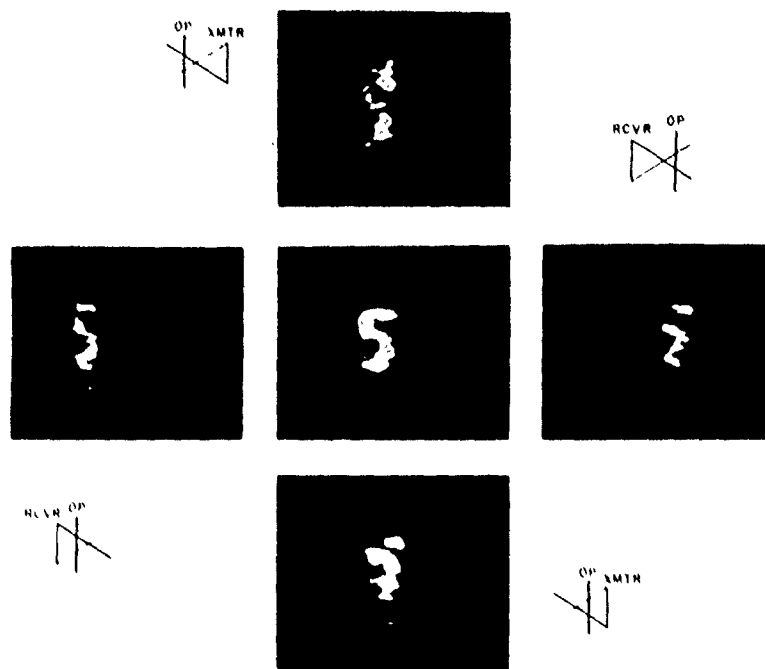


FIG. 8--Acoustic images obtained with an electronically scanned, electronically focused two-dimensional real time system. Corner photos show the effect of 25% defocus in the imaging system.

picture is shown in Fig. 9. We have not as yet tested the transmitter with an electronically focused receiver array, but hope to do so shortly.

IV. WEIGHTING OF THE ARRAY AND ERROR ANALYSIS

One of the principle problems associated with any phased array system is that associated with sidelobes. If the sidelobe level is R dB down from the main lobe, and an attempt is made to image two points A and B with point B more than R dB lower in intensity, the image of the point B may be obscured in the sidelobes of the stronger point source A . Thus, the dynamic range of an imaging

epoxy bonded to a mycalex backing. The array is covered with a thin mylar film. The elements have a center-to-center spacing of 47 mils, but only every other element was excited in the initial system.

In the first system we used FET amplifiers driven from taps on the SAW line, followed by diode mixers for the three frequencies involved, and transistor amplifiers. The system was subject to some phase and amplitude errors and leakage of signals at unwanted frequencies, as well as a low output. But it served to prove the feasibility of the ideas involved. Initially, we used an early developmental model of the receiver array already described with only 22 elements.

By placing an object between the transmitter and receiver, we were able to obtain a focused image, with a definition of approximately 2 mm in the x and y directions, a 60 cycle frame rate and a line time of approximately 100 μ sec. As predicted we could obtain a stationary focus in the y direction or move the line up and down at will by changing the frequency ω_2 manually, thus making it possible to examine an object slowly or fast. By using a slow chirp repeated at a 60 cycle rate we obtained a frame time of 60 cycles.

A picture of a letter S cut in a piece of rubber located 7 cm from the transmitter and 10 cm from the receiver is shown in Fig. 8. By changing the chirp rate by 25% in the horizontal direction, the letter S is seen to be defocused in the horizontal direction. Similarly by changing the chirp rate of the transmitter by 25%, the letter S is seen to be defocused in the vertical direction, as would be expected.

The transmitter system was rebuilt with different mixers and amplifiers, and a 24 element 1.8 MHz array with elements 47 mils apart. In this case, we used double balanced mixers (TI76514), which eliminated the problems with unwanted side-band frequencies. The mixers were followed by transistor amplifiers, (2N3906), and a signal with 20 V peak-to-peak output could be obtained at the transducers. We also made provision for trimming the output amplitude.

With this system we obtained, with Hamming weighting, a 20 dB sidelobe level. We took pictures of simple objects cut in rubber with the system, using a strip receiver mechanically scanned in the horizontal direction. Such a

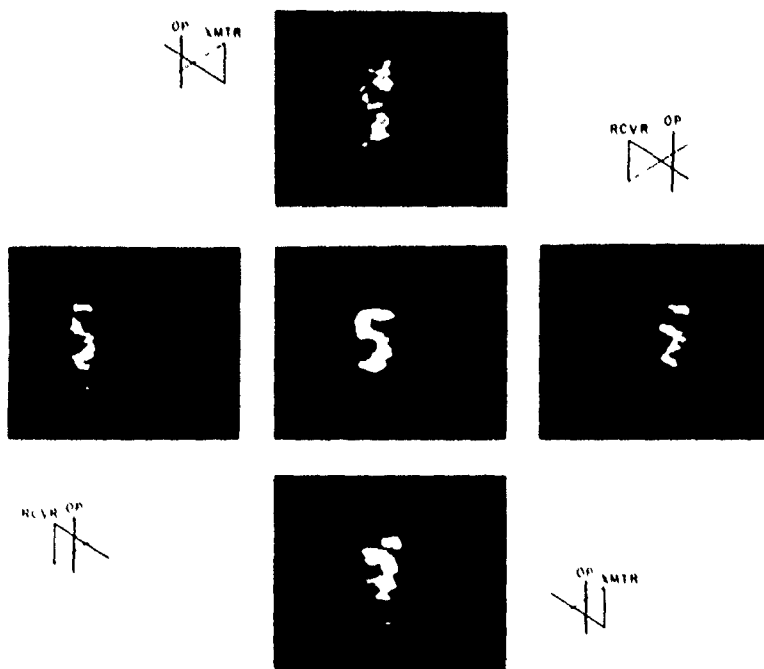
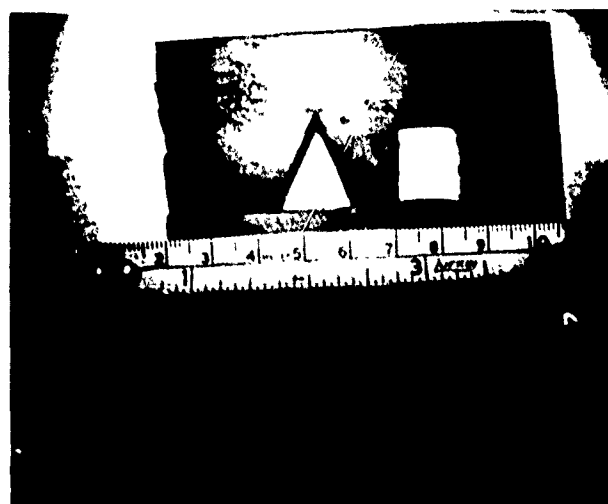


FIG. 8--Acoustic images obtained with an electronically scanned, electronically focused two-dimensional real time system. Corner photos show the effect of 25% defocus in the imaging system.

picture is shown in Fig. 9. We have not as yet tested the transmitter with an electronically focused receiver array, but hope to do so shortly.

IV. WEIGHTING OF THE ARRAY AND ERROR ANALYSIS

One of the principle problems associated with any phased array system is that associated with sidelobes. If the sidelobe level is R dB down from the main lobe, and an attempt is made to image two points A and B with point B more than R dB lower in intensity, the image of the point B may be obscured in the sidelobes of the stronger point source A . Thus, the dynamic range of an imaging



OPTICAL IMAGE



ACOUSTIC IMAGE

FIG. 9--Image obtained with Hamming weighted transmitter system.

system is limited by the sidelobe level.

There are several possible approaches to lowering the effective sidelobe level. One is to apodize the array, e.g., amplitude weight the response of the array. In an acoustic lens system, this is done in part automatically, because a convex lens tends to have more attenuation near its edges. With any electronic or physical lens, the response also tends to fall off with angle; this provides further apodization. A second approach, that used by Thurston,² is to use logarithmic amplifiers on each receiver element, and add the resultant signals after the appropriate phase matching, as already described. As all rays from a point source may be assumed to have equal amplitudes, this gives an image of a point source with a sidelobe level of just the same value as if the amplifiers were linear. However, now the signal from another point source would give an output R dB down in level only if it were far weaker relative to the main image. This is because of the logarithmic response of the amplifiers; if a 50 dB change in input signal corresponds to a 10:1 change in output power from the amplifier and a linear system had a 10 dB sidelobe level, this system would have a dynamic range of 50 dB. The full implications of this nonlinear processing technique are not entirely clear, but they do imply a lower effective sidelobe level at the expense of some loss in grey scale. A third approach is to use the same array for both transmission and reception. This tends to square the response of the system, and lower the effective sidelobe level to $\frac{1}{2} R$ dB.

Even with careful design, certain difficulties can arise when elements are missing, there is coupling between the elements, or there are phase errors in the system. By far the worst type of error is that due to missing elements. In this section we shall analyze the response of an array to a point source, and a distributed source, and show how this is affected by missing elements. We shall describe an analog technique which we have employed to check operating arrays, and a simple theory which gives easily calculated and accurate estimates of the effect of missing elements.

We consider a receiver array in which the amplitude response of the array at a point x is $F(x)$. We suppose that a signal of frequency ω_s from a source at the plane z

of amplitude $G(x')$ is incident on the array, and the array is focused by a chirp signal $\exp j(\omega_1 t + \mu t^2/2)$ which is mixed with the signals reaching it. The output of the array when focused on the plane z , ($\mu = \omega_s v^2 / z v_w$) is

$$H(t) = e^{j[(\omega_1 + \omega_s)t + (\mu/2)t^2]} \int_x \int_{x'} F(x) G(x') e^{-\frac{j\omega_1 x}{v}} \times e^{\frac{j\mu x}{v} (t - \frac{x'}{v})} dx dx'. \quad (15)$$

For the present purposes, we represent the response of the elements by the sampling function and write

$$F(x) = F(x_n) \sum \delta(x - x_n). \quad (16)$$

If again, we choose for simplicity the condition $\omega_1 x_n / v = 2\pi n$, which is equivalent to choosing a particular time for the start of the chirp, we can write the output in the form

$$H(t) = S(t) \int_{x'} e^{j \frac{\mu}{2} (\frac{x'}{2})^2} G(x') dx' \times \sum F(x_n) e^{\frac{j\mu x_n}{v} (t - \frac{x'}{v})}, \quad (17)$$

where $S(t) = \exp j(\omega t + \mu t^2/2)$, and is a function of unit magnitude. The signal from a point source at $x' = 0$ [$G(x') = \delta(x)$] is of the form

$$H(t) = S(t) \sum F(x_n) e^{\frac{j\mu x_n t}{v}} = S(t) \int F(x) e^{\frac{j\mu x t}{v}} dx. \quad (18)$$

Thus, the output from a focused array is the Fourier transform of the response of the array. All we need to know is

the response of the array to know the form of the output from the focused system.

Consider now, a uniform array $[F(x_n) = 1]$ with N elements a distance l apart, where $L = Nl$ is the length of the array. The output from this array will be

$$H(t) = S(t) \frac{\sin\left(\frac{\mu N l}{2v}\right)t}{\sin\left(\frac{\mu l t}{2v}\right)} \quad (19)$$

So the maximum output amplitude is at $t = 0$ and is of amplitude N , or N times the output from a single element. There are minor lobes at times $\mu N l t / 2v = (2n+1)\pi/2$, the first sidelobe being 13 dB reduced in amplitude from the main lobe. In addition there are grating lobes with their own sidelobes at $\mu l t / v = 2\pi m$, where m and n are integers.

A simple way of carrying out analog computations and illustrating this effect is to use a word generator to modulate an rf signal, then take the Fourier transform of the resultant signal in a spectrum analyzer. The result for a 32 element unapodized system is shown in Fig. 10(a). The 13 dB sidelobe level and the grating lobes can clearly be seen.

As a second example we can consider the use of Hamming weighting. In this case, taking $x = 0$ at the center of the array, $F(x_n)$ is chosen so that

$$F(x_n) = k + (1-k) \cos^2 \frac{\pi x_n}{L} \quad (20)$$

where L is the length of the array. Ideally for $k = 0.08$ the sidelobe level should be reduced by 43 dB from the main lobe. The maximum output for N elements will be

$$\begin{aligned} H(0) &= \frac{N(1+k)}{2} \\ &= 0.54N \quad (k = 0.08) \end{aligned} \quad (21)$$

For $k = 0.08$ the main lobe is 1.5 times as wide at the

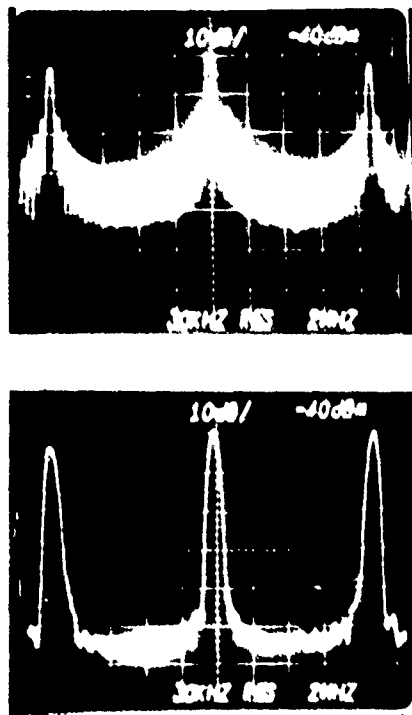


FIG. 10--(a) Top. Point response function for a 5 element uniform array. Note -13 dB sidelobes near the central lobe and the far grating sidelobes.
 (b) Bottom. Point response function for a 5 element Hamming weighted array. Note -33 dB sidelobes near in.

5 dB points as for the uniformly apodized array. An illustration of Hamming weighting, taken with the help of the analog technique, in a 5 element system, is shown in Fig. 10(b). It is clear that at the expense of a slight loss in definition, the use of apodization should be of great help in improving the sidelobe level.

We now consider the effect of errors. It is apparent that by using the formulae already given, we can calculate the effect of both amplitude and phase errors on the output

response. We have done this on a computer, and also employed our analog technique for the purpose. However, it is helpful to try and obtain some kind of analytic formulae with which we can estimate errors and find how many elements we can afford to have missing.

Suppose that the m^{th} element is missing. This is equivalent to subtracting an error term $e(t)$ from the output of magnitude

$$e(t) = S(t) F(x_m) e^{\frac{j\mu x_m t}{v}} \quad (22)$$

So the total output is

$$H(t) = H_0(t) - e(t) \quad (23)$$

where $H_0(t)$ corresponds to the output when there are no missing elements.

The period of the function $e(t)$ depends on the position x_m of the error. If it is in the center $e(t)/S(t)$ has virtually no phase change with time. If we suppose that the level of $e(t)$ is much larger than the sidelobe level in the error free array, we see that the sidelobe amplitude relative to the main lobe due to one missing element will be

$$R_m = \frac{F(x_m)}{\sum F(x_n) - F(x_m)} \quad (24)$$

In a Hamming weighted system, this corresponds to

$$R_m = \frac{2F(x_m)}{N(1+k) - F(x_m)} \quad (25)$$

Thus for a missing element at the center of the array, with $k = 0.08$

$$R_m = \frac{1}{0.54N - 1} \quad (26)$$

For $N = 32$ elements this corresponds to $R_m = 0.061$ or -24 dB.

A more exact calculation would take account of the side-lobe level already present, before the errors were introduced, i.e., 0.007 down from the main lobe. The true side-lobe level in the presence of errors would then be $0.061 + 0.007$ or -23 dB. The result agrees fairly well with the analog computer result shown in Fig. 11, and is almost exactly equal to the results of the computer calculation.

When there are several missing elements, the question is whether the effects are additive or tend to add only randomly, i.e., if there are M missing elements, is the amplitude error proportional to M or $M^{1/2}$. Unfortunately the former proposition is the more accurate, for if we suppose that there are several missing elements, the effect on the error signal is like that of an array made up of the missing elements. This array produces a signal with a main lobe in which the effect of all the elements is additive, and the main lobe tends to repeat itself in a distance, if the element spacing is periodic, corresponding to that of

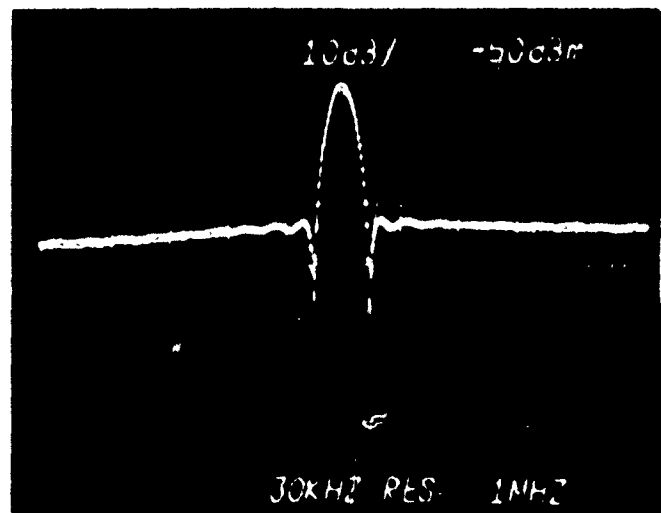


FIG. 11--Point response function for a 31 element Hamming weighted array with one central element missing [31 elements present]. Note that the absence of this single element raises the sidelobe level from -43 dB to -23 dB.

the grating lobes of the error array. If most of the elements that are missing are near the center of the array, the main lobe of the error array will be wider than that of the full array, so that there will be sidelobes of full amplitude near to the main lobe. More than likely, there will be other sidelobes of similar amplitude further out from the main lobe due to the quasiperiodicity of the error signal. We can therefore make a good estimate of the relative maximum sidelobe amplitude due to errors from the following formula:

$$R = \frac{\sum_{\text{error array}} F(x_n)}{\sum_{\text{full array}} F(x_n) - \sum_{\text{error array}} F(x_n)} \quad (27)$$

A picture of what occurs with 2 elements missing is shown in Fig. 12. The following table gives computed results for several cases, results taken with the analog system, and results obtained from the "quick" formula. The "quick" formula is seen to be accurate, and indicates that the errors due to missing elements tend to be directly additive, so that missing elements cause serious problems.

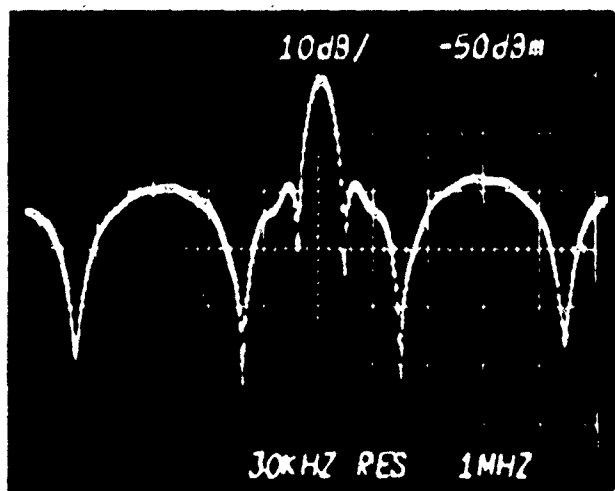


FIG. 12--Point response function for a 32 element Hamming weighted array with two elements missing [30 elements present, central element and third from center element missing]. Note sidelobe level is -18 dB.

TABLE I: Comparison of Sidelobe Level Calculation using Three Techniques. In all cases there are 32 elements [numbered -16, -15,-1, +1,15, 16]. Hamming Weighted.

Missing Elements	Sidelobe Level		
	"Quick" Calculation dB	Computer Calculation dB	Analog Measurement dB
1	-24	-23	-22
1 4	-18	-23	-18
1 12	-22	-22	-21
-10 1 12	-19.5	-19.5	-20
-1 +1	-17.5	-17.5	-16
-2 2	-17.6	-18.5	-18
-3 3	-18	-17	-17
-4 4	-18.5	-18	-18
-10 10	-26.5	-25.5	-26
-2 1 12	-16.5	-17	-16
-10 1	-16	-17	-16

We have examined possible ways of compensating for missing elements. One method is to increase the amplitude of the elements on each side of a missing element by a factor of 1.5. This does indeed lower the sidelobe level to the correct background level in the neighborhood of the main lobe. But as can be seen in the analog result of Fig. 13 and from the error theory, the amplitude at other times will vary as

$$e(t) \approx S(t) F(x_m) \left[1 - \cos \frac{\mu t}{v} \right] . \quad (28)$$

Thus, at a point halfway along to the main grating lobe, $\mu t/v = \pi$, and the error is now 3 times the original error signal. So the method is not a useful one. It is therefore vital to carry out the engineering on these phased arrays very carefully.

A further situation of interest is that associated with the use of an extended source, and with obstructions in the path of the acoustic beam, such as a rib in medical diagnostics. We deal with these problems by considering the error signal picked up at one element. Suppose first that this element is missing and we are concerned with the error signal from a uniform extended source, $[G(x') = 1]$ at plane z . It may be shown from Eq. (17) that the amplitude of the signal picked up by a single element is approximately

$$e(t) = \frac{1}{\ell} \left(\frac{\lambda z}{2} \right)^{1/2}_{\text{full}} F(x_m) S(t) , \quad (29)$$

whereas the signal picked up by the full array has a maximum amplitude $H_0(t)_{\text{max}} = N(1+k)/2$.

If R is the relative error signal from a point source, we see that the output from an extended source now varies between

$$1 - \left(\frac{\lambda z}{2\ell^2} \right)^{1/2} R < |H| < 1 + \left(\frac{\lambda z}{2\ell^2} \right)^{1/2} R . \quad (30)$$

If the sidelobe level were 25 dB, i.e., $R = 0.56$, $\lambda = 0.6$ mm, $\ell = 1.2$ mm, $z = 15$ cm, this formula would

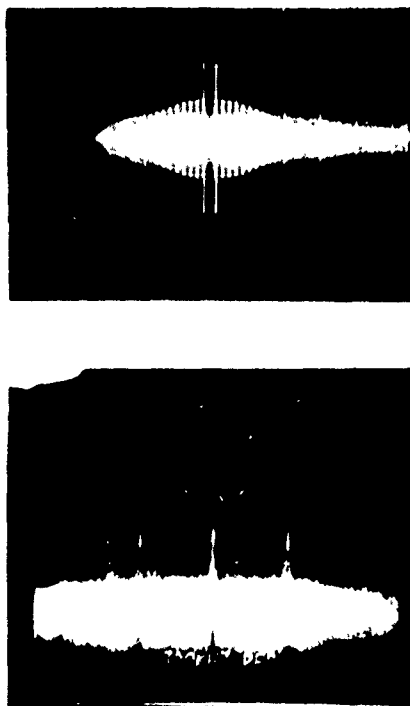


FIG. 13--Point response function for a 32 element Hamming weighted array with elements adjacent to the one missing element increased by 1.5 in amplitude.
Top - Compensated array with missing element.
Bottom - Point response function.
Comparing with Fig. 11, near sidelobes reduced but far sidelobes increased.

indicate a variation of amplitude from 0.7 to 1.3, i.e., an amplitude variation of over 5 dB and hence dark bands in observing a uniform extended source, a problem which we often encountered in our experimental systems. The basic reason for this effect is, of course, that the sidelobes from a uniform array of sources tend to add, while the main lobes do not.

On the other hand, this effect is helpful as far as obstructions in the path of the beam are concerned. As long as the obstruction subtends an angle at individual

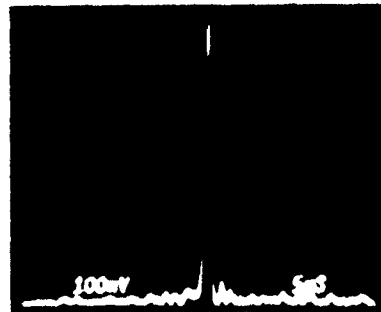
elements far less than their acceptance angles, it will only obscure a small part of the signal reaching an individual element in the array, and have a very small effect on the sidelobe level. The calculation can be carried out mathematically by treating the plane including the object as an extended source. The conclusions reached correspond to this simple physical picture.

V. CONCLUSIONS

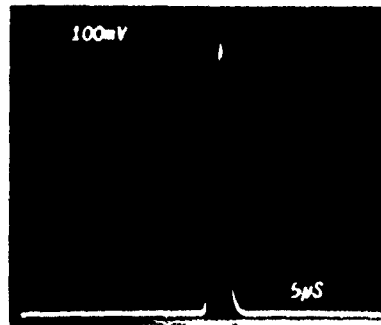
We have shown how to design one- and two-dimensional electronic focusing systems, and demonstrated that the principles of design are valid. A major problem is that associated with sidelobe reduction. Apodization is of great help for this purpose, but can fail in its intent if there are several missing elements. It should however be possible to obtain at least a -50 dB sidelobe level, and theoretically -45 dB by careful apodization and engineering design.

The image of an extended source will tend to have large variations in amplitude even with relatively low sidelobe levels, i.e., there will be dark bands in the picture. This is because of diffraction effects. By using a diffuse wide-band (noise modulated) source so eliminating coherence in the source, it should be possible to radically decrease this effect without loss of resolution. This approach needs further investigation.

An alternative approach with many additional advantages is to use a scanned pulsed source as well as a receiver. This makes it possible to range gate the system, i.e., obtain good resolution in the z direction as well as in the x direction. In such a system, if we pulse the source, we will obtain essentially the same resolution or better than that in a CW system, provided that the time difference between rays reaching the array from a point is less than the time for scan of one spot $t_s = d_s/v$ where $d_s = z\lambda/L$ is the resolution. We have carried out such experiments using a pulsed point source, as shown in Fig. 14. As the pulse length of the source is decreased, the received signal width decreases slightly. More important still, the sidelobes are cut off. In addition, the range resolution becomes equal in time to the transverse resolution t_s when pulse length is equal to t_s . It is possible to extend



GATED TRANSMITTER

PULSE WIDTH $\approx 50 \mu s$ $Z \approx 42 \text{ cm}$ 

GATED TRANSMITTER

PULSE WIDTH $\approx 2 \mu s$ $Z \approx 16.5'' = 41.9 \text{ cm}$

FIG. 11--Point response function obtained with an 84 element receiver system. (Top): Response with a long transmitter pulse. (Bottom): Response with a short transmitter pulse. Note elimination of sidelobes in the short pulse case.

this concept to envisage a system in which the array is used as a fast scan focused transmitter as well as receiver. Such an arrangement gives a moving point source at the object, should eliminate most of the sidelobe problems and give good range resolution for a B scan device.

The authors would like to acknowledge the fine technical assistance of D.J. Walsh, C.R. Hall, and L.C. Goddard.

REFERENCES

The work reported in this paper was sponsored partially by the Office of Naval Research, under Contract N00014-67-A-0112-0039; by the Naval Undersea Center, under Contract N00123-72-C-0866, and by Rockwell International Science Center under Grant RISC 74-20773.

1. J. Fraser, J. Havlice, G. Kino, W. Leung, H. Shaw, K. Toda, T. Waugh, D. Winslow, and L. Zitelli, "A Two-Dimensional Electronically Focused Imaging System," presented at the IEEE Group on Sonics and Ultrasonics Symposium, November 11-14, 1974.
2. F. L. Thurston and O. T. von Ramm, "A New Ultrasound Imaging Technique Employing Two-Dimensional Electronic Beam Steering," in Acoustical Holography, Vol. 5, edited by P.S. Green, Plenum Press, New York, 1974, p. 249.
3. C. E. Cook and M. Bernfeld, Radar Signals: An Introduction to Theory and Application, Academic Press, New York, 1967.

Acoustoelectric Interactions in Acoustic-Surface-Wave Devices

GORDON S. KINO, FELLOW, IEEE

Abstract—The principles of a wide range of acoustic-surface-wave devices employing acoustoelectric interactions with semiconductors are described. It is shown that acoustoelectric amplifiers can increase the dynamic range of a delay-line filter. Such devices have been operated on a CW basis and are beginning to become practical. The acoustic convolver and its derivative devices, the optical scanner, the acoustic focusing and imaging devices, and the storage correlator are described. Several of the signal processing applications of the convolver are discussed. Various types of constructional techniques, including the air gap convolver and acoustoelectric amplifier, the strip coupled and external diode convolvers, the use of piezoelectric semiconductors, deposition of a semiconductor on a piezoelectric substrate, and deposition of a piezoelectric material on a semiconducting substrate are discussed.

I. INTRODUCTION

ACOUSTIC SURFACE waves propagating along the surface of a piezoelectric material have an electric field associated with them; this makes it possible to obtain acoustoelectric interactions of the acoustic waves with the carriers in a semiconductor. We will review the basic types of acoustoelectric interactions, concentrating entirely on acoustic surface-wave devices. We will devote most of our attention to the subject of nonlinear effects, but, initially, we will discuss acoustoelectric amplifiers for completeness, because the basic acoustoelectric interaction theory is well illustrated by a consideration of their properties, and because these devices may find important applications in the future.

When a semiconductor or a metallic conductor is placed close to the surface of a piezoelectric material on which an acoustic wave is propagating, currents will flow in the conductor, and there will be a power loss associated with the acoustoelectric interaction. However, if a dc drift field is applied to drift the carriers in a direction parallel to the direction of propagation of the wave, energy can be delivered from the carriers to the wave when the drift velocity of the carriers is larger than the phase velocity of the wave. In this case, unilateral traveling wave amplification can be obtained; so a unilateral amplifier, based on this principle, can be constructed.

A second example of acoustoelectric interactions is that associated with nonlinear effects. Because of the highly nonlinear relation between the current and the field in a semiconductor, nonlinear acoustoelectric interactions between an acoustic wave and the semiconductor can be relatively strong. This makes it possible to devise various parametric types of devices. An important class of such devices are the so-called con-

volvers and correlators; these take the product of two signals and form the convolution or correlation integral of the signals. A recent development of this principle is a device which can store signals entering it and take the correlation of the stored signal with a later signal.

Yet another application of acoustoelectric interactions is associated with imaging. As carriers can be generated within a semiconductor when it is exposed to light, the nonlinear interactions of an acoustic wave with a semiconductor can be influenced by the presence of light. By this means, it is possible to utilize an acoustic pulse to scan one line of an optical image formed in a semiconductor. By using more complicated scanning waveforms, it is also possible to obtain spatial transforms of the optical image; this process is difficult to accomplish directly in other types of imaging devices.

There are closely related devices in which the acoustic surface waves do not interact directly with the semiconductor, but, instead, are sampled by means of taps along the delay line. The signals from these taps are read out into separate diodes or amplifiers, and the basic convolution process, already described, can be carried out in these external devices with such a hybrid system. One application of these principles is to use the tapped acoustic-surface-wave delay line as a phase reference, and utilize it for imaging acoustic waves sampled by an array of transducers, one transducer to each tap.

We see, therefore, that there is a very wide range of application of acoustoelectric interactions. Most of the devices which are based on this principle are still in the research stage, although acoustic convolvers and correlators are beginning to be tested in radar and communication systems.

II. ACOUSTOELECTRIC AMPLIFIERS

A. General Considerations

The designer of acoustic-surface-wave devices has to contend with several sources of loss, as well as with problems due to reflections from transducers, taps, and from the edges of the surface-wave device. In addition, there may be difficulties associated with excitation of bulk waves. The main causes of loss are associated with the material attenuation, diffraction phenomena, and mismatch losses at the transducers [1]. Such losses can be compensated for by the use of external amplifiers, either at the input or the output of the acoustic-surface-wave filter or delay line. The disadvantage of doing this is in the limitation of the dynamic range of the system.

Suppose that we consider a delay line with a total internal attenuation and transducer loss of L dB, and a maximum input power P_M due to saturation effects in the delay line or breakdown in the input transducer. A device of this kind will have a minimum noise figure of L dB relative to kTB , where k is Boltzmann's factor, T the temperature of the device, and B the bandwidth. It follows that the dynamic range of the device is $10 \log_{10}(P_M/kTB) - L$ dB.

Manuscript received January 5, 1976. The Stanford work described here is supported partially by ARPA through the Office of Naval Research under Contract N00014-75-C-0129, the National Science Foundation under Grant ENG75-18681, the United States Air Force under Contract F30602-74-C-0018, the Office of Naval Research under Contract N00014-75-C-0632, the Naval Undersea Center under Contract N00123-75-C-1385, and the United States Air Force under subcontract from North American Rockwell under Contract R1-74-20773.

The author is with the W. W. Hansen Laboratories of Physics, Stanford University, Stanford, CA 94305.

Copyright © 1976 by The Institute of Electrical and Electronics Engineers, Inc.
Printed in U.S.A. Annals No. 605PR024

The addition of amplifiers at either input or output can increase the minimum sensitivity or the maximum output power, but this limitation on dynamic range will still be present, and, in fact, may be more severe when amplifiers are used at the input or output. Such a limitation is not a serious one when relatively low loss delay lines are employed. However, in applications involving very long delay lines in which the internal losses may be 50 dB, or more, the dynamic range may be severely limited; or the situation may even be reached where the delay line is, in fact, not usable because of its excessive losses. As an example, if we consider a bismuth-germanium-oxide delay line with a saturation power of 0.2 watts and a bandwidth of 20 MHz, the dynamic range with only 3-dB insertion loss in each transducer would be 118 dB but with 10-dB loss in each transducer and 50-dB internal loss, the dynamic range is reduced to 54 dB. Furthermore, if the transmission loss were larger, perhaps as much as 100 or 200 dB, as it might typically be in a delay line with several milliseconds of delay, the dynamic range could easily be reduced to zero.

An additional difficulty with acoustic-surface-wave filters and delay lines is associated with reflections. For instance, an interdigital transducer can be regarded as a three-port network. If it is well matched at the electrical port and one acoustic port, it has a 3-dB loss, but a 6-dB reflection on one acoustic port; this gives rise to triple transit echoes [2], [3]. It is, therefore, common practice to operate with severely mismatched output transducers and, hence, higher loss to reduce the triple transit echo level.

It is apparent that, ideally, it would be useful to have an internal low noise unilateral amplifier within the delay line to eliminate internal reflection problems and increase the dynamic range. The noise figure of an ideal amplifier (0-dB noise figure, saturation power greater than that of the delay line) would be determined by the loss of the input transducer; and the maximum output power by the loss or breakdown of the output transducer. In practice active amplifiers have their own limitations due to excessive power dissipation, technological problems of construction, higher noise figures than desirable, and often lower output power than is desirable. Thus although such amplifiers have been demonstrated in principle and shown to operate in a manner well predicted by theory, they have not yet received wide acceptance in their applications to acoustic delay lines because their characteristics have not been good enough to make them competitive with delay lines using external amplifiers.

B. Types of Acoustoelectric Amplifiers

In this section we shall review the properties of acoustoelectric amplifiers, both in order to show the nature of the basic interactions, and to discuss the technological problems associated with their construction. A review of their properties is also of interest, because it will lead us to the basic configuration used in the acoustic convolver and to an understanding of the theoretical basis for study of interactions between acoustic surface waves and semiconductors.

There are several possible configurations which may be used to obtain interaction between a semiconductor and acoustic surface waves. One possibility is to propagate acoustic surface waves on the surface of a piezoelectric semiconductor, such as GaAs or CdS [4]–[8]. In the first case, the interaction tends to be very weak, due to the weak Rayleigh wave piezoelectric coupling coefficient of GaAs. In the second case, because the

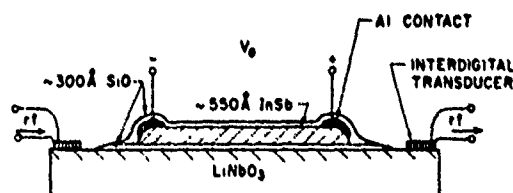


Fig. 1. A schematic of an acoustic amplifier using a film of InSb vacuum evaporated on to LiNbO₃ [9].

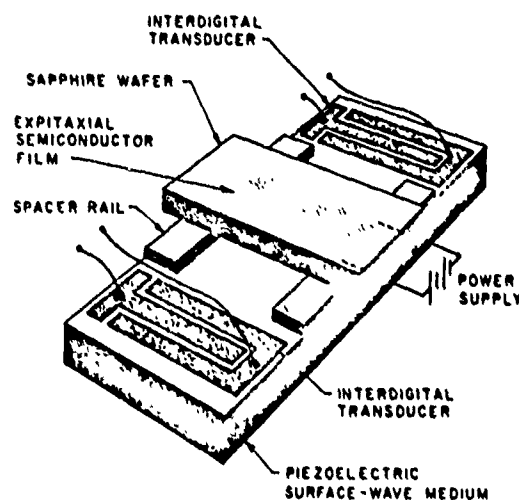


Fig. 2. A schematic of an "airgap" amplifier with silicon-on-sapphire spaced from LiNbO₃ by thin SiO₂ rails [11].

mobility of carriers in CdS is low, and it is difficult to obtain uniform and reproducible samples of the material, relatively little attention has been paid to its applications for acoustic surface-wave amplifiers. However, successful Bleustein-Gulyayev wave [5]–[8] amplifiers have been made with the use of these materials. In this case the interaction that occurs is with a type of wave which is closer in its properties to those of a bulk shear wave; this has a higher piezoelectric coupling coefficient than a Rayleigh surface wave.

For these reasons, the configurations that have been most commonly employed for acoustic-surface-wave amplifiers are of the types shown in Figs. 1 or 2. In Fig. 1, there is shown an amplifier in which the semiconductor consists of a vacuum evaporated film, typically of InSb [9] or CdSe [10] evaporated onto a piezoelectric substrate, usually LiNbO₃, although other materials such as Bi₁₂GeO₂₀ have been used on occasion [9]. An alternative configuration shown in Fig. 2, one on which much of the initial work in this field was carried out, is to use a material such as Si, separated from the piezoelectric substrate by a small airgap of the order of 1000 Å [11]. In the initial experiment, bulk silicon or germanium was placed against a PZT or LiNbO₃ substrate [11]–[13]. The fact that the surfaces are not perfectly flat was relied upon to prevent mechanical loading of the substrate by the semiconductor. In later experiments, illustrated in Fig. 1, SiO₂ rails were used to separate a silicon-on-sapphire-slice from the piezoelectric substrate [11].

More recently, a more reliable airgap configuration has been developed at Lincoln Laboratories for use with both amplifiers and convolvers. This configuration, illustrated in Fig. 3 in the form employed by Ralston, employs a large number of small posts approximately 4 μm square to maintain the spacing between the semiconductor and the piezoelectric substrate

[58] and Bers [59] that associated techniques like the measurement of acoustic loss, the measurement of the dc term associated with the nonlinearly induced potential, and the acoustoelectric effect [60], can also provide entirely new ways for measuring semiconductor parameters [58]. In addition, it has been observed from the results on surface state storage devices that the decay times of surface state traps can be measured directly by such techniques [33].

One of the basic problems with airgap devices is that the oxide layer is not covered by a material impervious to impurities. In addition, because there can be charges induced on the oxide surface and on the piezoelectric substrate by friction or other causes during assembly, the interaction can, in fact, be nonuniform over the length of the device. A simple technique which has virtually eliminated this kind of problem is, not to oxidize the surface in the normal way [15]. If the surface is left with a layer of oxide 20-50 Å thick, such as normally grows on a clean Si surface in air, a very large number of surface states is produced. In this case, which is different from that with a thick oxide, the Si underneath the thin oxide is normally depleted while the thick oxide on an n-type semiconductor normally induces accumulation at the surface. Because there is a large number of surface states present in this case, it is extremely difficult to change the internal conditions at the semiconductor by application of an external dc field. For the same reason, surface charges on the oxide or on the piezoelectric substrate, as well as charges trapped within the piezoelectric substrate, have very little influence on the convolver behavior and, therefore, it is much easier to make a uniform convolver. Furthermore, as the surface is normally depleted, this is the correct operating condition for optimum convolver efficiency. So the airgap convolver with a thin layer of oxide on the surface is the best to use for normal convolver operation. The surface traps themselves, as they have a slow response, do not influence the RB behavior and so the convolver operates in a predictable manner, as shown in Table II.

On the other hand, if good optical sensitivity is required, i.e., we require the carrier density within the depletion layer to be influenced by the presence of light, then the presence of a very large number of surface states of this kind appear to give poor optical sensitivity. This is basically because of the rapid recombination of generated carriers that occur. It is, therefore, important to eliminate surface effects as much as possible in optical devices. In a similar way, storage devices based on storage in surface states have problems with nonuniformity of surface states and are not easy to control. Thus it has become important to devise other techniques, equivalent to the use of a buried channel in the CCD, for constructing convolvers which eliminate the interactions at the surface. We will discuss these further, when we discuss optical imaging and storage devices.

E. Optical Imaging with Convolvers

The convolver configuration can be used to detect and scan optical images. It has already been pointed out that it is possible to make use of the nonlinear capacitive effects due to RB electric fields normal to the surface to obtain an electrical output signal which is a line scan of the image [42], [44], [46]. It is also possible to make use of the piezoresistive effect associated with the change in loss caused by the change in resistance due to the acoustic strain in the semiconductor itself. The latter type of effect has been employed very successfully

by Luukkala. He employs CdSe deposited on LiNbO₃ to obtain single line scans and, hence, constructs an image by mechanically scanning in the perpendicular direction [45]. Kornreich has also used this effect to make Fourier transform devices [47].

It is the author's opinion that, with the advent of the CCD technology, it is unlikely that direct optical imaging devices based on the use of acoustic waves are liable to be competitive with solid state TV imaging devices. This statement is not based on the theoretical definition or sensitivity of acoustic imaging devices. With sufficient development, it is possible that the results obtained could be comparable to the best CCD's. The devices are parallel processing devices, and do not read out the signal serially through the registers as in a CCD. Therefore, the readout can be nondestructive and the devices are not as sensitive to a missing element as a CCD. However, a considerable investment in technology would be required to make competitive optical imagers, and it is unlikely that a device with a considerably better performance than the highly developed CCD devices would be obtained in the long run. On the other hand, the acoustic imaging devices have unique capabilities of their own. These are difficult to duplicate in other devices and make them useful in certain specialized applications. Some examples are as follows.

- 1) The possibility of obtaining very fast scan rates.
- 2) The possibility of directly obtaining one and two dimensional spatial transforms of optical images.
- 3) The possibility of working with a wide range of optical detectors in both hybrid and monolithic configurations which would lead to new types of infrared sensitive devices.
- 4) The possibility of obtaining electronic focusing of optical images without the use of physical lenses.
- 5) The possibility of reconstruction of optical holograms in real time.

We will concentrate here on the application of the convolver configuration in which the output is taken from the system at the sum frequency of the input signals, although we shall also consider certain configurations in which the output is taken from the system at the input frequency, i.e., it is as if one of the input signals is of zero frequency. We shall not deal in detail with all the other alternative configurations which have been used for optical scanning, instead we shall emphasize transform techniques, a unique application of these devices.

We consider the configuration shown in Figs. 15 and 16(a), which is illustrated as an airgap device. Following the analysis for the convolver, it can be shown that, if the carrier density variation due to the presence of light is $n(z)$, and the two input signals are of frequencies ω_1 and ω_2 , respectively, the output from the device will be of the form

$$H(t) = A \exp [j(\omega_1 + \omega_2)t] \int_{-\infty}^{\infty} F\left(t - \frac{z}{v}\right) G\left(t + \frac{z}{v}\right) \cdot \exp \left[j(\omega_1 - \omega_2) \frac{z}{v} \right] n(z) dz \quad (3.15)$$

where the modulations of the two input signals are $F(t)$ and $G(t)$, respectively, and all spatial quantities are referred to the center of the device $z = 0$, with appropriate time changes. Suppose one input signal, the *scanning pulse*, is a delta function, i.e., $F(t) = \delta(t)$ and the other, the *reading pulse*, is a long CW pulse. In addition, if we assume that the system is degenerate

TABLE I
SOME MATERIALS SUITABLE FOR ACOUSTOELECTRIC ACOUSTIC SURFACE
WAVE DEVICES [1], [3], [18], [19]

Material	Rayleigh Wave Velocity V (m/s)	T ϵ_p/ϵ_0	$\Delta v/v$ (percent)
LiNbO ₃ , Y-cut, Z-prop.	3330	50.1	2.2
Quartz, Y-cut, X-prop.	3159	4.5	0.093
CdS, Y-cut, Z-prop.	1716	9.8	0.26
GaAs, Z-cut, 22.5°, X-prop.	2763	11.0	0.024
Bi ₁₂ GeO ₂₀ , [111]-cut [110] prop.	1708	38	0.68
ZnO, Z-cut, X-prop.	2680	10	0.045
PZT 4, X-prop.	2210	1385	2.4

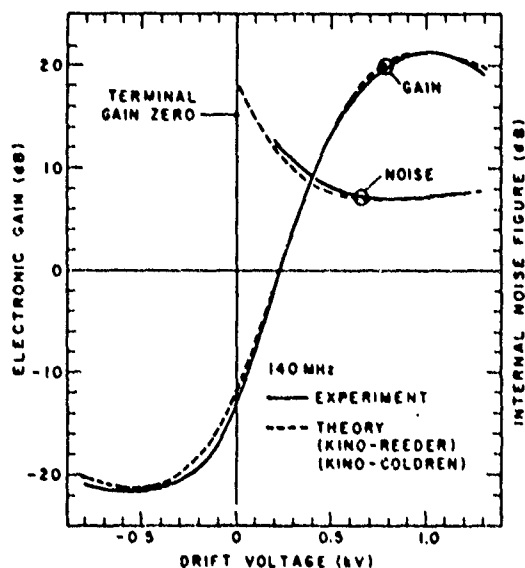


Fig. 4. Internal gain and internal noise figure versus voltage for a 5-mm long amplifier segment of the Ralston post supported silicon on sapphire amplifier [14]. Theoretical performance is calculated for the parameters $h = 0.13 \mu\text{m}$, $d = 0.56 \mu\text{m}$, $\mu = 800 \text{ cm}^2/\text{V}\cdot\text{s}$, $od = 2.5 \times 10^{-6} \text{ mho}$, 10 percent electrons trapped.

terial. Further examination of the theory shows that the higher the permittivity, the lower the optimum frequency. Therefore, PZT materials with their very high dielectric constants tend to be applicable at very low frequencies, whereas a material like LiNbO₃ is more suitable for applications in the UHF or VHF frequency range.

Some recent results for the gain variation with acoustic velocity of a cw silicon on sapphire amplifier taken by Ralston in the configuration of Fig. 3 are shown in Fig. 4. They are seen to be in good agreement with the theory. It would be expected that the internal electronic gain would be zero when the carrier velocity is equal to the acoustic velocity, and increase to a maximum value where

$$v_0/v_a = odM/\epsilon_0 + 1 \quad (2.8)$$

When the carrier drift velocity is less than the acoustic velocity or negative, i.e., for waves propagating in the opposite direction from the carrier drift velocity, there is enhanced attenuation due to the presence of the semiconductor. The attenuation is maximum where

$$v_0/v_a = 1 - odM/cv_a \quad (2.9)$$

The device, therefore, functions as a nonreciprocal device.

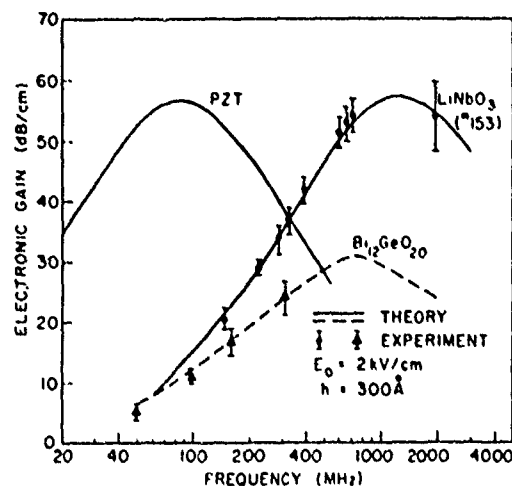


Fig. 5. A comparison of the measured frequency variation of the electronic gain with theory [17] for a vacuum deposited InSb amplifier of the type shown in Fig. 1 [9]. The curve for PZT-4 is a theoretical one. $d = 550 \text{ Å}$; $od = 35 \times 10^{-6} \text{ mho}$; $\mu = 350 \text{ cm}^2/\text{V}\cdot\text{s}$; $h = 300 \text{ Å}$ for the LiNbO₃ amplifier.

D. Experimental Devices

It will be noted that the optimum value of the drift velocity for maximum gain varies linearly with od . By working with a very low mobility semiconductor such as CdSe, with $100 \text{ cm}^2/\text{V}\cdot\text{s}$, it is possible to obtain a very-low conductivity. But, because of the low mobility, a very large drift field is required. Such conditions have been shown to be practical for CW operation by Solie in an accompanying paper [20]. In his work he divides the semiconductor up into small sections across which the dc potential is applied, so that the potential required across any section is relatively small, even though the applied fields may be as much as several kV/cm. In Solie's case, the applied fields in neighboring sections of semiconductor are of opposite sign so that alternate sections function as amplifiers and attenuators respectively, this implies that the device functions as a reciprocal amplifier. In earlier work by Lakm and Shaw [11], the applied fields in neighboring sections were of the same sign, in order to realize a low potential nonreciprocal amplifier.

The alternative approach employed by Lakm and Shaw [11], Coldren [9], Yamanouchi [21], and most recently, Ralston [14], is to work with as high a mobility semiconductor material as possible, with the minimum practical value of od , in order to obtain CW operation. In Ralston's case, he has worked with high quality silicon on sapphire with a mobility of $800 \text{ cm}^2/\text{V}\cdot\text{s}$ and an extremely low value of od of 2.5×10^{-6} to realize a CW amplifier [14].

In (2.7), for the gain per unit length there is a term which increases as $1/\lambda$, and another which decreases with the gap thickness in wavelengths. Hence the gain passes through a maximum value at a particular frequency which depends on the gap thickness and the dielectric constants involved. Some plots of measured and theoretical gain of an InSb on LiNbO₃ amplifier, measured by Coldren, as a function of frequency, are shown in Fig. 5 compared to the theoretical predictions. It will be seen that the results are in excellent agreement with theory. The operation of the device is, therefore, well understood.

Devices of this kind have typically given internal electronic gains of the order of 60 dB/cm in the 200-MHz range, with the maximum gain obtained at frequencies as high as 1 GHz. This maximum gain is determined by the saturation power of the

device, when it saturates on noise. The noise figure is predictable, and depends to some extent on trapping effects in the semiconductor. Some noise figure results are shown in Fig. 4. An 8-10 dB noise figure is a typical value for reasonable quality material. This implies a maximum saturation gain of about 80 dB. Thus the devices must normally have the gap between the semiconductor and the piezoelectric substrate optimized in thickness to cause the maximum gain to occur at the frequency of operation of interest.

Operating with InSb on a closed loop delay line of the type described by Coldren and Shaw in an accompanying paper [22], it has been possible to compensate for the loss of a wave passing under the semiconductor, around the back of the delay line, and returning and passing again under the semiconductor. After many transits, the attenuation in such delay lines can be extremely large, of the order of many hundreds of dB. By just compensating for this attenuation, it is possible to cancel it out and observe an output signal comparable to the input. Using a delay line with a 25- μ s loop delay, it was possible to operate it in the linear regime with approximately 150 loops of the delay lines, i.e., a total time delay of 3.75 ms. Beyond this point, because of the imperfect compensation of the loss by the gain, the output signal began to increase and the device became unstable. Operating in a saturated regime, where the output power was saturated, it was possible to increase the stable operating regime to approximately 10 ms. In all cases, of course, it was necessary to design the device very carefully so that the maximum gain was at a point very close to the frequency for which the minimum internal loss within the device, which was of the order of 15 dB per loop, was just compensated.

One other feature of this type of interaction which may be of importance in the future, is its application to so-called " $\Delta v/v$ " waveguides. As we have seen, when a semiconductor or metal is placed near the piezoelectric substrate, it lowers the effective Rayleigh wave velocity, due to its short circuiting of the RF fields. By using a narrow strip of semiconductor, the wave velocity in the semiconductor region will be lower than that of the region outside the semiconductor, and an amplifier can itself form a waveguide. Coldren, working with a 25- μ m wide layer of InSb, was able to construct such a waveguide amplifier, and operate it on a CW basis [22]. This was because the configuration allowed heat dissipation sideways from the semiconductor as well as downwards into the LiNbO₃ substrate. Such techniques have also been used to construct low loss waveguides by Hughes [23] and used for loop delay lines by Adams and Shaw [24].

The basic problem, of course, with a traveling wave semiconductor amplifier is the fact that, as the gain is increased, the length of the device becomes larger and hence the power dissipation increases. This is a very different situation from that of the electron beam traveling-wave tube. The state of the technology at the present time is that the devices are beginning to be operated reliably on a CW basis, but with noise figures and power dissipations considerably higher and efficiencies considerably lower than transistor amplifiers operating in the same frequency range. It is, therefore, not yet practical to operate these devices in short delay lines to compensate for internal losses. However, in special applications where very long delay lines are required and it is not possible to compensate for their losses externally, the use of such amplifiers may be approaching practicality. It is apparent, however, that further improvement in the power dissipation and in the noise figure of these amplifiers would be highly desirable. It this could be

accomplished, then the application of these amplifiers in delay line filters would be of great importance.

III. THE ACOUSTIC CONVOLVER

A. The Basic Principles

The most important application, to date, of the acoustoelectric effect is to the ASW convolver, whose operation is based on the nonlinear interaction between two acoustic surface waves. When two surface waves pass each other in opposite directions, it is possible to obtain an output signal at their sum frequency which is an integral of the product of the two signals within the device. This is equivalent to taking the convolution of the two input signals in real time.

In order to describe the principles of operation of the convolver, we first consider a simple piezoelectric surface-wave device in which there is no semiconductor present, but in which there can occur a nonlinear interaction between two acoustic surface waves propagating along the surface of the substrate. We suppose, initially, that there are two CW RF signals inserted at each end of the delay line with frequencies ω_1 and ω_2 , respectively. If the line is of length L , the signals at any point z along the device will be of the forms $\exp j\omega_1(t - z/v)$ and $\exp j\omega_2(t + z/v)$, respectively, where v is the acoustic velocity. Suppose now that there are nonlinear interactions between the two signals due to the nonlinear properties of the substrate. Then, in this piezoelectric material, second-order potentials will be generated at frequencies $\omega_1 \pm \omega_2$, $2\omega_1$, and $2\omega_2$ as well as dc potentials proportional respectively to the squares of the two input signals. At the plane z , the signal at the sum frequency will have an associated potential at the surface of the substrate of the form

$$\phi(t, z) = A \exp j[(\omega_1 + \omega_2)t - (\omega_1 - \omega_2)z/v] \quad (3.1)$$

where A is an arbitrary constant.

It is apparent that the signal at the sum frequency can be detected by an interdigital transducer of finger pair spacing l which is capable of responding to a wave with a propagation constant $k_3 = (\omega_1 - \omega_2)/v$, such that $k_3 l = 2\pi$. Perhaps, the most interesting case is the degenerate case, when $\omega_1 = \omega_2 = \omega$, so that $k_3 = 0$. Then the potential of the nonlinearly generated signal $\phi(t, z)$ does not vary with z , and can be detected between metal films laid down on the top surface and lower surface of the piezoelectric substrate. The two possible configurations for the output transducers are illustrated in Fig. 6 [25].

Now let us consider the form of the output from a device of this kind when the two input signals are modulated and have the forms $F(t) \exp j\omega t$, and $G(t) \exp j\omega t$, respectively. In this case, the degenerate convolver will yield an output of form

$$V = C e^{2j\omega t} \int F\left(t - \frac{z}{v}\right) G\left[t - \frac{(L-z)}{v}\right] dz \quad (3.2)$$

where C is a constant which is related to the strength of the nonlinear interaction, the distance between the input transducers is taken to be L , and the integration is carried out over the length of the output transducer L_0 .

If the spatial length of the acoustic surface input signals on the substrate is less than that of the output transducer L_0 , then the integral of (3.2) can be regarded as having infinite limits with complete generality. It is then convenient to substitute $t - z/v = \tau$ in (3.2), and write it in the form

$$V = D e^{2j\omega t} \int F(\tau) G(2t - \tau - T) d\tau \quad (3.3)$$

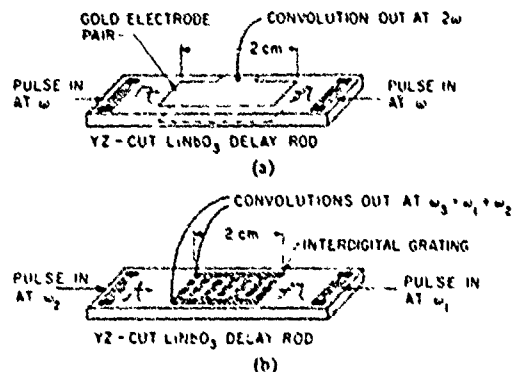


Fig. 6. Two possible configurations for an acoustic convolver. (a) A degenerate convolver with the output transducer consisting of metal films deposited on top and bottom of surfaces of the piezoelectric substrate. (b) A convolver with an interdigital output transducer.

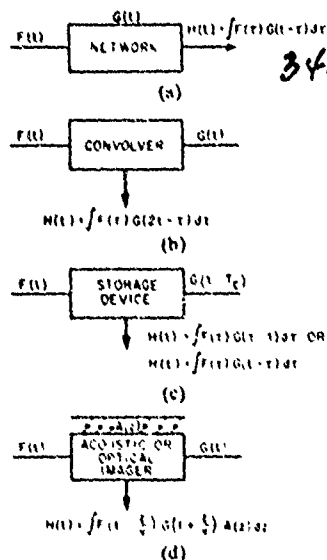


Fig. 7. Signal and image processing in convolver devices. (a) Signal processing by a network. (b) Signal processing in a convolver. (c) Signal processing in a storage correlator. (d) Image processing.

where D is a constant related to the strength of the interaction between the waves, and $T = L/v$ is the delay time of an acoustic surface-wave passing along the delay line.

Equation (3.3) will be recognized as being closely related to the convolution of the two input signals. The only difference from the true convolution is that the output signal is compressed by a factor of 2 in time, this is because the two acoustic surface waves pass each other at a velocity $2v$. This process of convolution is exactly what occurs when a signal is passed into a filter, where the output obtained is the convolution of the signal and the impulse response of the filter, as illustrated in Fig. 7(a). In the convolver, as illustrated in Fig. 7(b), because the reference consists of another signal, it is possible to change the reference or the filter response at will. Thus the convolver is, in principle, an extremely flexible device and may be used to recognize digital codes consisting of long pulse trains or analog codes, such as linear FM chirps. Such demonstrations were made with the early forms of the convolver, using both degenerate types of convolvers and nondegenerate convolvers with an interdigital output transducer. The reader is referred to the papers by Catarella [31] and Defranould [27] and Sohe [20] for some of the more recent results of this type.

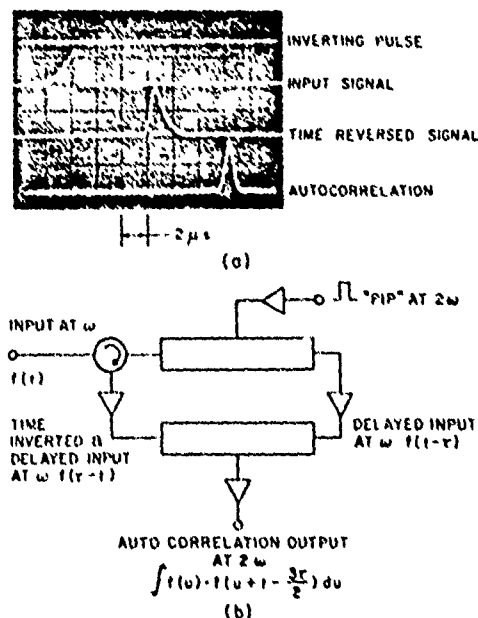


Fig. 8. Time inversion and autocorrelation of an asymmetrical triangle with two semiconductor acoustic surface wave convolvers.

It was also shown that time inverted signals could be obtained from the device by inserting a signal of frequency ω_1 into one end of the device, and a narrow pulse of frequency ω_3 at the center transducer to obtain a time inverted output signal at the input transducer of frequency $\omega_2 = \omega_3 - \omega_1$ [25]. So by using one device as a time inverter, and feeding its output into a second one which was used as a convolver, the correlation between two input signals could be obtained. An illustration of the results obtained by Gautier [26] using two degenerate semiconductor convolvers in this way is shown in Fig. 8. In his case, the dynamic range obtainable with the type of semiconductor convolver, a device to be described later which has more dynamic range, was only 20 dB. With a simple convolver using the weak nonlinearity in LiNbO₃, it would not have been possible to obtain this result, because of the limited dynamic range of the individual devices. Thus a basic problem is to obtain a sufficiently strong nonlinear interaction, so that the dynamic range of the device is not limited by the weakness of the interaction.

It is convenient to define a figure of merit of such devices, relating the output power P_3 to the input RF signal powers P_1 and P_2 , respectively, as

$$F \propto \frac{P_3}{P_1 P_2} \quad (3.4)$$

This figure of merit takes account of losses in the input transducer and the output transducer, as well as the strength of the nonlinear interaction. Typical LiNbO₃ convolvers for the 100-200 MHz frequency range, using an acoustic beamwidth $w = 1.27$ mm and output transducer length 2 cm, yielded a figure of merit corresponding to $F \sim -83$ dB [25]. This implies that, with $P_2 = 20$ dBm as the reference input, the output signal level would be reduced by 63 dB from the input signal. Thus if the saturation power of the input transducers was of the order of 20 dBm and the noise figure of the receiver was typically 90 dBm, the dynamic range of the device would be $20 - 63 - (-90) = 47$ dB.

A considerable improvement in the characteristics of convolvers can be obtained by narrowing the beamwidth w . In

this case, the power density is increased, and the efficiency of the device increases as $1/w^2$. By this means, it has been shown by Defranould and Macfeld in a paper given in this issue, that by reducing the beamwidth to 100 μm from 1 mm with strip coupled input transducers, they can obtain approximately a 20-dB improvement in efficiency, thus increasing the dynamic range by a corresponding amount [27].

B. Principles of Operation of Semiconductor Convolver

An alternative approach, to which a great deal of attention has been devoted, is to increase the strength of the nonlinear interaction by making use of the nonlinear response of a semiconductor coupled to the RF electric fields of the acoustic waves propagated along the piezoelectric delay line. Two types of interactions with semiconductors are possible: longitudinal interactions in which the nonlinearity is caused by the electric field parallel to the direction of propagation [20], [28] and transverse field interactions caused by an electric field perpendicular to the direction of propagation and to the surface of the semiconductor [25], [26], [29]-[31].

With the first type, because of symmetry, output from a convolver is only obtained when a drift field is applied to the semiconductor. So the interaction is essentially based on the nonlinear acoustoelectric effects which occur in an acoustic amplifier. In general, when a drift field is applied, the two waves passing through the device in opposite directions suffer unequal attenuations or amplification, and so the product signal obtained is not the true convolution of the two input signals. On the other hand, if the device is divided into short sections to which alternating drift fields are applied, then both signals will suffer equal attenuation, or better still growth, and a true convolution can be obtained with the additional advantage of compensation for attenuation within the device. Convolver with a figure of merit of $F = -16$ dBm, based on this principle, have been made by Solie [20] using CdSe laid down on LiNbO_3 . Some of his results are described in this issue. Therefore, we shall concentrate on the transverse field interaction devices.

The configuration which has received by far the most attention for use as a semiconductor convolver is of the type shown in Fig. 9. It will be seen that the basic construction is very similar to that of the acoustic amplifier. However, now the interaction is essentially between the electric field E , normal to the surface of the semiconductor and the carriers in the semiconductor. Typically, a relatively thick semiconductor layer, thicker than the layer used in the acoustic amplifier, is employed so that the parallel field component E_z tends to be shorted out.

Semiconductor depletion layer theory leads to the conclusion that a depletion layer of thickness l will be formed in an n-type semiconductor of donor density N_d such that

$$E = qN_d l / \epsilon \quad (3.5)$$

where E is the field normal to the surface and ϵ is the permittivity of the semiconductor. In turn, this implies that the potential across the depletion layer is

$$\phi = qN_d l^2 / 2\epsilon = \epsilon E^2 / 2qN_d \quad (3.6)$$

It is thus apparent that the potential formed across the depletion layer is proportional to the square of the field and varies inversely with the donor density. It is as if the semiconductor behaves as a distributed varactor, with a considerably stronger

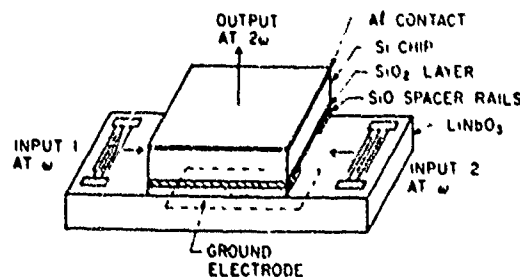


Fig. 9. A schematic of an "airgap" silicon convolver spaced by SiO rails [25], [29].

nonlinearity than can be obtained in the piezoelectric material itself.

By employing this principle, a convolver of the type shown in Fig. 9 can be constructed. In this case, the potential generated across the depletion layer at any point is proportional to the product of the two input signals. The output is detected between an electrode on the lower surface of the piezoelectric material, capacitively coupled to the surface of the depletion layer, and an electrode on the top surface of the semiconductor. The output potential will be proportional to the integral of the induced depletion layer potential along the length of the semiconductor.

The employment of a semiconductor in the convolver implies that several of the well known principles developed for other semiconductor devices can be incorporated within the convolver itself. As we have seen in Figs. 7(a) and (b), the convolver itself is equivalent to a network filter, with an arbitrary reference network determined by a second input signal. If storage in either p-n junctions, Schottky barriers, or surface states at the surface of the semiconductor can be employed, then it is possible, as illustrated in Fig. 7(c) to construct a storage device [32]-[37]. Alternatively, following the work on bulk waves by Melcher and Shuren [38] storage can be obtained in traps in CdS or other materials [39], [40]. In this case, a signal $F(t)$ can be read into the device and stored at the surface of the semiconductor as a spatial variation of charge along the surface of the semiconductor of the form $F(z/v)$. When a later signal $G(t)$ is read into the device, it is possible to obtain an output as illustrated in Fig. 7(c), which is either the convolution or the correlation of the two input signals. Now, however, the reference signal does not have to be read in at the same time as the signal to be interrogated. It can be read in within the storage time of the device, which can be in the range of a few microseconds to a few seconds, depending on the design of the device.

An example of the use of such devices could be to employ them in a radar system. Suppose, for instance, that a coded signal is emitted from the radar antenna and reflected from an object. The received signal is then stored in the correlator storage device. If a later signal from another part of the object or from a more distant object was received and then correlated with the earlier signal, the distortion due to the errors in the radar system itself, or due to inhomogeneities in the atmosphere, could be removed, for both the reference and the signal of interest would have suffered the same distortion. Such correlations would take place in real time, a considerable advantage in a sophisticated radar system [37], [41].

As a second example, we can consider the situation when the semiconductor is illuminated by an optical image [42]-[47]. If we regard the acoustic beam path as one line of the image,

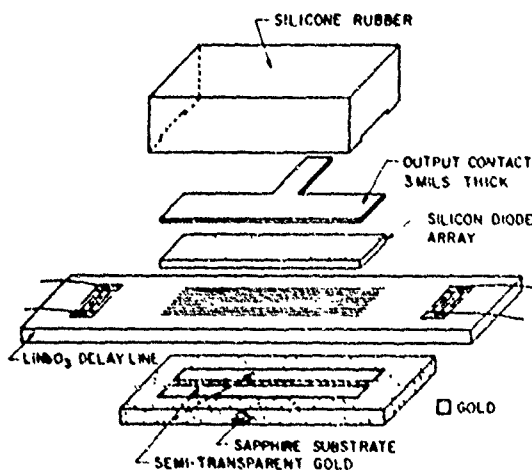


Fig. 10. An "airgap" convolver separated by $4 \mu\text{m}$ wide rails etched in LiNbO_3 [62]

then the carrier density along the semiconductor will depend on the external illumination. As we have already seen, the convolver output depends inversely on the carrier density. Therefore, the output of the convolver will depend on the change $A(z)$ in the output from a plane z due to the illumination. In general, when input signals $F(t)$ and $G(t)$ are inserted into the convolver, the output obtained will be that shown in Fig. 7(d). Thus we obtain a type of correlation between the illumination along one line of the image and the input signal.

Suppose one signal $F(t)$ is a delta function and the other a long pulse, then the output obtained will be a line scan of the image. On the other hand, if the input signals are coded, it is possible to obtain the Fourier transform, the Fresnel transform, or other coded transforms of the optical image. As suitable delay lines can be used to obtain the inverse transform of these coded signals, it is, therefore, possible to reconstruct the original image. In addition, it is possible to carry out various types of filtering processes to the transform image to eliminate unnecessary information within the image, and hence decrease the bandwidth. Furthermore, if a long code corresponding to the line time is used, any spot on the image is read for the complete line time rather than the spot time. Therefore, a considerable improvement in the signal-to-noise ratio of the order of the ratio of the line time to the spot time can be obtained [41], [46].

C. Construction Techniques for Semiconductor Convolver

It is apparent that the basic convolver configuration of Fig. 9 is very similar to that of the semiconductor amplifier already described, for which there are several similar constructional techniques. As we have already discussed, the semiconductor can be supported on SiO_2 rails to keep it mechanically cut of contact with the piezoelectric substrate in the region of the acoustic beam. But, better still, in order to provide more uniform gap spacing, the semiconductor substrate on which there may be p-n junctions or Schottky diodes can be supported on a number of thin rails parallel to the propagation path, each one being of the order of $4 \mu\text{m}$ wide, as illustrated in Fig. 10. As this dimension is much shorter than the wavelength, very little mechanical interaction with the acoustic waves is observed and the gap spacing can be made very uniform [53]. The basic technique of this kind has been pioneered by the group at Lincoln Laboratories [14], [15], [31], [32], [35],

[37] who support the semiconductor on randomly distributed small posts, using configurations of the kind shown in Fig. 3 and described more fully in another paper in this issue [31]. They obtain a uniformity of interaction better than 1 dB over a 3.8 cm length of silicon.

A severe problem with this type of device is the requirement for an airgap. This involves very careful optical polishing with severe mechanical tolerances, and a great deal of attention at all stages of the assembly and mask making to elimination of dust. There are alternative configurations which eliminate this particular difficulty. One employs a piezoelectric material, usually ZnO, laid down on Si by sputtering techniques, thus forming a monolithic device [48]–[52]. A second technique makes use of a piezoelectric semiconductor, such as GaAs, for the basic convolution interaction [44]. As the interaction takes place below the surface of the GaAs in a depletion layer, the uniformity of the interaction is excellent. The third technique is to use a thin semiconductor film, such as CdSe, laid down on LiNbO_3 [20]. Some of these configurations will be discussed further in Section III-G.

D. Semiconductor Convolver Theory

In order to understand the considerations entering into the design of these devices, it is necessary to derive the theory in somewhat more detail than the simplified version given as (3.6). An excellent treatment for flat band conditions at the surface has been given by Otto [54], who has obtained results which are physically meaningful. He gives criteria with which to judge the accuracy of a less rigorous theory outlined here, which is used to take account of other than flat-band conditions [26], [55].

We use Boltzmann's approximation for the carrier density: $n = n_0 \exp(q\psi/kT)$, $p = (n_i^2/n_0) \exp(-q\psi/kT)$, in an n-type semiconductor. The potential anywhere within the semiconductor is ψ with $\psi = 0$ and $n = n_0$. T , q are the electron temperature and charge, respectively, and k is Boltzmann's constant. We may, therefore, write Poisson's equation in the form [26], [55]

$$\frac{d^2\psi}{dy^2} = \frac{qn_0}{\epsilon} \{e^{q\psi/kT} - 1 - e^{q(2\phi_F - \psi)/kT}\} \quad (3.7)$$

where $\phi_F = -kT \ln(n_0/n_i)$ is the Fermi potential in the bulk semiconductor. After integration of (3.7) we find that

$$\frac{1}{2} F_s^2 = \frac{kTn_0}{\epsilon} \left[e^{q\phi_s/kT} - \frac{q\phi_s}{kT} - 1 + \frac{n_i^2}{n_0} \cdot \left(e^{-q\phi_s/kT} + \frac{q\phi_s}{kT} - 1 \right) \right] \quad (3.8)$$

where F_s , ϕ_s are the normal field and potential just inside the surface, respectively.

Equation (3.8) is, of course, the relation that is normally given in the treatment of the surface condition of semiconductors to determine the effective capacity of a depletion, accumulation or inversion layer [55]. In our case, we write $F_s = F_{s0} + F_{s1}$, where F_{s0} is the dc value of the surface field, and F_{s1} is the applied RF fields. Then the right-hand side of (3.8) can be expanded to second order in RF quantities

$$\phi_s = aE_{s0} + bF_{s1} + cE_{s1}^2. \quad (3.9)$$

We can thus determine both the first and second order perturbation in the RF potential, whatever the value of the dc

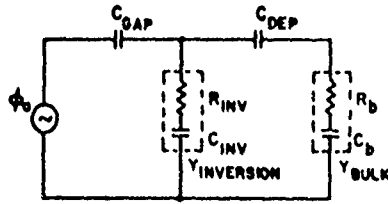


Fig. 11. Equivalent circuit used in the evaluation of linear coupling and loss in the semiconductor convolver.

surface potential. This treatment is valid providing carriers have time to reach thermal equilibrium. Such a situation is true in a depletion or accumulation layer, as well as at flat band, but may not necessarily be true in an inversion layer where the generation rate of carriers is very small.

The linear part of the relation (the term with the coefficient b) is of course closely related to the results obtained for the acoustic surface-wave amplifier, as (3.7), and can be summarized in terms of the equivalent circuit for a unit area shown in Fig. 11 [26]. In this circuit the potential source due to the acoustic surface wave is ϕ_a which can be related to the power P_a in the acoustic wave, as follows:

$$\frac{\phi_a^2}{2P_a} = \frac{1}{\omega(\epsilon_p + \epsilon_0)w} \frac{\Delta v(0)}{v}. \quad (3.10)$$

The gap coupling or capacity across the gap and oxide layer is C_{gap} , and the parameters of the semiconductor bulk are represented by a resistance R_b in series with a capacitance C_b . In addition there is the depletion layer capacity C_{dep} and the resistive and capacitive terms R_{inv} and C_{inv} denoting the shunting effect of the inversion layer, due to its interaction with the component of RF field parallel to the surface. The values of some of these quantities are [26]

$$\begin{aligned} C_{gap} &\approx \epsilon/l \\ C_{dep} &= \beta\epsilon_0/M(\beta h) \\ R_b &= 1/\sigma\beta \text{ (no accumulation at surface)} \\ C_b &= \epsilon/\lambda_d \text{ (no accumulation at surface)} \end{aligned} \quad (3.11)$$

where $M(\beta h)$ is given by (2.6). Note that if βh is small but $\epsilon_p \gg \epsilon_0$ and there is no oxide present $C_{gap} \approx \epsilon_0/h$, the capacity per unit area we might expect. Similarly when the surface is well depleted the capacity C_{depl} is just the expected capacity per unit area of the depletion layer, while C_b is the capacity across a Debye length λ_d of the bulk material, as might be expected. Similarly, R_b is associated with the resistance of a layer $\lambda/2\pi$ thick, the penetration depth of the acoustic wave.

In the complete circuit, including nonlinear effects, we can regard C_b and C_{dep} as being nonlinear capacitances driven by two sources ϕ_{a1} , ϕ_{a2} in series. The two special cases of most interest are: 1) the flat-band case for which $\phi_{s0} = E_{s0} = 0$, $C_{dep} = \infty$, and $c = -\epsilon/6qN_d$ in (3.9), 2) the surface is depleted $R_{inv} = \infty$, and $c = -\epsilon/2qN_d$ as we have already indicated in (3.6). The parameters c are, of course, proportional to the nonlinear parts of the bulk capacity C_b and depletion layer capacity C_{dep} , respectively. Thus the nonlinearity of the device tends to be stronger when it is depleted at the surface than in the flat band case. If the device, on the other hand, is accumulated at the surface, the effective carrier density at the surface is larger so C_b increases and R_b decreases and the device shows a correspondingly weaker nonlinearity.

It can be shown that the voltage V_{op} induced between the silicon and the grounded electrode of Fig. 9, assuming that the output is open-circuited, is

$$V_{op} = \mathfrak{N}/w(2P_{a1}P_{a2})^{1/2} \quad (3.12)$$

where for the flat-band case:

$$\mathfrak{N} = \frac{\sqrt{2}}{3} \frac{\omega^2}{qN_d v^2} \frac{\epsilon_0}{\epsilon(\epsilon_p + \epsilon_0)} \frac{1}{M^2} \frac{\Delta v}{v}. \quad (3.13)$$

Equation (3.13), which neglects diffusion effects, indicates that the normalized convolver efficiency parameter increases as the carrier density N_d is decreased. It would, therefore, appear to be desirable to work with a material with as low a carrier density and hence conductivity as possible. However, as the material conductivity is decreased, the transverse field interaction with the semiconductor begins to change the attenuation of the input signals, and the output drops due to this cause; so there is an optimum resistivity for maximum efficiency. This attenuation effect does not affect the output waveform shape, only its amplitude, because the total attenuation of the two oppositely directed input signals to any point z within the device is constant, and hence their product is constant, whatever the value of z . The attenuation per unit length α_r due to the acoustic surface-wave interaction with a semi-infinite semiconductor can be determined from an expression similar to that of (2.7) or by evaluating the power loss from the equivalent circuit. When this is done it can be shown that, in terms of α_r ,

$$\mathfrak{N} \approx \frac{\sqrt{2}}{3} \frac{\mu}{\omega v \epsilon_0} \alpha_r \quad (3.14)$$

where μ is the carrier mobility.

If we now include the propagation loss in a length L , in the expression for V_{op} will be seen that $V_{op} \propto \alpha_r \exp(-\alpha_r L)$ so it follows that the output is maximum where $\alpha_r L = 1$ or the attenuation is 8.6 dB as shown by Otto [54]. This result is valid whatever the value of the parameter M , which increases rapidly with the airgap thickness h . If there is a depletion layer present in series with the gap this increases the effective value of M still further, so the optimum value of resistivity required by the theoretical predictions tends to increase with gap thickness.

Some results of this type of theory which have been obtained by Gautier [26] are given in Figs. 12 and 13. Similar plots for different types of convolver configurations, which give good agreement with the experimental results, have also been made by Cafarella [31], Otto [54], and Khuri-Yakub [50]. It will be seen from Fig. 12, plotted for flat band, that with LiNbO_3 the optimum value of \mathfrak{N} is approximately 6×10^{-3} at 100 MHz, with conductivities in the range of 1-10 mho/m. However, as will be seen from Fig. 13 the \mathfrak{N} value increases as the surface is depleted although not by as much as the full factor of 3 to be expected from the nonlinear theory, because of the increase in the effective gap width. A comparison of experimental and theoretical results for two types of convolvers is given in Table II where the convolver efficiency F is also calculated taking account of the measured losses in the input and output circuits. It will be seen that the agreement between experiment and theory in these examples is excellent. When an inversion layer is present, it does not directly influence the second order nonlinear coupling coefficient; but, as can be seen from the equivalent circuit, its short-

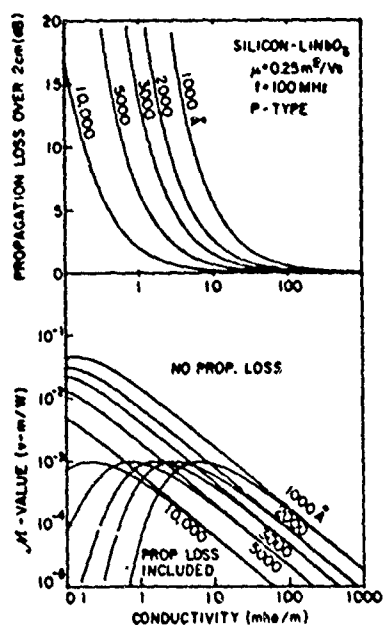


Fig. 12. Propagation loss and M -values versus conductivity for n-type silicon with various airgaps.

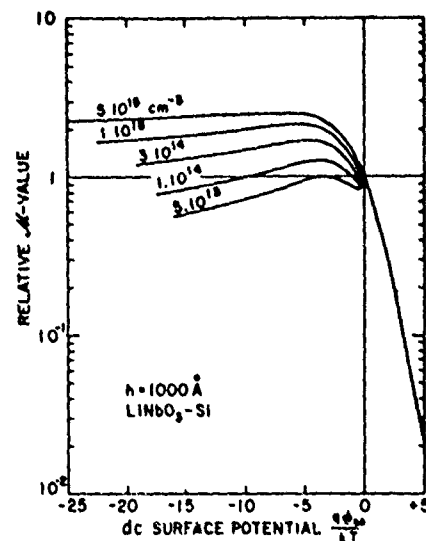


Fig. 13. The variation of the M -values for depleted or accumulated semiconductor surfaces.

TABLE II
 M -VALUES THEORY AND EXPERIMENT

Semiconductor: n-type Silicon; untreated; 2 cm long; $\mu = 0.1 \text{ m}^2/\text{V}\cdot\text{s}$
Piezoelectric: YZ LiNbO_3 ; $w = 1.25 \text{ mm}$; $h = 1500 \text{ Å}$; $f = 108 \text{ MHz}$
(111), (1 $\bar{1}\bar{1}$) $\text{Bi}_{12}\text{GeO}_{20}$; $w = 1.25 \text{ mm}$; $h = 3000 \text{ Å}$; $f = 52 \text{ MHz}$

Piezoelectric	LiNbO_3	$\text{Bi}_{12}\text{GeO}_{20}$
Si Resistivity ($\Omega \cdot \text{cm}$)	7	7
Two-Port Insertion Loss ^a	14	22
Convolution Efficiency F (dB) ^b	-56	-58
Output Circuit Efficiency ^c	0.4	0.7
M at Flat Band (theory)	4.0×10^{-3}	5.5×10^{-3}
M Depletion/ M Flat Band ^d	1.50	1.40
M Depletion (Theory)	6.0×10^{-3}	7.7×10^{-3}
M (Experiment) (V·m/W)	5.6×10^{-3}	7.0×10^{-3}

^aThis includes transducer and propagation losses.

^bRatio in dB of output terminal power (in 50 Ω) to product of input terminal powers. All powers in mW.

^cRatio of voltage actually developed across a 50- Ω load to V_{op} .

^dFrom Fig. 3.8 and similar one for BGO with 3000 Å (not given) ($q\phi_{30}/kT = -20$).

ing effect on the transverse fields decreases the RF potential seen by the free carriers. These effects have been taken into account by Gautier [26].

When his results are compared with experiments there is some discrepancy in the inversion layer region, and between the estimated flat-band potential and measured flat-band potential. This is due to the presence of surface states at the silicon dioxide interface, the well-known effect which occurs in semiconductor devices [55]. With careful control of the technology, the surface state density can be kept below 10^{10} states/cm², in which case surface states have a very small effect. More typically, with less careful control, the surface state density is of the order of 10^{11} states/cm². Thus, by measuring the discrepancy between the measured curves and the theoretical curves, one can measure the number of charged surface states by the difference in voltage between the theoretical and experimental curves [55]–[57]. This has been done and some of the results obtained by Gautier [26] are shown

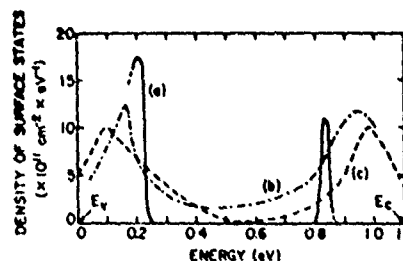


Fig. 14. Surface state density of Si-SiO₂ structure obtained by experimenters. (a) Gautier [26]. (b) Nicollian and Goetzberger [56]. (c) Deal et al. [57].

in Fig. 14. It will be seen that the results are comparable to although cruder than those obtained by other techniques.

The convolvers could be more carefully designed for measurements of the surface state density or free carrier properties rather than for other purposes. It has been shown by Das *et al.*

[58] and Bers [59] that associated techniques like the measurement of acoustic loss, the measurement of the dc term associated with the nonlinearly induced potential, and the acoustoelectric effect [60], can also provide entirely new ways for measuring semiconductor parameters [58]. In addition, it has been observed from the results on surface state storage devices that the decay times of surface state traps can be measured directly by such techniques [33].

One of the basic problems with airgap devices is that the oxide layer is not covered by a material impervious to impurities. In addition, because there can be charges induced on the oxide surface and on the piezoelectric substrate by friction or other causes during assembly, the interaction can, in fact, be nonuniform over the length of the device. A simple technique which has virtually eliminated this kind of problem is, not to oxidize the surface in the normal way [15]. If the surface is left with a layer of oxide 20-50 Å thick, such as normally grows on a clean Si surface in air, a very large number of surface states is produced. In this case, which is different from that with a thick oxide, the Si underneath the thin oxide is normally depleted while the thick oxide on an n-type semiconductor normally induces accumulation at the surface. Because there is a large number of surface states present in this case, it is extremely difficult to change the internal conditions at the semiconductor by application of an external dc field. For the same reason, surface charges on the oxide or on the piezoelectric substrate, as well as charges trapped within the piezoelectric substrate, have very little influence on the convolver behavior and, therefore, it is much easier to make a uniform convolver. Furthermore, as the surface is normally depleted, this is the correct operating condition for optimum convolver efficiency. So the airgap convolver with a thin layer of oxide on the surface is the best to use for normal convolver operation. The surface traps themselves, as they have a slow response, do not influence the RF behavior and so the convolver operates in a predictable manner, as shown in Table II.

On the other hand, if good optical sensitivity is required, i.e., we require the carrier density within the depletion layer to be influenced by the presence of light, then the presence of a very large number of surface states of this kind appear to give poor optical sensitivity. This is basically because of the rapid recombination of generated carriers that occur. It is, therefore, important to eliminate surface effects as much as possible in optical devices. In a similar way, storage devices based on storage in surface states have problems with nonuniformity of surface states and are not easy to control. Thus it has become important to devise other techniques, equivalent to the use of a buried channel in the CCD, for constructing convolvers which eliminate the interactions at the surface. We will discuss these further, when we discuss optical imaging and storage devices.

E. Optical Imaging with Convolvers

The convolver configuration can be used to detect and scan optical images. It has already been pointed out that it is possible to make use of the nonlinear capacitive effects due to RF electric fields normal to the surface to obtain an electrical output signal which is a line scan of the image [42], [44], [46]. It is also possible to make use of the piezoresistive effect associated with the change in loss caused by the change in resistance due to the acoustic strain in the semiconductor itself. The latter type of effect has been employed very successfully

by Luukkala. He employs CdSe deposited on LiNbO₃ to obtain single line scans and, hence, constructs an image by mechanically scanning in the perpendicular direction [45]. Kornreich has also used this effect to make Fourier transform devices [47].

It is the author's opinion that, with the advent of the CCD technology, it is unlikely that direct optical imaging devices based on the use of acoustic waves are liable to be competitive with solid state TV imaging devices. This statement is not based on the theoretical definition or sensitivity of acoustic imaging devices. With sufficient development, it is possible that the results obtained could be comparable to the best CCD's. The devices are parallel processing devices, and do not read out the signal serially through the registers as in a CCD. Therefore, the readout can be nondestructive and the devices are not as sensitive to a missing element as a CCD. However, a considerable investment in technology would be required to make competitive optical imagers, and it is unlikely that a device with a considerably better performance than the highly developed CCD devices would be obtained in the long run. On the other hand, the acoustic imaging devices have unique capabilities of their own. These are difficult to duplicate in other devices and make them useful in certain specialized applications. Some examples are as follows.

- 1) The possibility of obtaining very fast scan rates.
- 2) The possibility of directly obtaining one and two dimensional spatial transforms of optical images
- 3) The possibility of working with a wide range of optical detectors in both hybrid and monolithic configurations which would lead to new types of infrared sensitive devices
- 4) The possibility of obtaining electronic focusing of optical images without the use of physical lenses
- 5) The possibility of reconstruction of optical holograms in real time

We will concentrate here on the application of the convolver configuration in which the output is taken from the system at the sum frequency of the input signals, although we shall also consider certain configurations in which the output is taken from the system at the input frequency, i.e., it is as if one of the input signals is of zero frequency. We shall not deal in detail with all the other alternative configurations which have been used for optical scanning, instead we shall emphasize transform techniques, a unique application of these devices.

We consider the configuration shown in Figs. 15 and 16(a), which is illustrated as an airgap device. Following the analysis for the convolver, it can be shown that, if the carrier density variation due to the presence of light is $n(z)$, and the two input signals are of frequencies ω_1 and ω_2 , respectively, the output from the device will be of the form

$$H(t) = A \exp [j(\omega_1 + \omega_2)t] \int F\left(t - \frac{z}{v}\right) G\left(t + \frac{z}{v}\right) \cdot \exp \left[j(\omega_1 - \omega_2)z \right] n(z) dz \quad (3.15)$$

where the modulations of the two input signals are $F(t)$ and $G(t)$, respectively, and all spatial quantities are referred to the center of the device $z = 0$, with appropriate time changes. Suppose one input signal, the *scanning pulse*, is a delta function, i.e., $F(t) = \delta(t)$ and the other, the *reading pulse*, is a long CW pulse. In addition, if we assume that the system is degenerate

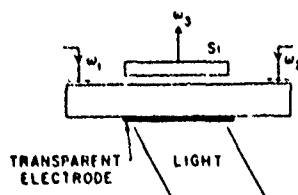


Fig. 15. A schematic of a convolver configuration for acoustic scanning of optical images.

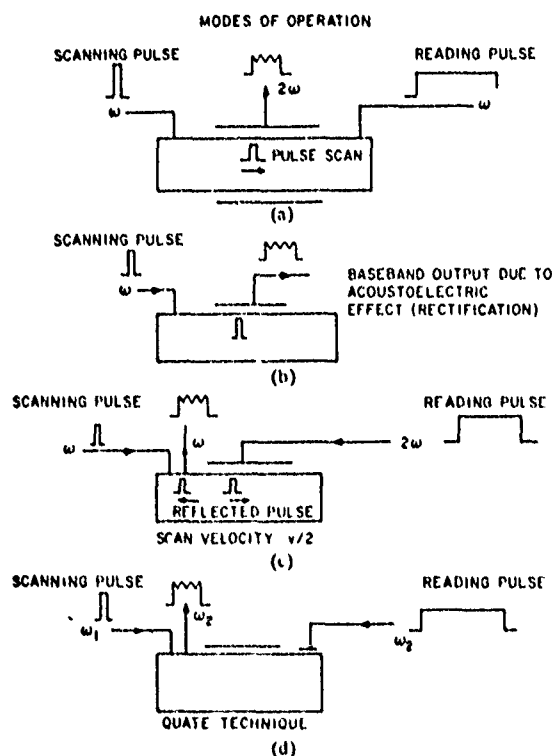


Fig. 16. Different operating modes of optical imaging devices. (a) A simple pulse scan [26]. (b) A device using the acoustoelectric effect [43]. (c) A device in which the readout is from a reflected pulse [45]. (d) The technique employed by Moll *et al.* [42].

so that $\omega_1 = \omega_2 = \omega$, we see that the output would be of the form $H(t) = An(vt) \exp 2j\omega t$. Thus we obtain a scan of one line of the image scanned at the acoustic velocity v . If a spot definition d_s is required, the time taken to scan a spot will be $t_s = d_s/v$; so the bandwidth required to obtain this spot definition will be of the order $B \sim 1/t_s$. If $T = L/v$ is the transit time of an acoustic wave over the length of the device, the number of resolvable spots will be $N = T/t_s$, or

$$N = BT. \quad (3.16)$$

Thus the number of resolvable spots is equal to the time-bandwidth product of the device. As the delay time involved is typically of the order of one-tenth of a typical TV line time, the corresponding bandwidth for the same number of resolvable spots will be of the order of a factor of 10 larger, while the scan time will be 10 times less than for a typical TV line scan.

Several alternative configurations which can be used for optical imaging by acoustic surface waves are shown in Fig. 16. The arrangement already described is shown in Fig. 16(a). In Fig. 16(b), a technique employed by Takada *et al.* [43], is shown, in which an output is obtained at baseband due to the

second order dc term generated by an RF scan pulse (the transverse acoustoelectric effect [60]). This technique has the advantage of a baseband output, but suffers from the problem of poor bandwidth because the output is taken out through a relatively small capacitor, the capacitance between the metal film and the silicon. However, with improvements in the technology, like the use of ZnO on Si, it may prove to be the simplest approach to scanning.

A third approach is shown in Fig. 16(c). This has the advantages that a high intensity reading pulse can be used; the scan rate is half that of the other configurations, because the scanning pulse travels to the point z and back to the input transducer. A problem with it is that attenuation along the scan path distorts the output signal, as it does in the method of Fig. 18(b). This technique has been used by Luukkala *et al.* in combination with illumination through a periodic grating with a $\lambda/2$ spacing to give strong reflections, as described below. In their case no reading pulse is required [45].

The fourth method shown in Fig. 16(d), historically the first, is due to Moll *et al.* [42]. In this case the attenuation of the reading pulse by the semiconductor is changed by the scanning pulse, due to the fact that a high intensity scanning pulse tends to deplete the semiconductor surface and hence lower the attenuation. By implementing this method in such a way as to measure the effect of the light on the storage time of carriers in surface state traps, a relatively sensitive optical scanning device was constructed [42].

One problem with these devices is their limited dynamic range. As an example, with the configuration of Fig. 16(a) there is an output from the convolver with no light present. When a depleted device is illuminated, the conditions approach flat band, and so there is a few decibel change in output. Typically this implies too small a dynamic range to be useful. Thus some stratagem is required to eliminate the "dark current".

One technique which has been used successfully in various forms, is to pass the light reaching the semiconductor through a relatively coarse optical grating of period l [26], [45], [46]. This introduces a periodicity into the semiconductor carrier density with a wavenumber $k_3 = 2\pi/l$. In this case, the output at the sum frequency will be of the form

$$H(t) = A \exp [j(\omega_1 + \omega_2)t] \int F\left(t - \frac{z}{v}\right) G\left(t + \frac{z}{v}\right) \cdot \exp \left[\frac{j(\omega_1 - \omega_2)z}{v} \right] \cos K_3 z \, dz. \quad (3.17)$$

It will be seen that a strong output is obtained if the difference frequency of the two input signals is such that $(\omega_1 - \omega_2)/v \approx K_3$. In this case the product of the periodic light variation and the two signals would generate a wave at the sum frequency $\omega_3 = \omega_1 + \omega_2$. The device acts to pick out the strong Fourier component of the light reaching it through the grating. On the other hand, the dark signal, i.e., the convolver output without light present, does not contain the periodic component with a wave number K_3 and, therefore, only gives very weak excitation of the output. With sufficient frequency separation or more exactly wavenumber separation of the input signals, this implies that the dynamic range of the device is limited basically at the lower level by noise and at the upper level by saturation.

The basic concepts of this idea have been checked by Gautier [26] who has obtained results in good agreement with the

theoretical predictions. The idea has also been used by Luukkala *et al.* [45] in a CdSe on LiNbO₃ piezoresistive device with only one input scanning signal at a frequency ω , and a grating with a $\lambda/2$ periodicity. The illumination gives rise to a reflected wave at the input frequency ω , and yields a good dynamic range.

It is apparent that devices of this kind are capable of responding to a particular Fourier component of the optical signal. Thus if one of the input frequencies is varied slowly, the output obtained from the convolver might be expected to correspond to the spatial Fourier component of the light with a wavenumber $K_3 = (\omega_1 - \omega_2)/v$.

This technique has been employed directly by Kornreich *et al.* [47]. They used only one input signal and employed a CdS film laid down on fused quartz, as illustrated in Fig. 17. In their experiment, an acoustic surface wave is induced in the substrate by the use of a wedge transducer. The strain associated with the acoustic surface waves, as with the Luukkala device [45], alters the effective band gap of the CdS and, hence, changes the photoconductivity due to an incident-light beam. If the acoustic input signal is at a frequency ω and hence has a wavenumber $k = \omega/v$, the resistance across the acoustic beam path will change uniformly if the light has a spatial Fourier component k . By varying the frequency of the acoustic wave signal slowly, it is, therefore, possible to obtain an output current which is a Fourier transform of the spatial pattern of the light.

One application of this principle, which has been demonstrated by Kornreich *et al.* [47], is to the determination of the optimum focus of an image. They make use of the fact that, when an image is well focused, the edges between light and dark regions are sharp and so there are high spatial frequencies present in the image. When the image is defocused, the higher spatial frequencies in the image are attenuated. Therefore, by observing the Fourier transform of the image and requiring the high-frequency components to be as strong as possible, they can determine accurately the point where the best focus of the image on the photoconductor sensor is obtained.

Returning now to the convolver configuration of Fig. 15, we consider the situation when the two input signals which are linear FM chirps with frequencies varying with time as $\omega_a = \omega_1 + \mu t$ and $\omega_b = \omega_2 - \mu t$, respectively, are inserted into the device. If a grating with a period corresponding to a wavenumber $(\omega_1 - \omega_2)/v$ is placed in front of the semiconductor, the output obtained will be of the form

$$G(t) = A \exp[j(\omega_1 + \omega_2)t] \int_{-L/2}^{L/2} n(z) \exp\left[-\frac{2j\mu t z}{v}\right] dz. \quad (3.18)$$

Thus the output is the spatial Fourier transform of the light intensity within the device. The device is, therefore, capable of taking a direct real-time Fourier transform of one line of an image.

It will be noted that now frequency corresponds to position, for if we consider a spot which can be represented as $n(z) = \delta(z - z_0)$, the output obtained varies as $\exp[j(\omega_1 + \omega_2 - 2\mu z_0/v)t]$, a change in position changes the output frequency. This result is understandable because with a normal type of scan, time is equivalent to position and so in the Fourier transform plane frequency is equivalent to position. Similarly, the definition normally depends on the highest frequency component

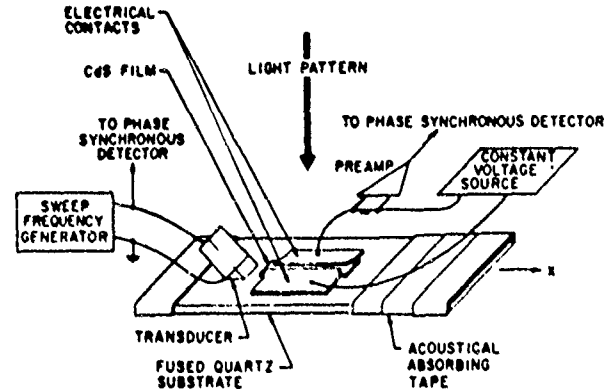


Fig. 17. The Fourier transform imaging device of Kornreich *et al.* [47].

available; in a Fourier transform device it depends on keeping the components with the largest value of μt or frequency excursion available so as to be able to recognize the higher order Fourier spatial components of $n(z)$.

It will be noted that a single spot in the image is now read out during the whole length of time the chirp signals are passing through the device, rather than for the spot time. Furthermore, the chirp length can be arbitrarily long, far longer than the time delay of an acoustic surface wave passing through the device. The maximum frequency bandwidth of the output from any point $|z_0| < L/2$ within the device is $B = 2\mu l/v = 2\mu T$, where T is the time delay of an acoustic wave passing through the length of the device. The total bandwidth of the two input chirps is $B_c = 2\mu T_c$, where T_c is the time length of an input chirp, where the maximum bandwidth B_c is twice that of an individual input transducer. It is shown in [26] and [46] that, if the inverse transform of the image is taken either in a spectrum analyzer, or in a real time chirp Z transform system, the minimum spot size obtainable is approximately $d_s = v/B_c$. It follows that the number of resolvable spots in the image is $N = L/d_s = B_c T$, i.e., the time-bandwidth of the device, and the resolution depends only on the total bandwidth B_c .

However, any spot in the image is now being read for the chirp time T_c . Therefore, the improvement in signal to noise ratio compared to that of the reading the image with a narrow pulse with a corresponding bandwidth B_c is

$$G = N \frac{T_c}{T} = N \frac{B_c}{B}. \quad (3.19)$$

We can, of course, also regard this improvement in signal-to-noise ratio as being due to a reduction in the bandwidth required for the far longer scanning time used. Thus, in this system, we have employed signal processing concepts to obtain a better signal-to-noise ratio, basically by taking a relatively long time to scan the image, and by using a more efficient scanning system which reads off any point in the image for the whole line time.

This scanning concept can be generalized to the use of an arbitrary code. When a coded signal is read into the device, the output obtained from one spot will be that code. If the output signal is inserted into a matched filter, a correlation peak corresponding to the spot will be obtained. Another spot in the image will correspond to a delayed correlation peak, but now the output will be improved in signal-to-noise ratio because of the longer scan time used.

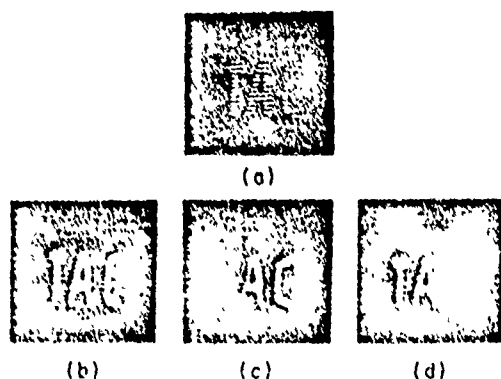


Fig. 18. (a) Two dimensional picture taken with the Fresnel transform imaging system. The chirp excursions are 9.8 and 7.6 MHz for 25 μ s. The minimum resolvable spot is $d_s \sim 0.25$ mm (50 points). (b), (c), (d) Effect of bandwidth limitations of the transform signal on the reconstituted image. (b) No limitation, (c) suppression of the lower frequencies, (d) suppression of the higher frequencies [26].

As an additional example, we can consider the use of two chirps of unequal chirp rates $\omega_a = \omega_1 + \mu_1 t$ and $\omega_b = \omega_2 + \mu_2 t$. In this case, it can be shown that a Fresnel transform of the image is obtained. If the input frequencies vary slowly, the output signal reduces essentially to the Fourier transform of the image. In the general case, the output signal can be inserted into a matched filter consisting of a dispersive delay line corresponding to a chirp rate $(\mu_1 - \mu_2)t$ to regenerate the original image.

An example of such signal processing is shown in Fig. 18. Here a simple image is scanned mechanically in one direction and electronically in the other. A Fresnel transform is taken and the inverse Fresnel transform taken by inserting the output signal into a matched filter [26]. It will be seen that, if certain frequencies are filtered out of the response, the definition remains essentially unchanged, but different parts of the picture are removed. This is because frequency now corresponds to distance in this quasi Fourier transform image.

One implication of these results is that the use of transform techniques makes it possible to remove mesential material from the picture without deteriorating its quality in any essential way. As an example, the low frequency spatial components can be filtered out by time gating the Fourier transform image thus tending to eliminate background illumination in an infrared device or "dark current" in an optical imaging device. It should also be possible to make two-dimensional scanned devices, either with acoustic waveguides to define the lines [24], or by using two orthogonal acoustic beams. Then one could obtain a direct raster scan of the two-dimensional transform of an optical image. By use of the storage devices to be discussed in the next section, which it should also be possible to make in a two dimensional form, it should be possible to reconstruct these two dimensional images. Arbitrary transforms should be obtainable in two-dimensional devices so that many of the powerful techniques of spatial filtering which have been suggested for use with optical images should be applicable in real time in devices of this kind. So far, no experiments have been carried out to prove these principles.

The theory that has been given leads to the conclusion that in a device of the order of 2 cm long, with a total transducer bandwidth of 100 MHz, it would be possible to obtain 600 resolvable spots. By increasing the bandwidth of the individual transducers or the length of the device, a much larger number of resolvable spots would be obtainable. However, in this case

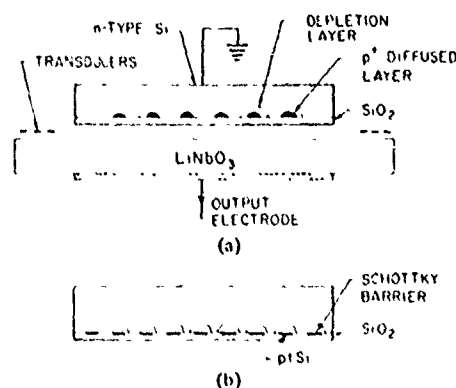


Fig. 19. (a) A convolver in which p^+ layers are diffused into an n-type substrate. The nonlinear interaction occurs in the junction depletion regions [34], [62]. (b) A convolver with Schottky barriers laid down on a semiconductor substrate.

we are assuming that the definition within the device is of the order of 30 μ m. Normally, as in other semiconductor photo-detectors, transverse diffusion of the carriers would limit the definition, and the modulation transfer factor MTF^2 would tend to fall off as the spatial period decreases. Thus, some means must be found to inhibit the carrier diffusion parallel to the semiconductor surface.

These conclusions are well born out by experiments carried out at flatband on these kinds of devices, where simple theories lead to results in good agreement with experiments [26]. On the other hand, when the device is run with the surface depleted, if it is n type, the holes generated in the depletion layer by the presence of light arrive at the surface and fill surface states. In this case, the storage time corresponds to the storage time in surface states. This is typically much longer than the corresponding recombination time in the bulk in a device operated at flatband. Thus if the recombination time is τ , and the generation rate of carriers due to incident light in the depletion layer of an n-type semiconductor is g per unit area, the number of holes per unit area generated by incident light will be $g\tau$. The holes that are generated will cause the surface potential to become more positive and, hence the depletion layer will become thinner. It is apparent then, that the longer the recombination time, the better the optical sensitivity of the device. A recombination time comparable to the frame time is, therefore, desirable.

Gautier has operated a device in such a depletion mode and obtained sensitivities of 3 μ W/cm² or 3 footcandles. The lower limit is because of the limited dynamic range due to the use of a coarse grating (10-MHz frequency difference) rather than by noise. This is two orders of magnitude better than for a device operated at flatband. However, the operation of a device in this mode is not practical because the image of the grating is incident on the semiconductor for long periods of time. In this case slow surface states are gradually filled up with carriers so that the device has a long term memory which is difficult to erase. The characteristics of this device, therefore, drift with time and its dynamic range decreases with time.

One way of eliminating this difficulty is to remove the interaction from the surface. This has been done both with storage devices and with optical imaging devices. Two configurations which are used are illustrated in Fig. 19. In one case (Fig. 19(a)), a large number of p^+ regions in a row are diffused into the semiconductor. These form p^+n junctions,

so that in thermal equilibrium, a depletion layer is formed under each p^+ region. If a junction is illuminated with light, the generated holes cannot travel parallel to the surface between two pairs of junctions because of the potential barrier at the n region. There should, therefore, be no sideways diffusion and the MTF should remain constant until the spatial periodicity in the image becomes comparable to the junction spacing. Furthermore, the holes which are generated in the depletion layer move towards the p^+ region, where their recombination time is extremely long, because any traps in that region are already saturated with holes. Thus the sensitivity of such a device to light can be very high [34], [62].

In a convolver, the p^+n junctions are chosen to be of the order of $\frac{1}{8}$ wavelength long with $\frac{1}{8}$ wavelength spacing between them, so as to minimize reflections. The junctions can consist of strips across the acoustic beam path, or small square or circular regions. In the first case, the strips must be well aligned with the acoustic beam, which is sometimes difficult with an airgap type of device. In the second case this requirement is not so important. Nonlinear interactions occur within the depletion layer, just as they would in a device with no junctions present. Now, however, as the interaction is below the surface and occurs in an area of the order of half the area of the total device [34] the efficiency tends to be decreased by a factor of approximately 6 dB, as appears to be the case in practical devices [62]. An advantage of this kind of device, as opposed to CCD's and most other photosensors is that the readout is a capacitive readout, rather than a current readout. It is, therefore, a nondestructive readout. The same image can be read out over and over again during the storage time of charges within the junction.

A second alternative to this configuration is to use Schottky barriers at the semiconductor surface, rather than p - n junctions. The storage time in Schottky barriers is dependent on the leakage current which is still very long, and the devices tend to have better response to RF signals. So the initial results look promising [35], [62].

F. External Diode and Strip Coupled Convolver

The most efficient airgap Si-LiNbO_3 convolvers that have been constructed have an overall efficiency $F = P_3/P_1P_2$ of ~ 42 dBm. After optimization for uniformity and large bandwidth, the efficiency is typically 20 dB worse than this figure. In these devices, the maximum input power is limited by the properties of the input transducers, while the minimum input power is limited by noise. For a reference power of P_2 of 20 dBm and an output circuit with a -90 dBm noise figure, $F = -42$ dBm yields an input noise figure of -68 dBm. The dynamic range for such devices is therefore of the order of 70-70 dB, which is adequate for many purposes. Therefore, it would certainly be desirable to arrive at alternative configurations with more efficiency and better sensitivity.

One such approach is to carry out the mixing process in external nonlinear devices, rather than in an internal device. This approach has been pioneered by Reeder *et al.* [63], [64]. They employ a surface-wave delay line with taps along the delay line. Each tap is connected to an external mixer, usually a diode, as illustrated in Fig. 20. The advantage of this system is that the nonlinear properties and impedances of the diodes can be chosen independently of the acoustic properties and piezoelectric coupling coefficient of the delay line material. Therefore, the device can be optimized for maximum efficiency.

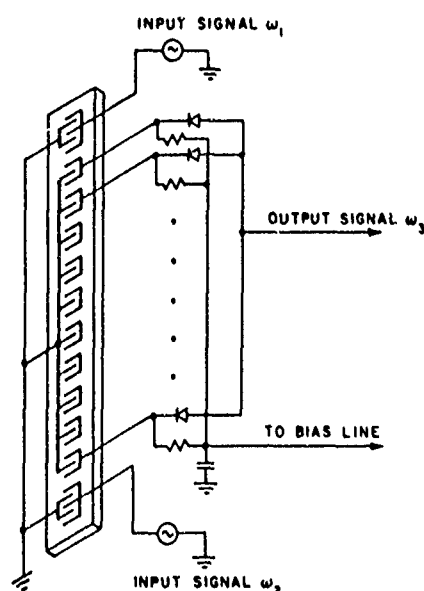


Fig. 20. An external diode convolver.

The mixers themselves can either make use of the nonlinear I - V characteristic of the diode, or a nonlinear reactive effect, as in the normal convolver.

Reeder's system makes use of the nonlinear resistive effect, so that it is necessary to have a dc return path for the diodes. In the shunt configuration shown, this return path is provided through resistors; the impedance of the diodes can be optimized by varying the bias applied to them. The optimum design of these arrays becomes a tradeoff between choosing the diode impedance for maximum power sensitivity or for minimum reflection from the individual elements of the array of tapped transducers. The tapped transducers themselves, because there are normally a large number of them, should be made with split $\frac{1}{8}$ wavelength fingers to minimize reflections from the fingers. The best sensitivity Reeder obtained corresponds to $F \sim -22$ dBm with saturation powers of the order of 0 dBm. By adjusting the current, he obtains a saturation power of 10 dBm with $F \sim -33$ dBm. Thus it will be seen that a considerable improvement in convolver efficiency can be obtained by this technique, although as the efficiency is made optimum, the saturation power is correspondingly decreased. Thus the dynamic range of the system is not necessarily greatly increased by the stratagem of using external mixers, but the sensitivity of the device can be considerably improved. The devices can be made very uniform, and Reeder has used 32 tap devices to obtain convolution of linear FM chirps, and efficient time reversal of signals in the same manner as a convolver [63].

A disadvantage of these devices is the fact that they only use a finite number of sampling points along the delay line, rather than continuous interaction as in the normal convolver. This makes it possible for the device to operate as a convolver with a number of different input frequencies, differing by integral multiples of a frequency which depends on the tap spacing L_T . Consider the situation when the two input frequencies are ω_1 and ω_2 , respectively, so that the outputs are obtained from the n th tap from the center of the device in the form $\exp j\omega_1(t - nL_T/v)$, $\exp j\omega_2(t + nL_T/v)$, respectively. After mixing, the output obtained from the system will be of the fol-

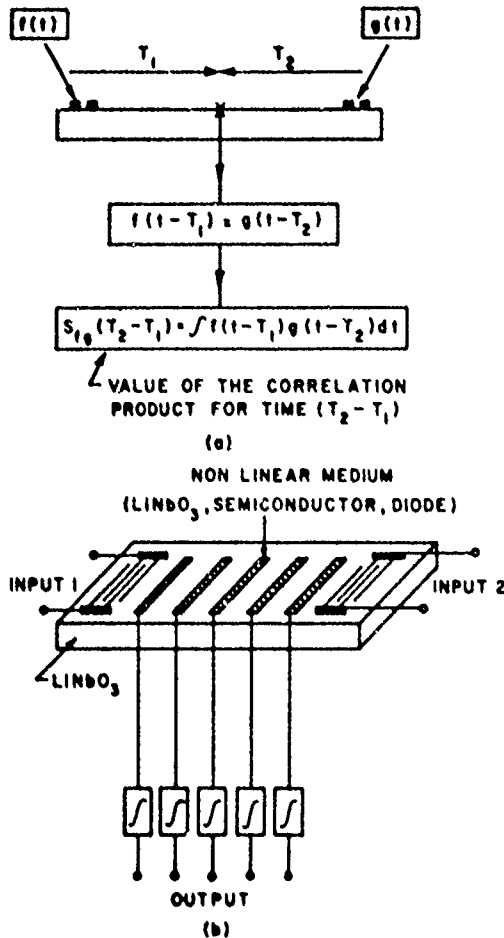


Fig. 21. The device used by Menager and Desormière to take real time correlation of millisecond signals [65].

lowing form

$$F(t) = A \exp[j(\omega_1 + \omega_2)t] \sum_n \exp\left[\frac{-jnL_T(\omega_1 - \omega_2)}{v}\right] + B e^{j(\omega_1 - \omega_2)t} \sum_n \exp\left[\frac{-jnL_T(\omega_1 + \omega_2)}{v}\right] \quad (3.20)$$

where A and B are constant. It is apparent that the output at the sum frequency $\omega_3 = \omega_1 + \omega_2$ is strong, i.e., the signals from all taps are in phase if

$$(\omega_1 - \omega_2)L_T/v = 2M\pi \quad (3.21)$$

where M is an integer. Thus because of the periodic spacing of the taps, it is possible for the convolver to operate at several different input frequencies, spaced by v/L_T . This result implies that the maximum bandwidth is limited by this frequency excursion, with larger bandwidths there would be aliasing of the input signals. Such a result is also implied by the sampling theorem which would indicate that at least two samples per RF modulation cycle are required.

External Integration A closely related form of device, devised by Menager and Desormière, integrates in time instead of space and takes the real time correlation of millisecond input signals [65]. With the configuration shown in Fig. 21, a num-

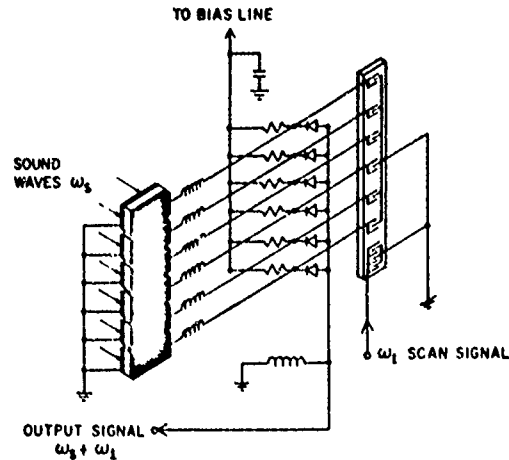


Fig. 22. Configuration used for acoustic focusing and scanning [67].

ber of separate silicon strips are placed along the device, each acting as a separate convolver. The signal output from an individual strip with acoustic delay times T_1 and T_2 , respectively, from the input transducers is

$$h(t, T_1, T_2) \propto f(t - T_1)g(t - T_2) \quad (3.22)$$

where the input signals are $f(t)$ and $g(t)$, respectively. The output from each convolver strip is fed into an integrator. The resultant time integration from each integrator is the integral of the product of the two input signals:

$$S_{fg}(T_2 - T_1) = \int f(t - T_1)g(t - T_2)dt. \quad (3.23)$$

By switching sequentially from one tap to the next, the times T_1 and T_2 can be varied and the correlation product of the two signals taken for several values of the variable $\tau = T_1 - T_2 = 2T_1 - T$ where T is the delay time through the device. Such a device could be useful for correlating digital codes and have a performance which would be competitive with existing digital correlators. The same approach should be possible by using the Reeder form of tapped delay line, with integrators on the outputs of each diode, with the outputs being taken at baseband frequencies [63].

Acoustic Imaging Devices. Another application of a tapped system of this kind is to an acoustic imaging device which has applications to sonar, nondestructive testing and medical imaging. In this device the convolver processing is used to focus and scan an image, or to take the Fresnel transform of the spatial variation of a signal arriving at an array of transducers. Consider as an example, the configuration shown in Fig. 22, in which low-frequency signals of frequency ω_s from each element of a linear array of piezoelectric transducers are mixed through the diodes with the scan signals from corresponding taps on the delay line, and the outputs summed [46], [66], [67]. In this case one input signal is that passing along the delay line, the rest are a set of signals arriving from the individual transducers. A plane wave signal arriving at an angle θ to the normal to the face of the n th transducer gives rise to an output from the transducer of the form $\exp[-j\omega_s nL_T \sin \theta/v_m]$ where v_m is the wave velocity in the acoustic medium and the transducer spacing is taken to be L_T for simplicity. If a signal of frequency ω_1 is inserted on the delay line, the product signal

obtained from the sum line will be of the form

$$F(t) = A \exp [j(\omega_1 + \omega_s)t] \sum \exp \left[-j \frac{\omega_1}{v} \pm \frac{\omega_s \sin \theta}{v_m} nL_T \right] \quad (3.24)$$

where A is a constant.

It follows that by changing the frequency of the input signal to the delay line, the differences in phase between the different transducers can be canceled out and a strong output signal obtained if

$$\frac{\omega_1}{v} \pm \frac{\omega_s \sin \theta}{v_m} = \frac{2M\pi}{L_T} \quad (3.25)$$

Thus by changing input signal frequency, it is possible to scan the angle θ of the incident beam which is received.

This idea can be extrapolated to allow for focusing of the input beam. If we generalize the situation to describe the problem of imaging a point (x, z) , where z is the distance from the array, the paraxial equation of optics leads to the conclusion that the phase ϕ_n at the n th transducer element due to a point source of frequency ω_s has a square-law variation phase along the array:

$$\phi_n = \omega_s t - \frac{\omega_s z}{v_m} - \frac{\omega_s (\lambda - nL_T)^2}{2zv_m} \quad (3.26)$$

It can be shown by the same type of analysis that if a linear FM chirp of frequency $\omega_1 + \mu t$, with a square-law variation of phase $\phi = \omega_1 t + \mu t^2/2$ is inserted into the delay line, the square-law variation of phase from the point source is cancelled out and a strong output signal is obtained if

$$\mu = \omega_s v^2 / zv_m \quad (3.27)$$

and ω_1 is chosen so that $\omega_1 L_T / v = 2M\pi$. This output is obtained at a time

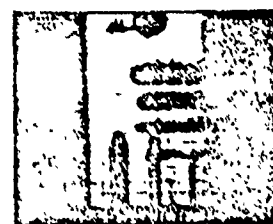
$$t = x/v. \quad (3.28)$$

Thus the device naturally scans along a line a distance z from the array at a velocity v , the focal length of the electronic lens is changed by changing the chirp rate μ . The definition of such a lens is the same as that of any other lens of the same aperture, or width $L = nL_T$, i.e., it is

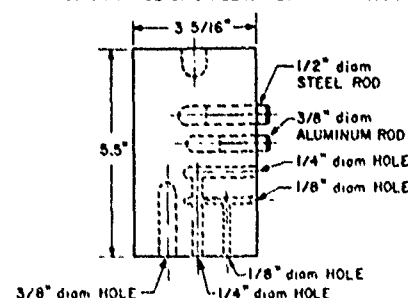
$$d_s = z\lambda_s / L. \quad (3.29)$$

where the acoustic wavelength in the medium is λ_s . The finite spacing of the taps gives rise to aliasing, as already mentioned, a phenomenon known as "grating lobes" in optics. This limits the field of view, or the number of resolvable spots between repeated images to approximately the number of taps in the delay line.

The basic concept of this system is easily generalized. By feeding input signals into the diodes and to the delay line, the device can be used with a transducer array as a transmitter. In practice, the diodes are usually replaced by balanced mixers and amplifiers. An example of a transmission picture taken of a 1 in thick aluminum block using two focused and scanned 32 element transmitter and receiver arrays facing each other with the block halfway in between them, is shown in Fig. 23. The results were obtained with an acoustic frequency f_s of 2.5 MHz, with no manual scanning of the block in the vertical direction, the acoustic beam being defined in the vertical direc-



TRANSMISSION IMAGE OF DRILLED ALUMINUM BLOCK



DRAWING OF ALUMINUM BLOCK

Fig. 23 Acoustic image of a 1 in thick aluminum block with holes drilled in it. The transmitter and receiver are both electronically focused and scanned in the x direction. Mechanical scanning is used in the y direction. The acoustic frequency is 2.5 MHz, the block is placed between two 30 element arrays 8 cm long, 28 cm apart [67].

tion by a thin slit [67]. This is the reason why the vertical definition of the picture is worse than the horizontal definition.

We have described here an imaging system based on the convolver principle which uses external acoustic transducers. The concept is not necessarily limited to the use of low frequency acoustic transducers. By using continuous convolvers and multiply tapped output transducers laid down on them, it should be possible to use the same principles at much higher acoustic frequencies in the UHF or VHF range. Similarly one could expect the concept to be applicable to phased array antenna systems. By using optical detectors it is possible to scan optical images, as we have already discussed. However, if a phase reference is employed, as is done in holography, then it should be possible by these techniques to either reconstruct holographic images already obtained on film, or to employ the device for focusing and scanning optical or infrared images. Thus the convolution principle employs acoustic signal processing techniques to provide a real-time scanning and focusing capability.

Strip Coupled Devices Before proceeding to other subjects, mention should be made of one other version of the tapped convolver system, the strip-coupled convolver [68], [69]. The construction of this type of convolver has been an attempt to eliminate some of the difficulties of the tapped external diode convolver, which involves making a hybrid type of device with many external connections. The basic idea here is to use single strips connected to diodes, rather than interdigital transducer taps. In this case, an array of $\lambda/8$ wide strips is laid down in the acoustic beam path. In the example given by Kino and Shreve [68], this was done by laying down the strips on a LiNbO_3 substrate, as shown in Fig. 23. By placing the semiconductor normally used for the convolver outside the beam path, good mechanical contact can be made between the semiconductor and the coupling strips. In this case, a semiconductor overlapping the end of the metal strips by distances of the order 25-100 μm was placed in contact

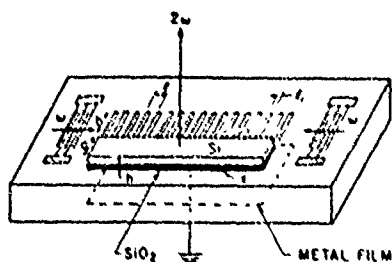


Fig. 24. A strip coupled convolver [68].

with the metal strips by mechanical pressure, the acoustic beam width itself being 1.25 mm.

Each metal strip, where it contacts the semiconductor, acts as an MOS diode, or equivalently, as a nonlinear capacitor. If a current I per unit length is induced on a strip of width l , length w by the acoustic wave and the overlap region of the diode is of length d , then the current density at the semiconductor is increased by a factor of approximately w/d over the value that would be obtained if a semiconductor were placed directly over the acoustic beam of width w . In the equivalent circuit of Fig. 11 this means reducing C_b and increasing R_b radically. Consequently, the displacement current density at the semiconductor is increased by the same ratio and the E field at the semiconductor is also increased by this value. It, therefore, follows that the nonlinear effects are increased by a ratio $(w/d)^2$. So the device is a far more efficient nonlinear convolver than the normal convolver. The reasons are the same as in the external diode system, a better impedance match has been obtained, although in this case the diodes are being used as reactive nonlinear devices rather than resistive devices.

By operating in this mode, Kino and Shreve [68], have constructed devices with an efficiency $F_T = P_3/P_1P_2 = -22$ dBm and a dynamic range of 80 dB, although with a slightly more limited dynamic range when the device is operated in a completely linear region, where the saturation powers are of the order of 0 dBm, just as in the external diode convolver.

The device, as demonstrated, was not necessarily very practical because it still involved obtaining a good mechanical contact. Adkins, has made such devices with silicon and aluminum nitride laid down side by side on a sapphire substrate [69]. The results are promising, although the efficiencies, as yet, have been low. But the basic principles have been well proven by his results. As we shall see, these principles are of great importance in storage devices because they lead to the conclusion that, when separate diodes are used to provide the basic nonlinearity of these devices, it is often useful to have metal contacts which are much larger than the actual area of the diode. In this case, radical improvement in convolver efficiency can be obtained, and the optimum design becomes a tradeoff between convolver efficiency and saturation power.

It should be noted that the same idea has been suggested for acoustic amplifiers [70]-[73]. In principle, it should be possible to make amplifiers with much larger gains per unit length. The only difference from the convolver configuration would be that the carriers between the strips would have to drift in the direction of propagation of the acoustic wave. In practice, none of these amplifiers have proved to be very successful. The basic reason for this, as shown by Maerfeld [71] and Blotkejaer [73], is that space harmonic interactions in these

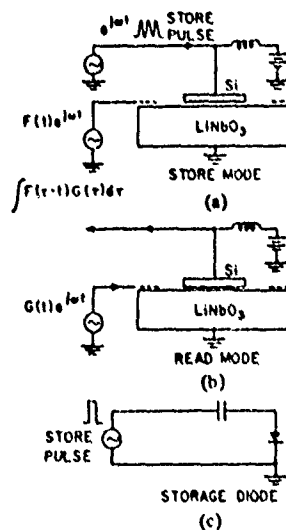


Fig. 25. A schematic of the system used for the storage correlator [32]. (a) Read in. (b) Read out. (c) Illustration of the storage mechanism in a diode.

devices are strong, and interaction with these harmonics can lead to acoustic losses. The acoustic losses due to this cause typically outweigh the improvements in acoustic gain obtained at the fundamental harmonic. In principle, the devices would work with a very large number of strips per wavelength, but in practice the mechanical requirements for doing this are too severe.

G Storage Correlator

The most recent development in acoustoelectric devices is the storage correlator. This device makes use, in its different forms, of one of several possible storage mechanisms such as storage in surface traps, bulk traps, in diodes, or by charging from an electron beam.

Consider the configuration shown in Fig. 25, which is the one first used by Beis and Cafarella [32]. Suppose an RF signal of frequency ω_1 is inserted into the convolver. This signal will give rise to a surface acoustic wave which varies as $\exp j(\omega_1 t - k_1 z)$ along the device. Now suppose that when the RF wave is passing under the semiconductor, a short RF pulse of frequency ω_1 is applied between the output plate of the convolver and the semiconductor, this excites an RF field which varies as $\exp j\omega_1 t$. The nonlinear interaction between this signal and the acoustic surface wave will then give rise to dc terms which vary as $\cos k_1 z$. If the semiconductor had been initially biased into depletion by a dc field, then the positive RF peaks would tend to move carriers towards the semiconductor surface and these carriers would be trapped in surface states. Thus a signal of the form $I(t) \exp j\omega_1 t$ inserted into the device will give rise to a variation in trap density of the form $I(t) \exp j\omega_1 t \cos k_1 z$.

In practice, the short RF burst required on the plate may consist of a single short pulse of one-half RF cycle. A second alternative first used by Hayakawa and Kino, is to work with a baseband pulse [33]. In this case, the stored information corresponds to the modulation of the RF signal (the positive RF peaks). In both cases, the trapped charge modulates the thickness of the depletion layer, so it affects the interaction of the semiconductor with any later signal read into it.

The stored information may be read out by using a reading signal which has the same spatial periodicity [32]. If an RF pulse is applied at the input interdigital transducer of the form $G(t) \exp j\omega_1 t$, an output will be obtained from the output electrode of the form

$$H(t) = A \exp(j\omega_1 t) \int F\left(-\frac{z}{v}\right) G\left(t - \frac{z}{v}\right) dz \quad (3.30)$$

where the integration is taken over the length of the output electrode. It will be observed that the output signal is the correlation of the reading signal $G(t)$ and the original stored signal $F(t)$. Alternatively, if a reading signal is inserted at the other end of the device of the form $G(t) \exp j\omega_1 t$, the output signal obtained will be of the form

$$H(t) = A \exp(j\omega_1 t) \int F\left(-\frac{z}{v}\right) G\left(t + \frac{z}{v}\right) dz. \quad (3.31)$$

In this case, the output is the convolution of the stored signal $F(t)$ with the reading signal $G(t)$. In both cases, if the reading signal is a δ function, the signal obtained at the output is the original stored signal or the time reversed version of the input signal respectively.

Similarly if the second method is used to store a baseband pulse [33], the output could be read out at baseband in the same way, or the device could be used as an acoustic convolver and the output read out from the plate at a frequency 2ω . The advantage of this technique is that if there is any carrier diffusion or the trapping time is slow, only relatively low-frequency information need be stored rather than the carrier frequency itself.

There are numerous other ways to use this device. For instance, if the reading signal is inserted on the plate electrode instead of at one of the interdigital transducers, it can be shown that the output signal obtained is either the correlation or the convolution of this signal with the stored signal, depending on which end of the device the signal was obtained from.

Electron Beam Storage: The earliest demonstration of such storage techniques did not involve the use of a semiconductor. Instead, Bert *et al.* [36] used a pulsed electron beam incident on the piezoelectric substrate, in their case, quartz. The reflection coefficient of the electrons was changed by the potential at the surface of the dielectric associated with the acoustic surface waves. Therefore, when the electron beam was pulsed sufficiently rapidly, charge was stored on the surface of the dielectric, which depended on the acoustic modulation. The stored charge could be erased from the device by pulsing it once more with an electron beam. At this time acoustic surface waves propagating in both directions were excited by the change in potential at the dielectric surface, and so either the original signal or a time reversed signal could be obtained from the storage device.

Distributed Diode Devices: More recently, the trend has been towards eliminating surface effects, and working with either Schottky barriers [35]–[37] or p-n junctions [34]. Just as with optical devices and the convolvers themselves, the problem of reproducibility and uniformity is made much simpler by employing interactions below the surface of the semiconductor. Furthermore, much better control over the read in times and storage times can be obtained. The work on Schottky barrier storage is covered in an accompanying

paper in this issue by Ingebrigtsen, so we shall not describe it in detail here [35]. Suffice it to say that if a row of Schottky barriers is laid down on the semiconductor in the configuration shown in Fig. 18(b), the Schottky barriers will normally be in thermal equilibrium, and therefore there will be depletion layers under them. Suppose now we pulse the silicon negative with respect to the grounded film underneath the substrate, as illustrated in Fig. 25(c). In this case, a Schottky barrier would be forward biased and the charge it would receive would be $Q = C_1 V$, where C_1 is the capacity of the Schottky barrier to ground and V the applied potential. If, now the pulse is removed, the Schottky barrier becomes reverse biased and the only way the charge can leak away from the electrode is through the leakage current of the Schottky diode. If, in the reverse biased condition, the leakage current or saturation current of the Schottky diode is I_s , the discharge time before the diode returns to equilibrium is approximately $\tau_D = Q/I_s = C_1 V/I_s$.

More generally, if a pulse has been applied to the device and there is an acoustic surface wave traveling along the surface, the total potential at the diode will depend on the sum of the potentials due to the acoustic surface wave and the applied pulse, as will the stored charge when the device is forward biased. It is apparent, then, because the Schottky barrier diode has a very rapid turn on time, i.e., the current rises very rapidly with voltage and, essentially instantaneously, it should be possible to charge such a diode in a few nanoseconds. On the other hand, the discharge time will depend basically on the leakage time. It is, therefore desirable to use a diode with as low a leakage current as possible. This, in turn, implies the use of a diode with as high a barrier potential as possible. For this reason, one of the best choices is a platinum-silicide diode in an n-type semiconductor which has a barrier potential of 0.86 eV. With such a diode, assuming that the external capacitances are comparable to the internal capacity of the diode when depleted, the discharge times are estimated to be in the range of 10–100 ms depending on the size of the contact electrode used with the diode. When the contact area is larger than that of the diode, the convolution efficiency is increased because the device acts as a strip coupled convolver, furthermore, because of the larger capacity of the contact to ground, the storage time is increased. The results are in reasonable agreement with the experiments. Schottky barrier diode arrays of this kind have been demonstrated by Ingebrigtsen to have read in times in the order of a few nanoseconds, and discharge times of as much as 100 ms. Correlation and convolution with good efficiency have been obtained with such diode arrays, and correlation of FM chirps and digital codes has been demonstrated.

Results of this type have also been obtained with p-n diode arrays by Maerfeld *et al.* [34] using the types of storage mode described. They have shown that although the read in times are of the order of 1 μ s, the storage times are correspondingly longer with p-n diodes. The storage time now depends on the decay time of stored minority carriers, which is relatively long. Maerfeld *et al.* have observed storage times of as much as 15 s in devices of this kind, using commercial Vidicon arrays for the p-n diode array.

One important application of these devices has already been mentioned [37]. In this application, correlation is carried out between a reference echo and an echo from the object of interest, thus making the requirements on the accuracy of the

radar system or propagation path much less severe. The same considerations apply to acoustic pulse reflection systems used for nondestructive testing and medical imaging. In this case the great advantage could be that when an acoustic transducer is placed in contact with an object, a reference signal from the contact could be obtained, which could be correlated with a signal from an echo deep within the object. Now it would be possible to compensate for an irregular contact, as well as the characteristics of the transducer itself.

The storage correlator is an obvious device for reconstructing transformed optical image signals. It has been shown by Ingebrigtsen [35], [37] that if the Schottky barrier electrode is made of a resistive material, polysilicon, the forward currents can be kept low. Therefore, when a second input signal is incident on the device, it can be read in and added to the original signal stored in the device without losing the information already present. Thus the device acts as an integrator. This makes it possible to store signal transforms within the device and thus carry out many of the processes already described for optical imaging, i.e., one can hope to obtain a type of holographic storage.

Further possibilities arise for two-dimensional systems. It is still very early to know where this work will lead but it would appear that bit storages of 10^5 bits/cm² should be possible in two-dimensional versions of this device [37]. Furthermore it should be possible to carry out storage in a holographic form, rather than directly. In addition, of course, it should be possible in two-dimensional devices, just as in the one-dimensional form, to correlate stored information with later information read into the device.

Storage in CdS Before leaving the subject of storage, it is important to bring the reader's attention to a closely related form of storage device suggested by Melcher and Shuen [38], which has the capability of very large storage capacity at extremely high bit rates. This is a bulk-wave device which employs CdS operated at cryogenic temperatures. Storage of the signals is in bulk traps, at low temperatures the probability for field assisted tunneling from bound states is

$$P = A(c_T |I|) \exp(-Bc_T |E|)$$

where c_T is the trap energy level. Thus the number of traps filled depends on the electric field strength.

Operation is in exactly the same manner as already described. An RF input signal $I(t) \exp j\omega_1 t$ excites a bulk wave, and a uniform RF field is introduced by a pair of electrodes on either side of the CdS crystal, just as in Fig. 25(a), if the silicon were replaced by a simple electrode. Readout follows the previous technique described. In this case, however, because of the low acoustic losses at 4 K, operation could be carried out at frequencies of 10 GHz, and storage obtained for several months. As this is a volume wave device, the implication is that the bit storage capacity could be of the order of 10^{11} /cm³ with extremely high bit rates.

Storage of acoustic wave signals in CdS has also been obtained at room temperature, using the normal Shockley-Read mechanism for filling bulk traps [39], [40], [55]. In this case, as is usual with CdS, the carrier conductivity was controlled by illumination, as shown in Fig. 26. Bleustein-Gulyaev [5], [6] waves were employed, with signal read into transducer 1, and readout of transducers 2 or 3. The plate electrode, in this case, was replaced by two electrodes between which an electric field parallel to the surface was in

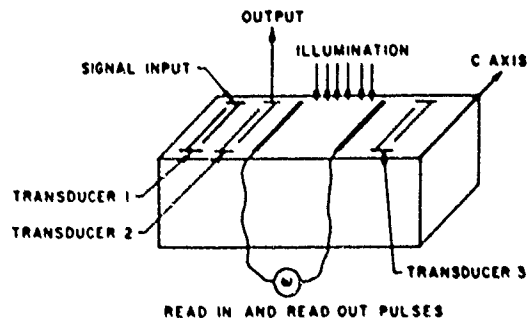


Fig. 26. The configuration used for storage of Bleustein-Gulyaev waves in CdS [39].

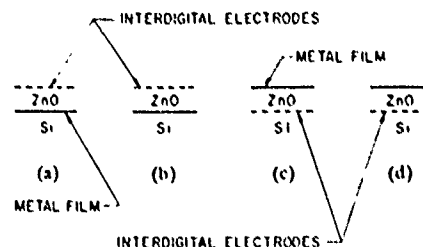


Fig. 37. The four configurations for an interdigital transducer on a nonpiezoelectric substrate: (a) The interdigital electrodes on top of the ZnO and a metal film at the interface; (b) Same as (a) but without a metal film at the interface; (c) The interdigital electrodes at the interface and a metal film on top of the ZnO; (d) Same as (c) but without metal film on top of the ZnO [48], [49].

duced. The experimental results of Maerfeld and Tournais indicated decay times of the order of 100–400 μ s, with relatively long read-in times of the order of 40 μ s [39]. Later work by Bastide *et al.* indicated 100 ms storage times with correspondingly longer read in times [40].

II. The ZnO on Si and ZnO on GaAs Convolver

We have described acoustoelectric devices in which the interaction is obtained between a semiconductor, usually silicon, and a piezoelectric substrate, usually lithium niobate, with the two materials separated from each other by means of an airgap. For this reason, a sophisticated mechanical technology is required with detailed optical finishing of both substrates. There are other approaches which are being tried to eliminate these kinds of difficulties. One is to deposit a semiconductor on a piezoelectric substrate [9], [10], [20]. A second method is to deposit AlN and Si on sapphire side by side and use coupling strips between them [69]. In this section we will describe yet another alternative, the deposition of ZnO, a piezoelectric material, on a semiconductor such as silicon or gallium arsenide. We believe that this approach is a viable one, not only because it can lead to useful convolvers and amplifiers, but in addition, as has been shown by Hickernell, the use of silicon technology makes it possible to construct switches, amplifiers, and other devices normally used in integrated circuit on the same substrate as the acoustic surface-wave device [48].

It was shown a few years ago by Hickernell that sputtered ZnO is an excellent material to lay down on a nonpiezoelectric substrate to obtain good coupling of acoustic surface waves [48]. Several configurations for obtaining coupling are possible and are shown in Fig. 27. They involve the use of an interdigital transducer, either on the top surface of the ZnO or at the interface, with a ground electrode sometimes placed on the opposite

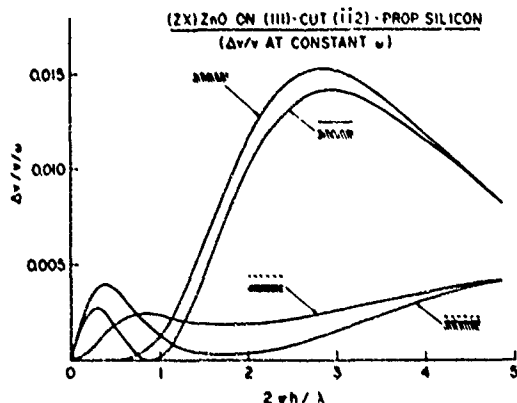


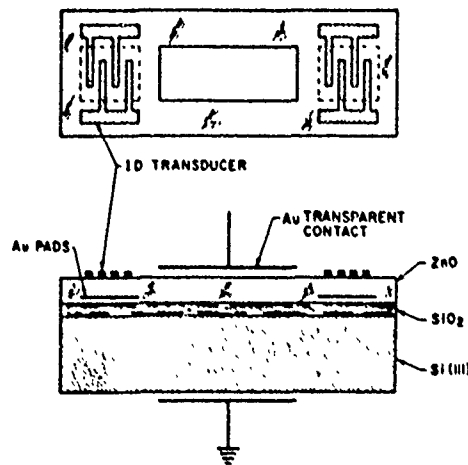
Fig. 28. The variation of $\Delta v/v$ for ZnO on semi-insulating Si, with four different configurations [49].

surface and sometimes missing. The theory of the coupling was worked out by Kino and Wagers [49] who showed that there is an optimum thickness for the ZnO. Curves of their results, which assume that the Si is semi-insulating, are given in Fig. 28. With a ground electrode present, there is a peak in the effective $\Delta v/v$, where the thickness of the ZnO is of the order of 0.05λ . There is a further much larger peak in $\Delta v/v$, with a value of 0.015 comparable to that of LiNbO_3 (0 022) where the thickness of the ZnO is approximately 0.4λ .

If it is required to introduce an acoustic surface wave on a conductive silicon semiconductor, it is usually convenient to work with an interdigital transducer on the top surface and a ground electrode under the ZnO. It will be observed that epitaxially grown piezoelectric material must be deposited at a high temperature and would both contaminate and be contaminated by the silicon. Therefore, a piezoelectric material which can be sputter deposited is normally employed. This usually implies the choice of either CdS or ZnO. The latter is easier to produce reproducibly in a semi-insulating form, in addition it has a higher coupling coefficient.

Hickernell has constructed ZnO on Si devices with the configuration of Fig. 27(d) growing a very thick layer of SiO_2 on top of the silicon, then laying down the required transducers before deposition of the ZnO [48]. However, in acoustoelectric devices the acoustic surface wave must interact with the silicon, therefore it is necessary to work with a relatively thin layer of SiO_2 . Furthermore, if a ZnO layer is laid down along the length of the acoustic path, it is desirable to have a relatively thin layer because the acoustic losses in the ZnO are relatively high. In this case most of the acoustic energy is in the underlying silicon, rather than in the ZnO layer.

A convolver may be constructed in this configuration, relatively simply, by placing an electrode on the top surface of the ZnO, as shown in Fig. 29 [50]–[52]. The device works in much the same manner as the normal convolver, except that now the effective value of $\Delta v/v$ is relatively low, and the optimum resistivity tends to be of the order of $50 \Omega \cdot \text{cm}$, although most of the operating devices that have been constructed have worked with somewhat lower resistivity material, the optimum resistivity not being very critical. Devices made in this configuration have given an efficiency of $1 - P_3/P_1P_2 = 58 \text{ dBm}$, the results comparing quite closely to a theory derived by Khuri-Yakub [50], which is based on the Gauthier theory already described [26]. The results indicate, in a simple convolver, the maximum efficiency to be expected is approxi-



MONOLITHIC CONVOLVER WITH ZnO/Si
Fig. 29. A schematic of a ZnO on Si convolver [50]–[52].

mately -52 dBm if all parameters are optimized, a figure about 10 dB worse than the best airgap convolvers.

The major disadvantages of this type of convolver are associated with the presence of surface state traps at the SiO_2 –Si interface, as well as traps at the SiO_2 –ZnO interface and within the ZnO itself. In particular, the traps within the ZnO are difficult to eliminate even in single crystal material, let alone in sputtered materials.

The trapping effects manifest themselves by tending to make the characteristics drift with time. If a dc potential is applied to the output electrode, traps will charge up or discharge and the characteristics of the convolver will tend to drift back to equilibrium in times as long as several days. The results depend very much on deposition conditions and have varied from laboratory to laboratory. Further, if it is attempted to use the devices for optical imaging, the problems are still more extreme because the presence of light can charge the traps [51], [52]. However, by applying short pulses to the device to bring it back to equilibrium before an optical scan, Elliott *et al.* were able to obtain reasonably reproducible results for acoustic scanning of optical images [52].

On the other hand, this storage mechanism itself can be used to give a semipermanent read in to a device of this kind, although the charge times are relatively slow. Such results, in both one and two-dimensional configurations, have been obtained by Coldren and are described in this issue [51].

One of the major advantages of a ZnO on Si device is the relatively small thickness of the ZnO, typically of the order of $1.5 \mu\text{m}$, compared to the thickness of LiNbO_3 in an airgap convolver, which is of the order of 1 mm . This implies that in a storage device, where it is necessary to apply a voltage to the plate to produce a given field at the surface of the semiconductor, the applied voltages must be orders of magnitude higher in an airgap LiNbO_3 device than in a ZnO on Si device. Thus, the ZnO on Si device can lead to storage devices which need relatively low applied voltages compared to other convolver devices where it is required to control the characteristics by external potentials applied to the plates.

Many of the same considerations for the elimination of surface effects and trapping effects which apply to airgap devices, also apply to the ZnO on Si devices. Thus devices have been

constructed with a row of Schottky barriers laid down underneath the ZnO layer. By growing a layer of sputtered SiO₂ above the Schottky barriers, Borden and Kino, in unpublished work, were able to show that trapping effects could be completely eliminated and no hysteresis was observed in the characteristics. Furthermore, by applying a pulse to the metal electrode, the characteristics of a convolver could be changed, i.e., there was Schottky barrier storage with decay times of as much as 100 ms. However, in this case, the maximum voltage required before saturation of the decay time set in, was of the order of 20 V. This should be compared to Ingebrigtsen's results with LiNbO₃ Schottky barrier airgap convolver where the onset of storage occurs with an applied dc voltage of the order of 300 V, a ratio which would be expected from the dimensions involved [35].

At the present time, complete storage correlation devices have not been made on ZnO on Si because of the relative inefficiency of these devices compared to the airgap convolvers, and hence their limited dynamic range. However, it has been possible to show that the convolution efficiency can be improved by waveguiding, i.e., tapering the width of the ZnO layer from 1 to 0.1 mm. This should lead to an improvement of 20 dB in efficiency. In fact, the improvement was 10 dB because of the additional losses due to the tapering. When this effect is taken into account, the internal improvement in convolver efficiency was indeed 20 dB [50].

With the demonstration that buried diode devices eliminate the trapping effects due to the presence of ZnO, one would expect that ZnO on Si convolvers will become practical devices which can be employed for many of the operations which have already been demonstrated with airgap convolvers.

Another very closely related approach, which has been demonstrated by Grudkowski *et al.* is to use ZnO on GaAs [44]. In this case, they only needed the ZnO in the transducer region to obtain strong input coupling. In the convolver region, a Schottky barrier was laid down on the GaAs and they employed the piezoelectric coupling of the GaAs itself. Such convolvers have yielded efficiencies very comparable to the ZnO on Si convolvers, but with extremely uniform output characteristics, i.e., uniformity along the length of the device better than any other device known to the author [44]. By using a Schottky barrier deposited on the GaAs these authors were also able to obtain storage for several seconds of pulses read into the device, and read this information out from the convolver. The decay time was extremely light sensitive, and so the device could be used for optical sensing. This particular approach is probably well worth pursuing as GaAs in relatively large sizes becomes more available.

IV. CONCLUSIONS

It has been shown in this paper that surface-wave acoustoelectric devices have reached a stage of development where they are being tried out in systems.

The best constructional technique presently employed is to separate the semiconductor from the piezoelectric substrate with posts or rails so as to maintain the uniformity of the airgap [14], [15]. Other techniques, such as the deposition of a semiconductor on the piezoelectric substrate [9], [20] or piezoelectric material on a semiconductor [48]-[52], are becoming practical and should lead to viable devices.

At the present time, acoustoelectric amplifiers are well understood and their performance can be predicted in detail

[9], [14], [17]. They provide the advantage of nonreciprocal amplification and can, in principle, give an increase in the dynamic range of a long delay line. However, they are not yet sufficiently developed to make these advantages useful in relatively low loss delay line filters rather than using external amplifiers. One application to acoustic convolvers with internal gain looks very promising [20].

Acoustic convolvers have the great advantage in that it is possible to obtain the convolution between a signal and a reference consisting of another signal. This means that the device configuration is relatively simple and does not require multiple taps. At the present time, devices with a large dynamic range, whose properties are uniform over their length, have been demonstrated in the laboratory and are beginning to be tested in radar systems. Such devices have been used as programmable matched filters in spread spectrum systems and should receive wide application in this field, as well as to radar systems [31], [74].

The convolver principle has been generalized to a wide range of new applications. It has been shown that the same basic configuration which involves the interaction between the semiconductor and a piezoelectric substrate can be employed for scanning of optical devices [42]-[47]. Because convolvers are able to take transforms relatively simply, it is possible to obtain Fourier transforms or other spatial transforms of optical images and reconstruct them in a matched filter or a second convolver [46], [47]. This technique should, in the end, lead to two-dimensional scanning devices capable of yielding arbitrary two-dimensional spatial transforms of optical images. There may also be important application to infrared imaging, because of the wide range of semiconductor materials that can be employed in this application, and because the type of sensing involves using the change in capacity of a junction or depletion layer rather than a current readout. This type of sensing is normally nondestructive, i.e., the image can be read over and over again.

A recent development is the storage correlator [32]-[40]. This device is capable of storing a signal read into it at relatively high bit rates, and then taking the correlation of this stored signal with a later signal read into it. Such devices have already demonstrated storage times of up to 15 seconds at relatively low bit rates [34]. Other devices have demonstrated storage of nanosecond pulses, with storage times of the order of 100 ms [35]. There is good promise that two-dimensional forms of these devices can be made with storage densities of the order of 10⁶ bits/cm² at high input bit rates [37]. Furthermore, because it is possible to integrate in these devices, i.e., add several stored signals to each other, a type of holographic storage is feasible. This implies that, because of the transform properties of convolvers, it should be possible to store the signals in transformed form, rather than directly, thus making properties of an individual element of the device somewhat less critical than in a direct storage device.

Recently, the convolver principle has been used in tapped delay lines and external mixers and integrators [63]-[65], [68], [69]. Such convolvers have excellent sensitivity. An application of these techniques is to the electronic focusing and imaging of bulk acoustic waves. This principle has important applications in nondestructive testing, medical imaging, and sonar, and could be generalized for use in phased array radar, high frequency acoustic imaging, and focusing and scanning of optical images [67].

The constructional techniques that have been developed are useful not only for acoustic devices themselves, but now it is possible to construct other types of semiconductor devices on the semiconducting substrate [48]. By using either GaAs for the acoustic devices or Si with ZnO overlay, it should be possible to construct a wide range of acoustic amplifiers, oscillators, and delay line filters on the same substrate as the other semiconductor devices typically needed in a complete system.

It is apparent that acoustoelectric interactions in acoustic surface wave devices have a wide range of applications. Many of the possibilities are described in this paper. As the devices are developed, new ones will no doubt be found with application to radar, sonar, acoustic and optical image processing, and to signal processing in communication systems.

ACKNOWLEDGMENT

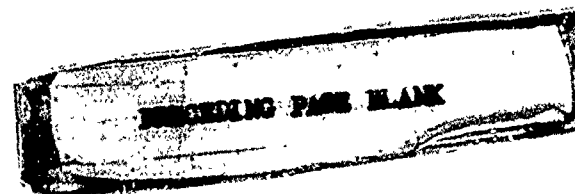
The author would like to thank C. F. Quate, H. J. Shaw, E. A. Stern, and B. A. Auld for many useful and stimulating discussions. He would also like to thank H. J. Shaw, B. T. Khuri-Yakub, and H. C. Tuan for very helpful comments on this paper, and H. Gautier, P. Borden, R. Joly, and B. T. Khuri-Yakub for use of some of their unpublished results.

REFERENCES

- [1] A. J. Slobodnik, Jr., "Surface acoustic waves and SAW materials," this issue, pp. 581-595.
- [2] S. Ramo, J. P. Whinnery, and T. Van Duzer, *Fields and Waves in Communication Electronics*. New York: Wiley, 1965.
- [3] B. A. Auld, *Acoustic Fields and Waves in Solids*, Vols. I and II. New York: Wiley-Interscience, 1973.
- [4] R. M. White and I. W. Voltmer, "Ultrasonic surface wave amplification on cadmium sulfide," *Appl. Phys. Lett.*, vol. 8, p. 40, Jan. 15, 1966.
- [5] R. M. White, "Surface elastic wave propagation and amplification," *IEEE Trans. Electron Devices*, vol. ED-14, pp. 181-189, 1967.
- [6] R. M. White, "Surface elastic waves," *Proc. IEEE*, vol. 58, pp. 1238-1276, Aug. 1970.
- [7] J. L. Bleustein, "A new surface wave in piezoelectrical materials," *Appl. Phys. Lett.*, vol. 13, no. 12, pp. 412-413, Dec. 15, 1968.
- [8] Y. V. Gulyaev, "Electroacoustic surface waves in solids," *Sov. Phys.-JETP Lett.*, vol. 9, p. 37, Jan. 1969.
- [9] S. Ludvik and C. F. Quate, "Amplification of a surface shear-wave mode in GaAs," *J. Appl. Phys.*, vol. 43, pp. 3619-3622, Sept. 1972.
- [10] C. Maerfeld, F. Gires, and P. Tournois, "Bleustein-Gulyaev surface wave amplification in CdS," *Appl. Phys. Lett.*, vol. 18, pp. 269-273, Apr. 1, 1971.
- [11] L. A. Coldren and G. S. Kino, "The InSb on a piezoelectric Rayleigh wave amplifier," *IEEE Trans. Electron Devices*, vol. ED-21, pp. 421-427, July 1974.
- [12] R. Hannebrikke and K. A. Ingebrigtsen, "Acoustoelectric amplification of surface waves in structure of cadmium selenide film on lithium niobate," *Electron. Lett.*, vol. 6, no. 16, p. 520, 1970.
- [13] K. M. Lakin and H. J. Shaw, "Surface wave delay line amplifiers," *IEEE Trans. Microwave Theory Tech.*, vol. MTT-17, pp. 912-920, Nov. 1969.
- [14] K. Yoshida and M. Yamashita, "Interaction between surface elastic waves and drifting carriers in layered system," *Japan J. Appl. Phys.*, vol. 7, pp. 1143-1144, Sept. 1968.
- [15] C. Tischer and S. Yando, "Amplification of acoustic surface waves in a coupled semiconductor piezoelectric system," *Appl. Phys. Lett.*, vol. 14, pp. 165, 1967.
- [16] R. W. Ralston, "Stable CW operation of gap coupled silicon on-sapphire to LiNbO₃ acoustoelectric amplifiers," presented at IEEE Ultrasonics Symposium, Los Angeles, CA, 1975, paper V5.
- [17] J. M. Smith, E. Stern, A. Bers, and J. Cafarella, "Surface acoustoelectric convolvers," in *Proc. 1973 IEEE Ultrasonics Symp.*, pp. 142-144.
- [18] R. Adler, "Simple theory of acoustic amplification," *IEEE Trans. Sonics Ultrasonics*, vol. SU-18, p. 116, July 1971.
- [19] G. S. Kino and T. M. Reeder, "A normal mode theory for Rayleigh wave amplifier," *IEEE Trans. Electron Devices*, vol. ED-18, pp. 909-920, Oct. 1971.
- [20] G. S. Kino and L. A. Coldren, "Noise figure calculation for the Rayleigh wave amplifier," *Appl. Phys. Lett.*, vol. 22, pp. 50-52, Jan. 1973.
- [21] A. J. Slobodnik, Jr., E. D. Conway, and R. T. Delmonico, *Micro-wave Acoustics Handbook, vol. 1A, Surface Wave Velocities*, Air Force Cambridge Research Lab., Oct. 1, 1973; Rep. AFRL-TR-73-0597.
- [22] C. S. Tseng and R. M. White, "Piezoelectric and elastic surface waves on basal planes of piezoelectric crystals," *J. Appl. Phys.*, vol. 38, no. 11, pp. 4274-4284, Oct. 1967.
- [23] L. P. Solie, "A new mode of operation for the surface-wave convolver," this issue, pp. 760-763.
- [24] —, "Acoustic surface wave convolver with bidirectional amplification," *Appl. Phys. Lett.*, vol. 25, pp. 7-9, July 1, 1974.
- [25] K. Yamanouchi, K. Abe, and K. Shibayama, "Propagation and amplification of Rayleigh waves and piezoelectric leaky surface waves in structure of InSb thin films on LiNbO₃," in *Proc. 5th Congr. (1973 Int.) Solid State Devices, Suppl. J. Japan Soc. Appl. Phys.*, vol. 43, pp. 203-207, 1974.
- [26] L. A. Coldren and H. J. Shaw, "Surface-wave long delay lines," this issue, pp. 598-609.
- [27] L. A. Coldren and G. S. Kino, "CW monolithic acoustic surface wave amplifier incorporated in a $\Delta V/V$ waveguide," *Appl. Phys. Lett.*, vol. 23, no. 3, pp. 117-118, Aug. 1973.
- [28] L. A. Coldren and R. V. Schmidt, "Acoustic surface wave $\Delta V/V$ waveguides on anisotropic substrates," *Appl. Phys. Lett.*, vol. 22, no. 10, p. 482, May 1973.
- [29] A. J. Hughes, "Elastic surface wave guidance by $\Delta V/V$ effect guidance structures," *J. Appl. Phys.*, vol. 43, no. 6, p. 2569, June 1972.
- [30] P. A. Adams, H. J. Shaw, D. K. Winslow, and L. T. Zitelh, "Waveguides for transverse resolution and surface acoustic wave optical sensors," presented at 1975 IEEE Ultrasonics Symposium, Los Angeles, CA, 1975, paper K5.
- [31] G. S. Kino, S. Ludvik, H. J. Shaw, W. R. Shreve, J. M. White, and D. K. Winslow, "Signal processing by parametric interactions in delay line devices," *IEEE Trans. Sonics Ultrasonics*, vol. SU-20, pp. 162-173, Apr. 1973.
- [32] H. R. Gautier, "Acoustic wave semiconductor convolver applied to electrical and optical signal processing," *Microwave Lab., W. W. Hansen Laboratories of Physics, Stanford Laboratories, Stanford, CA, ML Rep. 2448*, June 1975.
- [33] G. S. Kino and H. Gautier, "Convolution and parametric interaction with semiconductors," *J. Appl. Phys.*, vol. 44, no. 12, 1973.
- [34] P. Defranould and C. Maerfeld, "A SAW planar piezoelectric convolver," this issue, pp. 748-751.
- [35] W. C. Wang, "A novel ultrasonics oscillator and convolution integrator," presented at the Joint Services Technical Advisory Committee Meeting, Polytechnic Institute of Brooklyn, Brooklyn, NY, 1966.
- [36] W. C. Wang and P. Das, "Surface wave convolvers via space charge nonlinearity," in *Proc. 1972 IEEE Ultrasonics Symp.*, pp. 316-321, Oct. 1972.
- [37] O. W. Otto and N. J. Moll, "A lithium niobate silicon surface-wave convolver," *Electron. Lett.*, vol. 8, pp. 600-602, Nov. 30, 1972.
- [38] C. W. Lee and R. L. Gunshor, "Enhancement of nonlinearity in surface acoustic wave propagation from coupling to charge carriers," *Appl. Phys. Lett.*, vol. 20, no. 8, pp. 288-290, Apr. 1972.
- [39] J. H. Cafarella, W. M. Brown, F. Stern, and J. A. Alusow, "Acoustoelectric convolvers for programmable matched filtering in spread spectrum systems," this issue, pp. 756-759.
- [40] A. Bers and J. H. Cafarella, "Surface state memory in surface acoustoelectric correlator," *Appl. Phys. Lett.*, vol. 25, pp. 133-135, 1974.
- [41] H. Hayakawa and G. S. Kino, "Storage of acoustic signals in surface states in silicon," *Appl. Phys. Lett.*, vol. 25, pp. 176-180, 1974.
- [42] C. Maerfeld and P. Defranould, and P. Tournois, "Acoustic storage and processing devices using p-n diodes," *Appl. Phys. Lett.*, vol. 27, pp. 577-578, Dec. 1, 1975.
- [43] C. H. Maerfeld and P. Defranould, "A surface wave memory device using p-n diodes," presented at 1975 IEEE Ultrasonics Symp., Los Angeles, CA, paper V-3, 1975.
- [44] K. A. Ingebrigtsen, "The Schottky diode acoustoelectric memory and correlator—A novel programmable signal processor," this issue, pp. 764-769.

- K. A. Ingebrigtsen, R. A. Cohen, and R. W. Mountain, "A Schottky diode acoustic memory and correlator," *Appl. Phys. Lett.*, vol. 26, pp. 596-598, 1975.
- K. A. Ingebrigtsen, and E. Stern, "Coherent integration and correlation in a modified acoustoelectric memory correlator," *Appl. Phys. Lett.*, vol. 27, pp. 170-172, 1975.
- K. A. Ingebrigtsen, "Simultaneous storage of spatially orthogonal acoustic beams in a Schottky diode memory correlator," to be published in *Electron Lett.*
- [36] G. Kantorowicz, French Patent Applications 73 45234 (1973), and 74.19172 (1974).
- A. Bert, B. Epstein, and G. Kantorowicz, "Signal processing by electron beam interaction with piezoelectric surface waves," *IEEE Trans. Sonics Ultrasonics*, vol. SU-20, pp. 173-181, Apr. 1973.
- [37] E. Stern and R. C. Williamson, "A new adaptive signal processing concept," *Electron. Lett.*, vol. 10, no. 5, pp. 58-59, 1974.
- E. Stern, "Acoustic memories," presented at 1975 IEEE Ultrasonics Symposium, IEEE, Los Angeles, CA, paper V-1, 1975.
- [38] R. L. Melcher and N. S. Shiren, "Parametric electric field echoes in CdS," in *Proc. 1974 IEEE Ultrasonics Symp.*, pp. 558-560, 1974.
- N. S. Shiren and R. L. Melcher, "Acoustically induced charge transfer and storage in piezoelectric semiconductors," in *Proc. 1974 IEEE Ultrasonics Symp.*, pp. 572-578, 1974.
- R. L. Melcher and N. S. Shiren, "Electric field echoes and storage in piezoelectric semiconductors," in *Proc. Symp. Optical and Acoustical Microelectronics* (Polytechnic Institute of New York, April 1, 1974), Brooklyn, NY: Polytechnic Press, pp. 571-573.
- [39] C. Maerfeld and P. Tournois, "Bleustein-Gulyaev surface wave echoes and storage effects in CdS," in *Proc. 1974 IEEE Ultrasonics Symp.*, pp. 220-223, 1974.
- [40] G. Bastide, G. Cambon, and G. Sagnes, "One tenth second storage of surface acoustic signals in CdS," *Appl. Phys. Lett.*, vol. 27, pp. 168-170, Aug. 15, 1975.
- [41] C. E. Cook and M. Bernfeld, *Radar Signals—An Introduction in Theory and Application*, New York: Academic Press, 1967.
- [42] N. J. Moll, O. W. Otto, and C. F. Quate, "Scanning optical patterns with acoustic surface waves," *J. Phys.*, vol. 33, Colloque C-6, Suppl., pp. 231-234, 1972.
- C. F. Quate, "Optical image scanning with acoustic surface waves," *IEEE Trans. Sonics Ultrasonics*, vol. SU-21, pp. 283-288, Oct. 1974.
- [43] S. Takada, H. Hayakawa, and N. Mikoshiba, "Surface-wave-acoustoelectric scanner," in *Proc. 5th Congr. (1973 Int) on Solid State Devices*, pp. 194-198.
- [44] T. W. Grudkowski and C. F. Quate, "Optical image scanning using nonlinear surface wave interaction in GaAs," in *Proc. 1974 IEEE Ultrasonics Symp.*, pp. 749-752, 1974.
- , T. Grudkowski and C. F. Quate, "Acoustic-readout of charge storage on GaAs," *Appl. Phys. Lett.*, vol. 25, pp. 99-101, July 1974.
- [45] M. Luukkala and P. Merilainen, "Image scanning by acousto-electrooptic interaction," *Electron. Lett.*, vol. 10, pp. 80-81, 1974.
- M. Luukkala, P. Merilainen, and K. Saarinen, "Acousto resistive effects in thin film CdSe/LiNbO₃ delay line system," in *Proc. 1974 IEEE Ultrasonics Symp.*, pp. 345-348, 1974.
- [46] G. S. Kino, "Acoustical scanning of optical and acoustic images," in *Proc. Symp. Optical and Acoustical Microelectronics* (Polytechnic Institute of New York, April 1, 1974), Brooklyn, NY: Polytechnic Press, pp. 115-132.
- H. Gautier, G. S. Kino, and H. J. Shaw, "Acoustic transform techniques applied to optical imaging," in *Proc. 1974 IEEE Ultrasonics Symp.*, pp. 99-103, 1974.
- [47] P. G. Kornreich, S. T. Kowel, D. J. Fleming, N. T. Yang, A. Gupta, and O. Lewis, "DEFT: Direct electronic Fourier transforms of optical images," in *Proc. IEEE*, vol. 62, pp. 1072-1087, Aug. 1974.
- U. S. Patent 3 836 712, Sept. 17, 1974.
- S. T. Kowel, P. G. Kornreich, O. Lewis, A. Gupta, and R. Zawada, "Progress on two dimensional electronic Fourier transform (DEFT) devices," in *Proc. 1974 IEEE Ultrasonics Symp.*, pp. 763-767, 1974.
- [48] F. S. Hickernell, "DC triode sputtered zinc oxide surface elastic wave transducers," *J. Appl. Phys.*, vol. 44, pp. 1061-1071, Mar. 1973.
- F. S. Hickernell, "Zinc oxide thin-film surface-wave transducers," this issue, pp. 631-635.
- [49] G. S. Kino and R. S. Wagers, "Theory of interdigital couplers on nonpiezoelectric substrates," *J. Appl. Phys.*, vol. 44, pp. 1480-1488, April 1973.
- R. S. Wagers, G. S. Kino, P. Galle, and D. Winslow, "ZnO acoustic transducers utilizing crystalline gold substrata," in *Proc. 1972 IEEE Ultrasonics Symp.*, 1972.
- [50] B. T. Khuri-Yakub and G. S. Kino, "A monolithic zinc oxide on silicon convolver," *Appl. Phys. Lett.*, vol. 25, pp. 188-190, July 15, 1974.
- B. T. Khuri-Yakub, "The application of zinc oxide on silicon to surface acoustic wave devices," Microwave Laboratory, W. W. Hansen Laboratories of Physics, Stanford University, Stanford, CA, ML Rep. 2509, Dec. 1975.
- [51] L. A. Coldren, "Effect of bias field in a zinc-oxide-on-silicon acoustic convolver," *Appl. Phys. Lett.*, vol. 25, pp. 473-475, Nov. 1974.
- L. Coldren, "Zinc oxide on silicon memory cells scanned by acoustic surface waves," *Appl. Phys. Lett.*, vol. 26, pp. 137-139, Feb. 15, 1975.
- L. Coldren, "Zinc oxide/silicon memory array with optical or electrical writing and acoustic surface wave readout," presented at 1975 IEEE Ultrasonics Symp., Los Angeles, CA, paper K-6, 1975.
- , "Characteristics of zinc-oxide-on-silicon signal processing and storage devices," this issue, pp. 769-771.
- [52] K. L. Davis, "Storage of optical patterns in a zinc-oxide-on-silicon surface wave convolver," *Appl. Phys. Lett.*, vol. 26, pp. 143-145, 1975.
- J. K. Elliott, R. L. Gunshor, R. F. Pierrett, and K. L. Davis, "Zinc oxide-silicon monolithic acoustic surface wave optical image scanner," *Appl. Phys. Lett.*, vol. 27, pp. 179-181, 1975.
- J. K. Elliott, R. L. Gunshor, R. F. Pierrett, and K. L. Davis, "Characteristics of zinc oxide-silicon surface wave convolvers for optical imaging and memory," presented at 1975 IEEE Ultrasonics Symp., Los Angeles, CA, paper K-2, 1975.
- [53] P. Defranould, C. Maerfeld, M. Moulin, and B. Munier, "Comparison of some acoustically scanned optical imaging sensors," presented at 1975 IEEE Ultrasonics Symp., Los Angeles, CA, paper K-7, 1975.
- [54] O. W. Otto, "Theory for nonlinear coupling between a piezoelectric surface and an adjacent semiconductor," *J. Appl. Phys.*, vol. 45, pp. 4373-4383, 1974.
- [55] S. M. Sze, *Physics of Semiconductor Devices*. New York: Wiley Interscience, 1969.
- [56] E. H. Nicollian and A. Goetzberger, "The Si-SiO₂ interface—electrical properties as determined by the metal-insulator silicon conductance technique," *Bell Syst. Tech. J.*, vol. XLVI, no. 6, pp. 1055-1133, 1967.
- [57] B. E. Deal, E. L. MacKenna, and P. L. Castro, "Characteristics of fast surface states associated with SiO₂-Si and Si₃N₄-SiO₂ structures," *J. Electrochem. Soc.*, vol. 116, pp. 997-1005, 1969.
- [58] F. Das, M. E. Malamed, and R. T. Webster, "Determination of semiconductor surface properties using surface acoustic waves," *Appl. Phys. Lett.*, vol. 27, pp. 120-122, Aug. 1975.
- [59] A. Bers, J. H. Cafarella, and B. T. Burke, "Surface mobility measurements using surface acoustic waves," *Appl. Phys. Lett.*, vol. 22, pp. 399-401, Apr. 1973.
- [60] Y. V. Gulyaev, A. Y. Karabanov, A. M. Kmita, A. V. Medved, and S. S. Tursunov, "Theory of electronic absorption and amplification of surface acoustic waves in piezoelectric crystals," *Sov. Phys.—Solid State*, vol. 12, pp. 2085-2090, 1971.
- [61] T. Shiosaki, T. Kuroda, and A. Kawabata, "Application of surface waves to the study of semiconductor surface state using the separated-medium acoustoelectric effect," *Appl. Phys. Lett.*, vol. 26, no. 7, pp. 360-362, 1975.
- [62] R. Joly, Private commun.
- [63] T. M. Reeder and M. Gilden, "Convolution and correlation by nonlinear interaction in a diode-coupled tapped delay line," *Appl. Phys. Lett.*, vol. 22, no. 1, pp. 8-10, Jan. 1973.
- T. M. Reeder and T. W. Grudkowski, "Real time Fourier transform experiments using a 32 tap diode-convolver module," presented at 1975 IEEE Ultrasonics Symp., Los Angeles, CA, paper F-11, 1975.
- [64] D. P. Morgan, "Signal processing using the SAW diode convolver," in *Proc. 1973 IEEE Ultrasonics Symp.*, pp. 138-141, 1973.
- [65] O. Menager and B. Desormiere, "Surface acoustic wave tapped correlator using time integration," *Appl. Phys. Lett.*, vol. 27, pp. 1-2, July 1975.
- [66] O. W. Otto, "Equivalence of the electronically focused acoustic imaging device to a diode convolver," *Appl. Phys. Lett.*, vol. 25, pp. 267-268, Sept. 1974.
- [67] J. F. Havlice, G. S. Kino and C. F. Quate, "Electronically focused imaging device," *Appl. Phys. Lett.*, vol. 23, pp. 581-583, Dec. 1973.
- J. Fraser, J. Havlice, G. S. Kino, W. Leung, H. J. Shaw, K. Ioda, T. Waugh, D. Winslow, and L. I. Zetelli, "A two dimensional electronically focused imaging system," in *Proc. 1974 IEEE Ultrasonics Symp.*, pp. 19-23, 1974.
- G. S. Kino, C. DeSilva, J. Fraser, and T. Waugh, "New acoustic imaging system for non destructive testing," presented at 1975 IEEE Ultrasonics Symp., Los Angeles, CA, paper N-1, 1975.
- [68] G. S. Kino and W. R. Shreve, "Theory of strip coupled convolver," *J. Appl. Phys.*, vol. 44, pp. 3960-3968, Sept. 1973.

- [69] L. R. Adkins, "Strip coupled AlN and Si sapphire convolvers," in *Proc. 1973 IEEE Ultrasonics Symp.*, pp. 148-151, 1973.
- [70] R. Adler, "Surface wave amplifier with improved geometry," *Electron. Lett.*, vol. 8, pp. 65-66, 1972.
- [71] C. Maerfeld and P. T. Tournois, "An acoustic multistrip amplifier," in *Proc. 1972 IEEE Ultrasonics Symp.*, pp. 171-176, 1972.
- [72] C. Maerfeld and P. Tournois, "Perturbation theory for multistrip acoustoelectric surface wave amplifier," *Electron. Lett.*, vol. 9, pp. 113-114, Mar. 1973.
- [73] G. S. Kino and W. R. Shreve, "A strip coupled Rayleigh wave amplifier," in *Proc. IEEE Ultrasonics Symp.*, pp. 177-180, 1972.
- [74] R. Bløtekjaer, K. A. Ingebrigtsen, and H. Skeie, "Acoustic surface waves in piezoelectric materials with periodic metal strips on the surface," *IEEE Trans. Electron Devices*, vol. ED-20, pp. 1139-1146, Dec. 1973.
- [75] D. P. Morgan, J. M. Hannah, and J. H. Collins, "Spread-spectrum synchronizer using a SAW convolver and recirculation loop," this issue, pp. 751-753.



Study of Acoustic Wave Resonance in Piezoelectric PVF₂ Film

LE N. BUI, HERBERT J. SHAW, FELLOW, IEEE, AND LOUIS T. ZITELLI, MEMBER, IEEE

Abstract—Measurements have been made of the acoustic loss factor and piezoelectric coupling coefficient of poled polyvinylidene fluoride (PVF₂) plastic polymer films which are of interest for high-frequency ultrasonic applications. A theory for piezoelectric resonance in unsupported films was developed for interpretation of the measurements. Unloaded acoustic Q of approximately 14 has been observed at frequencies of 41 and 21.5 MHz for films of 25 and 50 μ thickness, respectively.

I. INTRODUCTION

IT HAS BEEN shown by a number of authors [1], [2] that polyvinylidene fluoride (PVF₂)¹ polymer plastic films can be rendered relatively strongly piezoelectric by a simple poling process, opening the way to new possibilities for the design of inexpensive ultrasonic transducers. The piezoelectric coupling constant and the acoustic loss factor of PVF₂ were determined by measurements of the components of the electrical impedance about acoustic resonance. Film samples were approximately 25 μ and 50 μ thick and had evaporated conducting electrodes on the film faces. The thickness dilatational vibration mode was employed, which is of interest for high-frequency transducers.

We have found that the properties of PVF₂ lead to piezoelectric resonance curves having different characteristics than those of the more familiar ceramic materials such as PZT. As a result, standard methods for measuring acoustic loss factor Q for the latter materials, involving the simple measurement of series and parallel resonances, are not applicable to PVF₂. We

have developed the piezoelectric resonator theory appropriate for the ranges of piezoelectric coupling factor k_t^2 and acoustic Q of PVF₂, and have used a comparison of theoretical and experimental response curves in obtaining quantitative measurements of these qualities.

II. THEORY

The theory of thin film microwave acoustic transducers for volume wave excitation has been covered extensively in the literature [3], [4]. However, in those treatments, the acoustic loss in the transducer is assumed small enough to be neglected, and the transducer element is considered in conjunction with an acoustic substrate into which acoustic energy generated by the transducer is radiated. Here, we formulate a one-dimensional model of a transducer including internal acoustic loss. We work with acoustically unloaded transducers, without a substrate. Using this model, quantitative predictions can be made for Q and k_t^2 which can be checked experimentally through simple impedance measurements.

We consider a piezoelectric resonator configuration consisting of a plate or film of piezoelectric material with conducting electrodes on both faces. It can be made to vibrate in one or more acoustic modes by application of a harmonic voltage across the two electrodes. The lateral dimensions of the resonator are assumed to be large compared to both its thickness and the acoustic wavelength. The sample orientation is chosen such that the resonator is excited in the thickness vibrational mode only. We assume that the electrode layers are acoustically thin, so as not to load the transducer.

Using the piezoelectric equations, equations of motion, electrical circuit equations, and boundary conditions, we derive the plane wave piezoelectric impedance matrix for the resonator. Internal acoustic loss is accounted for by introducing, in the expression for elastic stress, a term proportion to jS/Q .

Manuscript received August 16, 1976, revised December 20, 1976. This work was supported by the Office of Naval Research under Contract N00014-75-C-0632.

The authors are with the W. W. Hansen Laboratories of Physics, Stanford University, Stanford, CA 94305.

¹Sometimes referred to in the literature as (PVDI)

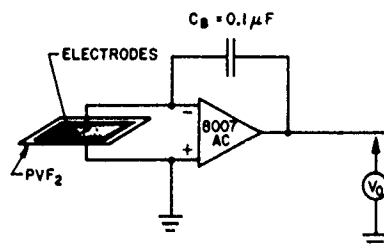


Fig. 1. Charge integration technique used to detect piezoelectricity in poled PVF₂ films.

where S is the strain and Q is the acoustic Q of the piezoelectric material defined as the ratio of acoustic energy stored to the acoustic energy lost per radian. We then calculate the electrical input impedance of the resonator, expressing the result in terms of an equivalent electrical series circuit. Further details on the derivation are shown in the Appendix.

The electrical impedance curves for the resonator are strong functions of Q in the vicinity of resonance, and curve fitting of experimental impedance values with theoretical curves allows determination of Q and the piezoelectric coupling constant k_t^2 for the piezoelectric material, which is defined as the ratio of electrical energy at the output to the total input mechanical energy.

III. EXPERIMENT

PVF₂ films exhibit relatively strong piezoelectricity when stretched, polarized under a relatively high dc field E_p at a moderate temperature T_p , and then cooled to room temperature with the dc field on. The piezoelectricity obtained depends on E_p , T_p , and the poling time. The origin of the piezoelectricity is not yet fully understood, although it is thought that the poling process increases true and/or polarization charges in the film through three kinds of process, namely, injection of homocharge from the electrode, dipole orientation in the film, and true charge separation in the film.

For the present experiments, we prepared samples by first evaporating chrome-gold electrodes of ~ 1000 Å thickness on both surfaces of PVF₂ films. The masses of the Cr-Au electrodes are 4% and 8% of the masses of the polymer films with thicknesses of 50 μ and 25 μ , respectively. The effects of these mass loadings are to decrease the resonant frequencies slightly; however, in the quantities of primary interest to us, k_t^2 and Q , these effects are small compared to the accuracy of measurement. The films were used as received from the manufacturer [5], and were not subjected to additional stretching. They were then poled using a dc field $E_p > 500$ kV/cm for 2 to 3 h in an oil bath at elevated temperature $T > 80^\circ\text{C}$.

After poling, we use the integrating circuit shown in Fig. 1 to test for the direct piezoelectric effect in the PVF₂ film. A stress applied to the film gives rise to an open circuit voltage across the electrodes on the film. Charge developed on the electrodes is integrated by the circuit shown and displayed as a dc output voltage. While the device of Fig. 1 could be used to measure piezoelectric constants quantitatively, we have not carried out the necessary calibration procedures for using it in this way. However, we find it useful as a qualitative check on

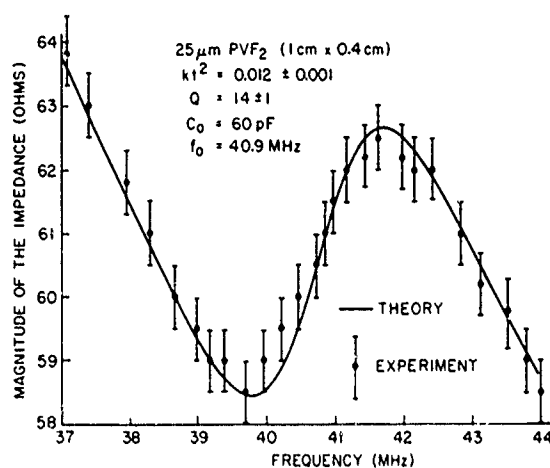


Fig. 2. Acoustically generated absolute electrical impedance of unloaded PVF₂ resonator ($\approx 25 \mu\text{m}$).

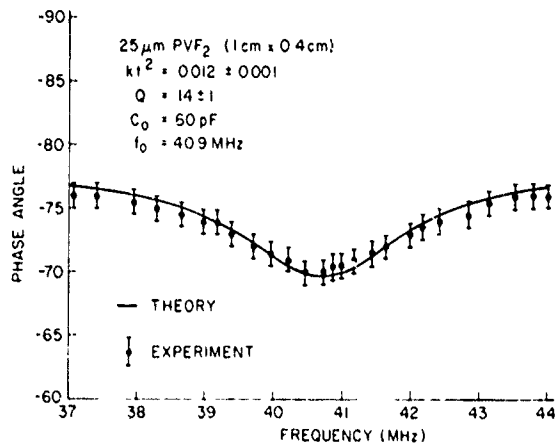


Fig. 3. Phase of electrical impedance of unloaded PVF₂ resonator ($\approx 25 \mu\text{m}$).

the poling process. In all cases, the quantitative evaluation of k_t^2 is carried out by means of electrical impedance measurements, as described below.

Figs. 2-5 are examples of matched theoretical and experimental curves of absolute value and phase of the electrical input impedance as functions of frequency for poled films of 25 μ and 50 μ thickness.

It is important that the parameters of the electrical circuit, namely, the lead inductance and the conduction loss of the electrodes, be measured carefully and properly accounted for before any comparison of theory and experiment is made. Contact impedance may be larger than the transducer loss impedance for resonators of moderate coupling constant. Values of Q and k_t^2 obtained from these curves are shown in Table I.

Since both Q and k_t^2 are unknown quantities to start with, the direct curve fitting of experimental impedance values with theoretical curves requires that one deals simultaneously with two variables. This lengthy process of quantitatively determining Q and k_t^2 is greatly facilitated if we use an approximation which allows us to obtain one unknown independently of the other. Our one-dimensional model of a lossy resonator shows that near resonance the ratio of the acoustic reactance X_a to

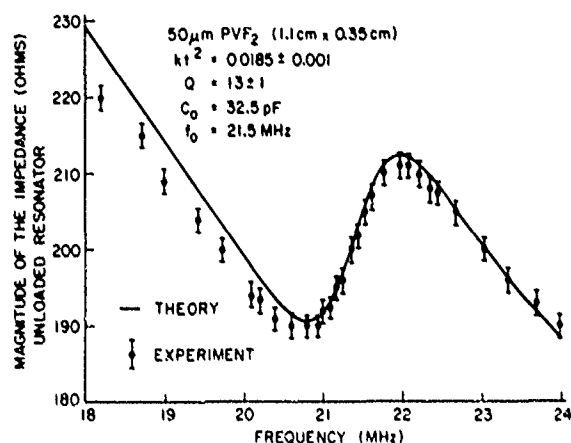


Fig. 4. Acoustically generated absolute electrical impedance of unloaded PVF₂ resonator ($\approx 50 \mu\text{m}$).

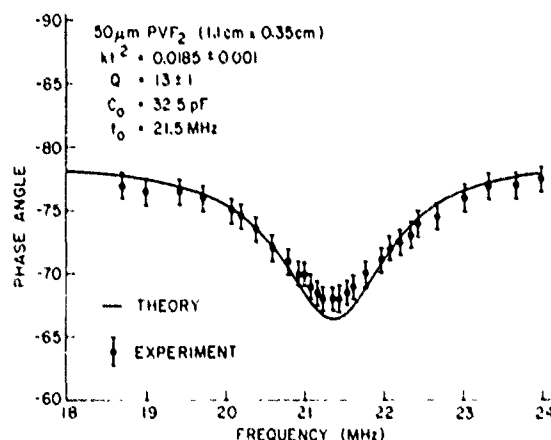


Fig. 5. Phase angle of electrical impedance of unloaded PVF₂ resonator ($\approx 50 \mu\text{m}$).

the acoustic resistance R_a plotted as a function of frequency normalized to the thickness resonance frequency is a straight line. The acoustic Q can be readily determined from the slope of the straight line with Q being equal to half the slope. Figs. 6 and 7 show that this method predicts a Q of 13.8, whereas all the theoretical curves in Figs. 2-5 were computed with a Q of 14 for $25 \mu\text{m}$ film and 13 for $50 \mu\text{m}$. The discrepancy between the two methods is less than six percent.

IV. DISCUSSION

An absolute-admittance method, sometimes called the two-frequency method, has been widely used for determining the properties of piezoelectric materials. This method uses a parallel equivalent circuit for a piezoelectric resonator described by Van Dyke [6] which consists of the series connection of an inductance L , a capacitance C , and a resistance R , in parallel with a second capacitance C_0 . The series resonance of the resonator, which corresponds to maximum admittance, is modeled by the resonance of the LC circuit, while the parallel resonance, which corresponds to minimum admittance, is modeled by the LC_0 circuit. The popularity of the method stems from its simplicity, where a complete evaluation of the equivalent

TABLE I
MEASURED ACOUSTIC PROPERTIES OF PVF₂ FILM

Film thickness	$\approx 25 \mu\text{m}$	$\approx 50 \mu\text{m}$
Poling conditions	1000 volts, 85°C , 18 hours	1000 volts, 115°C , 2 hours
Thickness resonant frequency	$\approx 21 \text{ MHz}$	$\approx 21.5 \text{ MHz}$
Acoustic impedance	$\approx 1.5 \times 10^6 \text{ kg s}^{-2} \text{ m}^{-2}$	$\approx 1.5 \times 10^6 \text{ kg s}^{-2} \text{ m}^{-2}$
Electromechanical coupling constant k_t	$11\% \pm 0.5\%$	$13.5\% \pm 0.5\%$
Unloaded Q	13 ± 1	13 ± 1
Inferred attenuation coefficient α for longitudinal acoustic plane waves in PVF ₂	$4^{\circ} \text{ nepers cm} \pm 5$	$21^{\circ} \text{ nepers cm} \pm 2$

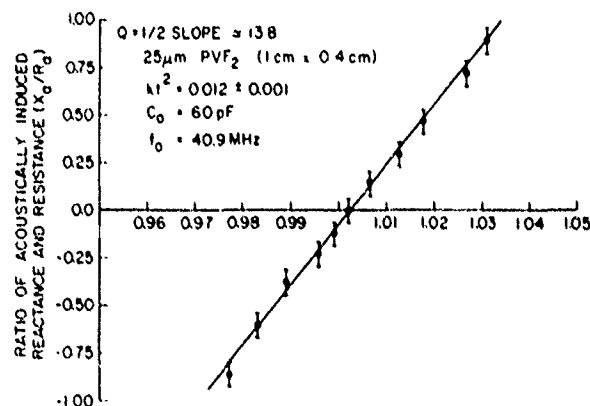


Fig. 6. Determination of acoustic Q_a independently of k_t^2 .

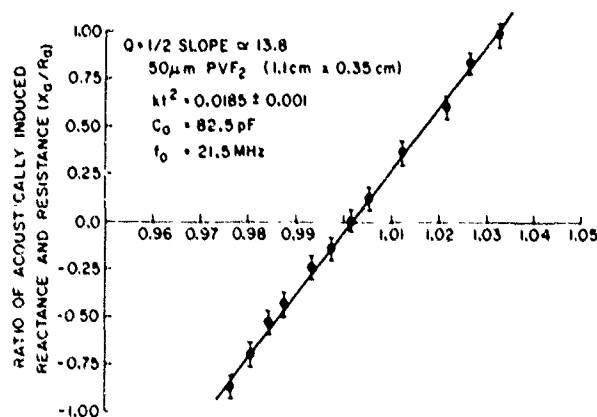


Fig. 7. Determination of acoustic Q_a independently of k_t^2 .

lent circuit constants requires only the measurement of the maximum absolute admittance, the minimum absolute admittance, the frequency of maximum absolute admittance, and the frequency of minimum absolute admittance. This method is highly accurate for resonators of high Q ($Q > 1000$) and relatively high Qk_t^2 product ($50 > Qk_t^2 > 10$) such as quartz. Martin [7] has extended the range of this method to include resonators of moderately low Q ($Q > 100$) and moderately low Qk_t^2 product, ($5 > Qk_t^2 > 1$) such as barium titanate, by deriving a new set of equations that improve the accuracy of determining resonator parameters from the same four mea-

TABLE II

Piezoelectric Materials	Q	Qk_t^2	Percent Error			
			Original two-frequency method		Modified two-frequency method [†]	
			k_t^2	Q	k_t^2	Q
Quartz	>1,000	>10	.0	.5	<.4	<.2
BaTiO ₃ ⁷	1.7	~1	15.0	-20	~2	~2
PZT-5A	6.5	>10	.1	-17	2	-1.
PVF ₂ (50 μ)	14	~0.5	65.0	-51	-21	~6
PVF ₂ (10 μ)	15	~1.1	15.0	-51	-51	9.

sured quantities. However, PVF₂ has a lower Qk_t^2 product ($Qk_t^2 < 0.25$), and for this case we have found that the above methods result in substantial errors in determining k_t^2 and Q.

When first working with PVF₂, with its Q unknown, we attempted to use the two-frequency methods for initial estimates and encountered inconsistencies. After applying the curve fitting process described above, it became apparent that the Qk_t^2 range for PVF₂ lies outside of the applicable ranges of the two-frequency methods. The quantitative errors which result from applying the two-frequency method to materials of low Qk_t^2 product are shown in Table II.

Since completing our work, we find that Ohgashi [8] has concurrently and independently made accurate measurements of Q and k_t^2 for PVF₂. He has used the parallel equivalent circuit of the resonator [6], but in contrast with the two-frequency method, he carried out the measurement over a large frequency range. He then varied the parameters R, L, C, and C₀ of the equivalent circuit to obtain the best theoretical fit of the admittance curve to the experimental data points. The Q and k_t^2 were then obtained from the parameters of the equivalent circuit.

Comparing the parallel equivalent circuit with our series circuit (described in the Appendix), they are found to give the same theoretical fit to the experimental PVF₂ curves. However, we believed the series model to be more convenient to use because it offers the possibility of determining Q independently of k_t^2 , which is of value if these two quantities happen to be unknown, as is usually the case with newly discovered materials.

Our measured values for the coupling coefficient k_t are less than the largest value reported [8] for PVF₂, which is 20 percent. We believe this difference results from using lower poling voltage and low poling temperature. This is consistent with the fact that our k_t for 50 μ m film is slightly greater than that obtained by Ohgashi, where our poling voltage was slightly higher.

We have consistently obtained larger values of Q than those obtained by Ohgashi (14 as compared to 9). These values of Q are constant for different samples and different thicknesses

One explanation is concerned with possible structural differences in the films. We used oriented films directly as received from Kureha Co., while Ohgashi started with unoriented sheets and uniaxially stretched them, and the stretching conditions may have been different.

APPENDIX

ANALYSIS OF AN UNLOADED AND LOSSY PIEZOELECTRIC RESONATOR

We give here a derivation of the series equivalent circuit for a lossy piezoelectric free resonator. We assume that the lateral dimensions of the resonator are large compared to its thickness so that a one-dimensional analysis can be made, and that the electrode layers are acoustically thin, so as not to load the resonator. We show in Fig. 8 the one-dimensional resonator with its associated electrical and acoustic variables upon which our derivation of the electrical series equivalent circuit are based [9]. The equations necessary for the derivation of the equivalent circuit are given below.

Piezoelectric Equations

$$T = e^F S - eE \quad (1)$$

$$D = \epsilon^S E + eS \quad (2)$$

Boundary Conditions

$$F_1 = -AT_1(0) \quad (3)$$

$$F_2 = -AT_2(l) \quad (4)$$

$$v_1 = v(0) \quad (5)$$

$$v_2 = v(l) \quad (6)$$

Acoustic Equations

$$\frac{dT}{dz} = \rho \omega^2 v \quad (7)$$

$$\frac{dv}{dz} = \frac{1}{\rho \omega S} \quad (8)$$

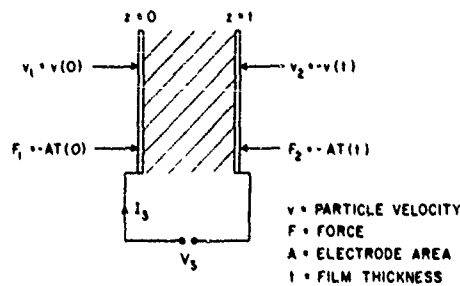


Fig. 8. Electrical and acoustic terminal variables of thin transducer.

The total current through the transducer is

$$I_3 = j\omega AD. \quad (9)$$

Since current is conserved, D must be uniform with z ($\partial D/\partial z = 0$). The voltage across the transducer is

$$V_3 = \int_0^l E dz. \quad (10)$$

We derive the plane wave equation for the lossy resonator by modifying one of the two standard linear piezoelectric equations that relate stress T , displacement current D , strain S , and electric field E . To account for internal acoustic losses, a new term is added to the stress equation (1), which then becomes

$$T = c^E S + j\omega\eta S - eE \quad (11)$$

where $j\omega\eta$ represents acoustic damping [9]. From (2) we express E in terms of D and S . We substitute that result into (11), which then becomes

$$T = (c^D + j\omega\eta)S - \frac{eD}{\epsilon^S} \quad (12)$$

where

$$c^D = c^E \left(1 + \frac{e^2}{c^E \epsilon^S} \right) \quad (13)$$

where c^D is the stiffened elastic constant and e is the piezoelectric coefficient. Next using the two acoustic equations, (7) and (8), and (12), the following wave equation for the medium is obtained.

$$\frac{\partial^2 v}{\partial z^2} + \frac{\omega^2 \rho}{c^D + j\omega\eta} v = 0 \quad (14)$$

where ρ is the density and v is the particle velocity. The above equation has a complex wave propagation constant $\gamma = \alpha + j\beta$ as expected for plane wave propagation in a lossy medium. Solutions to the wave equation are of the form

$$v = A \cos \gamma z + B \sin \gamma z \quad (15)$$

where

$$\gamma^2 = (\beta - j\alpha)^2 = \frac{\omega^2 \rho}{c^D + j\omega\eta} \quad (16)$$

Assuming small acoustic losses

$$\left(\frac{\omega^2 \eta^2}{c^D} \ll 1 \right)$$

we find

$$\alpha = \beta_a \frac{\omega\eta}{2c} \quad (17)$$

$$\beta \approx \beta_a = \omega \left(\frac{\rho}{c^D} \right)^{1/2} \quad (18)$$

where β_a is the wavenumber in the lossless case. The acoustic Q of the lossy resonator can be conveniently expressed in terms of the attenuation constant α and the propagation constant β as

$$Q = \frac{\beta}{2\alpha} = \frac{c^D}{\omega\eta}. \quad (19)$$

We solve the wave equation in terms of the particle velocities v_1 and v_2 using the boundary conditions of continuity of velocity (5) and (6) and obtain

$$v = \frac{v_1 \sin \gamma(t-z) - v_2 \sin \gamma z}{\sin \gamma t}. \quad (20)$$

We substitute (20) back into (8), (12), and the two boundary conditions of continuity of force (3), (4). One can characterize the acoustic resonator as a three-port network by expressing the two acoustic port variables F_1 , F_2 , and the electrical voltage V_3 in terms of v_1 , v_2 , and I_3 .

The electroacoustic properties of the piezoelectric transducer can then be described by the following 3×3 matrix:

$$\begin{bmatrix} F_1 \\ F_2 \\ V_3 \end{bmatrix} = -j \begin{bmatrix} B \coth \gamma t & B \csc h \gamma t & \frac{h}{\omega} \\ B \csc h \gamma t & B \coth \gamma t & \frac{h}{\omega} \\ \frac{h}{\omega} & \frac{h}{\omega} & \frac{1}{\omega C_0} \end{bmatrix} \begin{bmatrix} v_1 \\ v_2 \\ I_3 \end{bmatrix} \quad (21)$$

where $B = AZ_0(1 + j[1/(2Q)])$, $h = e/\epsilon^S$ is the piezoelectric constant, $C_0 = \epsilon^S A/t$ is the clamped capacitance of the piezoelectric transducer, and $Z_0 = (c^D \beta)/\omega$ is the acoustic impedance. The impedance matrix of (21) reduces to the more familiar lossless case if we set α equal to zero. The above impedance matrix enables us to determine the electrical equivalent circuit of any lossy transducer by solving for V_3/I_3 with the appropriate acoustic terminations F_1 and F_2 . If the transducer is loaded on both sides, then F_1 and F_2 take on finite values that are proportional to the acoustic impedances of their respective loads [3]. In our case where we are working with unloaded transducers, we set $F_1 = F_2 = 0$ and solve for the electrical impedance $Z_3 = V_3/I_3$. We express $\coth \gamma t$ and $\csc h \gamma t$ in terms of $\cosh \alpha t$, $\cos \beta t$, $\sinh \alpha t$ and $\cos \beta t$, with α related to β and Q through (19). We expand $\cosh \alpha t$ and $\sinh \alpha t$ to the first order of αt . The results show that the electrical behavior of a free piezoelectric resonator can be characterized by a circuit consisting of the total electrode capacitance C_0 in series with an acoustic loss resistance R_a and an

acoustic reactance X_a . The expressions for R_a and X_a are

$$R_a = \hat{R}_a \left(\frac{\omega_0}{\omega} \right) H_e(\theta) \quad (22)$$

$$X_a = \hat{R}_a \left(\frac{\omega_0}{\omega} \right)^2 H_o(\theta) \quad (23)$$

$$\hat{R}_a = \frac{8k_t^2}{\omega_0 C_0} \frac{Q}{\pi^2} \quad (24)$$

$$H_e(\theta) = \frac{\pi(\theta + \sin \theta)}{16Q^2 \left(\left(1 + \left(\frac{\theta}{4Q} \right)^2 \right) \cos^2 \frac{\theta}{2} + \left(\frac{\theta}{4Q} \right)^2 \sin^2 \frac{\theta}{2} \right)} \quad (25)$$

$$H_o(\theta) = \frac{\pi \left(\sin \theta - \frac{\theta}{4Q^2} \right)}{8Q \left(\left(1 + \left(\frac{\theta}{4Q} \right)^2 \right) \cos^2 \frac{\theta}{2} + \left(\frac{\theta}{4Q} \right)^2 \sin^2 \frac{\theta}{2} \right)} \quad (26)$$

where $k_t^2 = (e_{33}^2)/(c^D \epsilon_{33})$, $\theta = \pi(\omega/\omega_0)$ is the normalized frequency, and $\omega_0 = (\pi/r)(c^D/\rho)^{1/2}$ is the half-wave resonant frequency. Both R_a and X_a are functions of frequency and of the acoustic Q of the piezoelectric material. R_a attains its maximum value near the center frequency f_0 , while X_a becomes negative for a frequency greater than f_0 and positive for a frequency less than f_0 .

All of our impedance measurements were done at room temperature using a Hewlett-Packard model 4815-A RF vector

impedance meter. The total electrode capacitance C_0 was determined from measurements at frequencies far from resonance. Next, the coupling constant k_t^2 and the quality factor Q were used as adjustable parameters to get the best theoretical curve fit to the experimental data points. This process of choosing two variables at the same time is tedious. Examination of the behavior of the resonator near resonance offers us a new method for determining Q independently of k_t^2 . In (26), $\theta/(4Q^2)$ is negligible with respect to $\sin \theta$. We take the ratio of X_a to R_a and expand it around resonance:

$$\frac{X_a}{R_a} = 2Q \frac{\sin \theta}{\theta + \sin \theta} \cong -2Q\delta \quad (27)$$

where $\theta = \pi(1 + \delta)$. Thus Q can be conveniently determined from the slope of the ratio of X_a to R_a near resonance.

REFERENCES

- [1] H. Kawai, *Japan J. Appl. Phys.*, **8**, 975 (1969).
- [2] N. Murayama, K. Nakamura, H. Obara, and M. Segawa, *Ultrasonics*, **14**, 1, 15 (1976).
- [3] T. M. Reeder and D. K. Winslow, *IEEE Trans. MTT-17*, **11**, 927 (1969).
- [4] D. A. Berlincourt, D. R. Curran, and H. Jaffe, *Physical Acoustics*, W. P. Mason, Ed., Vol. 1A, Chapter 3, Academic Press, New York (1964).
- [5] Kreh Corporation of America, 420 Lexington Ave., New York, NY 10017.
- [6] K. S. Van Dyke, *Phys. Rev.*, **25**, 895 (1925).
- [7] G. E. Martin, *J. Acoust. Soc. Am.*, **26**, 3, 413 (1954).
- [8] H. Ohgashi, *J. Appl. Phys.*, **47**, 3, 949 (1976).
- [9] B. A. Auld, *Acoustic Fields and Waves in Solids*, Volume 1, Chapter 3, Wiley-Interscience, New York, 1973.

EXPERIMENTAL BROADBAND ULTRASONIC TRANSDUCERS USING PVF₂ PIEZOELECTRIC FILM

Indexing terms: Piezoelectric transducers, Thin-film devices

Broadband ultrasonic transducers using PVF₂ piezoelectric plastics films, combining efficient transduction with extremely wide and uniform passbands, have been fabricated using very simple procedures without any critical tolerances. Frequency spectra of impulsed transducers using films of 25 and 50 μ m thickness, centred at 10 and 5 MHz, respectively, are shown.

Introduction: Broadband ultrasonic transducers are important for a variety of purposes, including signal processing where large bandwidth is needed for high data rates, time-domain spectrometry where large bandwidth is needed to handle short pulses, and ultrasonic imaging where operation over a range of frequencies is necessary for obtaining optimum response from a variety of objects. We find that very broadband transducers can be easily constructed using poled PVF₂ films,^{1,2} using procedures which are much simpler than those involved in the construction of standard types using p.z.t. ceramic elements, and having bandpass characteristics which are broader and more uniform than commercial p.z.t. transducers.

Description of experimental transducers. The new transducers were formed by epoxy bonding a small piece of poled PVF₂ film to a brass rod. A sketch of a typical unit is shown in Fig. 1a. The brass rod serves as an acoustic backing, which acoustically loads the back side of the PVF₂ film, as well as providing mechanical support for the film. The brass rods for the present transducers are 25.4 mm in diameter, of arbitrary length and serve as a convenient handle for holding and positioning the transducer. Available transducer thicknesses of both 25 and 50 μ m were used to radiate rectangular acoustic beams of the approximate dimensions 6.4 \times 19.2 mm. The choice of the rectangular shape in this case was arbitrary and a change to any other shape would represent only a trivial modification.

Measured transducer characteristics. Experimental models of the above transducers have been operated in water, in both reflection and transmission modes, to determine bandwidth and insertion loss. In this operation, the device of Fig. 1a is simply submerged directly in the water tank, without any covering over the PVF₂ surface. Passband characteristics were determined by impulsing the transmitting transducer, and observing the output of the receiving transducer on a spectrum analyser. In the transmission mode, separate transducers were used for transmitting and receiving with sufficiently close spacing (25.4 mm) to avoid effects of diffraction and water attenuation. In the reflection mode, a single transducer performed as both transmitter and receiver, with the acoustic beam reflected from a glass surface located 12.7 mm from the transducer.

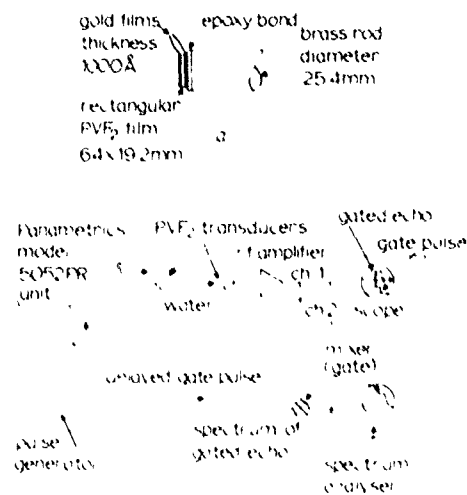


Fig. 1 System for spectrum analysis of echoes in water
a Schematic of PVF₂ transducer
b Block diagram of system

A block diagram of the experimental setup is shown in Fig. 1b for transmission-mode measurements. The system uses a standard Panametrics Model 5052 PR unit which delivers a very short electrical pulse to energise the transmitting transducer. The spectrum of the excitation pulse was observed on the spectrum analyser and found to be essentially flat between d.c. and 20 MHz. An electronic gate selects the desired echo from the output of the receiving transducer, separating it from the direct electromagnetic feedthrough pulse and other pulses in the multiply reflected acoustic pulse train. The selected echo is amplified and, along with the gate pulse, displayed on a 2-channel oscilloscope, and the spectrum of the echo is displayed on a spectrum analyser.

The spectra of the first echo for various transducers are shown in Fig. 2. The spectrum of a commercial 14 MHz transducer (Fig. 2a) is shown for purposes of comparison. The response of the 25 μ m PVF₂ transducers (Fig. 2b) is essentially flat from zero frequency to 20 MHz. The response of the 50 μ m PVF₂ transducers (Fig. 2c) is flat within 10 dB from 1 to 10 MHz. These are 'round-trip' spectra, i.e. the spectra of the pulses after experiencing two transductions. The round-trip insertion loss has the same order of magnitude as the commercial p.z.t. unit of Fig. 2a.

The lateral dimensions of the PVF₂ films are large compared with their thickness, so that the films vibrate in the thickness extensional mode. However, the observed thickness resonance frequencies correspond approximately to quarter-wave film thickness, rather than halfwave thickness as for unloaded PVF₂ resonators,^{3,4} because the impedance of the backing material is greater than that of the transducer. The ratio of the acoustic impedance of the brass backing to that of PVF₂ is approximately 11, and a ratio greater than about 1.4 is sufficient to shift the resonance frequency down to the vicinity of the quarter-wave frequency.⁵ The quarter-wave frequencies cannot be obtained accurately from the spectra of Fig. 2 because the thickness of the adhesive bond is not accurately known. However, it is comparable to that of the PVF₂ film, and, in any event, its effect would be to shift the resonance frequency further downward, to less than half the frequencies of unloaded films, and this is consistent with the results of Fig. 2.

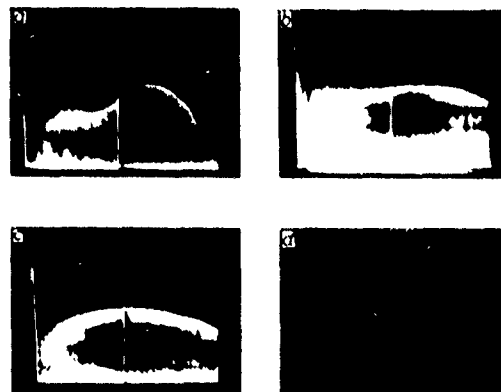


Fig. 2 Measured transducer characteristics

a Spectrum of p.z.t. transducer
b Spectrum of 25 μ m PVF₂ transducer
c Spectrum of 50 μ m PVF₂ transducer
d Impulse response of 50 μ m PVF₂ transducer

Analysis of the transient response of a transducer may be based on the assumption that, if an electrical impulse is applied, four ultrasonic pulses are generated, two at each face.⁶ For each of these two pairs of stress waves, one of the waves travels into the transducer and the other travels into either the water loading or the backing medium (Fig. 3). The resulting two pulses within the transducer travel backwards and forwards and are reflected and transmitted at the transducer faces. The degree of reflection depends on the characteristic impedances of the transducer, the loading and the backing medium. With our transducer configuration of brass PVF₂ water, the pulse generated at the PVF₂ water interface and travelling into the transducer is approximately ten times larger in magnitude than the corresponding pulse generated at the brass PVF₂ interface (because of the high

impedance of brass relative to PVF₂). Thus the output stress consists essentially of two stress waves, one launched from the front face directly into the water and the other launched from the front face into the backing and reflected from the back face into the water. The latter wave suffers little reflection at the PVF₂-water interface, because the acoustic impedances of PVF₂ and water are relatively close. The two stress waves are separated by the round-trip time in the transducer. This pair of stress waves is detected by a second transducer of the same thickness as the transmitting transducer as a bipolar pulse (Fig. 2d). The fact that the detected pulse is approximately bipolar indicates that acoustic energy generated within the PVF₂ transducer is efficiently coupled to water. Had it been otherwise, the detected pulse would have many cycles, owing to multiple reflections inside the transducer.

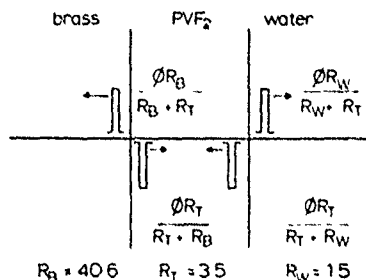


Fig. 3 Physical interpretation of response of piezoelectric transducer to electrical-impulse input

ϕ = stress/unit input voltage
 R = relative characteristic acoustic impedance

This is consistent with other measurements^{3,4} made on PVF₂, which show that the acoustic impedance of PVF₂ is close to that of water, as shown in Fig. 3. This is important in providing the clean pulse shown in Fig. 2d, in contributing to the very broad bandwidth of the transducer and in compensating for the lower piezoelectric coupling coefficient of PVF₂ compared with that of p.z.t., thus maintaining high transducer efficiency.

Acknowledgment: This work was supported by the US Office of Naval Research under Contract N00014-75-C-0632.

L. BUI
H. J. SHAW
L. T. ZITELLI

29th June 1976

W. W. Hansen Laboratories of Physics
Stanford University
Stanford, Calif. 94305, USA

References

- 1 KAWAI, H.: *Japan. J. Appl. Phys.*, 1965, 8, p. 975
- 2 MURAYAMA, N., NAKAMURA, K., OHARA, H., and SEGAWA, M.: *Ultrasonics*, 1976, 14, p. 15
- 3 BUI, L., SHAW, H. J., and ZITELLI, L. T.: 'Study of acoustic resonance in piezoelectric PVF₂ film', Edward L. Ginzton Laboratory Report 2570, Stanford University, 1976
- 4 OHGASHI, H.: *J. Appl. Phys.*, 1976, 47, p. 949
- 5 REEDER, T. M., and WINSLOW, D. K.: *IEEE Trans.*, 1969, MTT-17, p. 927
- 6 COOK, L. G.: *IRE A*, 1956, Pt. 9, p. 61

Correlation with the storage convolver*

P. G. Borden and G. S. Kino

Stanford University, Stanford, California, 94305
(Received 28 June 1976)

A *p-n* junction type storage convolver has been used to correlate FM chirps with time-bandwidth products of approximately 90, and to correlate echoes from an acoustic *A*-scan system which have been badly distorted by the source transducer.

PACS numbers: 43.60.+d, 43.85.+f, 72.50.+b

Recently, it has been suggested by Stern¹ that the storage correlator based on the acoustic surface wave convolver could be used to remove the inherent distortions in a radar system. When a radar emits a coded waveform and the reflected echo is correlated with the original reference code, good correlation is only obtained if the emitted waveform is not distorted by the system or the medium through which it passes. Thus, with the development of more sophisticated systems with large time-bandwidth products, the requirement on the radar system itself becomes very severe, as do the requirements on the lack of signal distortion along the path of the radar beam. Similar problems occur in acoustic pulse echo systems used in medical imaging, sonar, and nondestructive testing, where distortions due to the acoustic transducers and the medium itself can be severe.

In this paper we describe an experiment using a storage correlator to remove the worst errors of this type. We employed an acoustic transducer to emit an FM chirp which was reflected from a plastic plate in a water tank. The reflected echo was used as a reference stored in the storage correlator. A later echo was then correlated with the reference echo. Thus, both echoes

suffered the same distortion and a reasonable correlation peak could be obtained.

Our experiment employed the V-groove isolated *p-n* junction mesa diode array airgap convolver described by Joly.² When this device is used as a storage correlator, the V-groove isolation technique allows a small separation between diodes (4 μm) without sacrificing isolation between adjacent diodes.

Several modes of storage correlator operation have been previously described.³⁻⁶ In the present case, a charge pattern is written into the diode array through the nonlinear interaction of an rf signal applied to the diode array top plate (T) and the electric fields associated with a short acoustic pulse injected on the interdigital transducer (L) which travels along the delay line, as illustrated schematically in Fig. 2. After the storage interval, by applying an rf signal to the top plate (T), the convolution of this signal with the stored signal is obtained at the original input port, and the correlation of the two signals at the other acoustic port. In the present case, one transducer is used for a short input storage pulse, and the other for readout. In general, the output will be the correlation of the second top plate input signal and the stored signal.

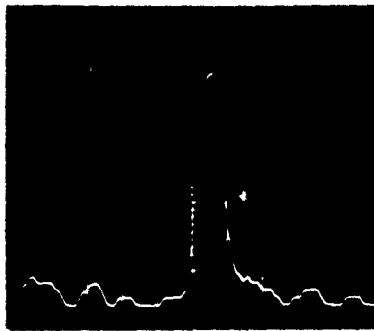


FIG. 1. Correlation peak obtained with two 6- μ sec-long 15-MHz BW chirps. Horizontal scale: 100 nsec/div.

Typical input levels are 25 dBm at the acoustic port, and 60 V $p-p$ at 98 MHz between the top plate and ground. The half-height storage time is 8 msec.

In a demonstration of high-frequency broadband linear FM chirp compression, the acoustic input was a 50-nsec 98-MHz pulse and the top plate signals were two 6- μ sec-long 15-MHz (90–105 MHz) chirps spaced 200 μ sec apart. The chirp bandwidth was limited by the bandwidth of the top plate matching network; the length limit was the acoustic length of the diode array.

Figure 1 shows the correlation peak obtained. The full width at half-maximum is less than 80 nsec, corresponding to a compression ratio of better than 75. This favorably compares to the time-bandwidth product of $(6 \mu\text{sec}) \times (15 \text{ MHz}) = 90$.

A practical application of this pulse compression technique is the elimination of resolution deterioration due to poor transducer response in a pulse echo system. To demonstrate this, a 3.25-MHz-center-frequency 2.5-MHz-bandwidth PZT transducer was placed 16 cm from a plastic block in a water tank, as illustrated in Fig. 2. The transducer was pulsed with a constant-amplitude linear FM chirp. A 6- μ sec-long 2.5-MHz

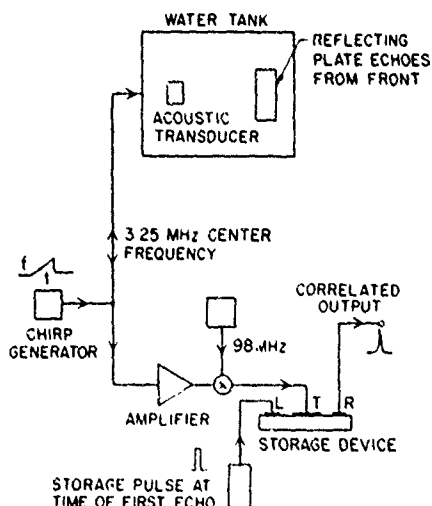


FIG. 2. Schematic of the acoustic pulse echo system.

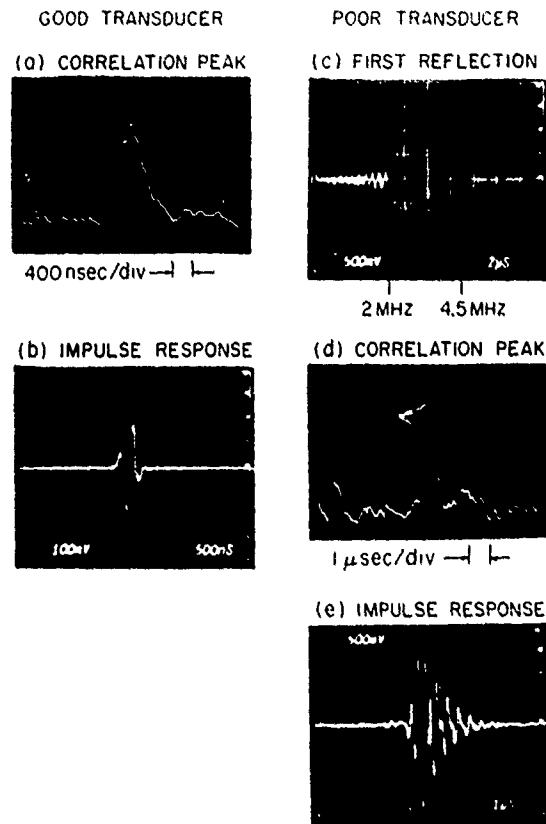


FIG. 3. Pulse echo experiment results with both good and poor transducers.

segment of the first reflected pulse from the plastic block was gated, mixed with 98 MHz, and stored in the correlator (see Fig. 2). The gate to the top plate was then reopened to allow correlation of a second echo pulse with the stored first reflected pulse. This second echo was the triple transit signal returning from the plastic block, reflected from the transducer face, and reflected a second time from the plastic block. The second echo was obtained approximately 210 μ sec after the first one used as the stored reference.

Figures 3(a) and 3(b) show the correlation peak and, for comparison, the impulse response of the transducer. The width of the correlation peak corresponds to a compression ratio of 9, compared with the TB limit of 15.

The same experiment was tried a second time with a poor-quality transducer that exhibited severe ringing in its impulse response. Figures 3(c)–3(e) show the first reflected pulse, correlation peak, and transducer impulse response, respectively. The correlation peak width was essentially the same as that obtained with the original high-quality transducer. This indicates that the resolution of the pulse echo system employing the storage correlator is much improved over that which could normally be obtained with a poor-quality transducer that severely distorts the original input signal.

The authors wish to thank J. Fraser for his help in setting up the acoustic pulse echo system.

*Work supported partially by the National Science Foundation under Grant NSF ENG75-18681, and partially by the Office of Naval Research under Contract N00014-75-O-0332.

¹E. Stern, invited Paper, 1975 IEEE Ultrasonics Symposium, Los Angeles (unpublished).

²R. Joly, preceding paper, Appl. Phys. Lett. 29, 525 (1976).

³A. Bers and J.H. Cafarella, Appl. Phys. Lett. 25, 133-135 (1974).

⁴H. Hayakawa and G.S. Kino, Appl. Phys. Lett. 25, 178-180 (1974).

⁵K. A. Ingebrigtsen, R. A. Cohen, and R.W. Mountain, Appl. Phys. Lett. 26, 596-598 (1975).

⁶C. Maerfeld, Ph. Defranould, and P. Tournols, Appl. Phys. Lett. 27, 577-578 (1975).

SUPERCONDUCTIVE TUNNELING INTO NIOBIUM-TIN THIN FILMS*

D.F. Moore

Department of Applied Physics, Stanford University, Stanford, CA 94305, U.S.A.

J.M. Rowell

Department of Applied Physics, Stanford University, Stanford, CA 94305, U.S.A.

and

Bell Laboratories, Murray Hill, NJ 0794, U.S.A.†

and

M.R. Beasley

Departments of Applied Physics and Electrical Engineering, Stanford University, Stanford, CA 94305, U.S.A.

(Received 2 April 1976 by H. Suhl)

Oxide-layer tunnel junctions exhibiting both quasi-particle and Josephson tunneling were produced by overlaying lead on niobium-tin thin films. The superconducting transition temperature and average energy gap of the Nb-Sn both increased as the tin concentration was increased toward Nb₃Sn and reached maximum values of 17.2 K and 3.2 meV, respectively, or $2\Delta = 4.3 kT_c$.

THE TECHNOLOGICAL IMPORTANCE of the A15-type superconductors, and their high transition temperatures and interesting lattice softening at low temperatures, has long made them intriguing candidates for superconductive tunneling studies. However, previous efforts to make both point contacts¹ and oxide-layer junctions²⁻⁵ have often resulted in less-than ideal tunneling characteristics. Only in the point contact measurements of Levinstein and Kunzler,¹ the proximity effect measurement of Bacon and Haemmerle² and the oxide tunneling of Shen³ was the energy gap 2Δ equal to or greater than the BCS value of $3.52 kT_c$. In many other cases (references 4-6 and references therein) very small energy gaps were observed, typically $\sim 1.5 kT_c$. We report here greatly improved oxide-layer tunnel junctions on thin films of niobium-tin (Nb-Sn). Both well-defined energy gaps and clear Josephson tunneling are obtained. We give a brief description of our results, including a study of the dependence of the energy gap of Nb-Sn on composition in the vicinity of stoichiometry. The gap is $\sim 4.3 kT_c$, suggesting that

these films have much cleaner surfaces than any samples available previously.

The films under study are produced for us by Hammond, Zubeck, and Hallak, using the dual electron beam codeposition technique developed by Hammond.⁷ The films are deposited on sapphire substrates held at 700-800°C, a temperature sufficient for the formation of well-reacted dense Nb₃Sn. A set of substrates along a line in the plane of the Nb and Sn sources gives a series of samples with a spread of composition from one deposition. The substrates were masked to produce a film ~ 0.5 mm wide. As the deposition rate is ~ 100 Å/sec, it is important to maintain uniformity of deposition within the last second of the run. For example, 0.5 sec of excess Sn deposition would seriously affect the tunneling characteristic, which is sensitive to material only within a coherence length (~ 50 Å) of the surface. The deposit was terminated by moving a shutter very rapidly in front of the substrates. After the system was cool (~ 30 min at 2×10^{-6} torr), it was vented with nitrogen. The film thickness ranged from 0.06 to 1.25 μ m. Electron micrographs show a smooth surface at 10,000 \times with the exception of the thicker films in the tin rich region.

The tunnel junctions are produced by exposure of the freshly deposited Nb-Sn to air and deposition of a lead counterelectrode. In general, the best current-voltage ($I-V$) characteristics are obtained for oxidation times of thirty minutes or less. Two examples are shown

* Work at Stanford supported by the National Science Foundation through the Center for Materials Research at Stanford University, by the Joint Services Electronics Program, and by the Air Force Office of Scientific Research, Air Force Systems Command, USAF, under Grant No. AFOSR 73-2435.

† Permanent address.

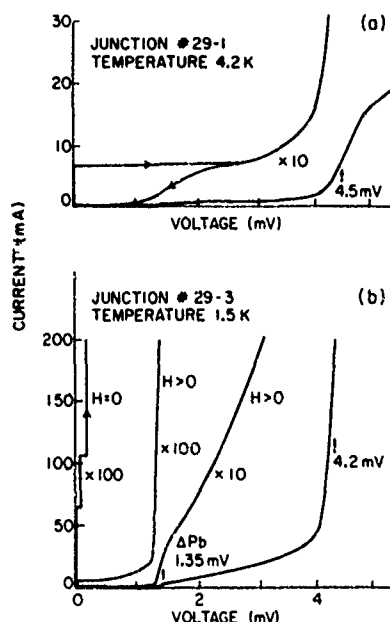


Fig. 1. Typical I - V characteristics of junctions on electron beam produced films. The "↑" indicates the rise in current at $\Delta_{\text{Nb-Sn}} + \Delta_{\text{Pb}}$ at 4.5 and 4.2 mV in (a) and (b), respectively.

in Fig. 1. In Fig. 1(a) the full I - V characteristic at 4.2°K for a low resistance junction is shown. The strong rise in the current at the sum of the energy gaps, $\Delta_{\text{Nb-Sn}} + \Delta_{\text{Pb}}$ (taken to be the point of maximum derivative in I - V), is evident. For this junction the ratio of the currents flowing just above and below the rise at $\Delta_{\text{Nb-Sn}} + \Delta_{\text{Pb}}$ is more than ten, at least five times better than previously reported. The expanded curve reveals clearly the Josephson tunnel current and the cusp at $\Delta_{\text{Nb-Sn}} - \Delta_{\text{Pb}}$. The maximum Josephson current is self-limited because the junctions are long compared with the Josephson penetration depth.

Figure 1(b) shows the I - V characteristic at low temperature of another junction from the same deposition but with slightly different composition. Prominent features here are Josephson tunneling with Fiske steps and, when the supercurrent is reduced by application of a magnetic field, a rise in the current at a voltage corresponding to Δ_{Pb} . For the better junctions such as these, the rise at Δ_{Pb} is strong and may indicate a small but finite density of electron states within the gap of the Nb-Sn. Many junctions exhibit a smaller inflection at Δ_{Pb} which is accompanied by subharmonic structure at Δ_{Pb}/n , where $n = 2, 3, 4, \dots$. In these cases the interpretation is less certain.

The I - V characteristics of these low resistance junctions were not explored at large voltages because the excessive bias currents required cause heating at the contacts. Longer oxidation times lead to higher junction resistances but also, unfortunately, to more conduction

below the gap and an increasing amount of curvature (dI/dV increasing with V) above $\Delta_{\text{Nb-Sn}} + \Delta_{\text{Pb}}$. After several days' oxidation in air the I - V characteristic is continuously curving, and it is difficult even to determine the energy gap. Junctions made by briefly heating the films in air, or by exposure to air of high humidity, also exhibit this curvature, which seems to be characteristic of thicker oxides. This behavior may result from the formation of metallic particles (Sn or Nb) within the mixed oxide.⁸ This difficulty has precluded a detailed study of the observed structure in the electron density of states in the Nb₃Sn due to phonons, but this will be possible with a smaller junction geometry.

The use of the codeposition technique in the phase-spread configuration lends itself ideally to a study of $\Delta_{\text{Nb-Sn}}$ as a function of film composition. Some typical results are shown in Fig. 2. The characteristics have been normalized to have the same differential

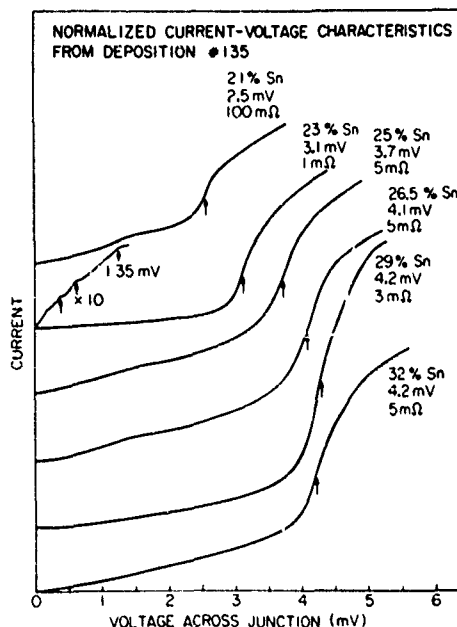


Fig. 2. Variation of characteristics with composition. Six junctions from twenty-four on a phase spread illustrating the variation of $\Delta_{\text{Nb-Sn}} + \Delta_{\text{Pb}}$ (indicated by arrow) with composition.

conductance at large bias voltages, and displaced vertically for clarity. The quality of the I - V curves shown in this figure is not as good as those shown in Fig. 1, reflecting their larger tunneling resistances. The major difference is the marked excess tunneling current below the gap, as mentioned above. Josephson tunneling is still evident, however, in most cases. The expanded region for the 23% Sn curve shows an example of the structure usually associated with the inflexion at Δ_{Pb} and its subharmonics.

The Nb-Sn energy gap values obtained from Fig. 2 (after subtracting the known gap for lead) and from five

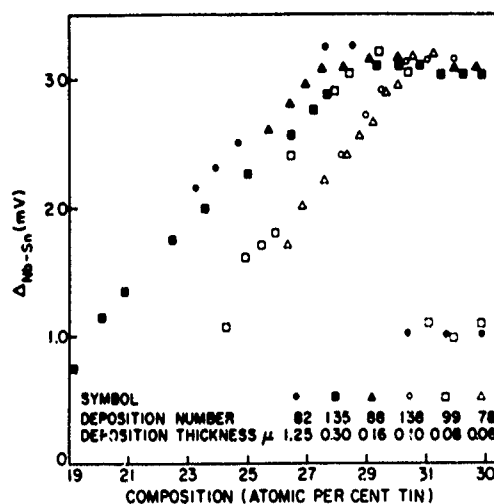


Fig. 3. Variation of Nb-Sn energy gaps with composition.

other depositions are plotted in Fig. 3. Although certain peculiarities are evident, the general behavior is clear. $\Delta_{\text{Nb-Sn}}$ increases smoothly with increasing tin composition from 19 at. % Sn through stoichiometry to about 29 at. % Sn where it levels off at a maximum value of about 3.2 meV and generally stays above 3.0 meV, at least up to 33 at. % Sn. The composition of the films was established at one point on each substrate by microprobe analysis augmented by Rutherford Backscattering studies, and the relative compositions are believed to be good to ± 1 at. %. The absolute values are only ± 2 at. %.⁹ The transition temperature measured inductively¹⁰ behaves in a similar manner, increasing to a maximum of 17.3 and 17.1°K for the thick and thin films, respectively. The ratio $2\Delta_{\text{Nb-Sn}}/kT_c$ is 4.3 near stoichiometry, where both $\Delta_{\text{Nb-Sn}}$ and T_c have their maximum values, indicating strong electron-phonon coupling.

The first peculiarity of Fig. 3 is that there are differences in the niobium-rich region although the variation of $\Delta_{\text{Nb-Sn}}$ with composition is similar for all depositions. Taken at face value the data suggests a systematic difference between the thick and thin films, but the significance of this fact is not clear. Moreover, there are possible differences in the state of strain, crystallographic orientation¹¹ and composition right at the surface of the films.

Depositions No. 82 and No. 99 show a precipitous drop in the observed $\Delta_{\text{Nb-Sn}}$ as the tin concentration is increased above 29 at. %. Individual junctions in the transition region show rises in the tunneling current corresponding to $\Delta_{\text{Nb-Sn}}$ both 3.0 and 0.7 meV. This occasional behavior, where the surface is bad but the bulk T_c remains high, certainly seems to be associated with the onset of a two phase region above 29 at. % Sn.^{12,13} But whether the low gap represents disorder or a phase separation toward the surface is not clear on the basis of present data.

In conclusion we find that oxide-layer tunnel junctions made on electron beam evaporated Nb-Sn are superior to those obtained previously by any means. The surface properties of these Nb-Sn films are quite reproducible, vary in a regular manner, and appear to reflect the bulk superconductivity of the films. This has made possible a study of the gap as a function of composition, and holds the promise of further detailed studies of the electronic properties of this important superconductor.

Acknowledgements – The authors are indebted to R.H. Hammond, R.B. Zubeck, and A. Hallak for their outstanding thin films of Nb₃Sn which made this work possible.

REFERENCES

1. LEVINSTEIN H.J. & KUNZLER J.E., *Phys. Lett.* **20**, 581 (1966). Nb₃Sn, $\Delta = 2.8$ meV, $2\Delta/kT_c = 3.6$. V₃Si, $2\Delta/kT_c = 1.8$ and 3.8. V₃Ge, $2\Delta/kT_c = 3.2$.
2. HAUSER, BACON D.D. & HAEMMERLE W.H., *Phys. Rev.* **151**, 196 (1966). V₃Si, $\Delta = 2.80$ meV, $2\Delta = 3.8 kT_c$.
3. SHEN L.Y.L., *Phys. Rev. Lett.* **29**, 1082 (1972). Nb₃Sn $\Delta = 2.5$ meV. $T_c = 16.4^\circ\text{K}$, $2\Delta = 3.5 kT_c$.
4. VEDENEEV, S.I., GOLOVASHKIN A.I., LEVCHENKO I.S. & MOTULEVICH G.P., *Zh. Eksp. Teor. Fiz.* **63**, 1010 (1972) [*Sov. Phys.-JEPT* **63**, 531 (1973)]. Nb₃Sn, $T_c = 17.8$ –18.3, $2\Delta \sim 2$ meV, $2\Delta/kT_c \sim 1.3$.
5. GREGORY J.A., BOSTOCK J., MACVICAR M.L.A. & ROSE R.M., *Phys. Lett.* **A46**, 201 (1973). Nb₃(Al_{0.75}Ge_{0.25}), $2\Delta = 1.3$ meV. $T_c = 17.5$ –19°K.
6. VEDENEEV S.I., *Fiz. Tverd. Tela* **17**, 939 (1975) [*Sov. Phys.-Solid State* **17**, 602 (1975)]. Codeposit Nb + Al, $T_c = 15.5$ –16.7, $2\Delta = 1.4$ meV, $2\Delta/kT_c = 1.0$.
7. HAMMOND R.H., *IEEE Trans. Mag.* **MAG-11**, 201 (1975).
8. ZELLER H.R. & GIAEVER I., *Phys. Rev.* **181**, 789 (1969).

9. A second microprobe, with a take-off angle of 52.5° instead of the 38.5° of the machine used to plot the data, gave compositions 2-3 at. % higher in niobium. This may be accounted for by the small variations in density and surface morphology seen in the electron micrographs of the films.
10. HOWARD R.E. (to be published).
11. X-ray diffractometer traces, supplemented by Reed X-ray camera photographs, indicate a strong preferred orientation of the Nb-Sn and the appearance of a second phase above 29 at. % Sn.
12. CHARLESWORTH J., MACPHAIL I. & MADSEN P., *J. Mat. Sci.* 5, 580 (1970)
13. HAMMOND R.H., NSF-RANN Semannual Progress Report, October 1974, M-1 Report No. 2362, p. 18-22.

HORIZONTAL SHEAR SURFACE WAVES ON CORRUGATED SURFACES

Indexing terms: Acoustic surface waves, Acoustic wave propagation

Experiments have been performed on horizontal shear surface-wave propagation along a corrugated surface. The results are in agreement with approximate theories used in analogous electromagnetic problems.

Introduction: A well known problem in electromagnetism concerns the propagation of a TM-type surface wave along an infinite corrugated surface.¹⁻⁶ The inset to Fig. 1 illustrates this structure for a substrate with finite thickness. In the electromagnetic case, the shaded region represents an isotropic dielectric with electrical-short-circuit boundary conditions on the corrugated and bottom surfaces. The structure is uniform along the x direction.

This problem provides a good example of the generation of solutions to new acoustics problems by utilising the analogy between Maxwell's equations and the acoustic-field equations.⁷ In the electromagnetic problem considered here, the x component of the magnetic field satisfies the 2-dimensional wave equation subject to boundary conditions requiring that the normal derivative of H_x be zero on all surfaces. The acoustic variable analogous to H_x is the x component of particle displacement velocity, which satisfies the ordinary wave equation in 2-dimensional isotropic problems of the kind considered here. At traction-free boundaries parallel to the x -axis, the normal derivative of v_x is required to be zero. This shows that the electromagnetic problem has an exact acoustic analogue in which the inset to Fig. 1 represents a free isotropic elastic plate with a uniform grating of slots cut into the upper surface. The known electromagnetic-surface-wave solution is therefore directly applicable to this new problem.

The acoustic analogue solution generated in this way represents a new type of horizontal shear surface wave. Although most surface-acoustic-wave research has been

concerned with Rayleigh waves, horizontally polarised surface waves are not unknown. Such waves exist on piezoelectric and magnetostrictive substrates, and also on layered isotropic substrates (Love waves). The waves considered here are unique in that they have a propagation velocity that is much slower than the bulk-shear-wave velocity and they also exhibit an upper cutoff frequency. These properties suggest potential applications in the areas of compact long delay lines and grating filters. It should be noted that these new surface waves require the presence of the corrugations and do not exist on a smooth surface, as Rayleigh surface waves do.

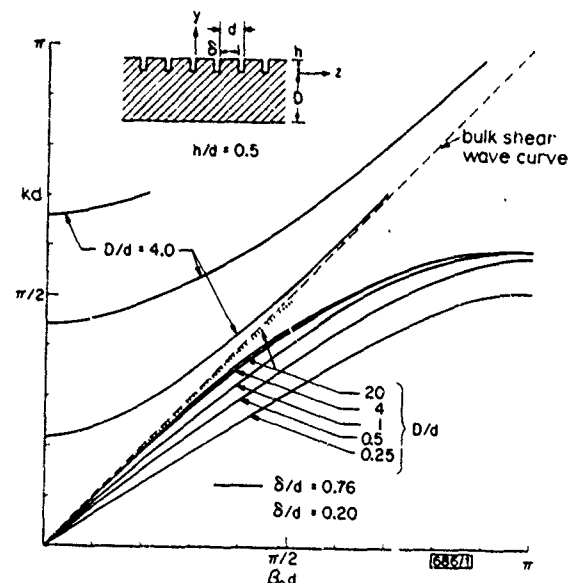


Fig. 1 Theoretical dispersion curves for horizontal shear-wave propagation on corrugated surface

Method of solution: Detailed treatments of the analysis are given in the electromagnetic references cited. Following Floquet's theorem, one expands the field for $y < 0$ in terms of 'spatial harmonics' $\exp(\beta_n + 2\pi n/d)z$. Inside the teeth ($y > 0$) the fields are expanded in terms of SH plate modes. Using an approximate method, we assume that only the dominant SH mode exists in the teeth and match the stress component T_{xz} on the plane $y = 0$ by Fourier analysis.^{3,4} For the continuity condition on v_z at the same plane, either matching of the field at the midpoints of the slots³ or matching the complex power flow⁵ is used. This leads to the dispersion relations

$$\frac{1}{kh \tan kh} = \frac{\delta}{d} \sum_{n=-\infty}^{\infty} \frac{1}{\alpha_n h \tanh \alpha_n D} \left(\frac{\sin \beta_n \delta/2}{\beta_n \delta/2} \right)^2$$

$$\mu = \begin{cases} 1, & \text{midpoint matching} \\ 2, & \text{power-flow matching} \end{cases}$$

$$\beta_n = \beta_0 + 2\pi n/d, \quad k = \omega/V_1, \quad \alpha_n^2 = \beta_n^2 - k^2$$

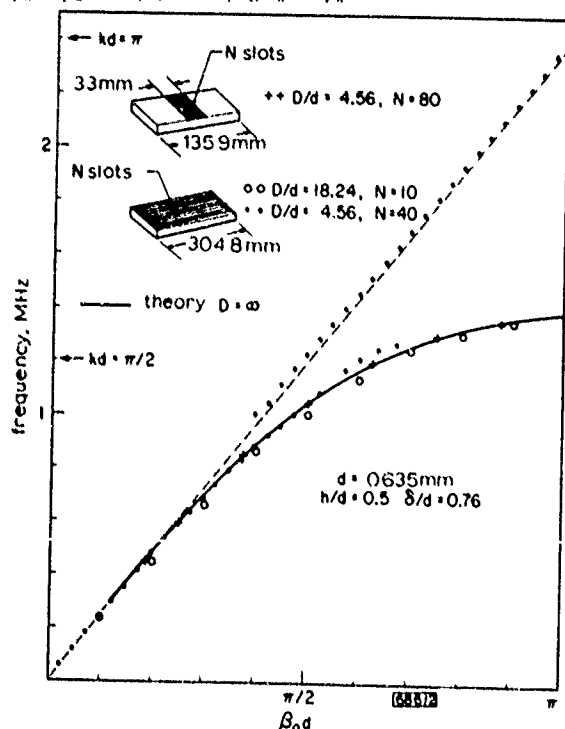


Fig. 2 Comparison of theory and experiment for 0.152 x 0.318 mm slots

In the $N = 80$ case, only a few of the observed resonance frequencies are shown

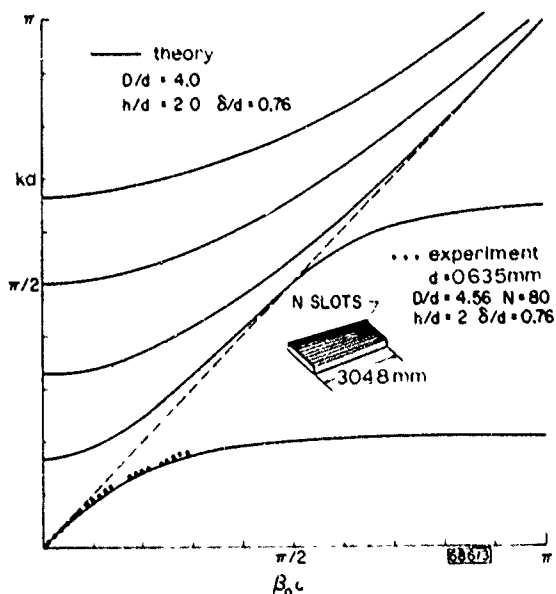


Fig. 3 Comparison of theory and experiment for 0.152 x 1.27 mm slots

Over the range of parameters used experimentally we have found little difference between $\mu = 1$ and $\mu = 2$, and the second value was used. Fig. 1 shows typical curves for a finite substrate thickness D , with the surface-wave solution below the broken diagonal and thickness modes for one value of D above the diagonal.

Results and discussion: The dispersion curves were measured by observing in transmission the resonance frequencies of a section of corrugated surface with traction-free ends (Figs. 2 and 3). Fabrication of the grating resonators was accomplished by sawing 0.152 mm slots in aluminium plate. The measurements were performed using a frequency synthesiser and p.z.t.-5A thickness shear input and output transducers affixed with Dow Resin 276-V9. The transducers were 0.864 mm thick and had a 25.4 mm horizontal aperture.

Surface-wave resonances occur at frequencies where the grating is an integral number of half wavelengths long. In an N -slot grating this means that

$$\beta_0 d = p\pi/N$$

where p is an integer. Measurements were made by observing the transmission resonances and counting back to zero to determine the mode index p . Results for various values of the parameters are plotted and compared with theoretical curves in Figs. 2 and 3. It is seen in Fig. 2 that the results are not sensitive to the lateral width of the grating. For the narrow grating, rubber dampers were placed along the grating edges to suppress diffraction effects. The experimental points above the broken diagonal correspond to the thickness modes shown in Fig. 1. These spurious responses create a problem in performing measurements near the surface-wave cutoff frequency. Comparison of the $kd = \pi/2$ points in Figs. 2 and 3 shows that the deeper slots give a greatly increased amount of wave slowing. A higher-order surface wave also appears in this case.

Because the polarisation of the surface wave is shear horizontal, there is no scattering from the surface mode into the thickness modes at the traction-free end faces of the resonator, contrary to the case of Rayleigh surface-wave reflections. However, the kind of transducer used does excite both types of modes. Although spurious-mode excitation can be somewhat reduced by careful placement of the transducer and by damping the lower surface of the plate, mode interference remains a problem in frequency regions where the two mode types overlap. This is clearly shown in Fig. 3, where the accuracy of the measurements deteriorates at the higher frequencies, but this can be avoided by using a smaller value of D to increase the thickness-mode frequencies.

The principal problems to be resolved in further study and exploitation of these waves are the development of suitable transducers and of techniques for fabricating narrow deep slots with smaller dimensions suitable for higher-frequency operation. Interdigital transducers⁶ and orientation-dependent etching⁹ are possible solutions to be examined.

Acknowledgment This work was supported by the US Office of Naval Research under Contract N00014-75-C-0632.

B. A. AULD
J. J. GAGNEPAIN*
M. TAN

13th October 1976

Edward L. Ginzton Laboratory
Stanford University
Stanford, Calif. 94305, USA

* Now at Ecole Nationale Supérieure de Chronométrie et Micromécanique, 25000 Besançon, France

References

- 1 ELLIOT, R. S.: 'On the theory of corrugated plane surfaces', *IRE Trans.*, 1934, AP-2, pp. 71-81
- 2 HURD, R. A.: 'The propagation of an electromagnetic wave along an infinite corrugated surface', *Can. J. Phys.*, 1954, 32, pp. 727-734
- 3 WATKINS, DEAN A.: 'Topics in electromagnetic theory' (Wiley, 1958), pp. 14-19
- 4 COLLIN, R. A.: 'Field theory of guided waves' (McGraw-Hill, 1960), pp. 465-469
- 5 REVENUE, R. M.: 'Electromagnetic slow wave systems' (Wiley, 1964), pp. 57-61
- 6 COLLIN, R. A. and ZUCKER, F. J.: 'Antenna theory - Part 2' (McGraw-Hill, 1969), pp. 229-232
- 7 AULD, B. A.: 'Acoustic fields and waves in solids - Vol. 1' (Wiley, 1973)
- 8 WHITE, R. M.: 'Surface elastic-wave propagation and amplification', *IEEE Trans.*, 1967, ED-14, pp. 181-189
- 9 ROSENFELD, R. C. and BEAN, K. E.: 'Fabrication of topographical ridge guides on silicon for VHF operation' Proceedings of IEEE ultrasonics symposium, 1972, Boston, Mass., pp. 186-189

PYROELECTRIC VIDICONS WITH IMPROVED READOUT

Indexing terms: Pyroelectric devices, Television camera tubes

The performance of a television camera using a pyroelectric Vidicon has been improved by the use of flyback gas pedestal generation and a low-relative-permittivity target material

Pyroelectric Vidicons provide television-compatible thermal images relatively cheaply and without the need for cooling. The performance of tubes described earlier¹ was limited by incomplete discharge of the pyroelectric target by the electron beam. The readout efficiency is governed by the magnitude of the positive swing of the target potential between scans (the 'pedestal' level).² In a gas-filled tube this potential excursion is obtained by collection of positive ions on the target surface, the ions being generated by collisions of the electron beam with the gas in the space between mesh and target. The difficulty encountered was that increasing the beam to raise the pedestal level caused defocusing, emphasised target defects and gave poor shading.

The development described here allows the pedestal level to be set independently of the readout beam. This is done by generating most of the pedestal during the line-flyback period. The normal positive-going blanking pulses on the cathode prevent electrons from reaching the target during flyback. Gas ions can still do so, however, and concurrent positive pulses applied to the control grid are used to increase the

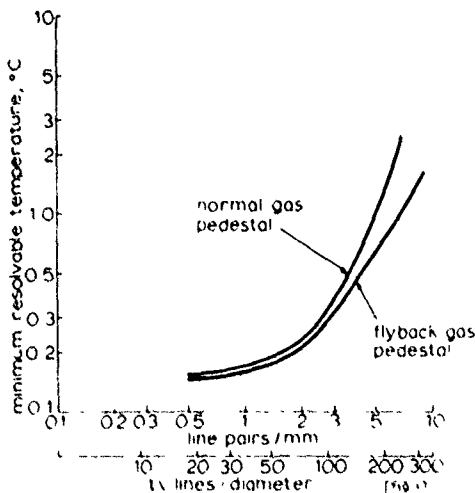


Fig. 1 Minimum resolvable temperature for panning mode (f1)
Pan rate 4.5 mm/s

beam current and so generate a large pedestal in this time. If necessary, additional pedestal can be obtained by lengthening the flyback time. Typical tubes, with a flyback time of 10 μ s, provide an equivalent mean pedestal current of 30 nA. On an 18 mm-diameter target, fully scanned by a 4 \times 3 raster, the corresponding instantaneous pedestal current is about 60 nA.

The readout efficiency, being a function of the potential swing on the target, can also be improved by substituting for TGS, the pyroelectric previously used, a material having lower relative permittivity. The deuterated isomorph of TGS is favoured, as it has a relative permittivity at 35 °C (the operating temperature in the camera) equal to 24, compared with 76 for TGS.³

Measurements, shown in Fig. 1, of the minimum resolvable temperature normalised by $f/1$ as before,¹ show the improvements that have been achieved by these means.

In the panning mode of operation, at 100 lines per picture height (approximately 3 line-pairs/mm) the m.r.t. is now 0.3 °C, compared with 2 °C previously. The improvement due to better readout is particularly marked at higher spatial frequencies; with the normal gas pedestal, the m.r.t. at 250 lines is close to 2.5 °C, whereas with the flyback it is 1 °C.

Fig. 2 shows the equivalent, minimum-resolvable-temperature curve for chopped operation. The improved readout

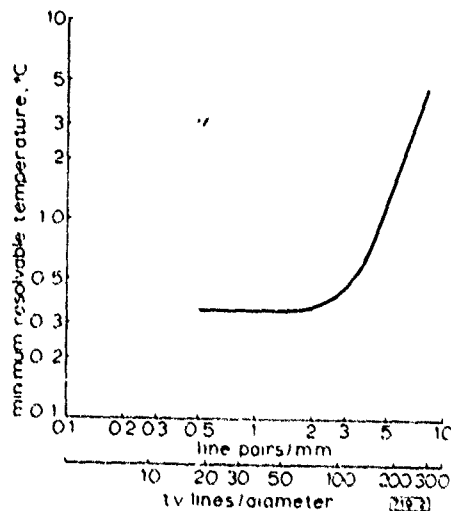


Fig. 2 Minimum resolvable temperature for chopped mode (f1)
With line flyback gas pedestal. Chopped frequency 25 Hz

allows a chopper frequency of 25 Hz to be used, each alternate field of video information being inverted to maintain a constant signal polarity.

The flyback system is the subject of a patent application

Acknowledgment. The work has been carried out with the support of the Procurement Executive, UK Ministry of Defence, sponsored by DCVD.

P. D. SIMON

2nd November 1976

EEI Ltd

Chelmsford, Essex, England

References

- 1 WATSON, R., SMITH, G., HARPER, B., and WREATHALL, W. M.: 'Infrared television performance of pyroelectric Vidicon at 8 to 14 μ m', *Electron Lett.*, 1973, 9, pp. 534-535
- 2 LOGAN, R. M., and WATSON, R.: 'Cathode potential stabilisation of the pyroelectric vidicon', *Infrared Phys.*, 1972, 12, pp. 17-28
- 3 HAYDEN, S. C., BALVINO, J. F., and LOYACONO, G. M.: 'An investigation of the figures of merit of triglycine sulphate (TGS) and its isomorphs', Proceedings of electro-optical systems design conference, San Francisco Calif., 1974, pp. 26-30

The Design of Efficient Broad-Band Piezoelectric Transducers

CHARLES S. DESILETS, MEMBER, IEEE, JOHN D. FRASER, AND GORDON S. KINO, FELLOW, IEEE

Abstract—A design method for acoustic thin disk transducers with high efficiency, broad bandwidth, and good impulse response is presented. This method is based on the use of quarter-wave matching layers between the piezoelectric material and the acoustic load. As is made evident using the transmission line model of Krimholtz, Leedom, and Matthaei, the finite thickness of the piezoelectric material must be taken into account in the matching layer design. Criteria for optimum broad-band transducer designs with a given piezoelectric material are developed which show the importance of a high electromechanical coupling coefficient. A method for obtaining Gaussian shaped passbands, necessary for optimum impulse response, is also shown. Several transducers have been built to illustrate this design approach with excellent agreement between theory and experiment. One such transducer has 3.2 dB round trip insertion loss and one octave bandwidth.

I. INTRODUCTION

A design method for acoustic thin disk transducers with large bandwidths, good sensitivity, and good impulse response is described in this paper. This method is based upon the concept that, for broad-band matching with high efficiency between a piezoelectric material with relatively high acoustic impedance and a relatively low impedance acoustic load, one or more quarter-wavelength matching sections must be used. The fact that the piezoelectric material itself must be regarded as a finite length transmission line is taken into account in the design of the matching layers. This significantly alters the choice of impedance for the matching sections.

In addition, considerable attention is devoted to the problem of obtaining a good impulse response. For this purpose, the requirement of a large bandwidth alone is not adequate. As the impulse response is the Fourier transform of the frequency response, the ideal bandpass characteristic for a short impulse response with minimum ringing is a Gaussian shape, and as shown by Sittig, a linear phase characteristic [1].

Several transducers have been built using this design approach and show characteristics in excellent agreement with the theory. One such transducer used lead metaniobate as the active material, acoustically matched into water with a single epoxy matching section, air backed, series inductively tuned, and matched electrically into 50 Ω . This transducer shows the desired flat response over the 40-percent, 3-dB passband, 6.5-dB round trip insertion loss at band center, and the predicted

impulse response. A second transducer using PZT-5A ceramic as the active element was acoustically matched into water, using two matching sections of a light borosilicate glass and epoxy, airbacked, series inductively tuned, and electrically matched into 50 Ω . The transducer has the predicted 65-percent, 3-dB bandwidth, 3.2-dB round trip insertion loss, and the predicted impulse response. A third transducer, using PZT-4 ceramic, and acoustically matched on the back with a high-loss high-impedance tungsten-loaded epoxy, was also built; this yielded approximately the desired Gaussian bandshape and the expected excellent three half-cycle impulse response.

The electrical input impedance of an acoustic transducer, and consequently the insertion loss and other parameters of interest, can be determined from the well-known one-dimensional Mason model [1]–[3]. In addition, the effects of complex acoustic load and backing impedances on the overall response at the transducer can be easily taken into account with this model. In several papers, notably those of Kossoff [4], Goll and Auld [5], Goll [6], Reader and Winslow [7], and Sittig [8], the effect of various acoustic matching techniques at the two acoustic ports of the transducer on the transducer characteristics have been analyzed. These approaches have included the use of high-loss backing materials and quarter-wave matching sections. However, the design of transducers with high sensitivity, broad bandwidth with low ripple, and short-duration impulse responses has remained largely a trial and error process. The authors believe that this is because the Mason model does not lend itself easily to physical interpretation of the effects of various acoustic and electrical matching schemes. This hampers the optimization of the transducer characteristics, such as the bandwidth, bandshape, and impulse response. Our design procedure, instead, is based on the transmission line model of Krimholtz, Leedom, and Matthaei, [9], [10] shown in Fig. 1. This has the advantage that it retains the intuitively satisfying transmission line nature of the transducer, but replaces the cumbersome distributed coupling of the piezoelectric effect with a single coupling point at the center of the transducer. The differences between distributed and single point coupling are included through a coupling transformer with a turns ratio that varies with frequency, and a series reactance.

Physical intuition and computation are facilitated with this model, since acoustic matching techniques typically use transmission line formalism, while the electrical matching techniques required in the frequency range of interest typically use lumped components. A series of computer programs has

Manuscript received May 20, 1977; revised October 19, 1977. This work was supported in part by the Office of Naval Research under Contract N00014-75-C-0632 and in part by the National Science Foundation under Grant ENG75-18681.

The authors are with the Edward L. Ginzton Laboratory, W. W. Hansen Laboratories of Physics, Stanford University, Stanford, CA 94305.

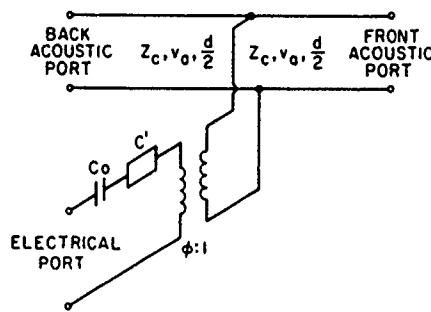


Fig. 1. Transmission-line model of piezoelectric transducer (after Krimholtz, Leedom, Mattheai).

been written to implement the design of transducers using this model. In these programs, the loss between the electrical and acoustic ports over the band can be computed, the electrical input impedance can be determined, and a single electrical matching network can be designed. The accuracy of such techniques is sufficient so that the effects of finite thickness bonds between the matching layers, of stray inductances and capacitances, and of excess electrical resistance show up strongly, and makes it possible to determine the nature of such errors in the construction. In addition, by using Fourier transform methods, the impulse response of the transducer can be predicted with good accuracy.

II. DESIGN THEORY

A. General Considerations

We first discuss some of the general criteria necessary to obtain broad-band low-loss matching for an electrical signal to the acoustic ports. For this purpose, we shall make use of the Krimholtz, Leedom, and Mattheai (KLM) model illustrated in Fig. 1. In this model, the piezoelectric transducer is represented by an acoustic transmission line tapped at its center, and driven by a perfect transformer of ratio $\phi:1$, where

$$\phi = k_T (\pi / \omega_0 c_0 Z_C)^{1/2} \text{ sinc} \left(\frac{\omega}{2\omega_0} \right) \quad (1)$$

with $\text{sinc } x = \sin(\pi x) / \pi x$.

The parameters are defined as follows:

- d thickness of the piezoelectric material;
- A area of the transducer;
- ϵ^S clamped dielectric constant;
- ρ mass density;
- c^D stiffened elastic constant;
- v_a stiffened acoustic velocity;
- Z_a stiffened acoustic impedance ($= \rho v_a$);
- e electromechanical coupling constant;
- k_T^2 effective piezoelectric coupling coefficient ($= e^2 / c^D \epsilon^S$);
- $Z_C = Z_a A$; and
- ω_0 half-wavelength resonant frequency of the transducer ($= \pi v_a / d$).

The transformer has a capacity in series with it of value $C_0 = \epsilon^S A / d$, the clamped capacitance of the transducer. There is

an additional reactance in series with the transformer which can be modeled as a variable capacitance of value:

$$C' = -C_0 / k_T^2 \text{ sinc}(\omega / \omega_0). \quad (2)$$

As $|C'| \gg |C_0|$, it only has a minor influence on the operation of the transducer.

General criteria for the maximum bandwidth obtainable from a transducer with minimum insertion loss can be calculated for the case where the acoustic ports of the transducer are terminated with pure resistive loads. The KLM equivalent circuit would then become a center tapped transmission line terminated by a load Z_L at one end and a load Z_R at the other. When $Z_L, Z_R < Z_C$, this transmission line has a resonance near ω_0 . The approximate acoustic Q , Q_a , of the resonator can be calculated by transforming the impedances Z_L, Z_R , to the center tap, where they have effective values Z_C^2 / Z_L and Z_C^2 / Z_R , respectively; this is a total resistance of value $R = Z_C^2 / (Z_L + Z_R)$. The resultant shorted quarter-wave transmission lines have a reactive impedance when placed in parallel of value $X = Z_C / 2 \tan(\pi \omega / 2 \omega_0)$. The acoustic Q can be estimated from the points where $X = R$, so that

$$Q_a \approx \left(\frac{\pi}{2} \frac{Z_C}{Z_R + Z_L} \right). \quad (3)$$

The electrical radiation resistance of the transducer at its center frequency is

$$R_{a0} = \frac{4k_T^2}{\pi \omega_0 C_0} \left(\frac{Z_C}{Z_R + Z_L} \right). \quad (4)$$

Therefore, the electrical Q , Q_e , of the series inductance tuned circuit at its center frequency, when supplied by a constant voltage source, is

$$Q_e = \frac{1}{\omega_0 C_0 R_{a0}} = \frac{\pi}{4k_T^2} \frac{(Z_R + Z_L)}{Z_C}. \quad (5)$$

The requirement that $Q_e = Q_a$ for optimum bandwidth yields the relation

$$\frac{Z_R + Z_L}{Z_C} = k_T \sqrt{2}. \quad (6)$$

Further examination of the equivalent circuit shows that the impedance presented at the transformer terminal, correct to first order in $\Omega = (\omega - \omega_0) / \omega_0$, is

$$Z_{IN} = \frac{Z_C^2}{Z_R + Z_L} - j\pi \Omega \left[\frac{Z_C^3}{(Z_R + Z_L)^2} \right]. \quad (7)$$

The reactive part of this impedance is like that of a negative inductance.

The reactance seen at the generator, including a series tuning inductance L chosen so that $\omega_0 L = 1 / \omega_0 C_0$, is

$$X = \frac{\Omega}{\omega_0 C_0} \left[2 - k_T^2 - 4k_T^2 \left(\frac{Z_C}{Z_R + Z_L} \right)^2 \right]. \quad (8)$$

This expression is correct to first order in Ω . The first term in (8) is due to L and C_0 in series, the second term is due to the capacitance C' in the equivalent circuit, and the third term is

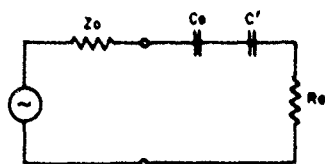


Fig. 2. Equivalent electrical lumped circuit of transducer terminated by matched loads at both acoustic ports.

due to the acoustic loading. It can be seen that, if the $k^2 \ll 4$, the first-order variation of the reactance X with frequency is minimized when $(Z_R + Z_L)$ is chosen to satisfy (6). Therefore, this choice of terminating impedance satisfied the requirement for approximate cancellation of the reactance, as well as a criterion for optimum matching from a constant voltage source.

If the impedance of the generator is chosen to equal R_{a0} , the efficiency of power transfer to the transducer is

$$\eta = \frac{4R_a R_{a0}}{(R_a + R_{a0})^2 + X^2} \quad (9)$$

Since $R_a = R_{a0}$ at the center frequency, and since the first order variations at the reactance with frequency are essentially eliminated, the efficiency η will have only fourth order variations with frequency due to the variation of X with frequency. First order variations of R with frequency only give rise to second order variations of η .

As an illustration of what occurs in several cases, consider the situation when both acoustic ports are terminated by impedances $Z_L = Z_R = Z_C$ [15], [16]. In this case, the equivalent circuit becomes that shown in Fig. 2. Half of the power is emitted from each acoustic port, and the effective resistance of the acoustic load seen at the electrical port is [2], [7], [8]

$$R_a = R_{a0}(\omega_0/\omega)^2 \sin^2(\pi\omega/2\pi_0) \quad (10)$$

where

$$R_{a0} = (2k^2/\pi)(1/\omega_0 C_0). \quad (11)$$

When the device is untuned, it can be shown that, if C' is neglected, the minimum power loss occurs with a generator impedance of $Z_0 = (R_{a0}^2 + 1/\omega_0^2 C_0^2)^{1/2}$. At the center frequency, this would correspond to an efficiency of power transfer from the generator to the load [3], [7], [8]

$$\eta = \frac{1}{1 + [1 + (\pi/2k^2)^2]^{1/2}} \approx \frac{2k^2}{\pi} \quad (12)$$

where, in this formula, the 3-dB loss due to having power emitted from both acoustic ports is taken into account. It is therefore desirable to use as high a coupling coefficient k^2 as possible, in order to obtain high efficiency with an untuned transducer. In this case, the best efficiency that might be expected with a PZT ceramic with $k^2 = 0.25$, would be 16 percent. Such a transducer would have a minimum round trip insertion loss of 16.0 dB.

The addition of tuning would ideally lower the minimum loss to 6 dB. A simple series inductance would give an electrical Q at the center frequency, when a source impedance

$Z_0 = R_{a0}$ is employed, of

$$Q_e = \pi/4k^2. \quad (13)$$

With $k^2 = 0.25$, the bandwidth would be narrowed to 32 percent instead of approximately 100 percent. If a constant voltage source were used, Q_e would then be $\pi/2k^2$, giving a bandwidth of 16 percent. It is, therefore, highly desirable to work with as large a coupling coefficient as possible to increase $R\omega_0 C_0$, and thus lower the electrical Q of the transducer.

A considerable improvement in efficiency can be obtained by leaving the left-hand side air backed, i.e., short circuiting the left-hand transmission line. In this case, if the right-hand transmission line is terminated by an impedance $Z_R = Z_C$, the effective resistance in the circuit of Fig. 1 is doubled, and the one way optimized efficiency at the center frequency ω_0 becomes 46 percent for $k^2 = 0.25$; the bandwidth of the series-tuned system then approaches 64 percent, with source impedance R_{a0} , or 32 percent for a constant voltage source.

It is also worthwhile to consider the important case, much used in practice, of a transmitter terminated on its left-hand side by a load Z_L close to the impedance of the transducer material. As an example, a PZT-5A transducer ($Z_L = Z_C = 34$) can be used to excite a wave in water ($Z_R = 1.5$). In this case, most of the power is emitted into the matched backing. If the voltage across the center point of the transmission line is V , the power emitted at the center frequency into the left-hand side is $V^2 Z_L / 2Z_C^2$, the power emitted into the right-hand side is $V^2 Z_R / 2Z_C^2$.

Following the previous arguments, it will be seen that since

$$R_{a0} = \frac{4k^2 Z_C}{\pi\omega_0 C_0(Z_R + Z_L)}$$

the maximum efficiency of an untuned transducer is

$$\eta = \frac{2Z_R}{(Z_L + Z_R) [1 + \pi(Z_R + Z_L)/4k^2 Z_C^2]^{1/2}} \quad (14)$$

The maximum efficiency for a PZT-5A transducer with a matched backing exciting a wave in water is 1.9 percent. If both sides are matched to the transducer material impedance $Z_R = Z_L = Z_C$, the maximum efficiency is that already calculated. If $Z_L = 0$ and Z_R is small, η can be made 100 percent.

B. Front Acoustic Load Line

The matching problem for a piezoelectric ceramic used to excite an acoustic wave in water is now considered. The impedance of the transducer material is typically 20 to 35, and that of the water is 1.5. Thus in the KLM model the impedance looking into the right-hand acoustic load line is like that of a transmission line with essentially a short circuit termination. The impedance is very high at the center frequency, but drops quickly to low values. Consequently, the bandwidth of the transducer is very small, unless the impedance at the center is kept low by using a backing termination.

Quarter-wave impedance transformers between the load and the piezoelectric ceramic will broaden out the frequency

TABLE I
MATCHING FORMULAS

Impedance	Z_{IN}	Z_2	Z_1	Z_L
One Section	Z_C^2/Z_T			Z_T
Two Sections	$Z_C^{3/2}/Z_T^{1/2}$	$Z_T^{2/3}/Z_C^{1/3}$		$Z_C^2/Z_T^{1/2}$
Three Sections	$Z_C^{5/2}/Z_T^{1/2}$	$Z_T^{3/4}/Z_C^{1/4}$	$Z_T^{6/7}/Z_C^{1/7}$	$Z_C^2/Z_T^{1/2}$

response characteristics, giving higher efficiency than transducers damped by a matched backing and broader acoustic bandwidth than undamped transducers. In the past, such transformers have been designed to match the load impedance to the characteristic impedance of the transducer material at the center frequency. A better procedure, which is adopted here, is to design the transformers to give a desirable impedance at the center terminal of the KLM model. Thus the front half of the transducer is itself treated as a quarter-wave matching layer, in addition to the quarter wave matching layers bonded to it. As opposed to the usual design procedure, Z_1 , the impedance of the first matching section is chosen to be the transducer material, so $Z_1 = Z_C$. The value of Z_{IN} , the input impedance to this section, is then determined. Thus a better broad-band match is obtained, because use is made of the extra matching layer which already exists in the device.

The design of quarter-wave transmission line matching sections has been formulated by Collin [11], Riblet [12], and Young [13] and others. Their designs call for the transmission line reflection coefficient magnitude $|r|$, or, alternatively, the power loss ratio $P_{LR} = 1/(1 - |r|^2)$, to exhibit either a maximally flat or Chebyshev response over the desired frequency passband. Larger passbands are achieved by the addition of more transformer sections.

A similar approach can be used in the design of the acoustic load line, although the acoustic impedance mismatches are typically much larger than the microwave ones; higher order terms are much bigger and should be included in the calculation of the reflection coefficient. Nevertheless, the design formulae developed for two and three layer transmission line sections can be applied to the acoustic case, and reasonably good results are obtained in exact numerical solutions.

As an illustration, the impedance formulae for the binomial transformer are given. This gives close agreement to the maximally flat case for a small number of matching sections.

$$\ln \frac{Z_n + 1}{Z_n} = 2^{-N} C_n^N \ln \frac{Z_T}{Z_{IN}} \quad (15)$$

where Z_T = terminating load impedance, Z_{IN} = input impedance of the transmission line system, Z_n = n th quarter-wave matching section impedance, C_n^N = binomial coefficient = $N!/n!(N-n)!$ and Z_R = effective impedance at the surface of the transducer

The results shown in Table I are used as the starting basis

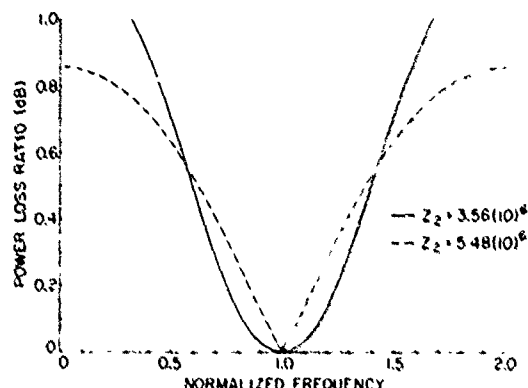


Fig. 3. Power loss ratios of front acoustic load line of lead metaniobate transducer matched with single quarter-wave plate.

for the transducer designs reported in this paper. In each case, Z_1 is the impedance Z_C of the transducer material.

As an example, consider the design of a transducer to be built using lead metaniobate with a water acoustic load. One bonded matching section is to be employed, and a maximally flat passband is desired for the front load line. Using Table I for the two layer transformer, and taking $Z_T = 1.5A$ and $Z_C = 20.0A$, the input impedance of the acoustic load line (Z_{IN}) is found to be 47.4A, over twice the material impedance. For comparison, the value obtained for this case by the criterion of (6) is 44.4A. So a two-section transformer is a good choice in this case.

The impedance of the matching layer (Z_2) is found to be 3.56A, which differs markedly from the value of 5.48A, the value calculated if the ceramic were assumed to be an infinite acoustic transmission line. The system tends to give a broader acoustic bandwidth, because the two matching layers have been taken into account and a broader electrical bandwidth with better efficiency, because it presents a higher electrical impedance at band center.

The power loss ratio (P_{LR}) through the matching layers is plotted as a function of frequency for both cases in Fig. 3. As can be seen, the ideal maximally flat response is obtained for the case when the matching layer impedance is 3.56A.

A similar calculation for a PZT-5A transducer matched into water ($Z_C = 34A$) yields a value of Z_{IN} for two matching sections of 96.2A, with three sections, $Z_{IN} = 53A$, $Z_2 = 8.9A$, $Z_3 = 2.34A$. The value of Z_{IN} for the three section matched system is slightly larger than the optimum value of $Z_{IN} = 48.2A$ using (6). So a three section transformer is a good choice in this case.

Therefore, it is concluded that the optimum lead metaniobate transducer matched to water requires only one extra matching layer with an impedance of 3.56, while the PZT-5A transducer requires two matching layers of impedances 8.92 and 2.34, respectively.

Wider passbands can be obtained for a given number of matching sections with Chebyshev response if passband ripple can be tolerated. As will be shown in the next section, the acoustic backing line, in general, limits the usable bandwidth of the transducer, so that this filter response is not as useful as might be. Moreover, the Chebyshev filter response yields

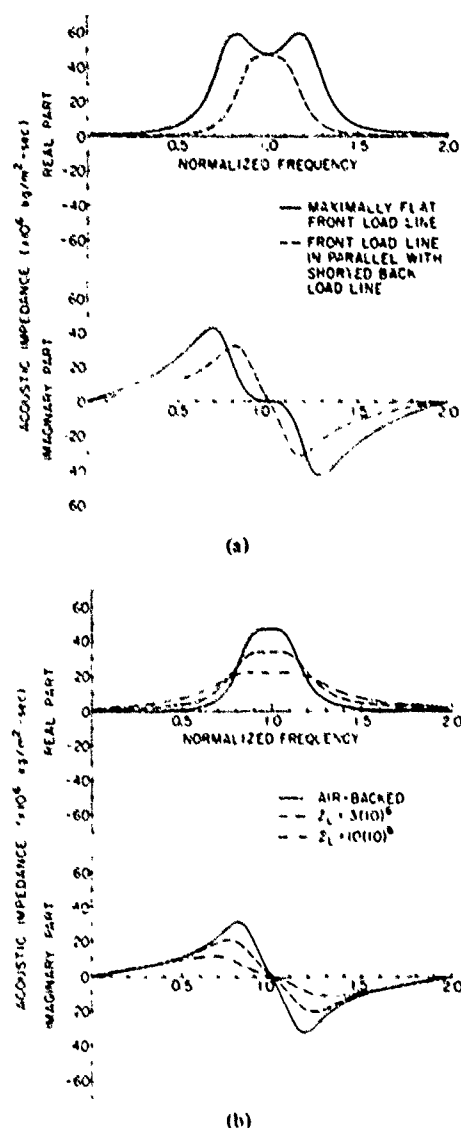


Fig. 4. (a) Effect of shorted back load line on acoustic impedance of maximally flat front load line. Lead metaniobate transducer (1.27 cm diameter). (b) Effect of resistively loaded back load line on acoustic impedance of maximally flat front load line. Lead metaniobate transducer (1.27 cm diameter).

steep skirts on the frequency response, which is undesirable in pulse-mode applications.

C. Back Acoustic Load Line

In the transmission line model, the acoustic impedance seen at the center node is the parallel combination of the input impedances of the front acoustic load line and the back acoustic load line. Ideally, the back load line should be designed to absorb as little power as possible, and to maintain or enhance the passband characteristics. As can be seen from (3) and (6), the optimum acoustic Q is expected to be

$$Q_d = \frac{\pi}{2(2k_f)^{1/2}} \quad (16)$$

This limits the useful bandwidth of an air-backed single quarter-wave matched PZT-5A transducer to about 45 percent, but numerical calculations indicate broader bandwidths in two layer matched transducers.

The effect of the shorted back load line on the input acoustic impedance is shown in Fig. 4(a), for the lead metaniobate transducer previously discussed. As can be seen, the bandwidth of the passband is considerably reduced and the band shape is considerably altered. As seen in Section A, the combination of the front load line with a low impedance shunted back load line is an optimum for high efficiency, broad-band designs. This is because the imaginary part of Z_{IN} varies linearly with frequency over the passband, so it tends to cancel out some of the errors introduced by the electroacoustic transformer and a simple tuned electrical tuning network. Such an effect does not occur with parallel inductance tuning, because the resistive part of the input impedance is changed by the presence of the inductor.

The next simplest back load line design would be the addition of a resistive load of impedance Z_L to the ceramic quarter-wave section. This is accomplished in practice by bonding a high loss material to the back of the piezoelectric ceramic to stimulate an infinite transmission line, so that no power is reflected back into the transducer from the back. The effect of resistive loads of varying impedance on Z_{IN} of the lead metaniobate transducer previously described is shown in Fig. 4(b). In general, as would be expected, the midband impedance is considerably reduced as the backing impedance is increased. When the backing impedance approaches Z_C , Z_{IN} becomes entirely resistive and equal to Z_C . It should be noted that most of the available power in this case is radiated into the back load line, since its impedance would be only about 40 percent of that of the front load line. With a large number of quarter-wave plates on the front load line Z_{IN} would approach Z_C , and the round trip insertion loss would approach 6 dB at best. In this case, Z_{IN} drops in value so broad-band electrical matching becomes more difficult. Thus this type of transducer would be optimized by using several quarter-wave plates with a more complicated matching network than just a simple inductance. Alternatively, the matching network could be omitted at the expense of a decrease in efficiency.

The use of a lossy backing of relatively low impedance is beneficial in the design of a quarter-wave matched transducer, however. The bandshape of Z_{IN} of a backed transducer changes as Z_L is increased, and becomes Gaussian shaped. The impulse response of the transducer is therefore improved, as will be described. The problem for the designer, then, becomes compromising bandshape versus insertion loss for this particular transducer configuration. A very low backing impedance of about 3 appears to be adequate for the single quarter-wave matched lead metaniobate transducer described above.

If the backing impedance were to be made large with respect to Z_C , Z_{IN} would approach a short circuit at the center frequency and increase to some peak value at approximately $\omega/\omega_0 = 0.5$ and $\omega/\omega_0 = 1.5$. The transducer could then be operated on a quarter-wave or three-quarter-wave resonance

Since in this case the electroacoustic transformer has a better response at low frequencies, a transducer built on this principle could be successfully operated as a quarter-wave transducer with only slight effects from the higher resonance. This design has been used by Bul *et al* [15] for a very broad bandwidth transducer which uses low impedance ($Z_C = 3.8\Omega$) PVF₂ as the piezoelectric element, mounted on a high impedance ($Z = 31\Omega$) brass backing. In this case, the electrical coupling is weak ($k^2 \approx 0.012$), but the acoustic matching to water is very good. Therefore, a large bandwidth untuned transducer can be constructed. This design would be difficult to use for transducers employing ferroelectric ceramics, since no backing material exists with a sufficiently high impedance.

D. Electrical Port

In order to minimize the insertion loss, the electrical input impedance of a transducer should be entirely real over the passband, and the radiation resistance (R_a) should equal the electrical source resistance (Z_0). For a lossless air backed transducer, the radiation resistance of the acoustic load is R_a . If the transducer has a resistive load on the back load line, the component of interest must be separated out from R_a . In addition, the frequency dependence of R_a should be tailored to fit some bandshape criterion, such as a Gaussian form, for optimum impulse response. As we have seen, the design of a low-loss, broad-band matching network is considerably eased if the electrical Q of the transducers is inherently low, which means using materials with large electroacoustic coupling constants (k^2).

The electroacoustic transformer in the transmission line model is frequency dependent, unlike the transformer in the Mason model. The impedance varies as $\text{sinc}^2(\omega/\omega_0)$. This function decreases with ω near $\omega = \omega_0$, so the radiation resistance tends to be higher at the low-frequency side of resonance. In the range $0.5 < \omega/\omega_0 < 1.5$, the variation of ϕ with frequency is almost linear. This effect is detrimental to the response of the transducer and should be compensated, either by an electrical tuning network or by weighting the high-frequency side of the passband by suitable acoustic matching. The latter approach, suggested first by Goll [6], is easily accomplished by increasing the thickness of the quarter-wave plate by a small amount, usually between 4 and 10 percent. The amount of this "skewing" has been determined empirically by trial and error computer simulation of the input impedance and insertion loss of the transducer in question. The effect of the quarter-wave plates operating at a slightly lower frequency than the ceramic compensates the frequency dependence of the transformer turns ratio, as can be seen in Fig. 5. The result is an approximately symmetrical bandshape, about a center frequency 90 to 96 percent of the half-wave resonant frequency of the ceramic.

The series reactance lumped element has a frequency dependence which varies as $(\sin \pi\omega/\omega_0)/\omega^2$. This term is always small compared to the reactance of the capacitor C_0 and can essentially be neglected in the design of octave bandwidth transducers.

The final intrinsic electrical element in the transmission line

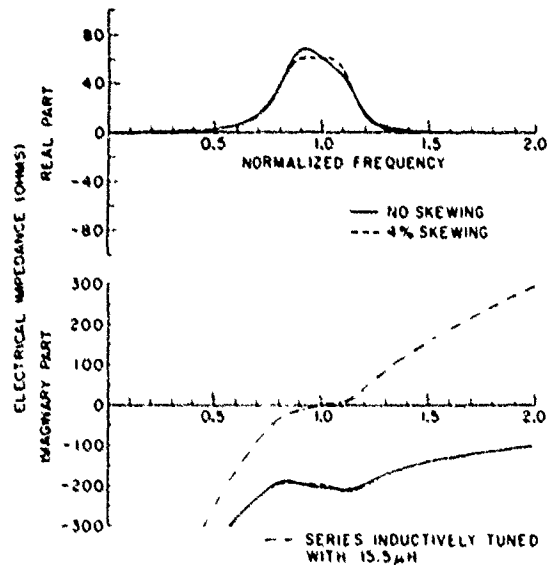


Fig. 5. Effects of increasing the thickness of single quarter plate 4 percent and series inductive tuning on electrical input impedance. Lead metanlobate transducer (1.27 cm diameter).

model is a capacitor C_0 , representing the zero-strain (clamped) capacitance of the piezoelectric material. As we have seen, for minimum insertion loss, this capacitance must be tuned out. This is most easily accomplished with a series inductance tuned for zero reactance at the center frequency, a procedure which is adequate for materials with large k^2 . Generally, a more sophisticated tuning network would be desirable for broader bandwidth operation.

In all cases, the design of an electrical matching network is highly dependent on the acoustic termination of the transducer. For the particular arrangement where the front matching plates are chosen to be maximally flat, the total imaginary part of the electrical input impedance is negative but varies like a negative inductance over the passband. Therefore, a series inductance rather than a parallel inductance just cancels the imaginary part of the impedance over the entire passband, as is discussed in Section A following (8) and as can be seen in Fig. 5. The input impedance thus becomes entirely real over the passband, as desired. An electrical transformer can then be employed to scale R_a up or down to the source impedance Z_0 . This is the design technique employed for the experimental transducers described in this paper.

E. Transient Response

A rigorous method of determining the transient response of a transducer is to take a Laplace transform of the frequency response as has been done by Onoe [4]. Further insight into the pulse response can be obtained by using paired echo theory in the manner described by Sittig [2]. Here we show how the KLM equivalent circuit can be employed directly to give some physical insight into the nature of the response. In this case, the series reactance C' seems to be of more importance. It is better represented by placing it on the acoustic side of the transformer as shown in Fig. 6. The effective reactance of this impedance now becomes

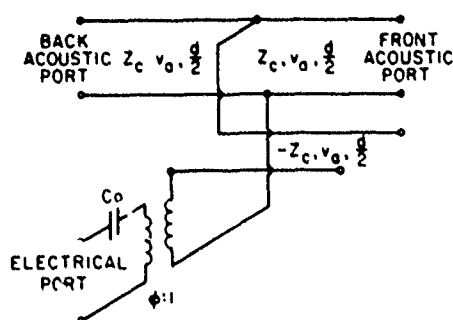


Fig. 6. Modified transmission-line model with series reactance represented by open circuited quarter-wave transmission line.

$$Z' = \frac{jZ_c}{2} \cot\left(\frac{\pi}{2} \frac{\omega}{\omega_0}\right). \quad (17)$$

Such a reactance may be represented by a transmission line of length $d/2$ with a negative characteristic impedance $-Z_c/2$, as shown in Fig. 6.

When the transformer is excited by a delta function of current, the current at its output can be determined by taking a Fourier transform of the function $\text{sinc}(\omega/2\omega_0)$. This yields a rectangular pulse of current which lasts for a time $T = \pi/\omega_0 = d/v_a$, i.e., half an RF cycle at the resonant frequency of the transducer. Physically, the transformer is representing the fact that the transducer is excited uniformly along its length.

Now consider what occurs when the transducer is excited by a step of voltage as illustrated in Fig. 7(a). An exact treatment is very difficult. However, it is apparent that the transformer will present a real impedance. Therefore, the input voltage will be differentiated and a delta function of current will be obtained at the output of the transformer, as shown in Fig. 7(b). Suppose now each end of the transmission line is terminated by the characteristic impedance Z_c . The impedance at the center point of the transducer, therefore, will be $Z_c/2$ in series with a negative impedance $-Z_c/2$, due to the negative impedance transmission line. Thus the delta function of current will excite, in turn, a delta function of current in the transmission line. A delta function of voltage will appear across this transmission line as shown in Fig. 7(c). After one-half RF cycle, a reflected pulse will also be emitted from the quarter-wave long negative impedance transmission line as seen in Fig. 7(c). This will be of opposite sign to the original pulse because the line is open circuited. These pulses will, in turn, excite a second set of pulses across the center terminal of the acoustic transmission line, as shown in Fig. 7(d), of opposite sign. The output obtained will be delayed but identical in form to that shown in Fig. 7(d) and is illustrated in Fig. 7(e).

The output is represented by a series of delta functions. However, as the impedance presented to the input load is finite, these delta functions will be rounded off so that a waveform more like that shown in Fig. 7(f) will be obtained.

A similar argument can be realized when the situation for a transducer with air backing is taken into account. This will give rise to an extra reflection at the air backing, so that the

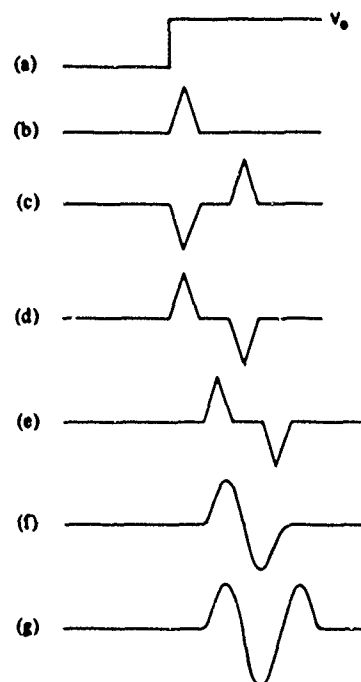


Fig. 7. Impulse response of transducer showing. (a) Step input voltage. (b) Current at output of transformer. (c) Voltage at input of negative impedance transmission line. (d) Voltage at center of line. (e) Voltage at output. (f) Voltage at output with finite impedance. (g) Voltage at output with air backing.

output obtained will have the form shown in Fig. 7(g). Excitation by a delta function pulse can be dealt with, going through the same type of analysis; this will give rise to similar results with slightly extended ringing.

A transient analysis of this kind is limited in its usefulness, although it can provide some physical feel for the problems entailed. A more useful technique in the long run is to employ a Laplace or Fourier transform to analyze the transient response of a transducer whose frequency response has already been determined theoretically [12]. On this basis, in order to obtain as clean a response as possible, a Gaussian output pulse is desired. But with a delta function input, i.e., a narrow pulse, this implies that the Fourier transform of this response in the frequency plane must be a Gaussian response. Thus, ideally, the frequency response of the transducer must be chosen to have a Gaussian shape. A square frequency response is not ideal because, although the bandwidth may be larger, it will tend to give a time response of the following kind:

$$F(t) = A \cos \omega_0 t \text{sinc} \frac{\Omega t}{2} \quad (18)$$

where ω_0 is the center frequency of the transducer as before, and Ω is its bandwidth. As might be expected, the addition of a relatively low impedance backing makes a difference to the transient response, and, in fact, tends to lead to a more Gaussian shape in the frequency response. Suitable transducers with reasonable transient response have been designed by bearing this consideration in mind and varying the backing impedance to obtain the best impulse response.

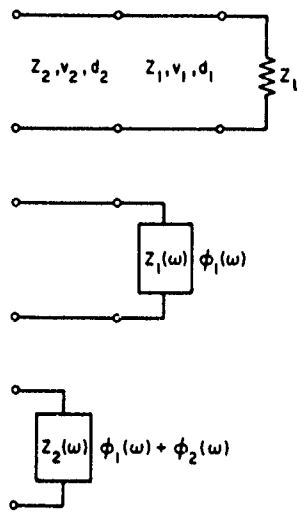


Fig. 8. Reduction of a load impedance Z_L through two quarter-wave plates of impedances Z_1, Z_2 , to an equivalent load impedance and phase shift, both functions of frequency.

III. COMPUTATION TECHNIQUES

A set of computer programs has been written to calculate the electrical impedance and insertion loss of a transducer as a function of frequency, and the impulse response as a function of time, by simulating the transmission line model of a transducer with arbitrary acoustic loads and matching layers at both the front and back acoustic ports, and with various electrical matching components. An iterative technique was used to refer the acoustic loads through the successive transmission line sections of the model to the center node, as shown in Fig. 8, using the standard transmission line impedance transformation formula for each section. At the same time, the phase shifts through each transmission line section and at each discontinuity calculated and kept for use in computing the transfer function of the transducer. Once the transmission line sections had been reduced to equivalent electrical impedance as functions of frequency, straightforward lumped circuit calculations were used to obtain the electrical impedance of the transducer, and the loss and phase shift from a known source, through an electrical matching network, to the load impedance representing the front load and matching layers. The calculation of the phase shift through the matching layers is made to determine the full transfer function as a function of frequency, which is then Fourier transformed to give the impulse response.

A simple formula has been derived for the phase shift through a matching layer. Consider an interface between media of impedances Z_{01}, Z_{02} , as shown in Fig. 9. If the wave impedance, looking to the right at the boundary, is Z_w , it can be shown that

$$\frac{v_1^+}{v_2^+} = \frac{Z_w + Z_{01}}{Z_w + Z_{02}} \quad (20)$$

where v_1^+, v_2^+ are forward wave velocity amplitudes. We also note that

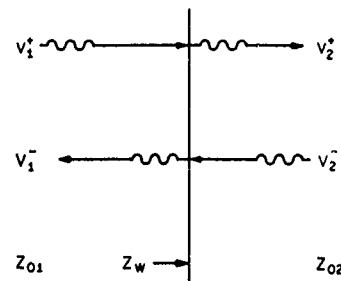


Fig. 9. Schematic diagram of forward and backward acoustic wave amplitudes at an interface.

$$\frac{v_1}{v_2} = \frac{v_1^+ + v_1^-}{v_2^+} = \frac{2Z_w}{Z_w + Z_{01}} \quad (21)$$

where v_1^+, v_1^- , and v_1 are the forward wave, backward wave, and total amplitude, respectively. The phase shifts between v_1^+ and v_2^+ and the phase shift between the forward wave and the total amplitude are just the phases of the complex ratio of impedance.

Since the wave impedance and the two characteristic impedances are available for each interface in turn, phase shift is easily calculated from (20). The phase between the equivalent current into the front load line and the forward going wave at the center node can be determined from (21).

IV. EXPERIMENTAL RESULTS

A 12.7-mm diameter, air-backed, single quarter-wave matched transducer was built using lead metaniobate as the active material. The parameters for the ceramic, supplied by Keramos Corp., and designated K-81 were measured using the technique of Bui *et al* [16] and determined to be as follows: $k_T^2 = 0.10$; mechanical $Q, Q_A = 24$; $\omega_0/2\pi = 2.06$ MHz, $\epsilon_{33} = 266 \epsilon_0$; $Z_C = 20.0$. A matching plate was fabricated by lapping a piece of Dow Epoxy Resin 332, hardened with metaphenylene-diamine to a thickness equal to a quarter-wavelength at $1.01 \omega_0$. The epoxy had a characteristic impedance of 3.38, slightly less than the optimal maximally flat value of 3.56.

The ceramic and epoxy plates were cleaned in organic solvents, heated for several hours to remove any absorbed solvents, and assembled in a dust-free laminar flow hood. The plates were bonded with epoxy under a nonuniform pressure device, as suggested by Papadakis [17], in order to remove trapped air bubbles and to insure a negligibly thin bond. The resulting assembly was mounted into a plastic housing. The electrical impedance was measured, and later a 13.9 μ H series tuning inductor and BNC connector were added.

The input electrical impedance of the untuned transducer is shown in Fig. 10(a). Excellent agreement with the theoretical calculation, which includes the finite loss of the ceramic, can be seen. The experimental electrical impedance was obtained using a Hewlett Packard Vector Impedance Meter. It can be seen that the impedance is very flat over the passband and slightly tilted because of the frequency dependence of the electroacoustic transformer. No quarter-wave plate "skewing" was used in this experiment. The imaginary part of the impedance shows a slight divergence from the theory at low frequen-

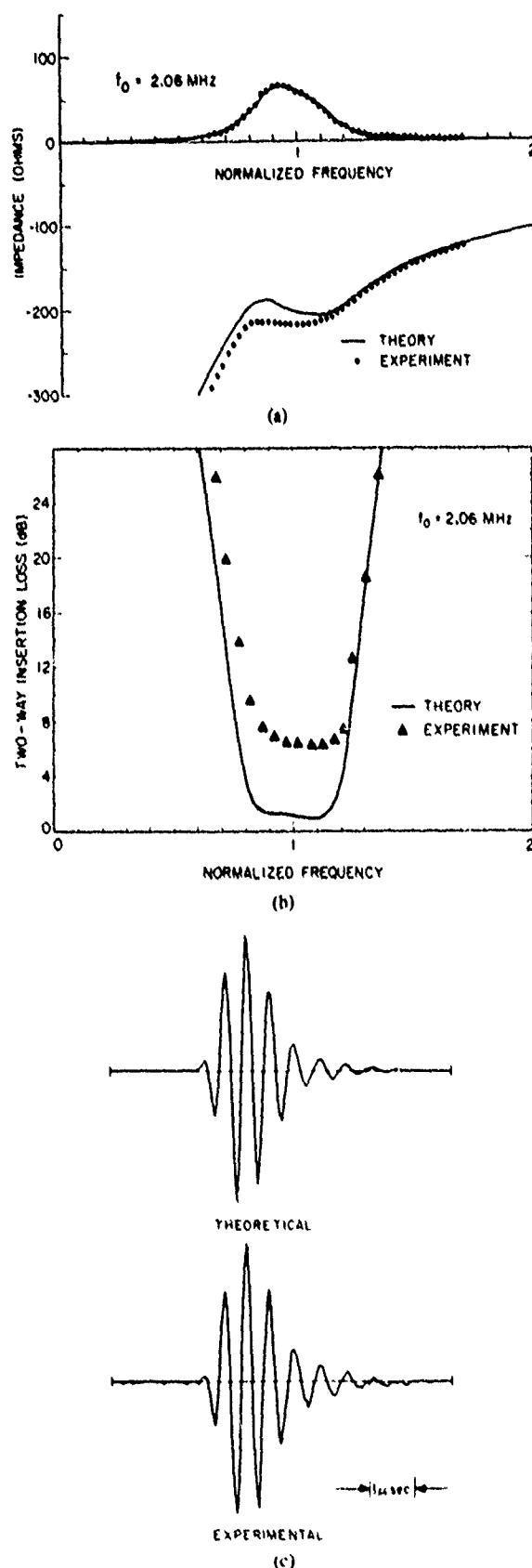


Fig. 10 Comparison of experimental results with theory for single quarter matched lead metaniobate transducer. (a) Electrical impedance (b) Two-way insertion loss (c) Impulse response

cies. This effect has not been satisfactorily explained yet, but could be due to two-dimensional effects not taken into account in the one-dimensional model.

An inductor of value $15.9 \mu\text{H}$ would be required to tune the transducer reactance at the center frequency. An available inductor of $13.9 \mu\text{H}$ was used. The two-way insertion loss of this transducer was measured by transmitting an acoustic wave from the transducer, excited by a $50\text{-}\Omega$ internal impedance tone-burst generator. The amplitude of the output of this generator into a $50\text{-}\Omega$ load was measured at each frequency, so as to determine the available power. The transmitted energy was reflected off of a perfectly reflecting air-water interface and received by the transducer loaded by the same $50\text{-}\Omega$ generator. A high-impedance probe was used to measure both the transmitted and received electrical voltages. The two-way insertion loss was calculated by comparing the available transmitted power and the received power as a function of frequency, and was compared to the theory, as shown in Fig. 10(b). The round trip insertion loss of the transducer was 6.5 dB at midband, compared to the theoretical value of 1 dB. The 3-dB bandwidth is 40 percent, as predicted, and the bandshape is flat over the passband, as designed. The additional 5.5-dB loss of the transducer over what was predicted is thought to be due to internal losses in the inductor and to phase cancellation, since the epoxy quarter-wave plate was slightly wedge-shaped.

A comparison of the experimental and theoretical impulse response of the untuned transducer is shown in Fig. 10(c). The theoretical impulse response was calculated by taking a fast Fourier transform of the transducer transform function, as previously described. The experimental results were obtained by shock exciting the transducer with a Panametrics Pulsar (Model 5050PR), using a $50\text{-}\Omega$ damping resistor in the circuit and digitizing the reflected echo off an air-water interface with a Biomation 8100 transient recorder sampled at a rate of 100 MHz. As can be seen, the agreement between theory and experiment is excellent.

A second transducer was designed using two quarter-wave plates on a 12.7 mm PZT-5A disk of resonant frequency 3.4 MHz. Chrome-nickel electrodes 200 nm thick were sputtered onto the transducer. These electrodes were negligibly thin acoustically at this frequency. This material was found to have parameters $k^2 = 0.25$, $\epsilon = 830 \epsilon_0$, and $Z_C = 34$, measured using standard techniques [18], [19]. Two available materials were chosen, a light borosilicate glass of impedance 11.0, and an epoxy of impedance 2.9. Calculations indicated that a flat and broad bandshape would be obtained if these plates were made a quarter-wave thick at 0.95 of the center frequency of the transducer; but in the plates actually produced, the equivalent numbers were 0.94 for the glass, and 1.00 for the epoxy. This 5-percent error in the thickness of epoxy plate was only $10 \mu\text{m}$, illustrating the difficulty of fabrication of these devices.

The quarter-wave plates were bonded successively to the PZT-5A disk with a low-viscosity epoxy, and the assembly was mounted in a plastic housing containing a series inductor to tune the impedance to a real value at the center frequency and an autotransformer to make this value 50Ω .

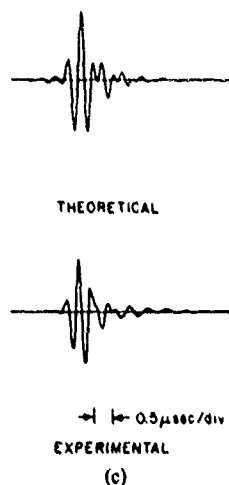
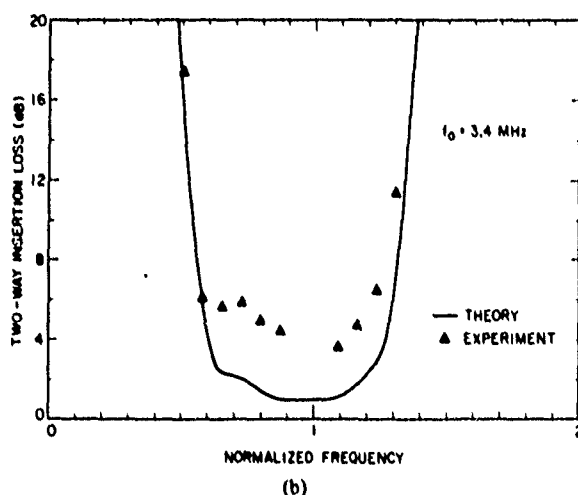
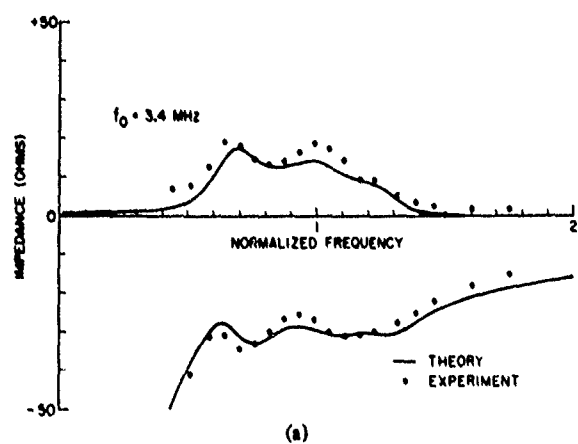


Fig. 11. Comparison of experimental results with theory for double quarter-wave matched PZT-5A transducer. (a) Electrical impedance. (b) Two-way insertion loss. (c) Impulse response.

The electrical impedance of the transducer was measured as a function of frequency before tuning, and is compared in Fig. 11(a) with the calculated values. After electrical matching, the round trip insertion loss as a function of frequency and impulse response were measured. The results of these

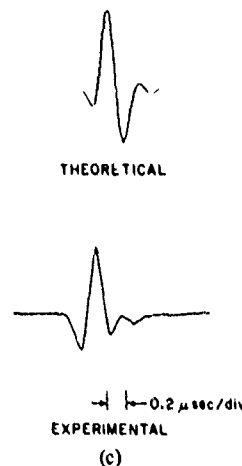
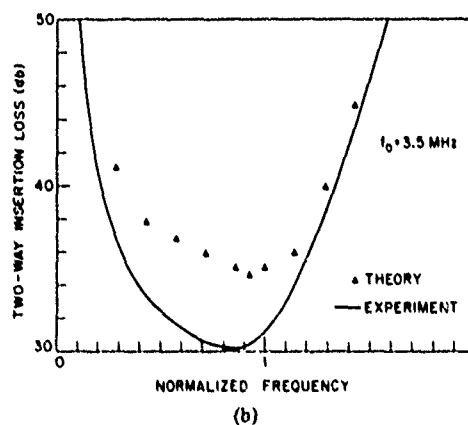
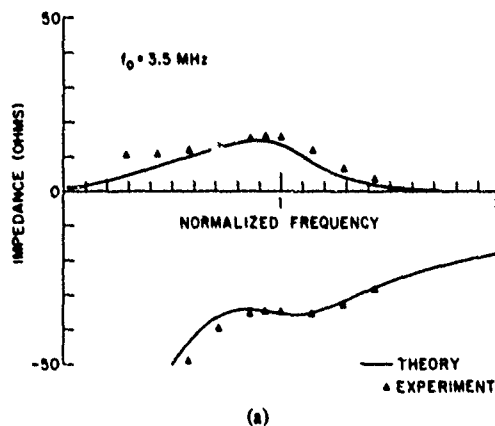


Fig. 12. Comparison of experimental results with theory for PZT-4 transducer matched with high-loss, high-impedance backing. (a) Electrical impedance. (b) Two-way insertion loss. (c) Impulse response.

measurements are compared to theory in Fig. 11(b) and (c). The measured insertion loss was 3.2 dB at 3.25 MHz, and the 3-dB bandwidth was from 2.0 to 4.2 MHz, greater than one octave. The impulse response was not as compact as one would like, but, as the calculation shows, this was to be expected from the rather square bandshape of this transducer design. Only about half of the measured insertion loss of 3.2 dB can be accounted for by losses in the electrical compo-

nents and by diffraction of the acoustic beam from a piston radiator; the rest may be due to nonuniformities in the epoxy quarter-wave plate and to deviation of the transducer model from the single mode piston radiator model.

For comparison, a simple disk transducer of PZT-4 was fabricated with no matching layers and a lossy tungsten-epoxy backing of impedance 26. The transducer disk was 12.7 mm in diameter and had a resonant frequency of 3.5 MHz. Its important material parameters were $k_T^2 = 0.24$, $\epsilon = 730 \epsilon_0$, and $Z_C = 34$. The impedance, insertion loss, and impulse response were measured as before. No electrical tuning was employed, and a 50- Ω source was used with a distance of 3.0 cm between the transducer and the reflector. These results are shown in Fig. 12(a), (b), and (c), respectively. In the impedance plot, note the small value of the resistance compared to the reactance at the center frequency. As was discussed earlier, this would lead to a high Q and narrow bandwidth if electrical tuning was used. The insertion loss plot shows the very high loss and broad, smooth bandshape characteristic of such transducers. The measured loss of 34.5 dB is close to the theoretical value of 30.2 dB. The 3-dB bandwidth is 105 percent. The outstanding property is the very compact impulse response.

V. CONCLUSION

A design technique for high-efficiency, broad-band piezoelectric transducers based on the transmission line transducer model of Krimholtz, Leedom, and Matthaei has been presented. Significantly improved quarter-wave matching techniques were demonstrated, both theoretically and experimentally. The method gives an estimate of optimum acoustic loading impedance for broad-band matching, and takes into account the transmission line nature of the piezoelectric transducer. Criteria for choice of materials for transducers and matching layers to achieve a desired bandwidth have been given, and the effects of a lossy backing on the electrical and acoustic Q 's and impulse response have been discussed. Experimental results have been given for several types of transducers, including one with 3.2-dB round trip insertion loss and 65-percent bandwidth.

REFERENCES

- [1] Sittig, E. K., "High Speed Ultrasonic Delay Line Design: A Restatement of Some Basic Considerations," *Proc. IEEE* 56-7, 1194-1202 (1968).
- [2] Meeker, T. R., "Thickness Mode Piezoelectric Transducers, *Ultrasonics*, 10-1, 26-36 (1972).
- [3] Mason, W. P., *Electromechanical Transducers and Wave Filters*, (Van Nostrand, Princeton, N.J., 1948).
- [4] Kossoff, G., "The Effects of Backing and Matching on the Performance of Piezoelectric Ceramic Transducers," *IEEE Trans. Sonics and Ultrasonics*, SU-13, 20-30 (March 1966).
- [5] Goll, J., and Auld, B. A., "Multilayer Impedance Matching Schemes for Broadbanding of Water Loaded Piezoelectric Transducers and High Q Resonators," *IEEE Trans. Sonics and Ultrasonics*, SU-22, 53-55 (January 1975).
- [6] Goll, J., Private Communication.
- [7] Reeder, T. M., and D. K. Winslow, "Characteristics of Microwave Acoustic Transducers for Volume Wave Excitation," *IEEE Trans. MTT-17*, 927-941 (1969).
- [8] Sittig, E. K., "Design and Technology of Piezoelectric Transducers for Frequencies above 100 MHz," *Physical Acoustics, Vol IX*, editors W. P. Mason and R. N. Thurston, Academic Press, New York, 221-275 (1972).
- [9] Krimholtz, R., Leedom, D., and Matthaei, G., "New Equivalent Circuits for Elementary Piezoelectric Transducers," *Electronics Letters* 6, 398-399 (June 1970).
- [10] Leedom, D., Krimholtz, R., and Matthaei, G., "Equivalent Circuits for Transducers Having Arbitrary Even-or-Odd-Symmetry Piezoelectric Excitation," *IEEE Trans. Sonics and Ultrasonics*, SU-18, 128-141 (July 1971).
- [11] Collin, R. E., "Theory and Design of Wide-Band Multisection Quarter-Wave Transformers," *Proc. IRE*, 43, 179-185 (February 1955).
- [12] Riblet, H., "General Synthesis of Quarter-Wave Impedance Transformers," *IRE Trans. MTT-5*, 36-43 (January 1957).
- [13] Young, L., "Tables for Cascaded Homogeneous Quarter-Wave Transformers," *IRE Trans. MTT-7*, 233-237 (April 1959).
- [14] Onoe, M. J. *Inst. Elec. Commun. Engrs. Japan* 44, 29 (1961) (Japanese), *J. Acoust. Soc. Am.* 34 (1964) 1247, *Physical Acoustics*, Vol. 1, Part A, edited by W. P. Mason, 1964, 468-475.
- [15] Bui, L. Shaw, H. J., and Zitelli, L. T., "Experimental Broadband Ultrasonic Transducers Using PVF₂ Piezoelectric Film," *Electronics Letters* 12, 393-394 (August 5, 1976).
- [16] Bui, L. Shaw, H. J., and Zitelli, L. T., "Study of Acoustic Wave Resonance," submitted to *IEEE Trans. Sonics and Ultrasonics*.
- [17] Papadakis, E. P., "Non-uniform Pressure Device for Bonding Thin Slabs to Substrates," *J. of Adhesion*, 3 (1971).
- [18] "I.R.E. Standards on Piezoelectric Crystals: Determination of the Elastic, Piezoelectric, and Dielectric Constants- the Electromechanical Coupling Factor, 1958," *Proc. IRE*, 46, 764-778 (April 1958).
- [19] "I.R.E. Standards Piezoelectric Crystals: Measurements of Piezoelectric Ceramics, 1961," *Proc. IRE*, 49, 1151-1169 (July 1961).

PIEZOELECTRIC SHEAR SURFACE WAVE GRATING RESONATORS

B. A. Auld and Bing-Hui Yeh
Edward L. Ginzton Laboratory
W. W. Hansen Laboratories of Physics
Stanford University
Stanford, California

Summary

This paper describes a new type of surface acoustic wave grating resonator in which the particle displacement of the surface wave is parallel to the surface. By contrast, the now well-known SAW (Rayleigh wave) grating resonator has its particle displacement in the sagittal plane.

In the SAW resonator the function of the grating structure, which consists of either grooves or metal strips, is to provide two highly reflecting Rayleigh wave mirrors, between which a standing wave is excited by means of an interdigital transducer. The basic function of the grating in the horizontal shear (SH) type of surface wave resonator considered here is quite different. An SH surface wave cannot exist on a homogeneous (unlayered) substrate in the absence of some periodic variation, such as a grating, along the surface. That is to say, the surface wave in this case is a vibrational mode of the grating itself. On the other hand, the grating is now not required to realize a highly reflecting mirror, because the SH motion reflects without spurious mode coupling at a traction-free boundary placed in any symmetry plane of the structure. For this reason this new type of resonator promises a substantial advantage in miniaturization compared with the conventional SAW resonator.

SH surface wave resonators on PZT-8, Y-cut X-propagating LiNbO_3 , and ST quartz have been fabricated and tested. Excitation was by means of an interdigital structure deposited on top of the grating teeth, and the dimensions were chosen to give a resonance in the region of 1 to 2 MHz. The groove depth was in the range of 0.01", and it was found that the diamond saw fabrication technique used did not provide adequate precision. Consequently the quality factors realized were low (< 3000), and use of relatively shallower etched grooves at higher frequencies is clearly called for.

Since a sufficient condition for the existence of this type of surface wave is a periodicity of the conditions along the surface, another technique for trapping the wave at the surface is deposition of an array of metal strips.

Key words Resonator, Grating, Horizontal Shear, Interdigital Transducer, PZT, Lithium Niobate, Quartz.

Introduction

In an earlier paper¹ the existence of a horizontally polarized shear (SH) surface wave on a corrugated substrate was demonstrated by virtue of the exact analogy between this elastic wave problem and the corresponding electromagnetic problem. An extensive literature exists for the latter case and the solutions given were found to be in good agreement with experimental results obtained for shear surface waves on a corrugated aluminum substrate. Observations were made by fabricating a finite length of corrugated surface (or grating) and measuring the transmission resonances with thickness shear transducers bonded to the ends of the finite length of grating. The surface nature of the wave was

confirmed by measuring gratings on substrates of different depths.

Although previous experiments confirmed the applicability of the electromagnetic solutions to the elastic wave problem, the transducers used excited both the surface wave of the grating and thickness waves of the substrate. The mode spectrum was therefore cluttered with many spurious responses and entirely unsuitable for resonator applications. The present paper describes an investigation of SH surface wave resonances on piezoelectric substrates. Efficient selective excitation of the grating is then achieved by suitably choosing the substrate orientation and depositing a transducer electrode on top of each tooth. As will be seen, individual resonant modes of a finite length of grating may be excited by suitably choosing the distribution of voltages applied to the electrode array.

It should be pointed out that the SH surface wave considered here is intimately related to the surface-skimming shear wave.^{2,3} The latter wave or, more properly, radiation pattern consists of a horizontally polarized shear elastic vibration skimming along the surface and slowly diffracting into the substrate. Diffraction losses are determined by the vertical directivity of the interdigital transducer (IDT) used for excitation. Consistent with the analogy of the IDT as an end-fire antenna array, the radiation pattern is sharpened and diffraction losses are reduced by increasing the length of the IDT. Addition of a grating structure to the surface permits the existence of a genuinely bound SH wave, which travels at a velocity slower than that of a bulk SH wave. If the IDT is suitably designed to synchronize with this bound wave, as in the case of a Rayleigh wave transducer, there will be essentially no diffraction loss into the substrate.

SH Waves on an Infinite Grating

One way of picturing an SH grating vibration is to imagine it as evolving from the standard tuning fork resonator shown in the upper left of Fig. 1. An analogous type of tuning fork, in which the arms move in face shear, is shown on the right. Stacking of a number of these resonators in an array leads to the tuning fork grating shown at the bottom of the figure, in which the dashed lines are traction-free surfaces. The basic SH grating (Fig. 2) evolves from this as the dimension is extended to infinity along the particle displacement direction and the individual supports are replaced by a continuous substrate. With a fixed tooth spacing d , the frequency increases with decreasing length of the teeth, just as in the case of the original tuning fork. The grating configuration provides a means for realizing a tuning fork type of resonance at frequencies where a single fork becomes too small to fabricate and mount.

Because the spatial period of the vibration in Fig. 2 is $2d$ the displacement field in the substrate can be written as the Fourier series shown in the figure, where a_n is the amplitude of the n^{th} Fourier component and the γ_n exponential coefficient γ_n is

related to the wavelength of a bulk shear wave by the equation on the line below. It follows from this that γ_n is real when $2d$ is less than a bulk shear wavelength. In this case all of the Fourier components decay exponentially into the substrate - that is, the motion is a surface vibration bound to the grating. This argument does not, of course, prove the existence of such a vibration, but its existence has already been demonstrated analytically in the case of the analogous electromagnetic problem.^{4,5}

The vibration shown in Fig. 2, which has a phase shift of π from one grating tooth to the next (the π -mode), is only one of many that can exist on this periodic structure. In the previous discussion, the grating was regarded as essentially an infinite array of tuning forks. Alternatively, one may look at the teeth as an array of cantilever supported face shear plate vibrators that are lightly coupled, one to the next, through the substrate. The vibration spectrum consists of a continuous distribution of coupled modes, analogous to the modes of a periodically mass-loaded vibrating string. In this case the phase shift from section to section is related to a continuous wave number $k = 2\pi/\lambda$, which takes the value π/d for the π -mode discussed above (Fig. 3).

As shown in References 4 and 5 the relationship between ω and k for this grating surface wave has the same form as for waves on the periodically loaded string. The frequency of the π -mode ($k = \pi/d$ in Fig. 3) corresponds to the lower edge of the stop band. Above this frequency the surface wave is nonpropagating (or cut-off). As the depth of the grating grooves is decreased, the frequency of the π -mode increases until the VSHEAR line is reached. This corresponds to the surface-skinning shear wave discussed above. In the so-called slow wave region below this line the solution is always a surface wave.

It should be emphasized that very little slowing is required to produce a well-confined surface wave. A Rayleigh wave, for example, has a phase velocity that is only some five percent below the bulk shear velocity but is confined to a depth less than a shear wavelength. One needs, therefore, only a shallow grating to trap the SH wave on the surface.

Finite Grating Resonators

To produce a standing surface wave resonance the grating structure must be terminated in a pair of mirror reflectors. In the standard SAW resonator these mirrors are realized by long (several hundred periods) grating arrays designed to operate in the cut-off region. For the SH surface wave resonator this is not necessary. A mirror can be realized by terminating the grating in a suitably located traction-free boundary. In the case of the π -mode this is easily seen by examining Fig. 2, where the particle displacement is along x and varies with y and z . From the symmetry of the vibration one has that the displacement u_x is maximum with respect to the z variation at the plane denoted by a dashed line in the figure. This means that the strain component S_{xz} and the stress component T_{xz} are zero on this plane. Since u_x is a function only of y and z , the stress components T_{yz} and T_{zz} are also zero - just the conditions required for a traction-free boundary, which acts as a perfect mirror. By further symmetry arguments one can show that the same boundary conditions acts as a perfect mirror for a surface wave with any wavenumber k .

Figure 4 gives the profile of an N section resonator contained between two such mirror reflectors.

As in any standing wave resonance, the resonance condition is that the length L be integral number n of half wavelengths or, equivalently, that $k = n\pi/ND$. For a 10-section resonator there are therefore ten modes of resonance, with frequencies determined from the dispersion diagram by the construction shown on the figure. A particular mode may be excited by applying the corresponding distribution of voltages to the electrodes located on the tops of the teeth. Our experiments have been performed on the π -mode in which alternate electrodes are excited 180° out of phase, as in a conventional IDT.

We have fabricated and tested three SH grating resonators with groove profile dimensions as given in the upper left of Fig. 4 and resonant frequencies for the π -mode in the range of 1 to 2.5 MHz. The resonator proper is defined by an electroded region on the top surface of a grooved block, large enough to eliminate edge effects and to permit probing of the vibration pattern outside the electrode region by means of small rubber damping pads. The grooves were first cut with a diamond saw, the top surface and reflecting edges were then polished, the electrodes deposited and the gold wire leads attached.

In these initial experiments no attempt was made to polish the inside of the grooves. As will be seen, this leads to problems with resonance broadening and coupling into spurious modes due to grating nonuniformity and surface roughness. It is clear that the best way to make these structures is by deep etching techniques.⁶

The importance of groove depth uniformity is clear from the dispersion curves in Fig. 4, where it is seen that the frequency of the π -mode is strongly dependent on the groove depth h . Nonuniform groove depth therefore causes different parts of the grating to resonate at different frequencies. This effect was observed in some of our gratings, where the vibration was found by mechanical probing to be localized in a small region of the grating. Tighter tolerances on the fabrication procedure were found to reduce this effect. It appears from these results that the resonance could be confined to a desired region of the surface by deliberately tailoring the depth profile of the grooves.

Mechanical probing of the resonators with small rubber pads confirmed the surface wave nature of the vibration and also demonstrated a lateral confinement of the vibration to the electroded region. A lateral decay distance of the order of 1 cm was observed outside the electroded region. This is due to mass loading by the electrodes, which effectively increases the depth of the grooves under the electrodes. Because of this lateral confinement transverse modes are also observed, as in standard SAW resonators.

PZT-8 Ceramic Resonator

The insert of Fig. 5 shows a highly schematic representation of the resonator geometry. Poling is in the direction indicated by the heavy arrow. Since it is not possible to pole over a 3" length, the block was fabricated from six 1/2" pieces carefully ground and bonded together with epoxy. No repolishing was performed after sawing the grooves, and the groove depth was measured to be approximately five percent greater at the left end of the grating than at the right. When the two halves of the grating were excited independently, different resonant frequencies were obtained - as expected, the lower frequency corresponding to the larger groove depth.

Figure 5 shows the measured input impedance characteristic for the entire grating - the small peak at 1.120 MHz corresponding to the deep end of the grating. A variation of groove depth in the order of five percent corresponds to a frequency variation in the order of one percent. The estimated resonator Q is of order 200, compared with a material Q of order 400 determined by pulse echo measurements in a large block.

We have also tested the same geometry as a Rayleigh wave grating resonator, with the poling in the vertical direction in Fig. 5. As anticipated the Q is much lower (of order 50) because traction-free boundaries do not act as good mirrors for Rayleigh wave motion.

Y-X Lithium Niobate Resonator

A lithium niobate resonator was made in order to more clearly isolate the effects of surface roughness and resonator geometry on the Q-factor. As shown in Fig. 6 a resonator of somewhat different dimensions was made on a single crystal block, using the same fabrication method. The top surface is Y-oriented and the grooves are along Z. By cutting the grooves before polishing the top surface and finishing afterwards, grooves with clean upper corners were obtained. They were, however, very fragile and had to be handled with great care.

The impedance curve in the figure is for an unsupported sample and exhibits a very dense spectrum of spurious bulk modes in the region of the main and transverse surface wave resonances. Appearance of strong spurious modes only in the region of surface wave resonance indicates that the spurious coupling is through mechanical imperfections of the grating and not directly from the electrodes.

Figure 7 shows, on the same scale, the impedance characteristics after gluing the ends of the lithium niobate block. The bulk modes are now strongly suppressed, although some spurious is still apparent near to two transverse resonances on the high frequency side of the main resonance. There is now a strong surface wave resonance with a maximum impedance of 300 k Ω , and Figs. 8 and 9 show that the maximum spurious response over the range from 1 to 7.5 MHz is 4 k Ω .

Figure 10 gives on a logarithmic scale the detailed impedance response in the vicinity of the resonance and antiresonance points. Because of the large number of spurious modes near the series resonance point, it is not possible to calculate the Q by the standard procedure, but it is estimated to be not more than 2000. This very low value is clearly due to the energy loss coupled into a large number of bulk modes and subsequently dissipated in the supports. Further precision in grating fabrication is obviously called for.

ST Quartz Resonator

Figure 11 shows the geometry of a grating resonator on a 39.3° "ST" quartz plate with the grooves along the X direction. Note that the thickness of the substrate is much less than in the other examples. Although the resonator is unmounted the spurious mode response is small compared with the lithium niobate case, and the response is clean outside the 10 kHz frequency range shown.

As in the PZT resonator the low frequency peak is attributed to nonuniformity of groove depth. Since this second peak occurs very close to the main series resonance point, it is not possible to arrive at an ac-

curate evaluation of Q. We estimate a value in the order of 3000.

Conclusions

In summary, we have experimentally verified the surface character of SH vibrations on deep grating structures and have measured some of the properties of grating resonators of this type operating on PZT-8, YX lithium niobate and ST quartz in the frequency range of 1 to 2 MHz. Q-factors obtained are low, not more than 3000. This is due in part to technical difficulties in accurately and uniformly fabricating the large grooves required at these low frequencies and in part to mode scattering due to the effect of substrate anisotropy on the behavior of the traction-free reflector surfaces.

The fabrication problems encountered point up the need to study shallower grating resonators operating at higher frequencies. As pointed out earlier, only a small amount of slowing is needed to trap the SH vibration on the surface, and the grooves need only be a small fraction of a wavelength in depth. Since the periodicity needed for wave trapping may also be induced by periodic boundary conditions on the surface, an attractive alternative is mass-loading or electrical short circuit strips deposited on the substrate surface.⁷

The major potential advantage of the SH grating resonator over the standard SAW structure is in its small size. Because the grating itself does not serve as a mirror, only a small number of periods is required. Also, the presence of a spectrum of resonator modes that can be selected by appropriate coding of the applied electrode voltages suggests the possibility of small multipole monolithic filters at very high frequencies.

Acknowledgements

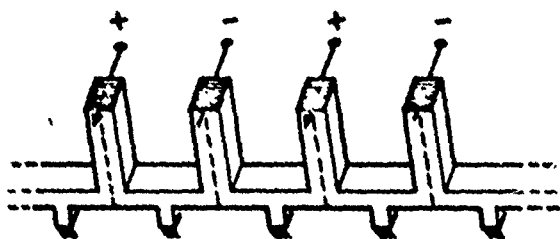
The authors wish to acknowledge the able technical assistance of W. Bond, L. Goddard, G. Kotler and D. Walsh.

This work was sponsored by the Joint Services Electronics Program under Contract N00014-75-C-0632.

References

1. B. A. Auld, J. J. Gagnepain and M. Tan, *Electronics Letters* **12**, pp. 650-651 (1976).
2. T. I. Browning and M. F. Lewis, these Proceedings.
3. K. H. Yen, K. L. Wang and R. S. Kagiwada, these Proceedings.
4. R. A. Hurd, *Can. J. Phys.* **32**, pp. 727-734 (1954).
5. R. A. Collin, "Field Theory of Guided Waves," pp. 465-469, McGraw-Hill (1960).
6. C. A. Adams and J. A. Kusters, these Proceedings.
7. A. A. Oliner and A. Hessel *Trans. IRE AP-7*, pp. 5201-5203 (1959).

TUNING FORK "GRATING"



TUNING FORK RESONATORS

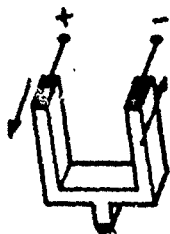
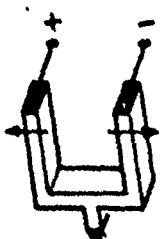
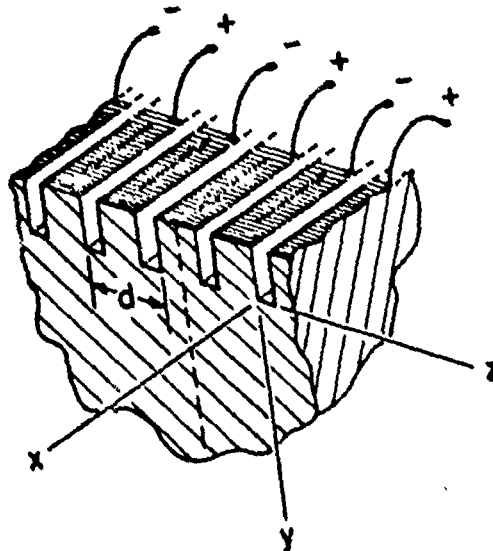


FIGURE 1. A Conventional flexural tuning fork resonator is shown in the upper left and a "face-shear" analogue in the upper right. The bottom of the figure shows a primitive horizontal shear grating resonator realized by stacking "face-shear" tuning forks.

INFINITE GRATING ON AN ISOTROPIC SUBSTRATE



$$u_x(y, z) = \sum_n a_n e^{\gamma_n y} e^{-i \frac{n\pi}{d} z}$$

$$-\gamma_n^2 = \left(\frac{2\pi}{\lambda_{\text{SHEAR}}} \right)^2 - \left(\frac{n\pi}{d} \right)^2 < 0$$

$$\text{WHEN } d < \frac{\lambda_{\text{SHEAR}}}{2}$$

SURFACE VIBRATION

FIGURE 2. Horizontal shear grating on a semi-infinite substrate. Vibration is in the n -mode.

WAVES ON PERIODIC STRUCTURES

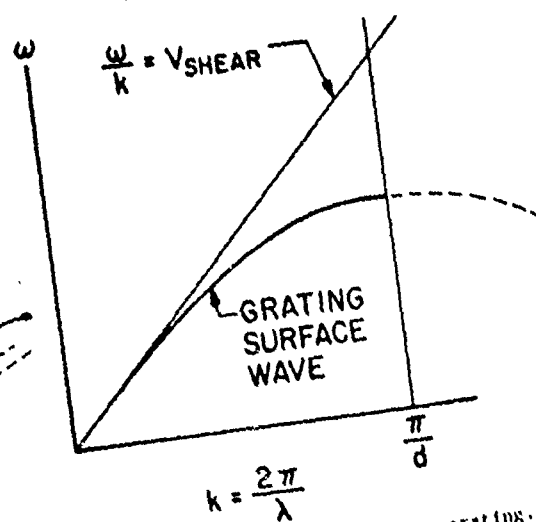
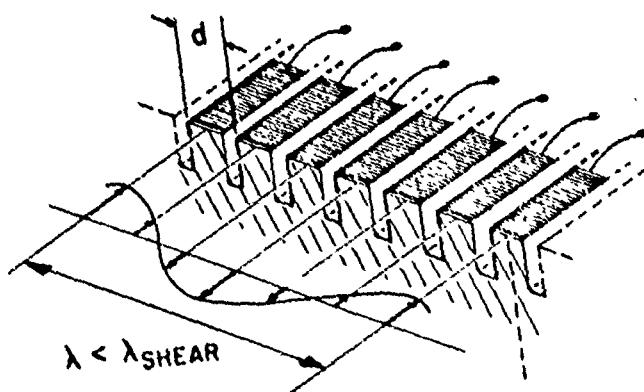


FIGURE 3. Typical form of the lowest branch of the dispersion relation for the horizontal shear grating.

RESONATOR GEOMETRY

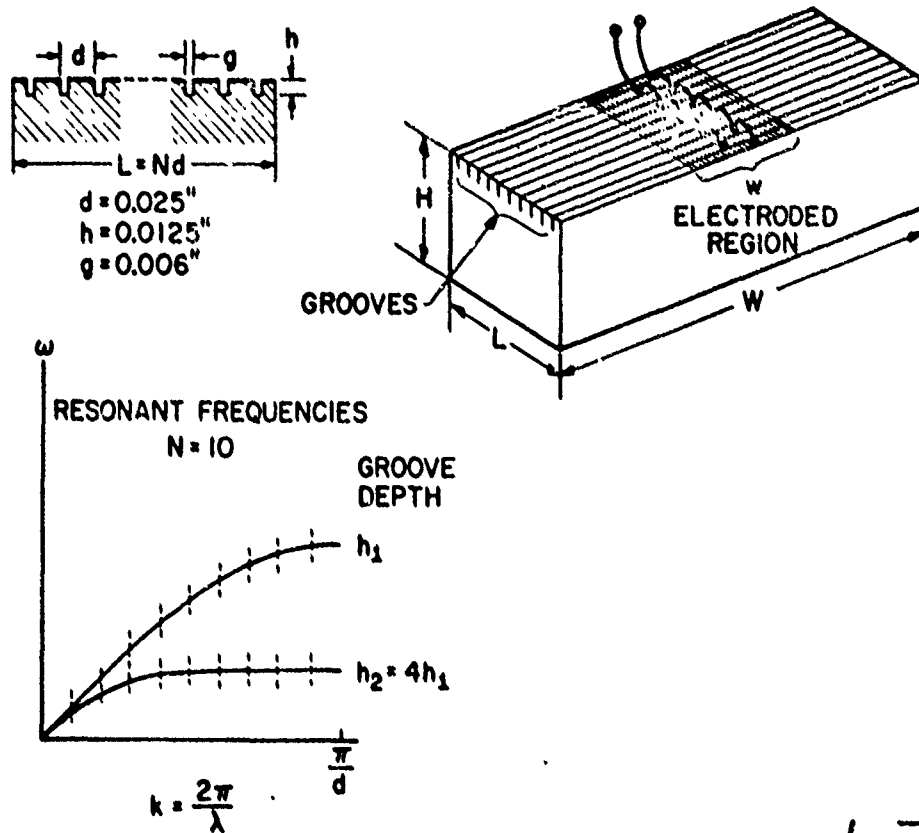


Fig. 4 Basic resonator structure and relationship between the dispersion relation and the resonant mode spectrum.

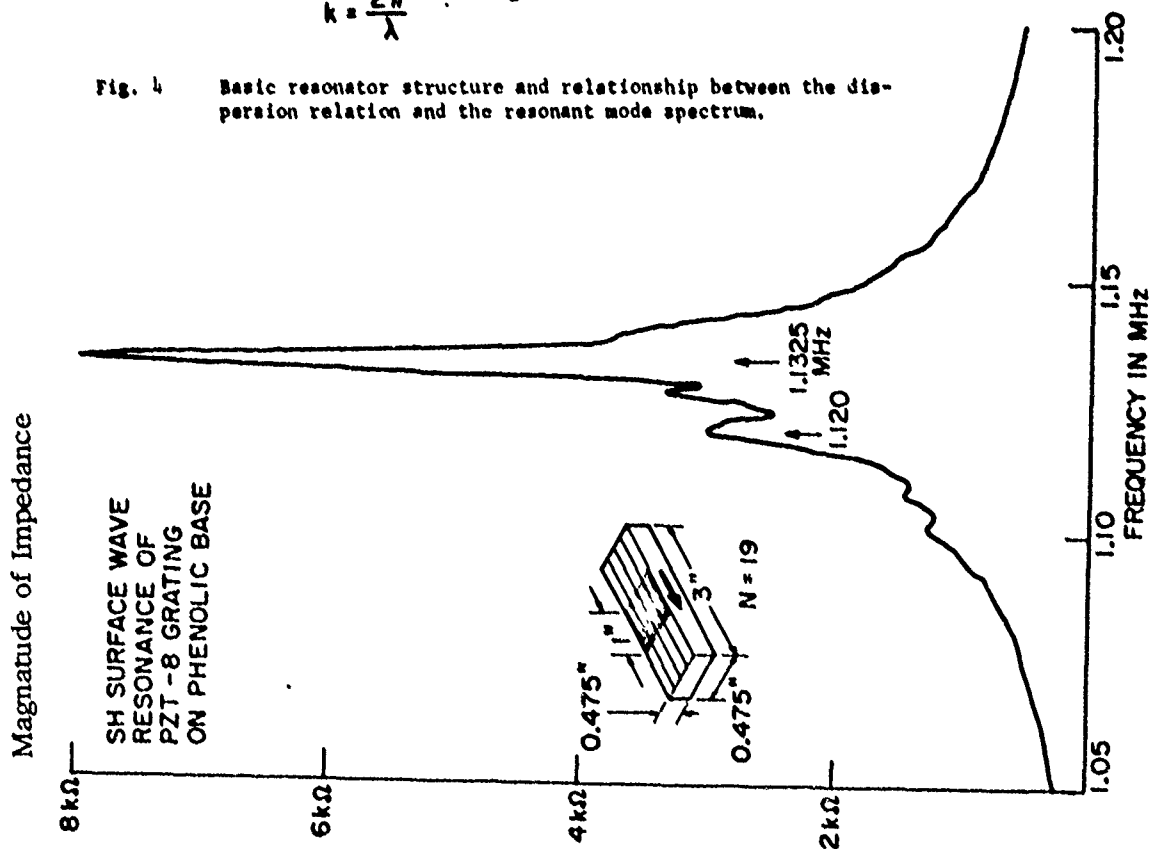


Fig. 5 Measured impedance-frequency curve of PZT-8 resonator. Poling direction is indicated by the heavy arrow.

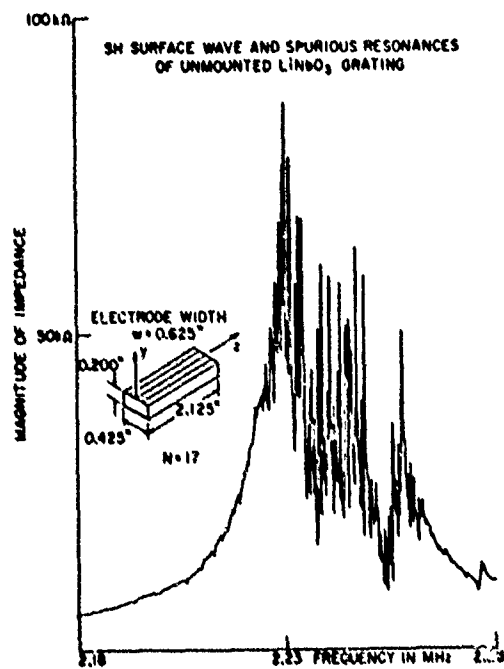


FIGURE 6. Impedance-frequency response of Y-oriented X-propagating LiNbO_3 grating resonator, showing a dense spectrum of spurious bulk resonances superposed on the main and trans-surface wave resonances. Area of the electrode region (not shown) is $0.425'' \times 0.625''$.

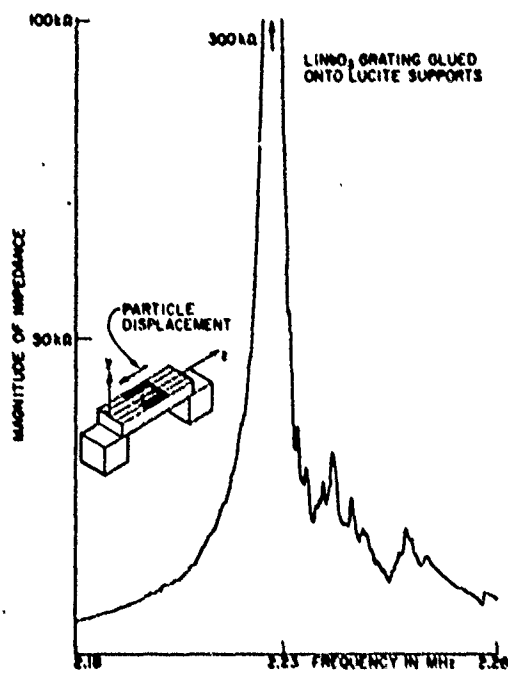


FIGURE 7. Same as Fig. 6, but with ends of the substrate glued to lucite supports. Note the two transverse mode resonances, with superimposed spurious resonances, on the high frequency side of the main resonance.

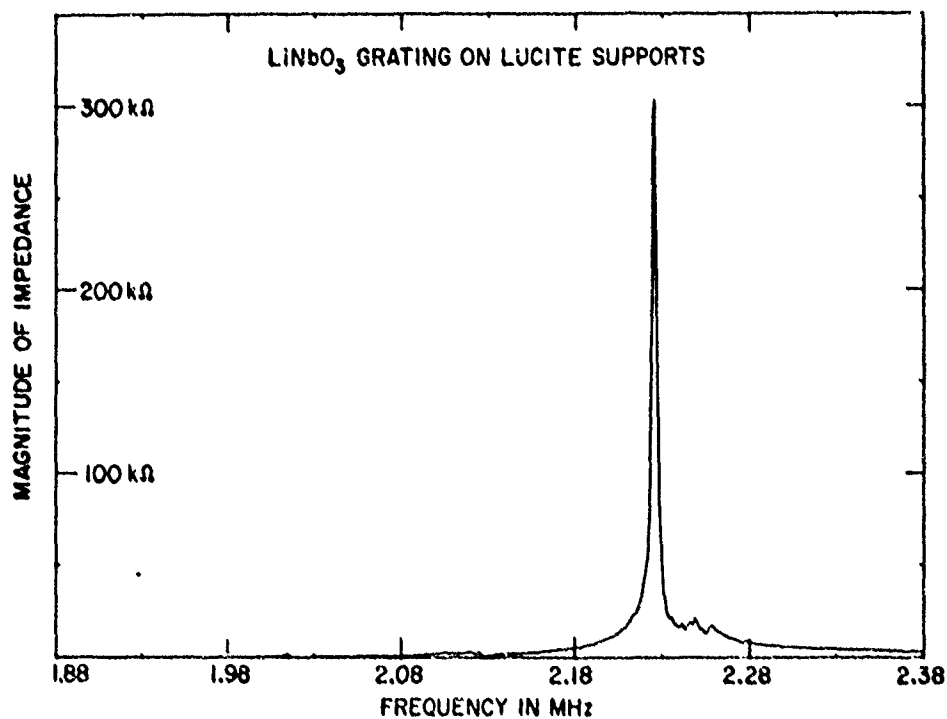


Fig. 8 Impedance-frequency curve of the LiNbO_3 grating, showing the peak of the main resonance and a wider portion of the skirts.

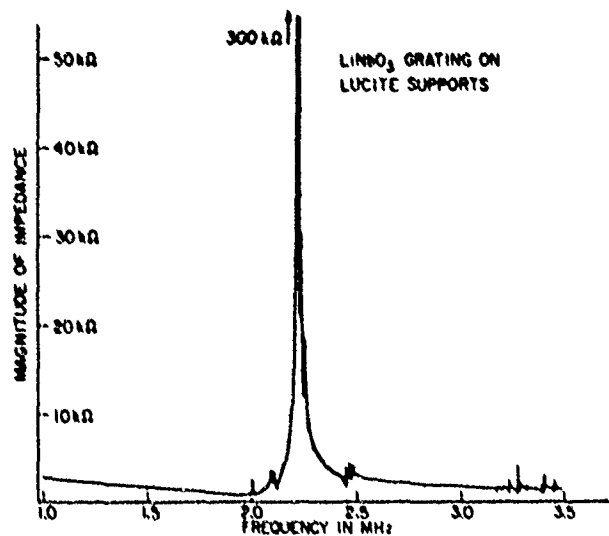


FIGURE 9. Illustration of the spurious mode response between 1 MHz and 3.5 MHz. Measurements out to 7.5 MHz showed a maximum spurious impedance peak of 4 kΩ over this frequency range.

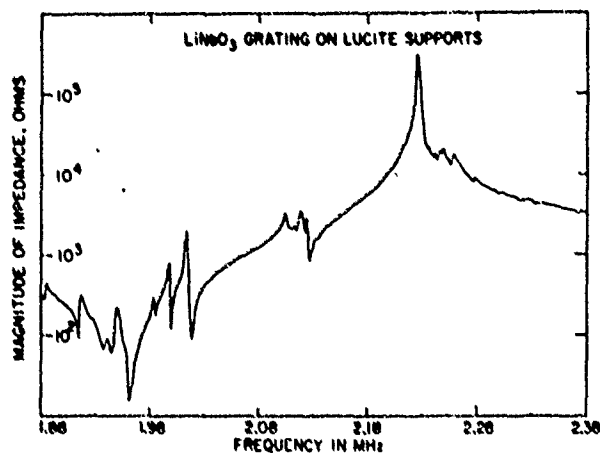


FIGURE 10. Logarithmic impedance curve in the vicinity of the resonance and antiresonance points.

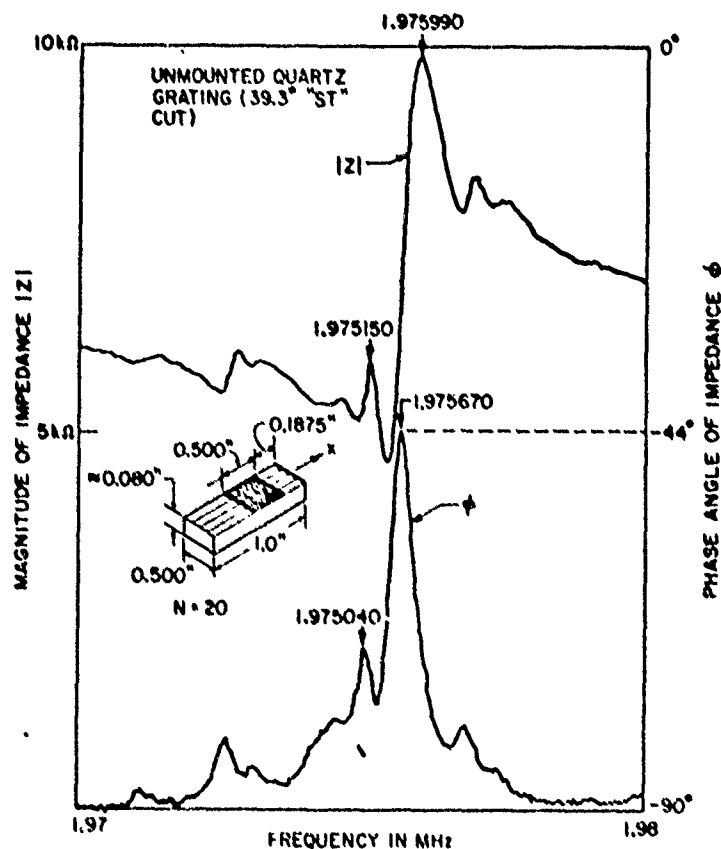


Fig. 11 Impedance-frequency curve of unmounted quartz grating on a 39.5° "ST" plate.

Phase imaging in reflection with the acoustic microscope

A. Atalar, C. F. Quate, and H. K. Wickramasinghe

Edward L. Ginzton Laboratory, Stanford University, Stanford, California 94305
(Received 22 August 1977; accepted for publication 3 October 1977)

When a polished surface of a single crystal is examined with a converging acoustic beam the reflected signal has a characteristic response that is dependent upon the elastic properties of the reflecting surface. This property can be used in the acoustic microscope to monitor the thickness of layers deposited on these surfaces and the small-scale variations of the elastic parameters in these materials.

PACS numbers: 43.20.Fn, 43.35.Yb, 43.35.Sx, 68.25.+j

In our studies of the acoustic reflections from smooth surfaces of single crystals we have learned that various materials have a characteristic response determined by the elastic properties of the surface itself. We use the acoustic microscope to monitor this effect. We have determined that metallic, or dielectric layers, deposited on these surfaces alter this response in such a way that we can determine the thickness of these layers and locate some of the subsurface defects.

In the microscope¹ we use a strongly converging beam normally incident to the liquid-solid interface at the surface of the object. It has been our usual practice to record micrographs with the sample surface at the focal point of the beam. There the beam is more or less collimated and the returning signal has a maximum value. The details and contours of the surface are portrayed with moderate contrast, as expected from conventional imaging theory. What is unexpected, at least to us, is the fact that the smooth surfaces with different elastic parameters generate reflected signals that have a distinct characteristic for each material. This distinction shows up when the sample is translated along the axis of the beam toward the lens. There we find important differences in the profile of the reflected beam as compared to the mirrorlike reflections from a rigid surface.² At this interface the velocity difference is large, the critical angles are small, and much of the incident energy is totally reflected. In analyzing this problem we decompose the incident beam into an angular spectrum of plane waves with incident angles extending from 0 (normal incidence) to 50° (the half-width of the beam). Those rays with an incident angle that is larger than the critical angles undergo total internal reflection. They are reflected with an amplitude equal to that of the incident ray and with a phase shift that is determined by the ratio of the incident angle to the critical angle. These phase shifts—known as the Goos-Hanchen shifts in optics³—alter the focal properties of the returning beam in a way that is unique to each material. The relative phase shifts for the totally reflected rays will change in the presence of a thin film at the interface and this too can be easily observed at the output of the transducer. We believe that this mechanism can be used to explain the reversals in image contrast that have been observed by Wilson⁴ in acoustic micrographs.

The geometry for the reflection microscope is depicted in Fig. 1. There element 1 is the piezoelectric transducer. It serves to convert the rf voltage across the film into a plane wave of sound propagating normal to the film. As a receiver for the wave reflected from

the sample it is sensitive to the phase of the returning wave. The output voltage is equal to the acoustic field of the returning pulse as integrated over the area of the transducer—an important feature of our system since we monitor and display the voltage amplitude, V . Element 2 is the acoustic lens which serves to focus the plane wave from the transducer into a waist at the focal point. Element 3 is the reflecting object that we want to characterize by translating this object along the z axis. Finally, we note that we use a 4-nsec pulse at the input and include a circulator to separate the input from the output. We also use time gating to separate the pulse reflected from the object from other spurious reflections.

We monitor the amplitude of the transducer voltage and record it as $V(z)$ in order to distinguish this displacement along the axis of the beam from the lateral scanning that is used to record conventional acoustic micrographs. The z coordinate is measured from the focal point and positive values correspond to lens-object spacings greater than the focal length.

These curves for $V(z)$ combine both the transducer response and the reflection characteristic of the object. We can separate these and analyze the transducer response by first assuming that the object is a rigid surface. The incident wave does not penetrate the interface of such an object and it is reflected as a mirror image. For this reflector the rf voltage across the transducer will reach its maximum value when the reflector is placed at the focal plane ($z = 0$). When the

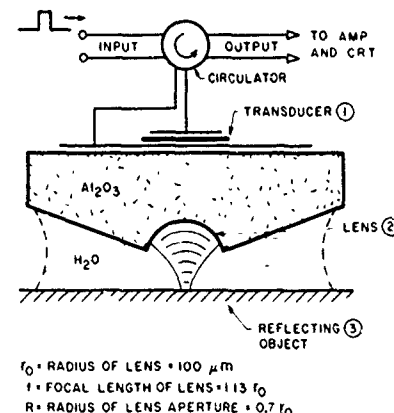


FIG. 1. The geometry of the acoustic transducer and lens used for the reflection mode of the acoustic microscope.

sample spacing is decreased (negative z) the reflected wave reaches the transducer in the form of a spherically diverging wave. There the transducer is excited with alternating regions of positive and negative phase and the integrated response is reduced. Similarly, the transducer response is reduced when the sample spacing is increased for then the reflected wave at the transducer is a converging spherical wave. If we neglect the transducer-lens spacing and assume that the system is lossless, we can work out a simple expression for $V(z)$. It is of the form $\sin[\pi(R/f)^2 z/\lambda_0] \pi(R/f)^2 z/\lambda_0$. The terms are defined in Fig. 1. For that lens this function with a maximum at $z=0$ has a null at $z = (f/R)^2 \lambda_0 = (1.13r_0/0.7r_0)^2 \lambda_0 = 2.6\lambda_0$. The rigid reflector model has been used by both Weglein and Kompfner⁵ to explain the contrast reversal that have been observed in micrographs of integrated circuits.⁴ This model is inadequate since different elastic materials produce the same response and this does not conform to our observations. The rigid model, therefore, needs to be replaced with a reflector that is elastic.

We can modify the relation for $V(z)$ given above by calculating the correct value for the reflectivity of the actual object. We begin as before by decomposing the incident beam into an angular spectrum of plane waves. Each of these plane waves is incident upon the interface with a different angle and we evaluate the amplitude r and the phase, ψ , of the reflectivity coefficient as a function of θ , the angle of incidence. Plots of these two parameters for some simple crystals⁶ immersed in water are shown in Fig. 2. We can see that the amplitude of the reflectivity coefficient is slightly less than unity when the incident angle is less than the critical angle and it is equal to unity for incident angles greater than the critical angle. The structure in this curve corresponds to the excitation of various modes in the solid.⁷ It need not concern us since most of the energy is returned toward the lens. We are concerned, however, with the phase of the reflected rays. Those rays with small incident angles are reflected with a zero phase shift, while those rays with large incident angles are reflected with a phase shift that approaches 2π . The information is contained in the phase of the reflected components, and with different materials and

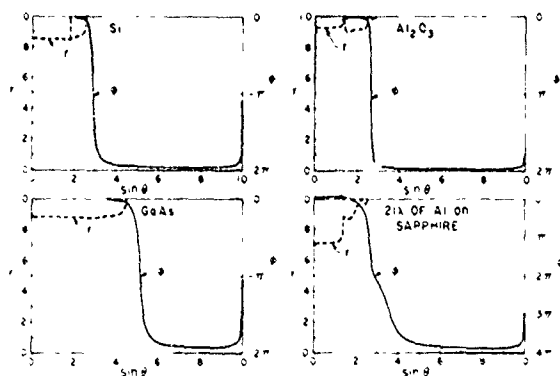


FIG. 2. The reflectivity for the labeled surfaces as a function of $\sin\theta$ where θ is the angle of incidence for plane waves. The reflection coefficient is given by $r \exp(j\psi)$. The amplitude and phase are plotted separately.

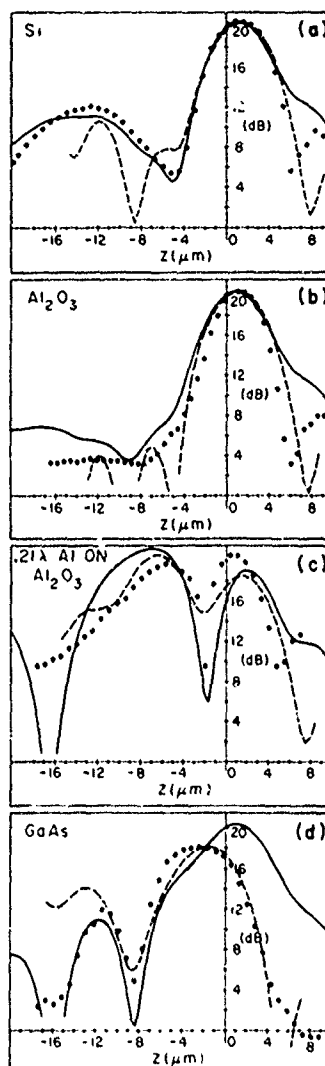


FIG. 3. The $V(z)$ curves representing the transducer output versus the lens-object spacing, z . The dotted points are the measured response at 750 MHz. The dashed curves are from the computer program which includes loss in the liquid. The solid curves come from the paraxial ray equations with a lossless fluid.

different layering both the critical angle itself and the slope of the curve are altered.

These curves for the reflectivity coefficient, amplitude, and phase are used to characterize each surface and they are used in calculating the response of the output transducer. A computer program has been written for this purpose and the computed curves for the four materials given in Fig. 2 are shown as the dashed lines in Fig. 3. We have also used the *paraxial ray* approximation as a second approach to calculate the $V(z)$ curve. There we assume that all of the waves in the Fourier decomposition intersect the z axis with a small angle. In a number of cases this gives a closed-form expression which adds a great deal to our physical insight. The calculated curves from the paraxial ray equations are shown as the solid lines in Fig. 3. The acoustic loss of the liquid has been neglected in these

curves. The measured results in Fig. 3 were recorded using a crystal with a transducer-lens spacing of 1.25 mm and the diffraction spreading of the beam over this length degrades the illumination of the lens. We suspect that this is the reason for the agreement between the paraxial ray equations and some of the experimental curves.

We have found in this study that the acoustic microscope can be used in conjunction with the axial translation of the sample to study the elastic properties of the surface on a dimensional scale that measures $1\ \mu$ in the lateral direction and $1\ \mu$ in depth. We believe that the information as gathered in this manner should be useful in studying subsurface defects, identifying different constituents that make up the surface in complex alloys, and in monitoring the layer thickness in fabricated microstructures. Although we have included no images here these curves do influence that work since small variations in the elastic parameters are more easily seen in the micrographs when the z -axis position coincides with the minimum of the curves of Fig. 3.

We want to express our appreciation to both R.G. Wilson and P.K. Tien for discussing their work with us prior to publication. This work was supported pri-

marily by the NBS/ARPA Program on Semiconductor Electronics and in part by the Joint Services Electronics Program (JSEP).

¹R. A. Lemons and C. F. Quate, Appl. Phys. Lett. 25, 251 (1974); C. F. Quate, *Semiconductor Silicon 1977*, Proc. Vol. 77-2, edited by H. R. Huff and E. Sirtl (Electrochemical Society, Princeton, 1977), p. 422.

²M. A. Breazeale has studied the reflection of acoustic beams from a water-steel interface and compared this with that from a water-aluminum interface. He finds that the profiles of the reflected beam are quite different. See M. A. Breazeale, L. Adler, and G. A. Scott, J. Appl. Phys. 48, 530 (1977).
³M. McGuirk, C. K. Carniglia, J. Opt. Soc. Am. 67, 103 (1977); 67, 121 (1977); P. K. Tien, Rev. Mod. Phys. 49, 361 (1977).

⁴R. G. Wilson, R. D. Weglein, and D. M. Bonnell, *Semiconductor Silicon 1977*, Proc. Vol. 77-2, edited by H. R. Huff and E. Sirtl (Electrochemical Society, Princeton, 1977), p. 431.

⁵R. D. Weglein and R. Kompfner (private communications).

⁶B. A. Auld, *Acoustic Fields and Waves in Solids* (Wiley-Interscience, New York, 1973), Vol. 1, Table A.4.

⁷L. M. Brekhovskikh, *Waves in Layered Media*, edited by R. T. Beyer (Academic, New York, 1960), p. 34.

ANTI-STOKES EMISSION AS A VUV AND SOFT X-RAY SOURCE*

S. E. Harris, J. Lukasik,[†] J. F. Young, and L. J. Zych
Edward L. Ginzton Laboratory
Stanford University
Stanford, California 94305

A VUV and soft x-ray light source based on spontaneous anti-Stokes scattering from atomic population stored in a metastable level is described. Unique properties of this source include: narrow linewidth, tunability, linear polarization, picosecond time scale, and quite high spectral brightness. We show how the maximum source brightness, within its narrow linewidth, is that of a blackbody at the temperature T of a metastable storage level. Experimental results showing laser induced emission at 569 \AA and 637 \AA from a He glow discharge are described. The use of the anti-Stokes process for direct, internal energy transfer from a storage species to a target species is discussed.

In this paper we discuss some of the properties of a new type of vacuum ultraviolet and soft x-ray light source [1,2]. The source is based on spontaneous anti-Stokes scattering from atomic population which is electrically stored in an appropriate metastable level. The source has several unique properties which include: narrow linewidth, tunability, picosecond time scale operation, linear polarization, and relatively high peak spectral brightness. We will see shortly that this peak spectral brightness corresponds to that of a blackbody at the temperature T of the storage level. A schematic of the anti-Stokes light source is shown in Fig.1.

Though anti-Stokes scattering is usually described in terms of a spontaneous scattering cross section, it is better for our purpose to describe it in terms of a spontaneous emission rate $A(\omega)$ induced by the laser pump field E_p at frequency ω_p [3]. This spontaneous emission rate at the vacuum ultraviolet frequency ω may be written

* Work jointly supported by the Office of Naval Research, the National Aeronautics and Space Administration under Contract No. NGL-05-020-103, the Advanced Research Projects Agency, and the Joint Services Electronics Program through the Office of Naval Research.

[†] On leave from the Laboratoire d'Optique Quantique du CNRS, Ecole Polytechnique, 91120 Palaiseau, France; recipient of the French-American CNRS-NSF Exchange Award.

$$\begin{aligned}
A(\omega) &= \frac{\omega^3 |\mu_{13}|^2}{3\pi\hbar\epsilon_0 c^3} \left[\sin^2 \left(\frac{1}{2} \tan^{-1} \frac{\mu_{23} E_p}{\hbar\Delta\omega} \right) \right] g(\omega - \omega_{VUV}) \\
&= \left(\frac{\omega}{\omega_{31}} \right)^3 A_{31} \left[\sin^2 \left(\frac{1}{2} \tan^{-1} \frac{\mu_{23} E_p}{\hbar\Delta\omega} \right) \right] g(\omega - \omega_{VUV}) \quad (1)
\end{aligned}$$

The quantity A_{31} is the Einstein A coefficient for spontaneous emission from level $|3\rangle$ to level $|1\rangle$. The lineshape $g(\omega - \omega_{VUV})$ is the convolution of the Doppler- or pressure-broadened linewidth of the $|1\rangle - |2\rangle$ transition, and $\Delta\omega$ is $\omega_{31} - \omega_{VUV}$.

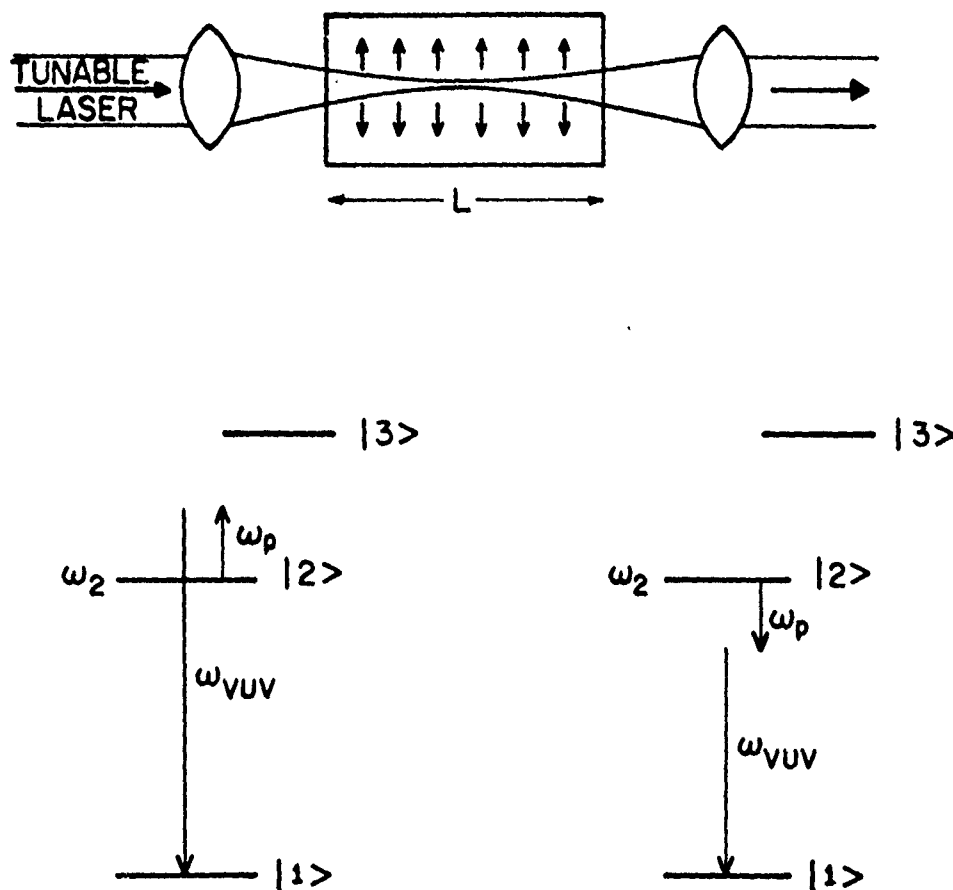


Fig.1 Schematic and energy level diagram for spontaneous anti-Stokes light source. An upper and lower sideband is obtained.

We see from (1) that as the laser pump field becomes large, the anti-Stokes emission rate approaches the Einstein coefficient A_{31} ; which at fixed oscillator strength f_{31} , increases as the square of the VUV frequency. The cross section for spontaneous scattering is related to the emission rate by $\sigma_{sp}(\omega) = \hbar\omega A(\omega)/(P/A)$, where P/A is the incident laser power density.

The key to understanding and optimizing this light source is the two-photon absorption which is created at the ultraviolet frequency ω_{VUV} in the presence of the laser pump frequency ω_p . For the range of laser power densities of interest here, both $A(\omega)$ and the two-photon absorption cross section $\sigma(\omega)$ increase linearly with laser power density, and are related to each other in the same manner as are the emission and absorption coefficients for single-photon processes, i.e., $\sigma(\omega) = (\pi^2 c^2 / \omega^2) A(\omega)$.

The brightness of the light source, $B(\omega)$ photons/(sec cm² steradian cm⁻¹), is determined by the interplay of the emissive and absorptive processes, and for an infinitely long cylinder of outer radius r_0 is given by [1,2]:

$$B(\omega) = \frac{\hbar \omega^3}{4\pi^3 c^2} \left[\frac{1}{\exp(\hbar \omega_{21}/kT) - 1} \right] \left\{ 1 - \exp[-\sigma(\omega)(N_1 - N_2)r_0] \right\} \quad (2a)$$

$$\sigma(\omega) = \frac{\pi \omega}{6c^2 \epsilon_0^2 \hbar^3} \left[\sum_i \left(\frac{\mu_{2i}\mu_{i1}}{\omega_i - \omega_{VUV}} + \frac{\mu_{2i}\mu_{i1}}{\omega_i + \omega_{VUV}} \right) \right]^2 \frac{P_p}{A} g(\omega - \omega_{VUV}) \quad (2b)$$

(mks units). T is the temperature of the metastable level, i.e., $N_2/N_1 = \exp(-\hbar \omega_{21}/kT)$; μ_{ij} are matrix elements; ω_i are the frequencies of the intermediate states; and P_p/A is the power density of the pump laser.

In the (two-photon) optically thin case, i.e., $\sigma(\omega)(N_1 - N_2)r_0 \ll 1$, $B(\omega)$ increases linearly with the laser power density and is the same as obtained from the usual spontaneous scattering cross section point of view. As the laser power density is increased and the medium becomes nominally two-photon opaque, i.e., $\sigma(\omega)(N_1 - N_2)r_0 = 1$, the brightness approaches a constant value equal to that of a blackbody radiator at the temperature T of the metastable level. Once the two-photon opaque or blackbody regime is attained on line center, the primary effect of a further increase in laser power density, cylinder radius r_0 , or ground state density N_1 is to increase the emission linewidth. The total number of emitted photons continues to increase slowly, and the brightness remains constant.

Before proceeding further, we note that anti-Stokes scattering in the VUV has been observed by BRÄUNLICH and LAMBROPOULOS [4], and has been discussed by ZERNIK [5] and VINDOGRADOV and YUKOV [6].

Experimental Results

In our first experiments [2] on this type of light source a glow discharge was used to store population in the $2s^1S$ level of He at $601 \text{ Å} \approx 166,272 \text{ cm}^{-1}$ (Fig. 2). The cw He glow discharge was produced in a 40 cm long quartz tube with a cylindrical hollow cathode and pin anode at opposite ends. Typically, the discharge current was 120 mA and the pressure was about 1 torr. A 0.9 cm long slit was cut through the side wall of the 4 mm ID capillary and served as an input slit for the VUV spectrometer. An actively mode-locked Nd:YAG oscillator-amplifier system produced a train of mode-locked pulses, each with a pulse length of ~ 100 psec. Approximately 10 pulses occurred within the half-power points of the train envelope. The laser was propagated down the discharge capillary tube and focused to an area of about $3 \times 10^{-4} \text{ cm}^2$ and a

confocal parameter $b \cong 5$ cm parallel to the input slit.

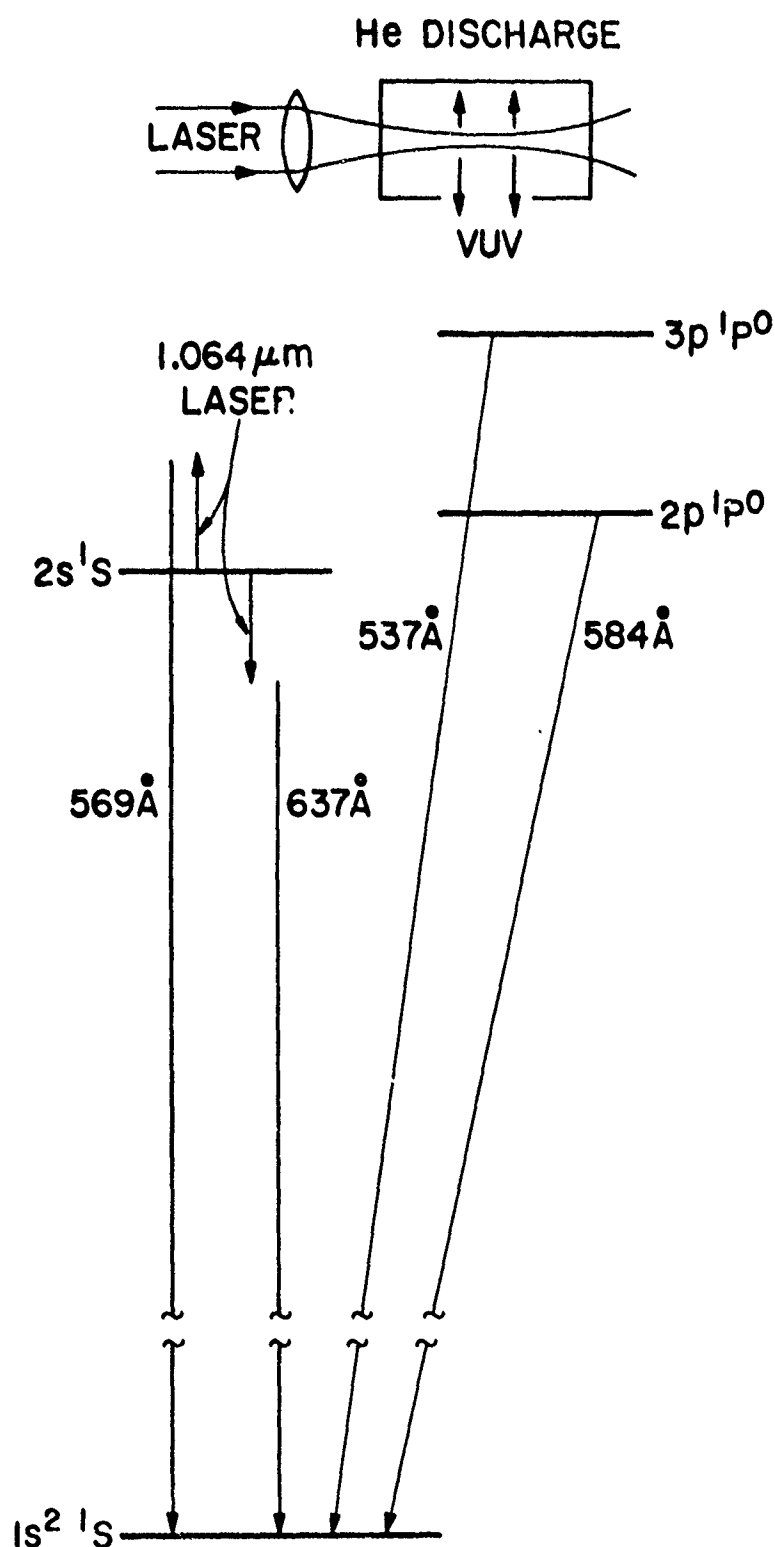


Fig.2 Energy level diagram for laser-induced emission in He.

The detection system consisted of a spiraltron, a fast preamplifier, a pulse height discriminator, a coincidence gate, and a counter. The coincidence gate was set to a width of 90 nsec overlapping the laser pulse train. Typically, 10^2 counts were registered per minute with a signal-to-noise ratio of about 100. The relatively low count rate was a result of the 3×10^{-9} laser duty cycle and the 2.5×10^{-8} ratio of detected photons to total photons generated. Since the source linewidth, even far into the blackbody regime, was well below the resolution of the spectrometer, the observed count rate was proportional to the integrated brightness, $\bar{B} \equiv \int B(\omega) d\omega$.

Using this system we observed laser induced emission at 569 Å, 637 Å, and 591 Å, as well as He resonance line emission at 584 Å, 537 Å, 522 Å, and 516 Å. The emission at 591 Å resulted from anti-Stokes scattering from the He $2s^3s$ level, and had an intensity of about 1/50 of the 569 Å radiation. Figure 3 shows the relative integrated brightness of the 569 Å radiation as a function of laser peak power density for three He pressures. The points represent the average of 5 one-minute counting intervals. The solid curves are theoretical calculations of \bar{B} . As described in [2], the curves were drawn using a value of the two-photon absorption coefficient of $\sigma(\omega_{VUV}) = 1.8 \times 10^{-26} (P_p/A) \text{ W/cm}^2$. The magnitude of each theoretical curve was determined by a least squares fit to the experimental points. Our results indicate that the ratio of metastable population to ground state population, $N_2/N_1 = 2.6 \times 10^{-5}$, which corresponds to a temperature $T = 22,700^\circ\text{K}$. These numbers were independent of pressure in this range to within $\pm 5\%$. At the highest power density and pressure of Fig. 3, the two-photon source had a laser induced optical depth of $r_0 N_1 \sigma(\omega_{VUV}) \sim 7$, well into the blackbody regime.

The relative intensities of the laser induced emission and the He resonance lines are compared in Table I for a pressure of 1.6 torr and a laser power density of 600 GW/cm². The instantaneous count rate was calculated from the accumulated count using the laser repetition rate and either the coincidence gate aperture time (for the resonance lines) or the effective 1 nsec total laser on-time. In order to estimate the brightness we calculated the linewidth of the 537 Å and 584 Å resonance lines for our geometry and pressure. Based on a Voigt profile, these are 3.2 cm⁻¹ and 5.6 cm⁻¹ respectively. The linewidth of the laser induced emission for these operating conditions was calculated as 1.3 cm⁻¹ at 569 Å and 1 cm⁻¹ at 637 Å. The second row of Table I also includes a geometrical factor of 2 to account for the larger effective radiating area of the resonance line source. Thus, we estimate that the peak induced emission at 569 Å is 140 times brighter than the strongest He resonance line. As a result of its greater detuning from the intermediate $2p^1P^0$ level, the brightness of the 637 Å emission is about 7 times smaller than that of the 569 Å emission.

One of the key properties of a laser-induced two-photon radiator is that its geometry is dominantly controlled by the pumping laser beam, instead of by the geometry of the discharge. This allows a two-photon radiator to have a temperature characteristic of the interior of a plasma or discharge. In a glow discharge similar to ours, in the interior, electron collisions cause the population of the $2p^1P$ level to be within a factor of three of the $2s^1S$ population. However, it is the exterior $2p^1P$ level atoms which to a large extent determine the temperature of the single-photon 584 Å radiator. As a result of the fact that these atoms are continuously radiating, as well as due to the lower electron density and temperature near the walls, their

temperature may be significantly lower; thereby probably accounting for the factor of 140 in relative brightness which we have observed. The attenuation and self-reversal of single-photon radiators which results from cold atoms, is also avoided in the two-photon radiator.

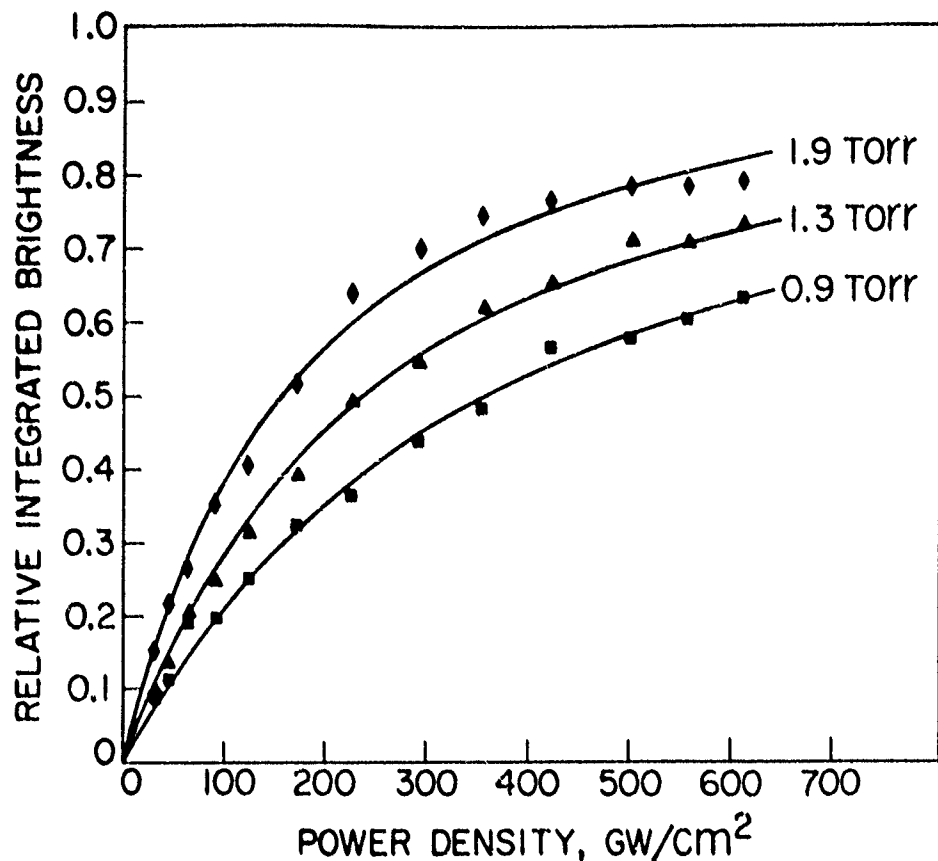


Fig. 3 Relative integrated brightness at 569 Å as a function of 1.06 μm laser peak power density. The theoretical curve at each pressure was determined by numerically integrating (2); the magnitude was determined by a least squares fit to the experimental points at that pressure.

Flashlamp Applications

One of the uses of this type of light source may be as a flashlamp for short wavelength lasers. To avoid the inefficiencies of short wavelength optics, it may be best to mix the target or lasing species directly with the lamp species. For example, neutral potassium at a density of perhaps 10^{14} atoms/cm³ might be mixed with He at a density of about 10^{19} atoms/cm³. The mixture would then be heated either electrically or by a CO₂ laser beam. At an appropriate time, an incident tunable laser pulse would cause the generation of spontaneous anti-Stokes radiation. This radiation would be absorbed by the neutral potassium, and cause the production of excited-state K⁺. A simplified energy level diagram for this type of interaction is shown in Fig. 4. As shown here, the anti-Stokes source would be tuned to an energy of 172,732 cm⁻¹ so as to cause an inner shell transition from the 3p⁶4s level to the 3p⁵4s4d level. A second laser beam of energy greater than 28,739 cm⁻¹ would carry this excited electron into the continuum causing the formation of the excited 3p⁵4s K⁺ ion. By tuning the anti-Stokes source to a discrete

Table 1 Comparison of resonance line radiation and laser induced emission at 1.6 torr and 600 GW/cm².

	Resonance Lines		Laser Induced Emission	
	537 Å	584 Å	569 Å	637 Å
Instantaneous Count Rate 10 ⁶ Counts/Sec	0.8	32.0	544	57
Estimated Peak Brightness* 10 ¹⁵ $\frac{\text{Photons}}{\text{sec cm}^2 \text{ sr cm}^{-1}}$	0.014	0.33	46	6.3

* The time averaged value is obtained by multiplying by the laser duty cycle of 3×10^{-9} .

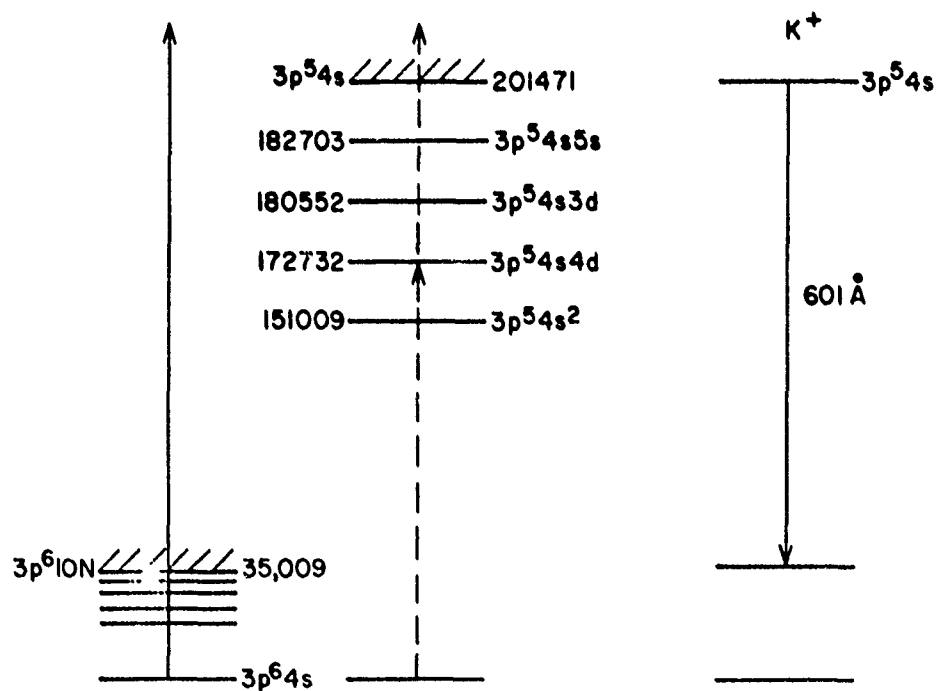


Fig. 4 Simplified energy level diagram for anti-Stokes pumping of K. The (left) solid arrow shows direct pumping to the continuum of an inner shell electron. The dashed arrows show two-photon pumping via an intermediate state.

intermediate state such as shown here, instead of tuning it directly into the continuum as shown by the solid arrow on the left side of Fig. 4, it should be possible to increase the cross section for absorption of the anti-Stokes radiation by about two orders of magnitude. This, in turn, allows operation at a K density much lower than would otherwise be possible, and mitigates, at least somewhat, the problem of the formation of ground state K^+ formed by collision with free electrons.

We should note that the energy required to cause lasing on the 601 Å line of K^+ is quite small. The calculated gain coefficient is $(2.1 \times 10^{-13}) N \text{ cm}^{-1}$, where N is the density of the potassium ions. A gain of e^{10} in a path length of 1 m requires an ion density of $5 \times 10^{11} \text{ atoms/cm}^3$. Assuming a confocal volume of about 1 cm^3 , this requires an energy of about 1 μJ . This energy must be deposited in a time short compared to the 0.6 nsec spontaneous decay time of the K^+ ion.

Before going further we should note that there are two problems associated with the K-He combination of Fig. 4. The first of these is the formation of ground state K ions by autoionization from the $3p^5 4s 4d$ level; the second and possibly more severe problem is the formation of ground state K ions by hot electrons in the discharge. During the afterglow, the density of these ions may rapidly reduce by formation of HeK^+ molecules.

There is an important advantage to the internal or mixed configuration which, in a sense, allows the blackbody limitation to be overcome: to the extent that the product of the single-photon absorption cross section and density of the target species is greater than the two-photon absorption cross section and (ground state) density of the storage species, the anti-Stokes photons will be absorbed by the target instead of reabsorbed by the generating species. For appropriate conditions, the effective anti-Stokes emission rate may then approach that of (1).

We should also briefly address the question of efficiency. At a detuning of 100 cm^{-1} from the 2p resonance line of He the cross section for spontaneous anti-Stokes scattering is $6 \times 10^{-20} \text{ cm}^2$, and varies as the inverse square of the detuning from the 2p level. Assuming an excited state He density of $10^{14} \text{ atoms/cm}^3$, a 1 m path length, and allowing for the energy conversion gain of a factor of 3^4 , the ratio of anti-Stokes power generated to laser power incident is about 2%. This assumes that the media is kept (two-photon) optically thin, or that equivalently, as discussed above, all of the energy is absorbed by the target species; and that the excited state population is not depleted.

In conclusion, the anti-Stokes light source has potential for producing radiation in the VUV and soft x-ray spectral regions with many laser-like properties. These include narrow linewidth, tunability, picosecond operation, and controllable polarization. The source may provide a valuable tool for studying the spectroscopy, fluorescent yield, and autoionizing rates of inner shell transitions. Its use as a pump for VUV and soft x-ray lasers is promising.

The authors acknowledge helpful discussions with Roger Falcone and John Willison.

References

1. S. E. Harris, Appl. Phys. Lett. 31, 498 (October 1977).
2. L. J. Zych, J. Lukasik, J. F. Young, and S. E. Harris, "Laser Induced Two-Photon Blackbody Radiation in the VUV," Phys. Rev. Lett. (to be published).
3. E. Courtens and A. Szoke, Phys. Rev. A 15, 1588 (1977).
4. P. Braunlich and P. Lambropoulos, Phys. Rev. Lett. 25, 135 (1970); Phys. Rev. Lett. 25, 986 (1970); and P. Braunlich, R. Hall, and P. Lambropoulos, Phys. Rev. A 5, 1013 (1972).
5. Wolfgang Zernik, Phys. Rev. 132, 520 (October 1963); Phys. Rev. A 133, 119 (January 1964).
6. A. V. Vinogradov and E. A. Yukov, Sov. J. Quant. Elect. 3, 163 (September-October 1973).

IV

Progress Reports, Technical Reports, Preprints, Publications, and Internal Memoranda Prepared Under the Sponsorship of JSEP [1 July 1973 through 30 September 1978]

Progress Reports, Technical Reports, Preprints, Publications, and Internal Memoranda Prepared under the Sponsorship of JSEP Contracts N00014-67-A-0112-0039 and N00014-75-C-0632 1 July 1973 through 30 September 1978.

H.L. Report No.

- | | |
|------|---|
| 2170 | Staff, "Microwave Research," Annual Status Report No. 6 for the period 1 June 1972 to 31 May 1973 (October 1973). |
| 2179 | C.M. Fortunko and H.J. Shaw, "Signal Transformation with Recirculating SAW Delay Lines," Preprint. Published in IEEE Trans. on Sonics and Ultrasonics <u>SU-21</u> , 1 (January 1974). |
| 2204 | G.S. Kino and H.J. Shaw, "Acoustic Surface Waves," Reprint from Scientific American <u>227</u> , 4, 51-68 (October 1972). |
| 2205 | J.F. Havlice, G.S. Kino, J.S. Kofol, and C.F. Quate, "An Electronically Focused Acoustic Imaging Device," Preprint (August 1973). Presented at the Fifth International Symposium on Acoustical Holography and Imaging, Palo Alto, California, July 18-20, 1973. |
| 2211 | J.F. Havlice, G.S. Kino, and C.F. Quate, "A New Acoustic Imaging Device," Preprint (September 1973). Presented at the International Conference on Solid State Devices, Tokyo, Japan. |
| 2218 | J.F. Havlice, G.S. Kino, and C.F. Quate, "Electronically Focused Acoustic Imaging Device," Technical Report (December 1973). Also, a Reprint from Appl. Phys. Letters <u>23</u> , 11, 581-583 (1 December 1973). |
| 2238 | C.F. Quate, "Optical Imaging Scanning with Acoustic Surface Waves," Preprint (December 1973). Presented at the IEEE Ultrasonics Symposium, November 5-7, 1973 at Monterey, California. |
| 2291 | Staff, "Microwave Research," Semiannual Status Report for the period 1 June - 31 December 1973 (March 1974). |
| 2294 | H. Hayakawa and G.S. Kino, "Storage of Acoustic Signals in Surface States in Silicon," Preprint (May 1974). Also published in Appl. Phys. Letters <u>25</u> , 4, 178-180 (15 August 1974). |
| 2297 | R.A. Lemons and C.F. Quate, "Integrated Circuits as Viewed with an Acoustic Microscope," Preprint (May 1974). Also published in Appl. Phys. Letters <u>25</u> , 5, 251-253 (1 September 1974). |

H.L. Report
No.

- 2333 G.S. Kino, "Acoustical Scanning of Optical and Acoustic Images," Preprint (July 1974). Appeared in the Proceedings of the Optical and Acoustical Micro-Electronics Symposium held in April 1974.
- 2335 J.H. Goll and B.A. Auld, "Multilayer Impedance Matching Schemes for Broadbanding of Water Loaded Piezoelectric Transducers and High Q Electric Resonators," Preprint (July 1974). Also published in IEEE Transactions on Sonics and Ultrasonics, Vol. SU-22, No. 1, 52-53 (January 1975).
- 2378 J. Fraser, J. Havlice, G.S. Kino, W. Leung, H.J. Shaw, K. Toda, T. Waugh, D.K. Winslow, and L. Zitelli, "A Two-Dimensional Electronically Focused Imaging System," Preprint (November 1974). Presented at the IEEE Group on Sonics and Ultrasonics Symposium, November 11-13, 1974.
- 2383 B.A. Auld, C. DeSilets, and G.S. Kino, "A New Acoustic Array for Acoustic Imaging," Preprint (November 1974). Presented at the IEEE Group on Sonics and Ultrasonics Symposium, November 11-13, 1974.
- 2445 J. Fraser, J. Havlice, G. Kino, W. Leung, H. Shaw, K. Toda, T. Waugh, D. Winslow, and L. Zitelli, "An Electronically Focused Two-Dimensional Acoustic Imaging System," Preprint. Reprinted from Acoustical Holography, Vol. 6, 275-304 (February 1975).
- 2453 R.A. Lemons and C.F. Quate, "Advances in Mechanically Scanned Acoustic Microscopy," Preprint. Presented at the 1974 IEEE Ultrasonics Symposium, Milwaukee, Wisconsin November 11-14, 1974 (June 1975).
- 2480 Staff, "Significant Accomplishments," for the period 1 June 1974 - 31 May 1975 (September 1975).
- 2482 C.S. DeSilets, J. Fraser, and G.S. Kino, "Transducer Arrays Suitable for Acoustic Imaging," Preprint (September 1975). Presented at the 1975 IEEE Ultrasonics Symposium at Los Angeles, September 22-24, 1975.
- 2518 G.S. Kino, "Acoustoelectric Interactions in Acoustic Interactions in Acoustic Surface Wave Devices," Preprint (May 1976). Published in Proceedings of the IEEE, 724-748 (May 1976).
- 2519 H.J. Shaw, "Degradation in Noise Figure Along a Chain of Noisy Networks," Internal Memorandum (January 1976).
- 2536 W.L. Bond, C.M. Fortunko, S.L. Quilici, H.J. Shaw, and J. Souquet, "Surface Acoustic Wave Probing with Spaced Interdigital Transducers," Preprint (February 1976).

H.L. Report
No.

- 2565 R. Kompfner, "The Invention of Traveling Wave Tubes," Reprint from IEEE Transactions on Electron Devices, Vol. ED-23, No. 7, 730-738 (July 1976).
- 2570 L. Bui, H.J. Shaw, and L.T. Zitelli, "Study of Acoustic Wave Resonance in Piezoelectric PVF₂ Film," Preprint (May 1976). Published in IEEE Transactions² on Sonics and Ultrasonics, Vol. SU-24, No. 5, 331-336 (September 1977).
- 2573 L. Bui, H.J. Shaw, and L.T. Zitelli, "Experimental Broad-band Ultrasonic Transducers using PVF₂ Piezoelectric Film," Preprint (May 1976). Published in Electronics Letters, Vol. 12, No. 16, 393-394 (5 August 1976).
- 2586 P.G. Borden and G.S. Kino, "Correlation with the Storage Convolver," Preprint (June 1976). Published in Appl. Phys. Letters, 29, No. 9, 527-529 (1 November 1976).
- 2605 D.F. Moore, J.M. Rowell, and M.R. Beasley, "Superconductive Tunneling into Niobium-Tin Thin Films," Reprint from Solid State Communications, Vol. 20, pp. 305-308 (1976).
- 2617 Staff, "Significant Accomplishments," for the period 1 June 1975 - 31 May 1976 (September 1976).
- 2622 B.A. Auld, J.J. Gagnepain, and M. Tan, "Horizontal Shear Surface Waves on Corrugated Surfaces," Preprint (October 1976). Published in Electronics Letters, Vol. 12, 650-651 (25 November 1976).
- 2689 C.F. Quate, "Recount of Program on Acoustic Microscopy," Internal Memorandum (April 1977). Presented at the Acoustic Microscopy Symposium-Workshop, Indianapolis, February 14-18, 1977.
- 2695 C.S. DeSilets, J.D. Fraser, and G.S. Kino, "The Design of Efficient Broadband Piezoelectric Transducers," Preprint (May 1977). Published in IEEE Transactions on Sonics and Ultrasonics, Vol. SU-25, No. 3 (May 1978), pp. 115-125.
- 2708 B.A. Auld and B.-H. Yeh, "Piezoelectric Shear Surface Wave Grating Resonators," Preprint (May 1977). To appear in the Proceedings of the 31st Annual Symposium on Frequency Control.
- 2709 G.S. Kino, "Acoustic Wave Measurements of Semiconductor Parameters," Preprint (June 1977). An invited paper to be presented at the International Symposium on Microwave Diagnostics and Semiconductors at Porvoo, Finland, July 13-15, 1977.

H.L. Report
No.

- 2735 A. Atalar, C.F. Quate, and H.K. Wickramasinghe, "Phase Imaging in Reflection with the Acoustic Microscope," Preprint (August 1977). Published in Appl. Phys. Letters 31, No. 12, 791-793 (15 December 1977).
- 2774 P.M. Grant, "Signal Processors Based on Combined Charge Coupled Devices and Surface Acoustic Wave Devices," Preprint (January 1978). Presented at the 1978 IEEE International Symposium on Circuits and Systems, New York City, May 1978.
- 2819 S.E. Harris, J. Lukasik, J.F. Young, and L.J. Zych, "Anti-Stokes Emission as a VUV and Soft X-ray Source," Preprint (June 1978).
- 2833 C.S. DeSilets, "Transducer Arrays Suitable for Acoustic Imaging," Internal Memorandum and Ph.D. Dissertation (June 1978).
- 2866 C.S. DeSilets, A.R. Selfridge, and G.S. Kino, "Highly Efficient Transducer Arrays Useful in Nondestructive Testing Applications," Preprint (September 1978). To appear in the 1978 Ultrasonics Symposium Proceedings.

UNCLASSIFIED

SECURITY CLASSIFICATION OF THIS PAGE (When Data Entered)

REPORT DOCUMENTATION PAGE		READ INSTRUCTIONS BEFORE COMPLETING FORM																				
1. REPORT NUMBER	2. GOVT. ACCESS. NO.	3. RECIPIENT'S CATALOG NO.																				
4. TITLE (and Subtitle) Research Support and Publications Activity for the Edward L. Ginzton Laboratory & JSEP Contract N00014-75-C-0632 [1 October 1978]		5. TYPE OF REPORT Technical																				
7. AUTHOR(S) M. Chodorow- Principal Investigator, and B.A. Auld, M.R. Beasley, S.E. Harris, G.S. Kino, C.F. Quate, H.J. Shaw and J.F. Young		6. PERFORMING ORG.'N REPORT NO. GL 2924																				
9. PERFORMING ORG.'N NAME AND ADDRESS Edward L. Ginzton Laboratory Stanford University Stanford, CA 94305		8. CONTRACT OR GRANT NO. N00014-75-C-0632																				
11. CONTROLLING OFFICE NAME AND ADDRESS Chairman, Joint Services Electronics Program [Through] Office of Naval Research 800 North Quincy Street, Arlington VA 22217		10. PROGRAM ELEMENT, PROJECT, TASK AREA & WORK UNIT NUMBERS																				
14. MONITORING AGENCY NAME & ADDRESS (if different from 11. above)		12. REPORT DATE 1 October 1978																				
		13. NO. OF PAGES 142																				
		15. SECURITY CLASS (of this report) UNCLASSIFIED																				
		15a. DECLASSIFICATION DOWNGRADING SCHEDULE																				
16. DISTRIBUTION STATEMENT (of this Report) Approved for public release; distribution unlimited.																						
17. DISTRIBUTION STATEMENT (of the Abstract entered in Block 20 if different from Report)																						
18. SUPPLEMENTARY NOTES																						
19. KEY WORDS (Continue on reverse side if necessary and identify by Block no.) <table border="0"> <tr> <td>Electronic Scanning</td> <td>Surface Acoustic Waves</td> <td>Multilayer Impedance Matching</td> <td>Anti-Stokes Emission</td> </tr> <tr> <td>Acoustic Beam Focusing</td> <td>Acoustic Radiation</td> <td>Piezoelectric PVF₂ Film</td> <td>VUV & Soft X-Ray Source</td> </tr> <tr> <td>Acoustic Imaging</td> <td>Ultrasonic Transducers</td> <td>Acousto-optic Interaction</td> <td>Quantum Electronics</td> </tr> <tr> <td>Acoustic Transducer Arrays</td> <td>SAW Delay Lines</td> <td>Superconductive Tunneling</td> <td>Lasers</td> </tr> <tr> <td>Nondestructive Testing</td> <td>Acoustic Microscopy</td> <td>Horizontal Shear Waves</td> <td>Solid State Devices</td> </tr> </table>			Electronic Scanning	Surface Acoustic Waves	Multilayer Impedance Matching	Anti-Stokes Emission	Acoustic Beam Focusing	Acoustic Radiation	Piezoelectric PVF ₂ Film	VUV & Soft X-Ray Source	Acoustic Imaging	Ultrasonic Transducers	Acousto-optic Interaction	Quantum Electronics	Acoustic Transducer Arrays	SAW Delay Lines	Superconductive Tunneling	Lasers	Nondestructive Testing	Acoustic Microscopy	Horizontal Shear Waves	Solid State Devices
Electronic Scanning	Surface Acoustic Waves	Multilayer Impedance Matching	Anti-Stokes Emission																			
Acoustic Beam Focusing	Acoustic Radiation	Piezoelectric PVF ₂ Film	VUV & Soft X-Ray Source																			
Acoustic Imaging	Ultrasonic Transducers	Acousto-optic Interaction	Quantum Electronics																			
Acoustic Transducer Arrays	SAW Delay Lines	Superconductive Tunneling	Lasers																			
Nondestructive Testing	Acoustic Microscopy	Horizontal Shear Waves	Solid State Devices																			
20. ABSTRACT (Continue on reverse side if necessary and identify by Block no.) <p>This report has been assembled and prepared to provide information concerning the general thrust of research programs with the E. L. Ginzton Laboratory- not only those of the JSEP project faculty- but other research faculty as well. It lists all ongoing research contracts and grants, including P.I., subject, sponsoring agency, annual rate and expiration date for each contract or grant. It includes copies of selected representative journal publications citing JSEP sponsorship, a list of all JSEP reports and publications for recent years and a Supplemental "Index of Reports" giving publication citations and abstracts for all Ginzton Laboratory programs from 1 January 1977 through 30 September 1978.</p>																						